

Recent advancements in modeling and simulations of ion channels

Edited by

Simone Furini, Luca Maragliano and Matteo Masetti

Published in

Frontiers in Molecular Biosciences



FRONTIERS EBOOK COPYRIGHT STATEMENT

The copyright in the text of individual articles in this ebook is the property of their respective authors or their respective institutions or funders. The copyright in graphics and images within each article may be subject to copyright of other parties. In both cases this is subject to a license granted to Frontiers.

The compilation of articles constituting this ebook is the property of Frontiers.

Each article within this ebook, and the ebook itself, are published under the most recent version of the Creative Commons CC-BY licence. The version current at the date of publication of this ebook is CC-BY 4.0. If the CC-BY licence is updated, the licence granted by Frontiers is automatically updated to the new version.

When exercising any right under the CC-BY licence, Frontiers must be attributed as the original publisher of the article or ebook, as applicable.

Authors have the responsibility of ensuring that any graphics or other materials which are the property of others may be included in the CC-BY licence, but this should be checked before relying on the CC-BY licence to reproduce those materials. Any copyright notices relating to those materials must be complied with.

Copyright and source acknowledgement notices may not be removed and must be displayed in any copy, derivative work or partial copy which includes the elements in question.

All copyright, and all rights therein, are protected by national and international copyright laws. The above represents a summary only. For further information please read Frontiers' Conditions for Website Use and Copyright Statement, and the applicable CC-BY licence.

ISSN 1664-8714
ISBN 978-2-83250-954-8
DOI 10.3389/978-2-83250-954-8

About Frontiers

Frontiers is more than just an open access publisher of scholarly articles: it is a pioneering approach to the world of academia, radically improving the way scholarly research is managed. The grand vision of Frontiers is a world where all people have an equal opportunity to seek, share and generate knowledge. Frontiers provides immediate and permanent online open access to all its publications, but this alone is not enough to realize our grand goals.

Frontiers journal series

The Frontiers journal series is a multi-tier and interdisciplinary set of open-access, online journals, promising a paradigm shift from the current review, selection and dissemination processes in academic publishing. All Frontiers journals are driven by researchers for researchers; therefore, they constitute a service to the scholarly community. At the same time, the *Frontiers journal series* operates on a revolutionary invention, the tiered publishing system, initially addressing specific communities of scholars, and gradually climbing up to broader public understanding, thus serving the interests of the lay society, too.

Dedication to quality

Each Frontiers article is a landmark of the highest quality, thanks to genuinely collaborative interactions between authors and review editors, who include some of the world's best academicians. Research must be certified by peers before entering a stream of knowledge that may eventually reach the public - and shape society; therefore, Frontiers only applies the most rigorous and unbiased reviews. Frontiers revolutionizes research publishing by freely delivering the most outstanding research, evaluated with no bias from both the academic and social point of view. By applying the most advanced information technologies, Frontiers is catapulting scholarly publishing into a new generation.

What are Frontiers Research Topics?

Frontiers Research Topics are very popular trademarks of the *Frontiers journals series*: they are collections of at least ten articles, all centered on a particular subject. With their unique mix of varied contributions from Original Research to Review Articles, Frontiers Research Topics unify the most influential researchers, the latest key findings and historical advances in a hot research area.

Find out more on how to host your own Frontiers Research Topic or contribute to one as an author by contacting the Frontiers editorial office: frontiersin.org/about/contact

Recent advancements in modeling and simulations of ion channels

Topic editors

Simone Furini — University of Bologna, Italy

Luca Maragliano — Marche Polytechnic University, Italy

Matteo Masetti — University of Bologna, Italy

Citation

Furini, S., Maragliano, L., Masetti, M., eds. (2022). *Recent advancements in modeling and simulations of ion channels*. Lausanne: Frontiers Media SA.
doi: 10.3389/978-2-83250-954-8

Table of contents

04	Editorial: Recent advancements in modeling and simulations of ion channels Simone Furini, Luca Maragliano and Matteo Masetti
06	The Impact of Mutation L138F/L210F on the Orai Channel: A Molecular Dynamics Simulation Study Xiaoqian Zhang, Hua Yu, Xiangdong Liu and Chen Song
15	Unveiling the Gating Mechanism of CRAC Channel: A Computational Study Carlo Guardiani, Delia Sun and Alberto Giacomello
34	Exploring K_v1.2 Channel Inactivation Through MD Simulations and Network Analysis Flavio Costa, Carlo Guardiani and Alberto Giacomello
43	From Acid Activation Mechanisms of Proton Conduction to Design of Inhibitors of the M2 Proton Channel of Influenza A Virus Elnaz Aledavood, Beatrice Selmi, Carolina Estarellas, Matteo Masetti and F. Javier Luque
64	Molecular Insights Into Binding and Activation of the Human KCNQ2 Channel by Retigabine Barbara Garofalo, Alexandre M.J.J. Bonvin, Andrea Bosin, Francesco P. Di Giorgio, Rosella Ombrato and Attilio V. Vargiu
78	Unifying Single-Channel Permeability From Rare-Event Sampling and Steady-State Flux Yi-Chun Lin and Yun Lyna Luo
88	Exploring the Conformational Impact of Glycine Receptor TM1-2 Mutations Through Coarse-Grained Analysis and Atomistic Simulations Anil Ranu Mhashal, Ozge Yoluk and Laura Orellana
105	A Multi-Scale Approach to Model K⁺ Permeation Through the KcsA Channel T. L. Horng, R. S. Chen, M. V. Leonardi, F. Franciolini and L. Catacuzzeno
120	Chanalyzer: A Computational Geometry Approach for the Analysis of Protein Channel Shape and Dynamics Andrea Raffo, Luca Gagliardi, Ulderico Fugacci, Luca Sagresti, Simone Grandinetti, Giuseppe Brancato, Silvia Biasotti and Walter Rocchia
129	Role of TM3 in claudin-15 strand flexibility: A molecular dynamics study Shadi Fuladi, Sarah McGuinness and Fatemeh Khalili-Araghi



OPEN ACCESS

EDITED AND REVIEWED BY
Massimiliano Bonomi,
Institut Pasteur, France

*CORRESPONDENCE

Matteo Masetti,
matteo.masetti4@unibo.it
Simone Furini,
simone.furini@unibo.it
Luca Maragliano,
luca.maragliano@iit.it

SPECIALTY SECTION

This article was submitted to Biological
Modeling and Simulation,
a section of the journal
Frontiers in Molecular Biosciences

RECEIVED 14 November 2022

ACCEPTED 16 November 2022

PUBLISHED 22 November 2022

CITATION

Furini S, Maragliano L and Masetti M
(2022), Editorial: Recent advancements
in modeling and simulations of
ion channels.
Front. Mol. Biosci. 9:1098216.
doi: 10.3389/fmolb.2022.1098216

COPYRIGHT

© 2022 Furini, Maragliano and Masetti.
This is an open-access article
distributed under the terms of the
[Creative Commons Attribution License
\(CC BY\)](#). The use, distribution or
reproduction in other forums is
permitted, provided the original
author(s) and the copyright owner(s) are
credited and that the original
publication in this journal is cited, in
accordance with accepted academic
practice. No use, distribution or
reproduction is permitted which does
not comply with these terms.

Editorial: Recent advancements in modeling and simulations of ion channels

Simone Furini^{1*}, Luca Maragliano^{2,3*} and Matteo Masetti^{4*}

¹Department of Electrical, Electronic and Information Engineering “Guglielmo Marconi”, Alma Mater Studiorum–University of Bologna, Cesena, Italy, ²Department of Life and Environmental Sciences, Polytechnic University of Marche, Ancona, Italy, ³Center for Synaptic Neuroscience and Technology (NSYN@UniGe), Istituto Italiano di Tecnologia, Genova, Italy, ⁴Department of Pharmacy and Biotechnology, Alma Mater Studiorum–University of Bologna, Bologna, Italy

KEYWORDS

molecular dynamics simulation, enhanced sampling algorithms, multiscale modeling, channel gating mechanism, ion conduction

Editorial on the Research Topic

Recent advancements in modeling and simulations of ion channels

Computational modeling and simulations have long been recognized as key tools for a detailed characterization of ion channel functionality, which is pivotal for a deeper understanding of several physiological and pathophysiological processes. This is particularly relevant in light of the currently available computational resources that finally allow studying the complex molecular mechanisms driving conduction, selectivity, and gating. Still, the need to provide a direct link with experimental measurements calls for advanced simulation frameworks, including enhanced sampling techniques and/or multiscale models, while adequate analysis tools must be devised to cope with an ever-increasing amount of data. Articles on this Research Topic reflect the close interplay among these aspects and provide insight into advances in computational simulations in the field of ion channels both from a methodological and application standpoint.

Gating and allosteric activation of the Orai protein belonging to the calcium-release activated calcium (CRAC) channel family is an example of complex molecular mechanisms that can be untangled through computational approaches. By performing repeated sub-microsecond-long molecular dynamics (MD) simulations based on the Orai crystal structure from *Drosophila melanogaster* (dOrai), [Zhang et al.](#) showed that increased pore hydration in the gain-of-function L210F mutant facilitates channel opening with respect to the wildtype (WT) channel, regardless of activator binding. The dOrai gating mechanism was instead explicitly investigated through enhanced sampling by [Guardiani et al.](#) A complex allosteric propagation mechanism going from the activator binding site to the inner helices was revealed through contact map analysis, which was recapitulated into a gating mechanism involving a “steric brake” and the formation of vacuum bubbles inside the pore. Contact map analysis, complemented with network analysis, was also exploited by [Costa et al.](#) for highlighting the molecular determinants underlying the inactivation mechanism of the voltage-gated

potassium channel $K_v1.2$. The approach allowed the authors to identify two distinct allosteric pathways coupling the voltage-sensing domain and the pore domain to the selectivity filter, where channel inactivation is expected to occur. The allosteric pathways were compared with those obtained from nine mutants known to impair the inactivation mechanism, supporting their hypothesis.

The system size required to correctly describe the molecular assemblies under investigation is critical to consider when facing ion channel modeling. For studying the claudin-15 strands and their role in tight junctions, [Fuladi et al.](#) adopted a combination of all-atom and hybrid resolution schemes, which allowed them to simulate double-membrane systems up to the sub-micrometer length scale. By comparing the dynamics of the WT and A134P mutant, the authors showed that the mutation significantly affects the mechanical properties of the strands, including lateral flexibility and persistence length. Rationalizing the impact of mutations on the dynamics and function of a member of the superfamily of pentameric ligand-gated ion channels (PLGICs), the Glycine Receptor (GlyR), was instead the subject of the contribution by [Mhashal et al.](#) Through the integration of bioinformatics tools and structural analysis, the authors identified three mutations reported in human tumors linked to the disruption of glycinergic currents that were expected to impact GlyR conformation. Then, by mapping the MD trajectories on a low-dimensionality space capturing the conformational variability encoded in several functional states of the channel, they highlighted a divergent behavior of the mutants with respect to the WT. This example emphasizes the role played by sophisticated analysis tools both in planning and interpreting simulation results. In this context, [Raffo et al.](#) presented a novel analysis method for the geometrical characterization of the shape and dynamics of ion channels which does not rely on user-dependent parameters, like the pore axis, and that is specifically devised for processing MD trajectories.

Modulation of channels' dynamics and functionality through ligand binding is another aspect of ion channel research that can benefit from advances in computational simulations. For example, [Garofalo et al.](#) characterized the binding mode of the small-molecule modulator retigabine to the $K_v7.2$ channel through an elaborate computational framework involving homology modeling, MD simulations, and ensemble docking. Specifically, they showed that retigabine can bind multiple functional states of the channel and provided molecular insights into the ligand-induced activation process. The importance of channels as pharmaceutical targets was also underscored by [Aledavood et al.](#) In their Review, the authors provide a comprehensive picture of the structural and mechanistic aspects related to the function of the M2 proton channel of the Influenza A virus, and how this knowledge can be exploited for computer-aided drug design, especially in light of the emergence of resistant strains.

Ion permeation is perhaps the most distinctive feature of ion channel functionality that poses specific challenges to modeling

and simulations. [Lin and Luo](#) presented a systematic benchmark of widespread approaches to single-channel permeability calculation applied on a carbon nanotube as a small-conductance ion channel model. Comparing results obtained from enhanced sampling methods like umbrella sampling and milestoning on the one hand, and out-of-equilibrium steady-state flux under applied voltage on the other, they discuss the advantages and drawbacks of the different techniques, providing useful guidelines for further investigations in the field. Finally, a bottom-up multiscale approach was developed by [Horng et al.](#) to study the longtime controversial mechanism of K^+ permeation through the prototypical KcsA channel. The proposed method is based on a kinetic model fed with rate constants obtained from enhanced sampling. In this way, they managed to estimate current-voltage and current-concentration characteristics, providing a link between atomic structures and single-channel experimental data.

Overall, the studies presented in this Research Topic demonstrate the liveliness of computational methods in the field of ion channels and how methodological advances in simulations and analysis frameworks are fostering a better understanding of the molecular mechanisms responsible for their functionality.

Author contributions

All authors listed have made a substantial, direct, and intellectual contribution to the work and approved it for publication.

Acknowledgments

We thank all the contributors and reviewers of this Research Topic.

Conflict of interest

The authors declare that the research was conducted in the absence of any commercial or financial relationships that could be construed as a potential conflict of interest.

Publisher's note

All claims expressed in this article are solely those of the authors and do not necessarily represent those of their affiliated organizations, or those of the publisher, the editors and the reviewers. Any product that may be evaluated in this article, or claim that may be made by its manufacturer, is not guaranteed or endorsed by the publisher.



The Impact of Mutation L138F/L210F on the Orai Channel: A Molecular Dynamics Simulation Study

Xiaoqian Zhang^{1,2†}, Hua Yu^{1,3*†}, Xiangdong Liu² and Chen Song^{1,4*}

¹Center for Quantitative Biology, Academy for Advanced Interdisciplinary Studies, Peking University, Beijing, China, ²School of Physics, Shandong University, Jinan, China, ³College of Plant Protection, Shandong Agricultural University, Taian, China,

⁴Peking-Tsinghua Center for Life Sciences, Academy for Advanced Interdisciplinary Studies, Peking University, Beijing, China

OPEN ACCESS

Edited by:

Luca Maragliano,
Marche Polytechnic University, Italy

Reviewed by:

Albert Lau,
Johns Hopkins University,
United States
Riccardo Nifosi,
National Research Council (CNR), Italy

*Correspondence:

Hua Yu
yuh@sdau.edu.cn
Chen Song
c.song@pku.edu.cn

[†]These authors have contributed
equally to this work.

Specialty section:

This article was submitted to
Biological Modeling and Simulation,
a section of the journal
Frontiers in Molecular Biosciences

Received: 08 August 2021

Accepted: 17 September 2021

Published: 02 November 2021

Citation:

Zhang X, Yu H, Liu X and Song C
(2021) The Impact of Mutation L138F/
L210F on the Orai Channel: A
Molecular Dynamics Simulation Study.
Front. Mol. Biosci. 8:755247.
doi: 10.3389/fmolb.2021.755247

The calcium release-activated calcium channel, composed of the Orai channel and the STIM protein, plays a crucial role in maintaining the Ca^{2+} concentration in cells. Previous studies showed that the L138F mutation in the human Orai1 creates a constitutively open channel independent of STIM, causing severe myopathy, but how the L138F mutation activates Orai1 is still unclear. Here, based on the crystal structure of *Drosophila melanogaster* Orai (dOrai), molecular dynamics simulations for the wild-type (WT) and the L210F (corresponding to L138F in the human Orai1) mutant were conducted to investigate their structural and dynamical properties. The results showed that the L210F dOrai mutant tends to have a more hydrated hydrophobic region (V174 to F171), as well as more dilated basic region (K163 to R155) and selectivity filter (E178). Sodium ions were located deeper in the mutant than in the wild-type. Further analysis revealed two local but essential conformational changes that may be the key to the activation. A rotation of F210, a previously unobserved feature, was found to result in the opening of the K163 gate through hydrophobic interactions. At the same time, a counter-clockwise rotation of F171 occurred more frequently in the mutant, resulting in a wider hydrophobic gate with more hydration. Ultimately, the opening of the two gates may facilitate the opening of the Orai channel independent of STIM.

Keywords: orai, mutation, gating, ion channel, molecular dynamics

INTRODUCTION

Calcium ions, as an essential second messenger in cells, regulate a wide range of physiological processes. Store-operated calcium entry (SOCE) was identified to explain how depletion of endoplasmic reticulum (ER) Ca^{2+} stores evokes Ca^{2+} influx across the plasma membrane. (Putney, 1986). Up to now, the relatively well-studied SOCE channel is the “calcium release-activated calcium” (CRAC) channel, which is involved in numerous cell activities such as gene transcription, muscle contraction, secretion, cell proliferation, differentiation and apoptosis etc. (Engh et al., 2012; Feske et al., 2012; Soboloff et al., 2012; Prakriya and Lewis, 2015) Both loss-of-function and gain-of-function mutations of the CRAC channel lead to devastating immunodeficiencies, bleeding disorders and muscle weakness. (Feske et al., 2005; Feske, 2010; Endo et al., 2015; Garibaldi et al., 2017). In recent decades, our understanding of the operational mechanisms of the CRAC channel including the gating mechanism has been greatly advanced, with the discovery of its molecular components, stromal interaction molecule (STIM) and the

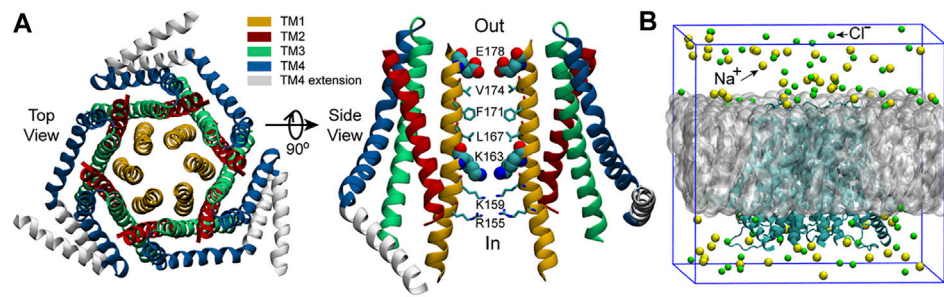


FIGURE 1 | The structure of dOrai and the initial simulation system. **(A)** The crystal structure of *Drosophila melanogaster* Orai obtained from the Protein Data Bank (PDB ID: 4HKR) (Hou et al., 2012). In the right panel, only two opposing subunits are shown for clarity. The SF of the pore, E178, and the starting residue of the basic region, K163, are shown with the VDW representation, the other pore residues are shown with Licorice representation in VMD (visual molecular dynamics) (Humphrey et al., 1996). **(B)** The initial simulation system. The grey sphere represents the POPC bilayer. Water molecules are not shown here but included in the simulations.

pore-forming protein Orai. (Liou et al., 2005; Prakriya et al., 2006). The STIMs are single-pass ER transmembrane proteins, function as the sensor of the Ca^{2+} concentration inside the ER, bind to and activate Orai channels. (Liou et al., 2005; Stathopulos et al., 2006). Two mammalian homologs, STIM1 and STIM2, are included in the STIMs family and the former one is more widely studied. Orai, the calcium channel that opens to permit the influx of the calcium ions, locates on the plasma membrane and contains three closely conserved mammalian homologs, Orai1, Orai2 and Orai3. (Vig et al., 2006; Hoth et al., 2013).

Orai1 has a high calcium selectivity (>1000-fold over Na^+) and low conductivity (<1 pS). (Hogan et al., 2010; Prakriya and Lewis, 2006). According to the structure of Orai (Figure 1A), (McNally et al., 2009; Zhou et al., 2010; Hou et al., 2012) the transmembrane Orai is composed of six subunits with a central pore formed by six helices denoted as transmembrane one (TM1). TM1 are surrounded by two rings: one is composed of TM2 and TM3, the other is TM4. There is another helix which extends into the cytosol, termed TM4 extension. As TM1 helices are tightly wrapped by TM2 and TM3 helices, they may have limited space to expand to allow the CRAC channel open. (Liou et al., 2005; Roos et al., 2005). The TM1 helices can be divided into four distinct regions (Figure 1A): the selectivity filter (SF) - a ring of glutamates (E178), the hydrophobic region (V174, F171, L167), the basic region (K163, K159, R155) and the cytosolic region. (Hou et al., 2012). The glutamate-ring (E178) functions as a SF and makes the channel have a high calcium ion selectivity, which is the most significant feature of Orai channels. Mutation of the residue E178 to aspartate disrupts Ca^{2+} -selectivity. (Yeromin et al., 2006). The well-packed side chains of V174, F171 and L167 form the inner wall of the hydrophobic region, having extensive hydrophobic interactions with one another, and are strictly conserved among Orai channels. (McNally et al., 2012; Gudlur et al., 2014). These hydrophobic residues are located at the center of the protein, which likely form a gate of the pore. The V174A mutation yields an activated channel with altered ion selectivity even if its pore structure shows no obvious changes compared to the wild-type (WT), and a slight difference of the

number of water molecules in the hydrophobic region is enough to change the conduction state of the pore, (Dong et al., 2013), indicating the significant role of the hydrophobic region in gating. Another important region locates in the lower part of the channel and lines by three basic residues (K163, K159 and R155), creating an unexpected positively charged environment for the pore that conducts cations. Generally, K163 corresponds to the narrowest point of the pore, resulting in large electrostatic repulsion between this positively charged residue and cations passing by. Therefore, K163 is believed to be the other gate of the pore and jointly regulates the channel state together with the hydrophobic gate. (Zhang et al., 2011).

Molecular dynamics (MD) simulation is a powerful tool to study the gating and permeation mechanisms of ion channels, which can provide detailed dynamic information. Based on the crystal structure of the closed dOrai (Hou et al., 2012), many MD works have been done to understand the gating and permeation processes through simulations of the WT dOrai/hOrai1 (Orai1 of human), or dOrai/hOrai1 mutants that were either constitutively open or loss-of-function. Mutations on the TM1 were the first to get attention as TM1 constitutes the pore. Through simulations of the dOrai V174A mutant, Dong et al. revealed the regulation of pore waters to the ion permeation and the counterion-assisted cation transport mechanism of Orai. (Dong et al., 2013; Dong et al., 2014). Through simulations for the dOrai V174A, F171V and F171Y mutants, Yamashita et al. revealed the counter-clockwise rotation of F171. (Yamashita et al., 2017). The hOrai1 E106D mutant (corresponding to dOrai E178D mutant) was used to study the binding site of the selective inhibitor Synta66. (Waldherr et al., 2020). These simulations were all performed with CHARMM36/27 (MacKerell et al., 1998) force field. Mutations on the TM2, such as hOrai1 H134A, L138F, A137V and R91G (TM1) (corresponding to dOrai H206A, L210F, A209V and R163G mutants) were investigated to show the regulation of TM2 to the channel states through transmembrane helix connectivity, particularly via the hydrogen bonding in the H134A mutant. (Frischauf et al., 2017). Mutations on the extracellular loops (loop1 between TM1 and TM2, and loop3 between TM3 and

TM4), such as hOrai1 D110A, R210A, K214A and R210A/K214A, were systematically studied, which revealed the presence of an extracellular Ca^{2+} -accumulating region at the pore entrance of hOrai1. (Frischauf et al., 2015). These above two work were performed with the OPLS (Tirado-Rives, 1988) (Optimized Potentials for Liquid Simulations) all-atom force field. In addition, the pore hydration and degrees of the counter-clockwise rotation of F171 were also investigated in several TM2 mutants (dOrai H206S/C/Q/Y mutants) with CHARMM36 force field. (Yeung et al., 2018). Through conventional molecular dynamics with CHARMM36 force field and Brownian dynamics, a mutation on TM3 (dOrai E262Q) was studied, which revealed the key role of the configuration of residues K270 on the selectivity of the pore. (Alavizargar et al., 2018). Besides, a series of double point mutants that involve both a gain-of-function and a loss-of-function single point mutations were studied, which confirmed the dominant role of loss-of-function mutations (hOrai1 K85E/H134A, H134A/E149K, H134A/L174D and H134A/S239W mutants, corresponding to dOrai K157E/H206A, H206A/E221K, H206A/L246D and H206A/S311W mutants). (Tiffner et al., 2021). Multiple point mutants were also investigated. A series of multiple point mutations on basic residues were studied and revealed the promotion of the inner basic residues to the opening of the outer hydrophobic gate (dOrai R155S/K159S/R163S, R155S/K159S/R163S/V174A, R155S/K159S/R163S/W148A, K159S/K163S/V174A, K159S/K163S, K163W/V174A and K163W mutants). (Yamashita et al., 2019). This work was also performed with CHARMM36 force field.

The aforementioned computational studies have provided highly valuable insight for understanding the gating and permeation mechanisms of Orai channels. In the meantime, previous experiments have also shown that the L138F mutation in human Orai1 yields a constitutively permeant channel that allows ion conduction in the absence of STIM1, and the constitutively active L138F mutant channel can cause severe myopathy. (Endo et al., 2015). However, the activation mechanism of the L138F Orai1 mutant is not well studied yet. The structure of human Orai1 has not been resolved so far, while the closed state crystal structure of dOrai, which shares 73% sequence identity with human Orai1 within the transmembrane region, has been resolved by Hou et al. at a resolution of 3.35 Å (Figure 1A). (Hou et al., 2012) The L138F mutation in human Orai1 corresponds to the mutation L210F in dOrai of *Drosophila melanogaster*. In order to better understand how L210F mutation activates the channel, molecular dynamics (MD) simulations for the WT and the L210F mutant channels were carried out. Our results revealed a previously unobserved rotation of the residue F210 in the mutant, and the larger rotation angle of F210 in the mutant might be the origin of the activation of the L210F mutant. It was also observed that the rotation of F171 may also play an important role for the activation, as previously reported (Yamashita et al., 2017). Therefore, our simulation results reveal a plausible activation mechanism of the L210F dOrai mutant and may provide a new perspective for understanding the activation mechanism of CRAC channels.

MATERIALS AND METHODS

Molecular Dynamics Simulations

The crystal structure of *Drosophila melanogaster* Orai obtained from the Protein Data Bank (PDB ID: 4HKR) (Hou et al., 2012) was used as the starting structure. MODELLER (Fiser et al., 2000) was used to build the missing residues of the TM1-TM2 loop (residue number: 181–190) and the TM2-TM3 loop (residue number: 220–235) on the basis of the starting structure. After that, the complete WT dOrai structure was used to construct the initial simulation system of the WT dOrai (Figure 1B) using the bilayer-builder module of CHARMM-GUI (Jo et al., 2010) with the channel axis oriented along the z-axis. The above complete WT dOrai structure was also used to construct the initial simulation system of the L210F dOrai mutant (Figure 1B) in a very similar way, except that in the PDB Info section, the mutation option under PDB manipulation was chosen and L210 of all the six chains were set to mutate to F210 in CHARMM-GUI. For each system, the protein was embedded within a 1-palmitoyl-2-oleoyl-sn-glycero-3-Phosphatidylcholine (POPC) bilayer with 150 mM NaCl to neutralize the system. The final system size was $110.3 \times 110.3 \times 105.3 \text{ Å}^3$ and there were around 116k atoms in the simulation system.

All the molecular dynamics simulations were conducted using GROMACS 5.1.3 (Abraham et al., 2015) with CHARMM36 (MacKerell et al., 1998; Klauda et al., 2010; Best et al., 2012) force field and TIP3P (Jorgensen et al., 1983) water model. A 500-ps NVT equilibration and a 500-ps NPT equilibration were performed after energy minimization. Then, three 500-ns production simulations with different starting velocities were conducted for each system. Position restraints with a force constant of 1,000 kJ/mol/nm² (Soboloff et al., 2012) were applied on the backbone atoms of the protein for the equilibration simulations. The periodic boundary conditions were used and the time step was 2 fs. The velocity-rescaling algorithm (Bussi et al., 2007) with a time constant of 0.5 ps was used to maintain the temperature at 310 K. Protein, membrane, and water and ions were coupled separately. The Parrinello-Rahman algorithm (Parrinello and Rahman, 1981) with a time constant of 5 ps was used to maintain the pressure at 1.0 Bar. The Particle-Mesh-Ewald (PME) (Essmann et al., 1995) method was used to calculate electrostatics and the van der Waals interactions were computed within a cut-off of 1.2 nm. VMD (Humphrey et al., 1996) was used to view trajectories and render figures.

RESULTS

Structural Stability of the WT Orai and the L210F Mutant

The root mean square deviation (RMSD) of all six trajectories for both the WT and the L210F mutant were monitored to evaluate their structural changes and stability. The results showed that the systems reached equilibrium states at about 300 ns (Figures 2A,B) with the $\text{C}\alpha$ -RMSD of the WT and the mutant converging to 0.41 and 0.47 nm respectively. This time scale

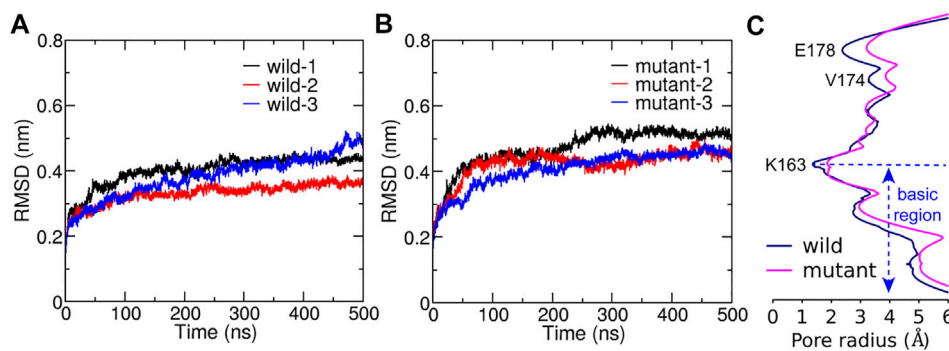


FIGURE 2 | The structural stability during simulations and the average pore radius after reaching equilibrium. C α -RMSD of the WT (A) and the L210F mutant (B). Three trajectories are represented in red, blue and black, respectively. (C) The average pore radii. The average pore radii for the WT and the L210F mutant were obtained by calculating the pore radius of the average structures obtained from the last 200 ns of all of the three trajectories for each protein. Hole 2.0 (Smart et al., 1996) was used to calculate the radius with all the hydrogen atoms removed in the calculation.

and the RMSD values were slightly larger than the work of Amcheslavsky et al. (Amcheslavsky et al., 2015) and Frischauf et al. (Frischauf et al., 2017), in which the values were roughly 120 ns and 0.2 nm. As Amcheslavsky et al. (Amcheslavsky et al., 2015) discussed, the smaller RMSD in their work may be caused by different system setups that can stabilize the protein structure, such as the addition of phosphates in the basic region, using of neutralized protonation states, addition of cation ions (Ca²⁺ or Gd³⁺) in the SF and addition of cholesterol into the membrane. Our results were more comparable to the work of Dong et al. (Dong et al., 2013) owing to similar simulation setups, indicating that the stability of Orai can be influenced by the surrounding environment. In addition, the RMSD of the mutant experienced a larger increase during the initial stage of the simulations, reflecting the influence of the residue mutation on the structure (Figure 2B).

The pore radius was calculated to evaluate the effect of the L210F mutation on the channel state (Figure 2C and Supplementary Figure S1). The simulation results revealed three significant radius changes of the mutant (Figure 2C). The first one occurred in the SF, the glutamate ring - E178, which binds and transports Ca²⁺ selectively. The pore radius at E178 of the L210F mutant expanded by approximately 1 Å compared with the WT channel. An increase in the radius of the SF may increase the chance of ion binding and thus improve the probability of ions entering into the pore for the mutant. The second change was at the starting residue of the hydrophobic region, V174. The dilation of V174 in the mutant may allow more water molecules to stay at this entrance of the hydrophobic region, which lays a good foundation for water to further occupy the following hydrophobic region. The third change occurred in the basic region, where nearly the whole segment of the mutant was wider than the WT. The increase of the basic region radius can not only reduce the steric hindrance, but also reduce the electrostatic exclusion between the basic residues and cation ions passing through this cationic channel. Moreover, the constriction site of the channel, the K163 gate located at the beginning of the basic region, expanded significantly in the

mutant channel (Figure 2C), which might be a key step for the activation of the L210F mutant.

The Rotation of the Residue L/F210

A rotation angle defined by two vectors, which were determined by two carbon atoms of residue 210 and the pore axis, was calculated to evaluate the rotation of the residue around its rotation axis that is parallel to the z-axis and passes through C α of residue 210 (detailed definition in Figure 3A). The results revealed a previously unobserved rotation of the residue L/F210. L210 in the WT channel had two populated distributions of the rotation angle (Figure 3B). The peaks of the two distributions were at about 5 and 50°, respectively. In contrast to L210, only one major distribution with a higher peak located at about 50° was observed for F210 in the mutant channel (Figure 3B). Therefore, it appeared that L210 could have two major conformations, in which the side chain of L210 either points to the pore axis or rotates clockwise for about 50°. The two conformations are equally stable as they show nearly identical distribution and free energies (Supplementary Figure S2). In the mutant, F210 showed only one major conformation, in which it preferred to rotate clockwise for about 50° owing to the lowest free energy (Supplementary Figure S2). F210 also showed larger maximum rotation compared to L210, reaching 80–90° where F210 would be pointing to a nearly tangential direction of the pore. These conformations with large rotation angles kept F210 farther away from the pore-lining helix (TM1), which will probably generate a pulling effect on the TM1 through hydrophobic interactions with A166 on the TM1 of the same subunit (Supplementary Figure S3) and leave more room for the TM1 to expand outward. This may be the reason that caused the expansion of the basic region located in the TM1 adjacent to F210 in the mutant channel (Supplementary Figure S3).

The Counter-Clockwise Rotation of the Residue F171

It was reported that the opening of the Orai channel is accompanied by the counter-clockwise rotation of the residue

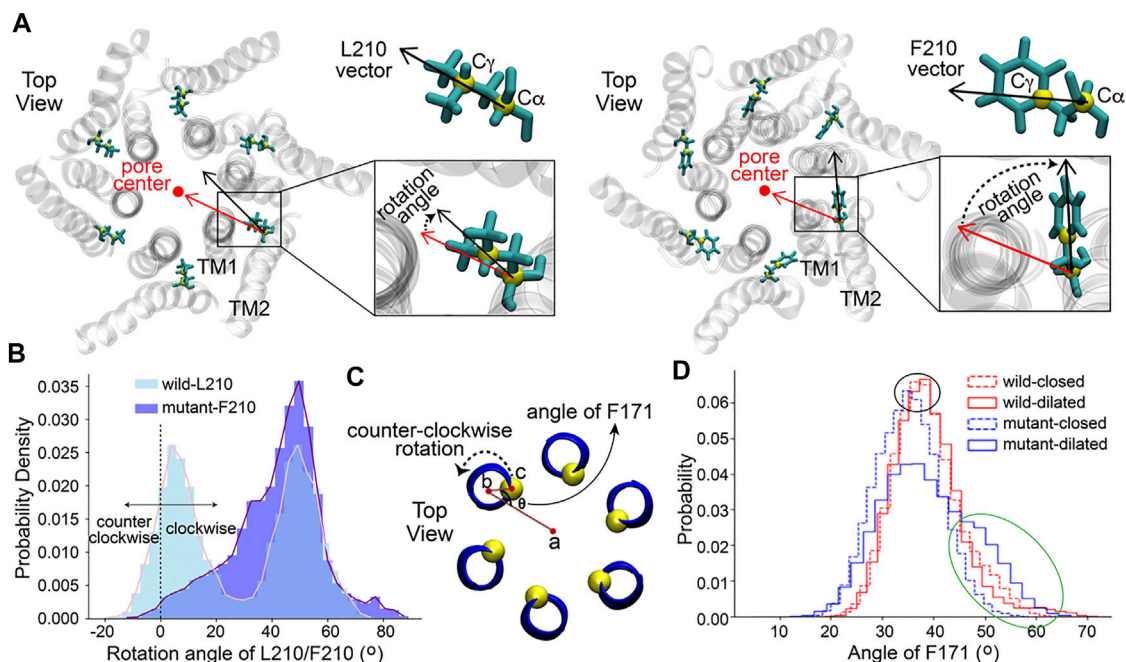


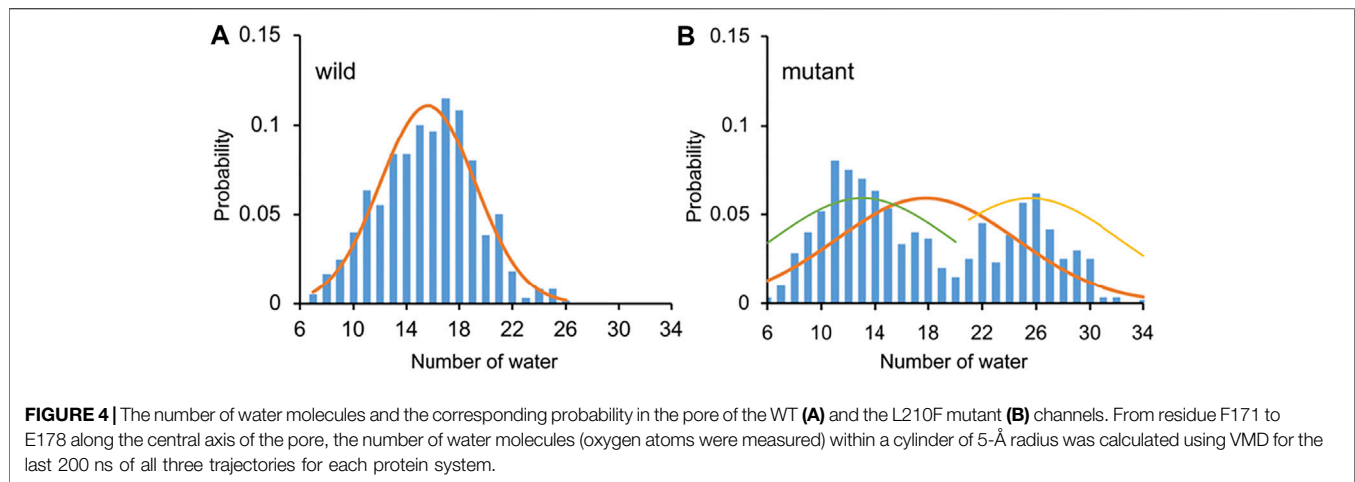
FIGURE 3 | The rotation of residues L/F210 and F171. **(A)** The definition of the rotation angle of L/F210. The rotation angle was defined by the black and red vectors. The red vector was determined by the projections of C α of residue 210 and the pore center onto the XY plane, and the pore center was the geometry center of C α atoms of all the six TM1s. The black vectors of L/F210 were determined by the projection of C α and C γ onto the XY plane. Only the TM1 and TM2 in each subunit are shown for clarity. One frame of the simulation is shown with gray transparent NewCartoon as an example. L210 and F210 are shown with Licorice. **(B)** The distribution of the rotation angle of L/F210. The last 200 ns of each trajectory was used for this analysis. VMD was used for the calculations. **(C)** The definition of the angle of F171 (top view). Point a was obtained by projecting the center of the channel on the XY plane. Similarly, point b was determined by the geometry center of two helices centered on F171 (residues 169–173), and point c was C α of F171. The axis of rotation passed through point b and was parallel to the channel axis. **(D)** The distribution of the angle of F171. The four data sets, wild-closed, wild-dilated, mutant-closed and mutant-dilated, were classified with a pore radius of 2 Å at the K163 gate. 500 ns of each trajectory was used for the analysis. VMD was used for the calculations.

F171 (Yamashita et al., 2017), which is located on the TM1 in the middle of the hydrophobic gate and is some distance away from the mutation point L/F210 (Figure 1A and Supplementary Figure S3). The presence of the hydrophobic gate increases the energy barrier of ion permeation, while the rotation of the residue F171 may reduce this barrier, contributing to the activation of the channel (Yamashita et al., 2017). Here, the orientation angle of F171 (definition (Yamashita et al., 2017) in Figure 3C) was calculated to measure the dynamics of this residue in our simulations. Firstly, in order to investigate the angle of F171 in a more detailed pore radius range, the structures of each channel obtained from MD simulations were classified into two classes according to the pore radius at the K163 gate, which is the constriction site of the channels. Structures with a radius at K163 of less than 2 Å were classified as the closed state while structures with a K163 radius of more than 2 Å were classified as the dilated state. As a result, four data sets: wild-closed (10,123 frames), wild-dilated (4,877 frames), mutant-closed (5,175 frames) and mutant-dilated (9,825 frames) were obtained. The results of the angle showed a very similar distribution among the wild-closed, wild-dilated and mutant-closed data sets with the most frequent angles of 35–40° (Figure 3D, the black oval). These distributions were supposed

to be caused by the normal fluctuations of F171. However, the angle distribution of the mutant-dilated data set was different, with a probability increase of angles above 45° (Figure 3D, the green oval, about 45–65°) and a probability decrease of angles around 35–40°. A larger rotation angle of F171 will keep this residue pointing away from the pore axis, which will further allow more hydration at this site. This appears to be caused by the dilation of V174, on the basis of the structural change at F210 in the mutant (Figure 2C), and will lead to a more open hydrophobic gate. Therefore, the angles above 45° were believed to make contributions to the opening of the hydrophobic gate of the mutant. Then, the effective counter-clockwise rotation of F171 that might open the hydrophobic gate was about 10–30° (45\65 minus 35) after eliminating its normal fluctuations.

Water in the Pore

The Orai channel has two gates, the residue K163 gate in the basic region and the hydrophobic gate (residues F171–V174). Previous studies have shown that even if the radius of the Orai channel does not significantly change, a limited increase of hydration in the pore is enough to regulate the conduction state (Dong et al., 2013), suggesting the importance of the hydrophobic gate. Hence,



the number of water molecules in the pore, as an important indicator of the conductivity of the channel, was calculated to measure the hydration difference between the WT and the L210F mutant channels. The water distributions in the region from residues F171 to E178 were measured. This region includes the hydrophobic region and the SF, which was reported to be the area of the most significant water distribution difference. (Dong et al., 2013). The results showed that the distribution of the number of water molecules was relatively concentrated with the average number of 16 in the pore of the WT (Figure 4A). However, the distribution showed two peaks in the L210F mutant (Figure 4B). A low-hydration distribution and a high-hydration distribution were observed, and the average number for the whole distribution was about 18 (Figure 4B), larger than the average number in the WT. Besides, the mutant can have a hydration number as high as ~30, a value the WT channel never reached. Accordingly, the highly hydrated structures of the L210F mutant were supposed to reduce the energy barrier of ions passing through the hydrophobic gate and thus facilitate ion permeation.

Na⁺ in the Pore

Although the Orai channels are highly selective for Ca²⁺, Na⁺ was often used in the study of the conductivity of CRAC channels as Na⁺ can permeate at a much higher rate in the absence of Ca²⁺, (Prakriya and Lewis, 2006; Hogan et al., 2010), which makes it easier for better sampling in MD simulations. The position and the number of Na⁺ ions within the pore were calculated to observe the behavior of Na⁺ ions in the WT and the L210F mutant channels. The results showed that Na⁺ ions were mainly distributed in the upper part of the pore (Figures 5A,B). Three binding sites, residues E178, D182 and D184, were observed (Supplementary Figure S4), among which E178 was the most dominant one. Na⁺ ions permeated deeper in the mutant than in the WT (below E178 in the mutant and a little above E178 in the WT, Figures 5A,B), and the most frequent numbers of Na⁺ ions in this region were 7 and 9 for the WT and the mutant, respectively (Figures 5C,D). Therefore, it seems that the L210F mutation moderately

modified the distribution of Na⁺ ions along the pore, causing more Na⁺ accumulation at the entrance of the pore and increasing the probability of ions passing through, which is consistent with the fact that the L210F mutant is constitutively open to cations. However, no spontaneous Na⁺ permeation was observed in our MD process, probably due to the extremely low conductivity of the L138F Orai1 (equals to the L210F dOrai here) mutant (Frischauf et al., 2017) and the lacking of a fully open structure.

Cl⁻ in the Pore

As previous studies showed anion-assisted cation permeation in the V174A Orai channel (also a constitutively open channel), (Dong et al., 2014), the position and number of Cl⁻ ions within the pore were calculated to analyze the behavior of Cl⁻ ions in the WT and the L210F mutant channels in our simulations as well. The results showed that Cl⁻ ions were mainly distributed in the intracellular region, specifically referring to the basic region including residue K163 and the residues below it (Figures 5E,F). The most frequent numbers of Cl⁻ ions were 16 and 15 in the WT and the mutant channels, respectively (Figures 5G,H), showing no appreciable difference. Previous molecular dynamics simulations reported that Cl⁻ ions in the basic region of the open V174A mutant can flow out to the extracellular side of the pore under electric field conditions, coordinating with Na⁺ ions in the pore to form an energetically more favorable cluster to help the influx of Na⁺ ions. (Dong et al., 2014). It seems that the mutation L210F does not alter the Cl⁻ occupation around the basic region or its role in assisting cation permeation.

DISCUSSION

In this paper, based on the crystal structure of *Drosophila melanogaster* Orai, we investigated the detailed channel structures and the water and ion distributions for both the WT and the L210F mutant channels by using molecular dynamics simulations. The results revealed two small but

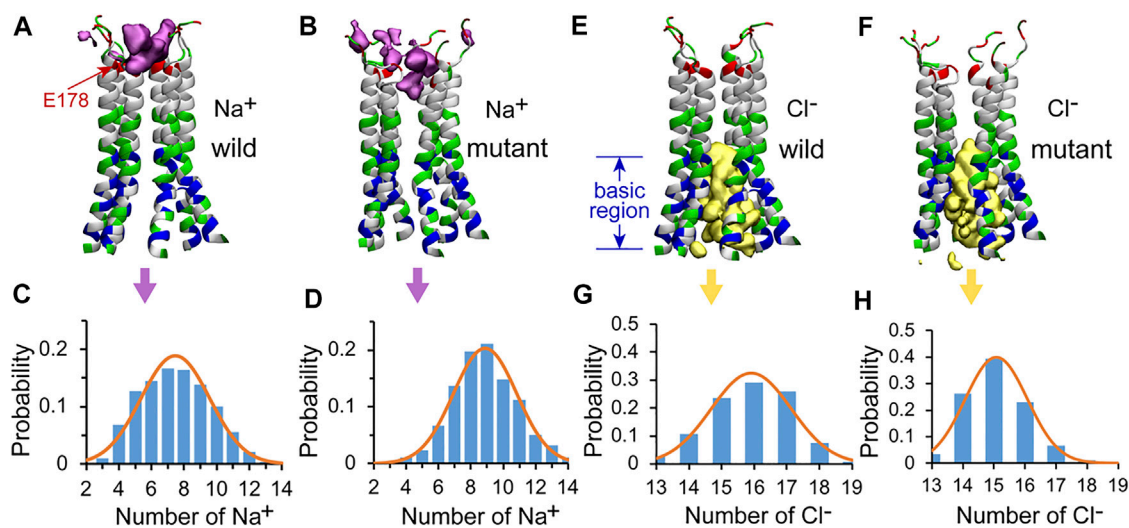


FIGURE 5 | The distributions of Na⁺ and Cl⁻ in the pore of the channel. The isosurface of Na⁺ ion density in the WT (A) and the L210F mutant (B) channels. The number of Na⁺ ions and corresponding probability in the pore of the WT (C) and the L210F mutant (D) channels. The isosurface of Cl⁻ ion density in the WT (E) and the L210F mutant (F) channels. The number of Cl⁻ ions and corresponding probability in the pore of the WT (G) and the L210F mutant (H) channels. The isosurface of Na⁺ and Cl⁻ ion densities are shown in pink and yellow with isosurface values of 0.02 and 0.06, respectively. Only residues from W148 to D184 along the central axis of the pore, the number of Na⁺ and Cl⁻ ions within a cylinder of 10-Å radius were calculated using VMD for the last 200 ns of all three trajectories for each protein system.

essential conformational changes resulting from the L210F mutation. Firstly, an previously unobserved rotation of residue F210 initiated the channel opening in the L210F mutant. F210 in the mutant had larger outward rotation than L210 in the WT, resulting in the dilation of the basic region and the K163 gate. At the same time, a 20-degree (on average) counter-clockwise rotation of F171 in the hydrophobic gate occurred more frequently and allowed more hydration at the hydrophobic region, which can potentially lead to the opening of the hydrophobic gate. Collectively, the rotation of F210 and F171, leading to the opening of the two gates of the channel, may create a constitutively open L210F mutant. Therefore, our results may shed further light on the disease of myopathy caused by the L138F mutation in human Orai1, by providing insight into the detailed structure and activation mechanism of the L210F mutant.

This is the first time that the rotation of the residue 210 is characterized to be the key origin of the activation for the L210F mutant channel. In contrast to the WT L210 that has two equally distributed rotation angles, the mutant F210 showed a predominantly larger clockwise rotation, which leaves more room for the TM1 helices to expand outward, dilating the basic region and the K163 gate. The expansion of the basic region involved hydrophobic interactions between TM2 and TM1 in the same subunit, suggesting the important role of the transmembrane helix (TH) interaction network on the channel gating. Apparently, the regulation of the TH network may work in more than one way. In Frischauf's work for another constitutively open H134A Orai1 mutant (equals to the H206A dOrai mutant), the regulation of the TH connectivity on the channel gating is shown in the disruption of hydrogen bonds between H134 on the TM2 and two residues on the TM1

(S93 and S97). (Frischauf et al., 2017). Notably, the L138F Orai1 mutant (equals to the L210F dOrai here) is also studied through molecular dynamics simulations in the same work, which showed that the enhanced hydrophobic contacts between TM2 and TM1 through L138F mutation trigger more flexibility of the pore, and then one water chain enters into the hydrophobic region and opens the pore. (Frischauf et al., 2017). These results are generally consistent with ours, both of which emphasize the importance of the hydrophobic interaction between TM2 and TM1 and water chain or hydration in the hydrophobic region. However, our results revealed a previously unnoticed rotation of residue 210, which may be the origin of the activation. Apart from the rotation of the residue 210, the rotation of F171 observed in our simulation, which was also reported to be required in other constitutively open channels V174A and F171Y in Yamashita's work (Yamashita et al., 2017), may also be an important factor for gating.

Notably, no significant rotational movement of F171 or TM1 was observed from the open conformation of the H206A dOrai (equals to the H134A Orai1) resolved at 3.3 Å resolution by cryo-EM recently (Hou et al., 2020), indicating that multiple activation mechanisms may be utilized by different mutants. The regulation of the TH network is also shown in the dilation of the filter. TM1, TM2 and TM3 in two adjacent subunits may participate in this process (Supplementary Figure S5). The residue K270 on the TM3 was reported to regulate the filter selectivity through conformation dynamics and the filter dilation was also observed in the previous study. (Alavizargar et al., 2018). In our study, the radius of the K270 ring was dilated in the L210F mutant (the average radius of K270 ring in the WT and the

mutant: 12.30 Å and 13.33 Å), which was probably caused by the expansion of the filter through electrostatic interactions (**Supplementary Figure S5**). However, how the mutation of residue 210 allosterically affects K270 is still not clear. Further simulations and analysis are undergoing to focus on the selectivity difference between the WT and the L210F mutant using a new calcium model, (Zhang et al., 2020), which will hopefully provide a better understanding on this aspect.

The dilation of the entire pore obtained in our simulations for the L210F mutant is consistent with the recently obtained open-state cryo-EM structure of the H206A dOrai mutant (Hou et al., 2020). Both H206A and L210F mutations occur on the TM2 and construct constitutively open channels with some selectivity for Ca^{2+} remained, so some structural similarity of the pore may exist among the H206A mutant, the L210F mutant and the WT Orai. (Frischauf et al., 2017). The dilation of the filter in the open channels didn't get much attention previously. In some previous simulations (Frischauf et al., 2017), the filter of the constitutively open channel is nearly the same with the closed Orai, since Ca^{2+} were trapped in the filter in both simulations owing to strong interactions between Ca^{2+} and protein. Here, we didn't include Ca^{2+} in our simulations, following the protocol of other previous simulations (Dong et al., 2013), and therefore the filter was more flexible to reach a more dilated state in the mutant, in agreement with the filter dilation as observed in the open-state H206A structure (Hou et al., 2020). In addition, it was reported that the WT Orai1 experiences some filter conformational changes when it is activated by STIM1 (Gudlur et al., 2014), suggesting that the filter conformation may be different for the open channel and the closed channel. Still, it should be noted that both the L210F Orai mutant and the H206A cryo-EM structure may not fully mimic the STIM-dependent Orai gating since their conductivity and selectivity are not the same after all.

REFERENCES

- Abraham, M. J., Murtola, T., Schulz, R., Páll, S., Smith, J. C., Hess, B., et al. (2015). GROMACS: High Performance Molecular Simulations through Multi-Level Parallelism from Laptops to Supercomputers. *Software* 1–2 (C), 19–25. doi:10.1016/j.softx.2015.06.001
- Alavizargar, A., Berti, C., Ejtehadi, M. R., and Furini, S. (2018). Molecular Dynamics Simulations of Orai Reveal How the Third Transmembrane Segment Contributes to Hydration and Ca^{2+} Selectivity in Calcium Release-Activated Calcium Channels. *J. Phys. Chem. B* 122 (16), 4407–4417. doi:10.1021/acs.jpcc.7b12453
- Amcheslavsky, A., Wood, M. L., Yeromin, A. V., Parker, I., Freitas, J. A., Tobias, D. J., et al. (2015). Molecular Biophysics of Orai Store-Operated Ca^{2+} Channels. *Biophys. J.* 108 (2), 237–246. doi:10.1016/j.bpj.2014.11.3473
- Best, R. B., Zhu, X., Shim, J., Lopes, P. E. M., Mittal, J., Feig, M., et al. (2012). Optimization of the Additive CHARMM All-Atom Protein Force Field Targeting Improved Sampling of the Backbone ϕ , ψ and Side-Chain χ_1 and χ_2 Dihedral Angles. *J. Chem. Theor. Comput.* 8 (9), 3257–3273. doi:10.1021/ct300400x
- Bussi, G., Donadio, D., and Parrinello, M. (2007). Canonical Sampling through Velocity Rescaling. *J. Chem. Phys.* 126 (1), 014101. doi:10.1063/1.2408420

DATA AVAILABILITY STATEMENT

The original contributions presented in the study are included in the article/**Supplementary Material**, further inquiries can be directed to the corresponding authors.

AUTHOR CONTRIBUTIONS

XZ and HY performed the MD simulations and analysis. XL and CS supervised the project and provided resources. All authors participated in the writing of the article.

FUNDING

The research was supported by the National Natural Science Foundation of China (21873006 and 32071251 to CS) and the National Key Research & Development Program of the Ministry of Science and Technology of China (2016YFA0500401 and 2021YFE0108100 to CS). Part of the molecular dynamics simulation was performed on the Computing Platform of the Center for Life Sciences at Peking University.

ACKNOWLEDGMENTS

We thank Dr. Xiaolan Xu who inspired us to work on this project and discussed with us.

SUPPLEMENTARY MATERIAL

The supplementary material for this article can be found online at: <https://www.frontiersin.org/articles/10.3389/fmolb.2021.755247/full#supplementary-material>

- Dong, H., Fiorin, G., Carnevale, V., Treptow, W., and Klein, M. L. (2013). Pore Waters Regulate Ion Permeation in a Calcium Release-Activated Calcium Channel. *Proc. Natl. Acad. Sci.* 110 (43), 17332–17337. doi:10.1073/pnas.1316969110
- Dong, H., Klein, M. L., and Fiorin, G. (2014). Counterion-Assisted Cation Transport in a Biological Calcium Channel. *J. Phys. Chem. B* 118 (32), 9668–9676. doi:10.1021/jp505987
- Endo, Y., Noguchi, S., Hara, Y., Hayashi, Y. K., Motomura, K., Miyatake, S., et al. (2015). Dominant Mutations in ORAI1 Cause Tubular Aggregate Myopathy with Hypocalcemia via Constitutive Activation of Store-Operated Ca^{2+} Channels. *Hum. Mol. Genet.* 24 (3), 637–648. doi:10.1093/hmg/ddu477
- Engh, A., Somasundaram, A., and Prakriya, M. (2012). Permeation and Gating Mechanisms in Store-Operated CRAC Channels. *Front. Biosci. (Landmark Ed)* 17, 1613–1626. doi:10.2741/4007
- Essmann, U., Perera, L., Berkowitz, M. L., Darden, T., Lee, H., and Pedersen, L. G. (1995). A Smooth Particle Mesh Ewald Method. *J. Chem. Phys.* 103 (19), 8577–8593. doi:10.1063/1.470117
- Feske, S. (2010). CRAC Channelopathies. *Pflugers Arch. Eur. J. Physiol.* 460 (2), 417–435. doi:10.1007/s00424-009-0777-5
- Feske, S., Prakriya, M., Rao, A., and Lewis, R. S. (2005). A Severe Defect in CRAC Ca^{2+} Channel Activation and Altered K^{+} Channel Gating in T Cells from Immunodeficient Patients. *J. Exp. Med.* 202 (5), 651–662. doi:10.1084/jem.20050687

- Feske, S., Skolnik, E. Y., and Prakriya, M. (2012). Ion Channels and Transporters in Lymphocyte Function and Immunity. *Nat. Rev. Immunol.* 12 (7), 532–547. doi:10.1038/nri3233
- Fiser, A., Do, R. K. G., and Šali, A. (2000). Modeling of Loops in Protein Structures. *Protein Sci.* 9 (9), 1753–1773. doi:10.1110/ps.9.9.1753
- Frischauf, I., Litviňuková, M., Schober, R., Zayats, V., Svobodová, B., Bonhenry, D., et al. (2017). Transmembrane helix Connectivity in Orai1 Controls Two gates for Calcium-dependent Transcription. *Sci. Signal.* 10 (507), eaa0358. doi:10.1126/scisignal.aao0358
- Frischauf, I., Zayats, V., Deix, M., Hochreiter, A., Jardin, I., Muik, M., et al. (2015). A Calcium-Accumulating Region, CAR, in the Channel Orai1 Enhances Ca²⁺ Permeation and SOCE-Induced Gene Transcription. *Sci. Signal.* 8 (408), ra131. doi:10.1126/scisignal.aab1901
- Garibaldi, M., Fattori, F., Riva, B., Labasse, C., Brochier, G., Ottaviani, P., et al. (2017). A Novel Gain-Of-Function Mutation in Orai1 causes Late-Onset Tubular Aggregate Myopathy and Congenital Miosis. *Clin. Genet.* 91 (5), 780–786. doi:10.1111/cge.12888
- Gudlur, A., Quintana, A., Zhou, Y., Hirve, N., Mahapatra, S., and Hogan, P. G. (2014). STIM1 Triggers a Gating Rearrangement at the Extracellular Mouth of the Orai1 Channel. *Nat. Commun.* 5 (1), 5164. doi:10.1038/ncomms6164
- Hogan, P. G., Lewis, R. S., and Rao, A. (2010). Molecular Basis of Calcium Signaling in Lymphocytes: STIM and Orai. *Annu. Rev. Immunol.* 28, 491–533. doi:10.1146/annurev.immunol.021908.132550
- Hoth, M., and Niemeyer, B. A. (2013). The Neglected CRAC Proteins: Orai2, Orai3, and STIM2. *Curr. Top. Membr.* 71, 237–271. doi:10.1016/b978-0-12-407870-3.00010-x
- Hou, X., Outhwaite, I. R., Pedi, L., and Long, S. B. (2020). Cryo-EM Structure of the Calcium Release-Activated Calcium Channel Orai in an Open Conformation. *eLife* 9, e62772. doi:10.7554/eLife.62772
- Hou, X., Pedi, L., Diver, M. M., and Long, S. B. (2012). Crystal Structure of the Calcium Release-Activated Calcium Channel Orai. *Science* 338, 1308–1313. doi:10.1126/science.1228757
- Humphrey, W., Dalke, A., and Schulten, K. (1996). VMD: Visual Molecular Dynamics. *J. Mol. Graph.* 14 (1), 33–38. doi:10.1016/0263-7855(96)00018-5
- Jo, S., Kim, T., Iyer, V. G., and Im, W. (2010). CHARMM-GUI: a Web-Based Graphical User Interface for CHARMM. *J. Comput. Chem.* 29 (11), 1859–1865. doi:10.1002/jcc.20945
- Jorgensen, W. L., Chandrasekhar, J., Madura, J. D., Impey, R. W., and Klein, M. L. (1983). Comparison of Simple Potential Functions for Simulating Liquid Water. *J. Chem. Phys.* 79 (2), 926–935. doi:10.1063/1.445869
- Klauda, J. B., Venable, R. M., Freites, J. A., O'Connor, J. W., Tobias, D. J., Mondragon-Ramirez, C., et al. (2010). Update of the CHARMM All-Atom Additive Force Field for Lipids: Validation on Six Lipid Types. *J. Phys. Chem. B* 114 (23), 7830–7843. doi:10.1021/jp101759q
- Liou, J., Kim, M. L., Do Heo, W., Jones, J. T., Myers, J. W., Ferrell, J. E., et al. (2005). STIM Is a Ca²⁺ Sensor Essential for Ca²⁺-Store-Depletion-Triggered Ca²⁺ Influx. *Curr. Biol.* 15 (13), 1235–1241. doi:10.1016/j.cub.2005.05.055
- MacKerell, A. D., Bashford, D., Bellott, M., Dunbrack, R. L., Evanseck, J. D., Field, M. J., et al. (1998). All-Atom Empirical Potential for Molecular Modeling and Dynamics Studies of Proteins†. *J. Phys. Chem. B* 102 (18), 3586–3616. doi:10.1021/jp973084f
- McNally, B. A., Somasundaram, A., Yamashita, M., and Prakriya, M. (2012). Gated Regulation of CRAC Channel Ion Selectivity by STIM1. *Nature* 482 (7384), 241–245. doi:10.1038/nature10752
- McNally, B. A., Yamashita, M., Engh, A., and Prakriya, M. (2009). Structural Determinants of Ion Permeation in CRAC Channels. *Proc. Natl. Acad. Sci. U S A* 106 (52), 22516–22521. doi:10.1073/pnas.0909574106
- Parrinello, M., and Rahman, A. (1981). Polymorphic Transitions in Single Crystals: A New Molecular Dynamics Method. *J. Appl. Phys.* 52 (12), 7182–7190. doi:10.1063/1.328693
- Prakriya, M., Feske, S., Gwack, Y., Srikanth, S., Rao, A., and Hogan, P. G. (2006). Orai1 Is an Essential Pore Subunit of the CRAC Channel. *Nature* 443 (7108), 230–233. doi:10.1038/nature05122
- Prakriya, M., and Lewis, R. S. (2006). Regulation of CRAC Channel Activity by Recruitment of Silent Channels to a High Open-Probability Gating Mode. *J. Gen. Physiol.* 128 (3), 373–386. doi:10.1085/jgp.200609588
- Prakriya, M., and Lewis, R. S. (2015). Store-Operated Calcium Channels. *Physiol. Rev.* 95 (4), 1383–1436. doi:10.1152/physrev.00020.2014
- Putney, J. W. (1986). A Model for Receptor-Regulated Calcium Entry. *Cell Calcium* 7 (1), 1–12. doi:10.1016/0143-4160(86)90026-6
- Roos, J., DiGregorio, P. J., Yeromin, A. V., Ohlsen, K., Lioudyno, M., Zhang, S., et al. (2005). STIM1, an Essential and Conserved Component of Store-Operated Ca²⁺ Channel Function. *J. Cell Biol.* 169 (3), 435–445. doi:10.1083/jcb.200502019
- Smart, O. S., Neduvellil, J. G., Wang, X., Wallace, B. A., and Sansom, M. S. P. (1996). HOLE: a Program for the Analysis of the Pore Dimensions of Ion Channel Structural Models. *J. Mol. Graph.* 14 (6), 354–360. doi:10.1016/s0263-7855(97)00009-x
- Soboloff, J., Rothberg, B. S., Madesh, M., and Gill, D. L. (2012). STIM Proteins: Dynamic Calcium Signal Transducers. *Nat. Rev. Mol. Cell Biol.* 13 (9), 549–565. doi:10.1038/nrm3414
- Stathopoulos, P. B., Li, G.-Y., Plevin, M. J., Ames, J. B., and Ikura, M. (2006). Stored Ca²⁺ Depletion-Induced Oligomerization of Stromal Interaction Molecule 1 (STIM1) via the EF-SAM Region. *J. Biol. Chem.* 281 (47), 35855–35862. doi:10.1074/jbc.m608247200
- Tiffner, A., Schober, R., Höglinger, C., Bonhenry, D., Pandey, S., Lunz, V., et al. (2021). CRAC Channel Opening Is Determined by a Series of Orai1 Gating Checkpoints in the Transmembrane and Cytosolic Regions. *J. Biol. Chem.* 296, 100224. doi:10.1074/jbc.ra120.015548
- Tirado-Rives, J. (1988). The OPLS [Optimized Potentials for Liquid Simulations] Potential Functions for Proteins, Energy Minimizations for Crystals of Cyclic Peptides and Crambin. *J. Am. Chem. Soc.* 110, 1657–1666. doi:10.1021/ja00214a001
- Vig, M., Beck, A., Billingsley, J. M., Lis, A., Parvez, S., Peinelt, C., et al. (2006). CRACM1 Multimers Form the Ion-Selective Pore of the CRAC Channel. *Curr. Biol.* 16 (20), 2073–2079. doi:10.1016/j.cub.2006.08.085
- Waldherr, L., Tiffner, A., Mishra, D., Sallinger, M., Schober, R., Frischauf, I., et al. (2020). Blockage of Store-Operated Ca²⁺ Influx by Synta66 Is Mediated by Direct Inhibition of the Ca²⁺ Selective Orai1 Pore. *Cancers (Basel)* 12 (10), 2876. doi:10.3390/cancers12102876
- Yamashita, M., Ing, C. E., Yeung, P. S., Maneshi, M. M., Pomès, R., and Prakriya, M. (2019). The Basic Residues in the Orai1 Channel Inner Pore Promote Opening of the Outer Hydrophobic Gate. *J. Gen. Physiol.* 152 (1), e201912397. doi:10.1085/jgp.201912397
- Yamashita, M., Yeung, P. S.-W., Ing, C. E., McNally, B. A., Pomès, R., and Prakriya, M. (2017). STIM1 Activates CRAC Channels through Rotation of the Pore helix to Open a Hydrophobic Gate. *Nat. Commun.* 8 (1), 14512. doi:10.1038/ncomms14512
- Yeromin, A. V., Zhang, S. L., Jiang, W., Yu, Y., Safrina, O., and Cahalan, M. D. (2006). Molecular Identification of the CRAC Channel by Altered Ion Selectivity in a Mutant of Orai. *Nature* 443, 226–229. doi:10.1038/nature05108
- Yeung, P. S.-W., Yamashita, M., Ing, C. E., Pomès, R., Freymann, D. M., and Prakriya, M. (2018). Mapping the Functional Anatomy of Orai1 Transmembrane Domains for CRAC Channel Gating. *Proc. Natl. Acad. Sci. USA* 115 (22), E5193–E5202. doi:10.1073/pnas.1718373115
- Zhang, A., Yu, H., Liu, C., and Song, C. (2020). The Ca²⁺ Permeation Mechanism of the Ryanodine Receptor Revealed by a Multi-Site Ion Model. *Nat. Commun.* 11 (1), 922. doi:10.1038/s41467-020-14573-w
- Zhang, S. L., Yeromin, A. V., Hu, J., Amcheslavsky, A., Zheng, H., and Cahalan, M. D. (2011). Mutations in Orai1 Transmembrane Segment 1 Cause STIM1-independent Activation of Orai1 Channels at glycine 98 and Channel Closure at Arginine 91. *Proc. Natl. Acad. Sci.* 108 (43), 17838–17843. doi:10.1073/pnas.1114821108
- Zhou, Y., Ramachandran, S., Oh-hora, M., Rao, A., and Hogan, P. G. (2010). Pore Architecture of the Orai1 Store-Operated Calcium Channel. *Proc. Natl. Acad. Sci.* 107 (11), 4896–4901. doi:10.1073/pnas.1001169107

Conflict of Interest: The authors declare that the research was conducted in the absence of any commercial or financial relationships that could be construed as a potential conflict of interest.

Publisher's Note: All claims expressed in this article are solely those of the authors and do not necessarily represent those of their affiliated organizations, or those of the publisher, the editors and the reviewers. Any product that may be evaluated in this article, or claim that may be made by its manufacturer, is not guaranteed or endorsed by the publisher.

Copyright © 2021 Zhang, Yu, Liu and Song. This is an open-access article distributed under the terms of the Creative Commons Attribution License (CC BY). The use, distribution or reproduction in other forums is permitted, provided the original author(s) and the copyright owner(s) are credited and that the original publication in this journal is cited, in accordance with accepted academic practice. No use, distribution or reproduction is permitted which does not comply with these terms.



Unveiling the Gating Mechanism of CRAC Channel: A Computational Study

Carlo Guardiani, Delia Sun and Alberto Giacomello*

Dipartimento di Ingegneria Meccanica e Aerospaziale, Sapienza Università di Roma, Rome, Italy

OPEN ACCESS

Edited by:

Luca Maragliano,
Marche Polytechnic University, Italy

Reviewed by:

Vincenzo Carnevale,
Temple University, United States
Murali Prakriya,
Northwestern University,
United States

*Correspondence:

Alberto Giacomello
alberto.giacomello@uniroma1.it

Specialty section:

This article was submitted to
Biological Modeling and Simulation,
a section of the journal
Frontiers in Molecular Biosciences

Received: 09 September 2021

Accepted: 17 November 2021

Published: 14 December 2021

Citation:

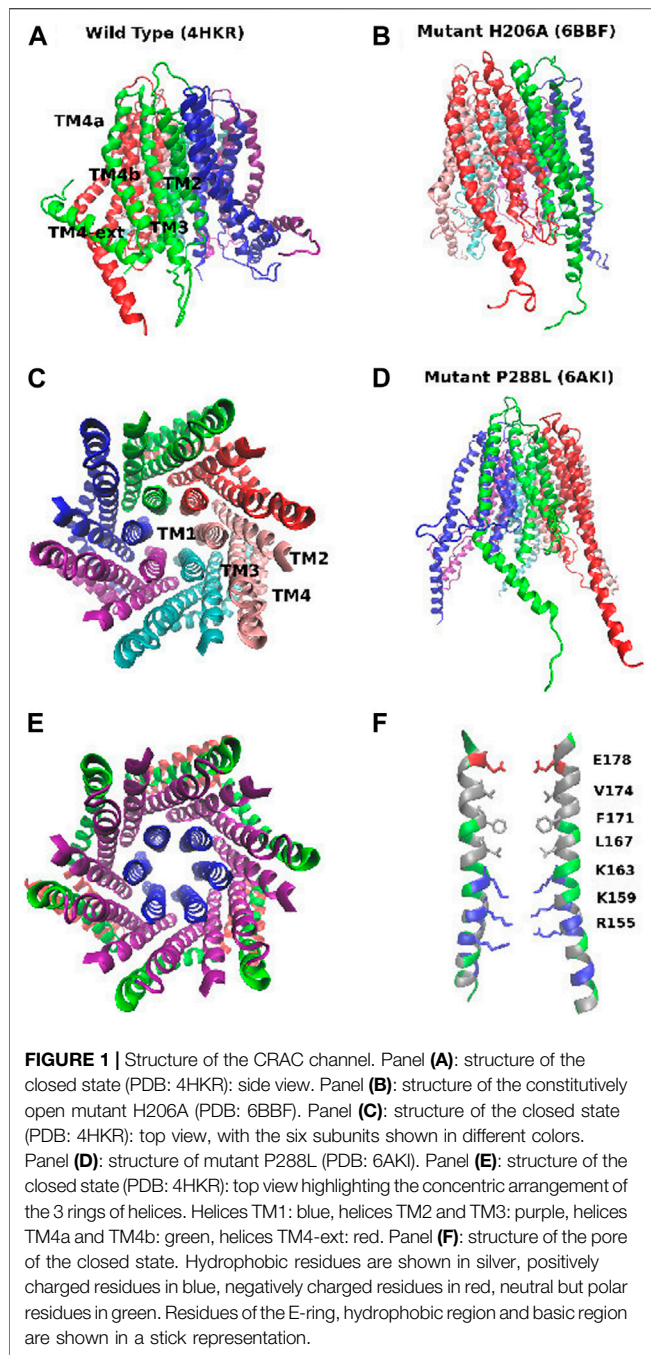
Guardiani C, Sun D and Giacomello A
(2021) Unveiling the Gating
Mechanism of CRAC Channel: A
Computational Study.
Front. Mol. Biosci. 8:773388.
doi: 10.3389/fmolb.2021.773388

CRAC channel is ubiquitous and its importance in the regulation of the immune system is testified by the severe immunodeficiencies caused by its mutations. In this work we took advantage of the availability of open and closed structures of this channel to run for the first time simulations of the whole gating process reaching the relevant time-scale with an enhanced sampling technique, Targeted Molecular Dynamics. Our simulations highlighted a complex allosteric propagation of the conformational change from peripheral helices, where the activator STIM1 binds, to the central pore helices. In agreement with mutagenesis data, our simulations revealed the key role of residue H206 whose displacement creates an empty space behind the hydrophobic region of the pore, thus releasing a steric brake and allowing the opening of the channel. Conversely, the process of pore closing culminates with the formation of a bubble that occludes the pore even in the absence of steric block. This mechanism, known as “hydrophobic gating”, has been observed in an increasing number of biological ion channels and also in artificial nanopores. Our study therefore shows promise not only to better understand the molecular origin of diseases caused by disrupted calcium signaling, but also to clarify the mode of action of hydrophobically gated ion channels, possibly even suggesting strategies for the biomimetic design of synthetic nanopores.

Keywords: CRAC channel, gating mechanism, hydrophobic gating, allosteric gating, molecular dynamics, targeted molecular dynamics, pore helix rotation, structural instability of P288L

1 INTRODUCTION

The ubiquitous Calcium Release Activated Calcium channel (CRAC) mediates Ca^{2+} -influx through the plasma membrane of non-excitable cells in metazoans activating communication cascades that elicit a wide range of functions (Prakriya and Lewis, 2015) like gene expression, cell proliferation, secretion of inflammatory mediators, and cell migration. The importance of CRAC channel is highlighted by the pathological effects of both gain of function and loss of function mutations (Lacruz and Feske, 2015). While loss of function mutations cause the severe combined immunodeficiency (SCID)-like disease, autoimmunity, muscular hypotonia, and ectodermal dysplasia, gain of function mutations have been linked to non-syndromic tubular aggregate myopathy and York platelet and Stormorken syndromes. Although structures of the closed and open states are available (Hou et al., 2012, 2018; Liu et al., 2019) and despite a significant body of experimental research (Yamashita et al., 2017; Yeung et al., 2018), the gating mechanism of this channel is still a matter of debate, a central issue being the allosteric propagation (Zhou et al., 2019; Yeung et al., 2020) of the signal from the activator binding site to the central pore helices.



The CRAC channel mediates the store operated calcium entry (SOCE) (Prakriya and Lewis, 2015), a process of calcium influx triggered by the depletion of the calcium stores of the endoplasmic reticulum (ER). When ER calcium stores are depleted, calcium dissociates from the calcium-sensing, luminal EF-hand domain of STIM1, a single pass protein of the ER membrane. STIM1 then migrates to the junctions between ER and plasma membranes where it oligomerizes and undergoes a conformational transition that exposes the CRAC activation domain (CAD) (Park et al., 2009). The interaction of STIM1 CAD domain with CRAC outermost helices (TM4) induces the

opening of the CRAC channel that results in an influx of calcium that refills the stores of the ER and activates a number of signalling pathways including those necessary for the activation of immune response genes in T cells (Feske et al., 2005).

There are three human isoforms of CRAC encoded by genes Orai1, 2, and 3 (Prakriya and Lewis, 2015). Since an experimental structure of the human CRAC channel is not yet available, most computational works (Dong et al., 2013, 2014; Yamashita et al., 2017) (including ours) have been performed on the *Drosophila melanogaster* protein encoded by gene Orai that shares 73% sequence identity with Orai1. From a structural point of view, CRAC is a homo-hexamer (Hou et al., 2012) with each of the six identical subunits formed by four trans-membrane helices. CRAC helices are arranged in three concentric layers. Helix TM1 forms the innermost layer that lines the pore, helices TM2 and TM3 form the central layer and helix TM4 forms the outermost layer. The pore wall of this channel exhibits an extremely complex composition. Close to the extra-cellular mouth E178 forms a negatively charged glutamate ring that imparts cation selectivity and thus acts as a Selectivity Filter. The central part of the pore is occupied by a hydrophobic region with three rings of hydrophobic residues (L167, F171 and V174). Finally, close to the cytosolic mouth we find a basic region with three rings of positively charged residues (R155, K159 and K163).

Three main experimental structures of CRAC are currently available (Figure 1). The structure with PDB code 4HKR (Hou et al., 2012) corresponds to the closed state. The structure is characterized by a narrow pore and a double bent TM4 helix that is thus split into three helical segments: TM4a on the extracellular side, the central TM4b, and the TM4-ext helix on the cytosolic side. The TM4-ext helices of neighbouring subunits associate with one another to form a coiled-coil structure that is believed to be the docking point of the STIM1 activator. Besides the closed state, recently the structures of two constitutively open mutants have been disclosed, P288L (PDB: 6AKI) (Liu et al., 2019) and H206A (PDB: 6BBF) (Hou et al., 2018). While 6BBF is characterized by a wide pore and fully extended TM4 helices, 6AKI shows an arrangement of the pore helices similar to that of the closed state (4HKR) with partially bent TM4 helices.

Many aspects of CRAC channel need to be clarified. For instance the assignment of structure 4HKR to the closed state based on experimental calcium flow measurements, is at odds with a pore radius (Figure 2) that is everywhere large enough to accommodate a water molecule or a dehydrated calcium ion. The functional occlusion coexisting with a geometric permeability of the pore suggests a *hydrophobic gating* mechanism (Aryal et al., 2015) i.e. a phenomenon of evaporation in nanoconfinement whereby the formation of a vapour bubble stops the flow of liquid water and ions. Indeed, the hydrophobic region of the pore would seem ideally suited for this kind of mechanism. Many computational studies have monitored the amount of water in CRAC pore and, even if there is a consensus that the water content of the hydrophobic region in the closed state is very low, the results still show a significant variability. Yeung et al. (2018), for instance, show a trajectory where the bubble appears and disappears intermittently for the first ~100 ns but the pore is fully

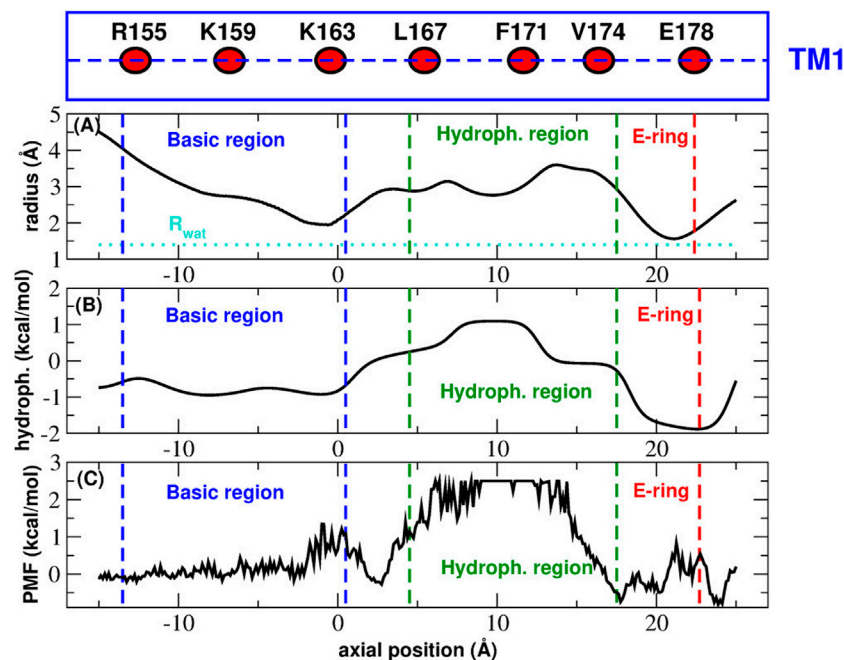


FIGURE 2 | Functional state assignment of CRAC structure 4HKR. Panel (A): average radius profile during the equilibrium simulation. The dotted line corresponds to the radius of a water molecule. Panel (B): hydrophobicity profile. In the Wimley-White scale positive and negative hydrophobicity values correspond to hydrophobic and hydrophilic amino acids respectively. Panel (C): Potential of Mean Force of water permeation as a function of the position along the axis of the pore. The blue and green dashed lines mark the boundaries of the basic and hydrophobic region respectively. The red dashed lines shows the position of the glutamate ring. The box above Panel (A) is a cartoon representation of helix TM1 showing the position of the key residues (average position of the center of mass of C_{α} atoms) along the helix axis (dashed line).

wetted for the remaining ~250 ns. In the work by Dong et al., (2013), on the other hand, a proper bubble never forms and, even in the closed state, the hydrophobic region is always crossed by a number of thin chains of water molecules. These results are at odds with those reported by Frischauf et al. (2019). These authors simulated a homology model of human CRAC discovering that in the wild type the hydrophobic region is always fully dewetted.

Another controversial issue regards the gating mechanism. In an early paper Yamashita et al. (2017) proposed a mechanism based on a rotation of pore helices aimed at displacing the bulky side chains of hydrophobic residues occluding the hydrophobic region. The rotation of pore helices, however, was not confirmed by the simulations of Frischauf et al. (2019), neither was it observed in the crystal structures of P288L (Liu et al., 2019) and H206A (Hou et al., 2018) mutants.

The major unresolved question about CRAC channel, however, concerns the molecular mechanism by which the STIM1 gating signal is communicated at large distance to the pore region (Zhou et al., 2019; Yeung et al., 2020). The existence of a highly cooperative and strongly allosteric gating mechanism is supported by the discovery (Nesin et al., 2014; Boehm et al., 2017; Garibaldi et al., 2017) of an increasing number of pathologic mutations located far from the pore region. This evidence suggests that the transmembrane domains of CRAC channel may be involved in the process of propagation of the wave of conformational change that originates at the STIM1 binding site on helices TM4 and heads to the hydrophobic region

of the pore helices where the gating motion occurs. Within this framework, the gating mechanism would not just require a localized motion of the pore helices, but a globally concerted motion involving the whole protein. A significant work on this issue has been performed by Yeung et al. (2018) who performed scanning mutagenesis to identify a number of residues in transmembrane domains whose mutation leads to constitutive activation of the pore. In particular, they identified the role of *steric brake* of H206 and they highlighted the importance of a cluster of hydrophobic residues at the TM1-TM2/3 interface.

In this work we took advantage of the availability of closed (Hou et al., 2012) and open state (Hou et al., 2018; Liu et al., 2019) structures to simulate for the first time the conformational transition from the closed to the open state and *vice versa*. Since this process is likely to occur at least on the milli-second time-scale, it cannot be simulated with equilibrium MD techniques. We thus resorted to Targeted MD (Schlitter et al., 1994), an enhanced sampling technique that steers the system between given end states applying a biasing potential to the RMSD between the current and target conformations. Since its introduction, a number of successful applications have shown that TMD can yield qualitatively correct pathways of conformational changes. As an example, TMD was used to study the activation pathway of β_2 adrenergic receptor (Xiao et al., 2015), the allosteric mechanism of calmodulin opening (Liang et al., 2017), and the role of the cytoplasmic domain in the gating of KcsA channel (Li et al., 2013). Before running TMD, we

ran equilibrium simulations of the available closed and open structures. The spontaneous formation of a bubble occluding the pore of the closed state in the absence of steric block, highlighted a mechanism of hydrophobic gating (Aryal et al., 2015). The simulation of the putatively open mutants H206A and P288L showed for the first time that the former was structurally stable while the latter underwent a spontaneous bending of helices TM4. This led us to suggest that P288L is more likely an intermediate in the gating process than the open state. As a result we chose the H206A structure as the open state to use in TMD simulations. In agreement with Yamashita et al. (2017), the TMD simulations showed rotation of pore helices contributing to the change of pore radius even if an important role also appears to be played by TM1 helix displacement. The analysis of TMD simulations highlighted two important events in the gating mechanism: a coordinated motion of helices TM1, TM3, and TM4b that leads to the opening of the basic region of the pore and a displacement of the side chain of H206 creating an empty space behind the hydrophobic region of helices TM1. This mechanism appears to be consistent with the steric brake model put forward by Yeung et al. (2018).

The paper is organized as follows. In **Section 2.1** and **Section 2.2** we present the equilibrium simulations of the closed and putatively open states respectively. In **Section 2.3** we analyze TMD simulations first focusing on the rotation of pore helices (**Section 2.3.1**). We then discuss the results of the contact analysis (**Section 2.3.2**) and the analysis of inter-helical distances (**Section 2.3.3**) that highlight important details of the gating mechanism. Finally, **Section 3** is devoted to the discussion, while **Section 4** illustrates the methods employed in our calculations.

2 RESULTS

2.1 Equilibrium Simulation of the Closed State

Our analysis of the CRAC channel began with the equilibrium simulation of the closed state (PDB ID: 4HKR). The functional state of an ion channel is customarily predicted (Rao et al., 2019) on the grounds of the radius profile. **Supplementary Figure S1** shows the radius profile of the crystal structure and the profile of the radius averaged along the equilibrium simulations. Both profiles are everywhere larger than the radius of a single water molecule showing the absence of steric obstruction. From a purely geometric point of view the channel is thus expected to be water-permeable. This prediction is confirmed by the space filling representation of the pore shown in **Supplementary Figure S2**. According to the color code employed by the HOLE program (Smart et al., 1996), green regions are wide enough to accommodate no more than a single water molecule, while blue regions can accommodate two or more water molecules. **Supplementary Figure S2** shows a bottleneck at the level of the Glu-ring and other two at the level of the basic region. In these points, the side chains project towards the center of the pore reducing its radius but there is still enough space for a single chain of water molecules. Except for these three points the pore can everywhere be occupied by two or more water molecules.

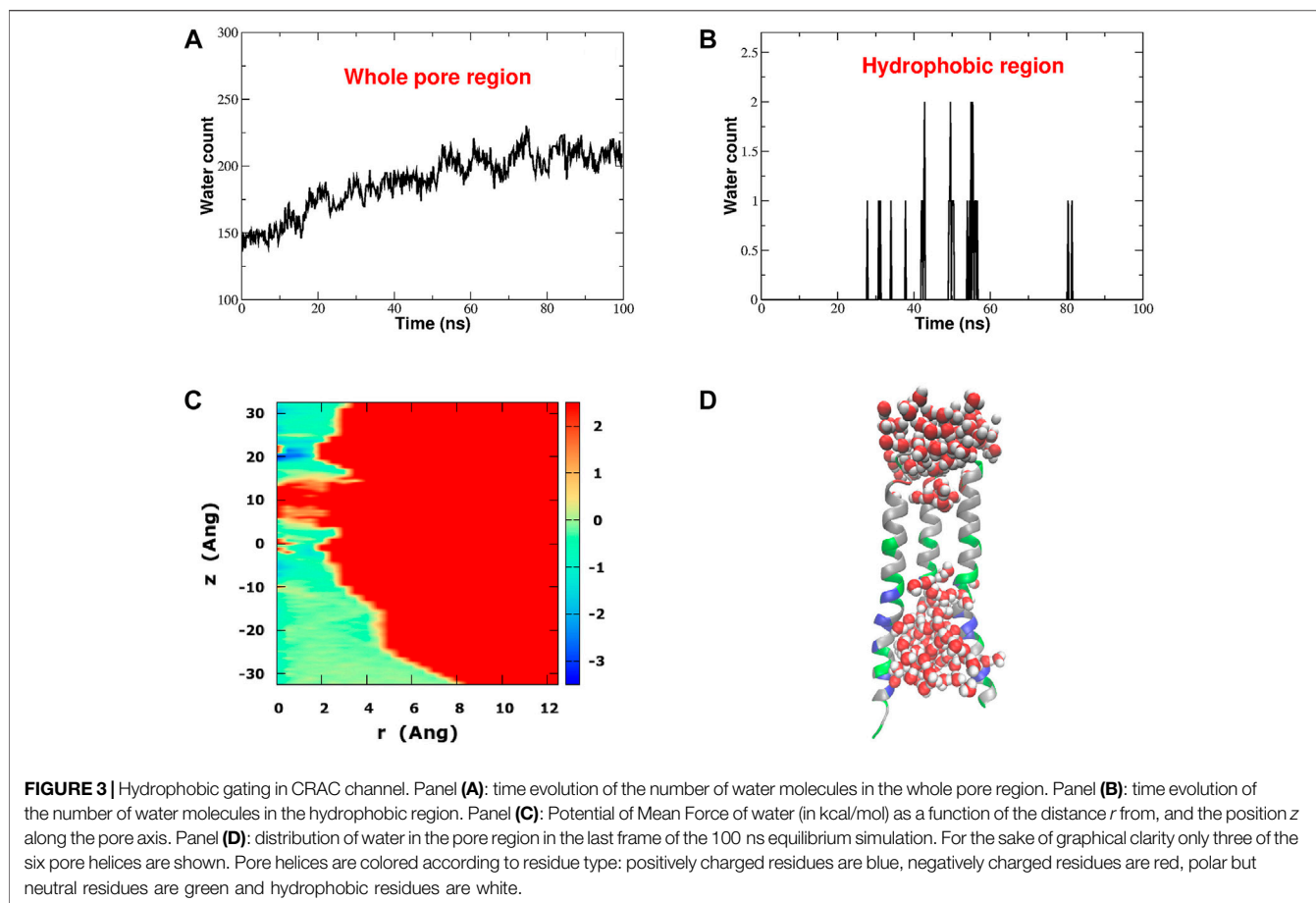
This analysis is inconsistent with the electrophysiological characterization of this structure (Hou et al., 2012) clearly showing it corresponds to the closed state. This inconsistency can be explained if the radius profile is compared with the hydrophobicity profile and the Potential of Mean Force of water permeation (**Figure 2**). **Figure 2** shows that, even if in principle the pore is wide enough to host one or more water molecules (**Figure 2A**), the chemistry of the wall determines a peak of the hydrophobicity profile (**Figure 2B**) corresponding to the hydrophobic region of the pore. The hydrophobicity peak also corresponds to the maximum of the Potential of Mean Force for water permeation (**Figure 2C**). Taken together, these results suggest that the pore is functionally occluded even in the absence of steric block, which is the signature of *hydrophobic gating*.

Hydrophobic gating is a phenomenon of evaporation in conditions of nanoconfinement (Roth et al., 2008). If the water-wall interactions are weaker than water-water interactions, a bubble may form, preventing the flow of liquid water and ions. This pattern is clearly manifested in our equilibrium simulation. **Figure 3** shows the time evolution of the number of water molecules in the whole pore region (**Figure 3A**) and in the hydrophobic region (**Figure 3B**). The water count in the whole pore slightly increases during the first half of the simulation and eventually it stabilizes around an average value of 200 water molecules. Conversely, if we restrict our attention to the hydrophobic region, this district appears to be almost always devoid of water save for a few occasional intrusions of 1 or 2 water molecules at the boundary with the Glu-ring and the basic region. Indeed **Figure 3D**, corresponding to the final frame of the simulation, shows that the hydrophobic region of the pore is dry. The bubble appears early, already during the constrained stage of the equilibration, and it is stably maintained throughout the whole simulation of 100 ns. As a result, the radial-axial PMF of water permeation reported in **Figure 3C**, highlights a high free energy zone (in red) in the hydrophobic region where water has very little likelihood to reside.

2.2 Equilibrium Simulation of Putatively Open States

The main purpose of this work is to study the gating transition steering the CRAC channel from the open to the closed state and back using Targeted Molecular Dynamics simulations (Schlitter et al., 1994). Since this technique requires knowledge of the end states of the transition, it is extremely important to computationally characterize the recently resolved structures of two putatively open states, mutants H206A (PDB ID: 6BBF) (Hou et al., 2018) and P288L (PDB ID: 6AKI) (Liu et al., 2019). This analysis will allow us to choose the most appropriate conformation to use as the open state in TMD simulations.

Figure 4 shows the radius profile of the crystal structures of the closed and open states (**Figure 4A**) as well as the radius profile averaged during the equilibrium simulation of the three systems (**Figure 4B**). The radius profiles of the experimental structures are very similar at the level of the Glu-ring, but in the



hydrophobic and basic regions the pore of 6BBF appears to be much larger than that of the other two structures. Interestingly enough, even if 6AKI was predicted (Liu et al., 2019) to represent the open state, its radius profile is much more similar to that of the closed state (4HKR) than to that of the other putatively open state (6BBF). During the equilibrium simulation, the radius profile of 6AKI tended to drift towards that of 6BBF until it settled on a curve intermediate between those of the closed state (4HKR) and of the other putatively open state (6BBF). As shown in **Figure 4C**, the different pore geometries affect the Potential of Mean Force of water permeation. As expected, the closed state is characterized by a high free energy barrier at the level of the hydrophobic region where the vacuum bubble prevents the flow of liquid water. Conversely, during the equilibrium simulation the wide pore of 6BBF is completely water filled. Since water density inside the pore is comparable to that in the bulk, the PMF profile is almost flat. Finally, the PMF profile of 6AKI also shows a barrier, smaller than that of the closed state but higher than what expected for an open state. The origin of this barrier can be understood monitoring the number of water molecules in the hydrophobic region of the three systems (**Figure 4D**). The plot clearly shows that, during the first 40 ns of the simulation, the hydrophobic region of 6AKI is also occupied by a bubble, which, during the second half of the trajectory, becomes water-filled. The process is also shown in **Supplementary Movie SM1**. This event,

similar to a spontaneous transition from the closed to the open state, suggests the opportunity of a deeper investigation on the structural stability of 6AKI.

Figure 5 reports the time evolution of the RMSD distance between 6AKI and the experimental structures of 4HKR and 6BBF during the equilibrium simulation of mutant P288L. In this calculation the two structures have been aligned using all backbone atoms while the actual RMSD calculation has been performed using all backbone atoms (**Figure 5A**), the backbone atoms of helices TM4 (**Figure 5B**) and the backbone atoms of the pore helices (**Figure 5C**). **Figure 5A**, shows that, during the equilibrium simulation, 6AKI becomes increasingly similar to both 4HKR and 6BBF but, unexpectedly for a putatively open structure, it is more similar to 4HKR than to 6BBF. **Figure 5B** shows that the increasing similarity between 6AKI and 4HKR is due to some structural rearrangement at the level of the outermost ring of helices. Indeed, as also shown in **Supplementary Movie SM1**, at the beginning of the simulation, TM4 helices of 6AKI are in an extended conformation, but during the run they spontaneously bend adopting a structural arrangement similar to that of the closed state. Finally, **Figure 5C** shows that no major structural rearrangement occurs at the level of the pore helices, even if, also in this district, 6AKI appears to be more similar to 4HKR than to 6BBF. The disruption of the bubble must thus be ascribed

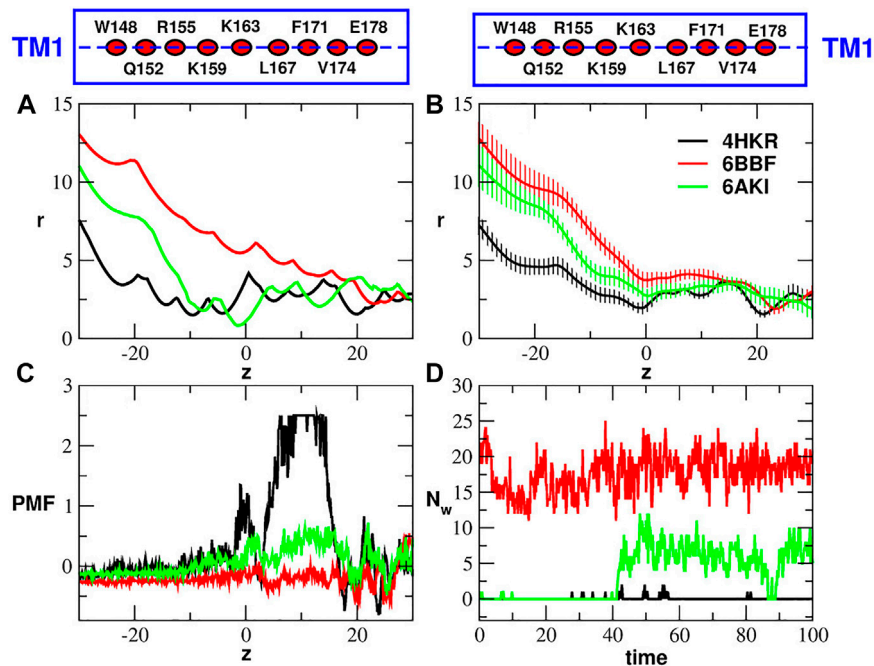


FIGURE 4 | Comparison of closed and putatively open structures. Panel (A): radius profiles of the crystal structure of the wild type (4HKR) and the two putatively open structures (6BBF and 6AKI). Panel (B): average radius profiles computed during the equilibrium simulations of 4HKR, 6BBF and 6AKI. The error is quantified by the standard deviation of the radius. In panels (A) and (B) the pore radius r and the position along the pore axis z are both expressed in Å. Panel (C): Potential of Mean Force of water (in kcal/mol) as a function of the axial position z (in Å). Panel (D): number of water molecules N_w in the hydrophobic region as a function of simulation time (in ns). The boxes above Panels (A) and (B) are cartoon representations of helix TM1 showing the position of the key residues (average position of the center of mass of C_α atoms) along the helix axis (dashed lines).

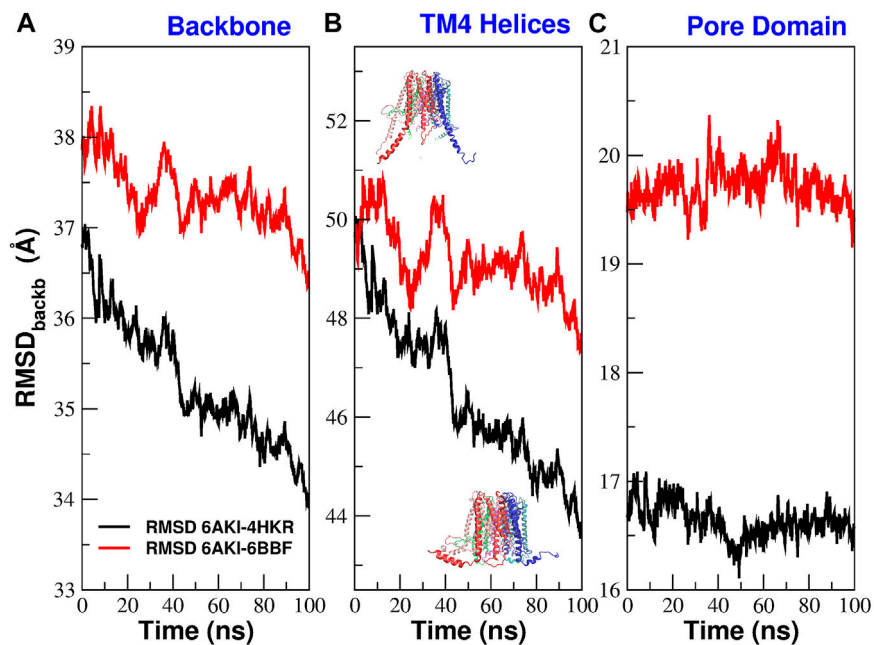


FIGURE 5 | Evolution during the equilibrium simulation of the RMSD between 6AKI and the crystal structures of 4HKR and 6BBF. Structure superposition was performed using all backbone atoms. The actual RMSD was computed using different subsets of atoms. In panel (A) the RMSD was computed using all backbone atoms; in panel (B) it was computed using the backbone atoms of helices TM4; the overlaid structures represent the initial conformation of 6AKI with extended TM4 helices and the final configuration with bent TM4 helices; in panel (C) the RMSD calculation was performed using the backbone atoms of the pore helices.

to some fine tuning of the pore conformation. In order to assess the variability across runs of the 6AKI-4HKR and 6AKI-6BBF RMSD, we performed a block average analysis (Frenkel and Smit, 2002) of the equilibrium simulation of 6AKI. Details can be found in the Supplementary Material section *Analysis of RMSD variability* where we also comment on the seemingly large RMSD values appearing in **Figure 5**.

The structural instability exhibited by 6AKI suggests that this structure is unlikely to represent the open state and more probably corresponds to an intermediate or a conformation on the slope of the free energy barrier which separates the closed state (4HKR) and the open state (6BBF). However, if we represent the free energy profile as a function of a single collective variable, a structural transition that brings 6AKI closer to 4HKR would automatically move it away from 6BBF and *vice versa* (**Supplementary Figure S3A**). This would be inconsistent with what observed in the RMSD analysis, i.e., that, during the simulations, 6AKI tends to get closer to both 6BBF and 4HKR. This seeming contradiction can be solved by considering that free energy is more realistically a function of several collective variables (**Supplementary Figure S3B**).

2.3 Targeted Molecular Dynamics Simulations

In order to reproduce the conformational transition from the closed to the open state and *vice versa* we ran Targeted Molecular Dynamics simulations (Schlitter et al., 1994). Due to the structural instability of mutant P288L (PDB: 6AKI) (Liu et al., 2019) we chose as open state the structure of mutant H206A (PDB: 6BBF) (Hou et al., 2018), while the structure of the wild type solved by Hou et al (PDB: 4HKR) (Hou et al., 2012) was considered as representative of the closed state. Specifically, we ran two TMD simulations: a 100 ns simulation from the closed to the open state and a 500 ns simulation from the open to the closed state. As can be noted, these simulations are extremely long as compared to the typical length of TMD simulations reported in the literature (1 ns or less) (Schlitter et al., 1994; Xiao et al., 2015; Liang et al., 2017; Li et al., 2013). The length of our simulations was not required to induce the structural transition but rather for the destruction or formation of the bubble in the hydrophobic region of the pore. This behaviour is not completely unexpected considering that in TMD the biasing potential is applied to the protein structure while water molecules redistribute spontaneously as a result of the changing chemical environment around them. In addition, the formation/destruction of the bubble is typically a first order transition, which, once triggered by structural changes, can be irreversible on the simulation timescale (Giacomello and Roth, 2020); therefore very slow changes in the biasing potential are needed to avoid artifact. In this regard, it is also notable that the O → C simulation had to be 5 times longer than the C → O simulation. This suggests that the energy barrier in the O → C transition is higher than that in the C → O transition implying a lower free energy of the open state as compared to the closed configuration. The water content of the pore is monitored in **Figure 6**. If we consider the water count in the whole pore (**Figures 6A,B**), we can note that the

number of water molecules increases or decreases in a rather gradual way. However, if we focus on the hydrophobic region only (**Figures 6C,D**), we observe an abrupt transition where the number of water molecules directly jumps from zero to the final value or vice versa. This behaviour suggests that bubble formation or destruction is a rare event possibly related to the overcoming of a high energy barrier. Moreover, this highly cooperative transition was also predicted in the thermodynamic model by Roth et al. (2008) where gating occurs in a narrow window of pore radii or hydrophobicities. Finally, the fact that bubble formation and destruction occurs at the end of the simulation both in the opening and closing transition, suggests the process to be strongly hysteretic, possibly due to the presence of hidden collective variables. This issue will be the object of a future investigation using techniques successfully applied in both model nanopores (Tinti et al., 2017; Camisasca et al., 2020) and biological ion channels (Costa et al., 2021). A more detailed description of the water and ion distribution in the pore is provided in the Supplementary Material section *Water and ion distribution during TMD simulations*.

2.3.1 Rotation of Pore Helices, SASA and Pore Radius

A long-standing controversy in CRAC channel literature concerns the gating mechanism, that, according to some authors (Yamashita et al., 2017), is due to a rotation of pore helices; however, this event was not confirmed in a number of subsequent experimental (Hou et al., 2018; Liu et al., 2019) and computational works (Frischauf et al., 2019). Section *Rotation of pore helices* and **Supplementary Figure S14** in the Supplementary Material show that the pore helices of CRAC channel have an intrinsic tendency to rotation that is present even during equilibrium simulations; in addition, the rotations seen in the experimental structures, reported in **Supplementary Table S4**, show good agreement with those observed in simulations. In the following we characterise rotation occurring during biased simulations. **Figures 7A,B** show that rotation of pore helices does occur during the TMD simulations. However, the rotation angles measured at different levels along the pore axis suggest that rotation does not occur as a rigid body rotation but rather as a twisting. It is also noteworthy that the rotation angles of the Glu-ring and hydrophobic region are much smaller than those of the basic region, presumably because the latter is located close to the N-terminus where chain constraints are expected to be weaker.

The value of the rotation angle of the hydrophobic region averaged along the last 20 ns of the C → O simulation is ~11° while the value averaged during the last 100 ns of the O → C simulation is ~16°. These values are in reasonably good agreement with the average helix rotation of ~15° at residue F171 measured by Yamashita et al. (2017). It is important to note that, while our rotations were measured during a conformational transition from the open to the closed state and back, the rotation angles reported by Yamashita et al. (2017) are due to frequent spontaneous conformational fluctuations from the crystallographic structure that they measured during

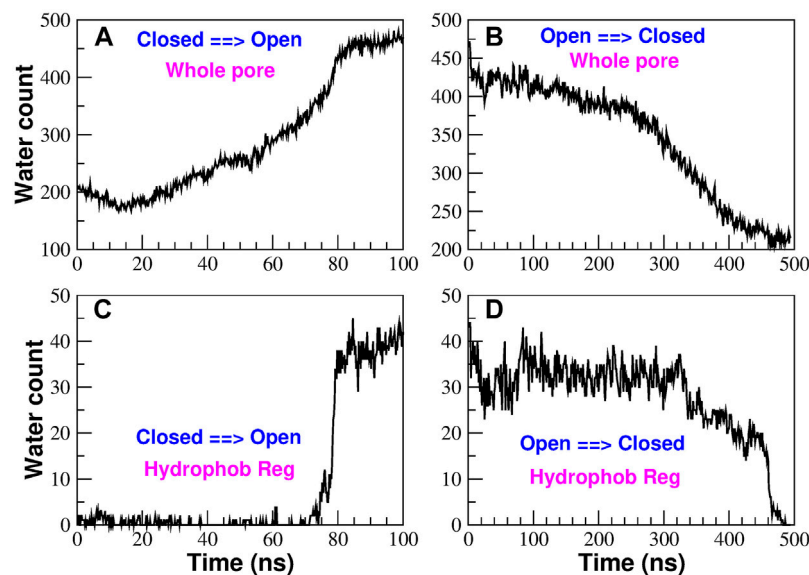


FIGURE 6 | Time evolution of the water content in the pore region during the TMD simulations. Panels (A) and (B) show the number of water molecules in the whole pore region in the opening and closing simulation respectively. Panels (C) and (D) monitor the water count in the hydrophobic region on the opening [panel (C)] and closing [panel (D)] simulations.

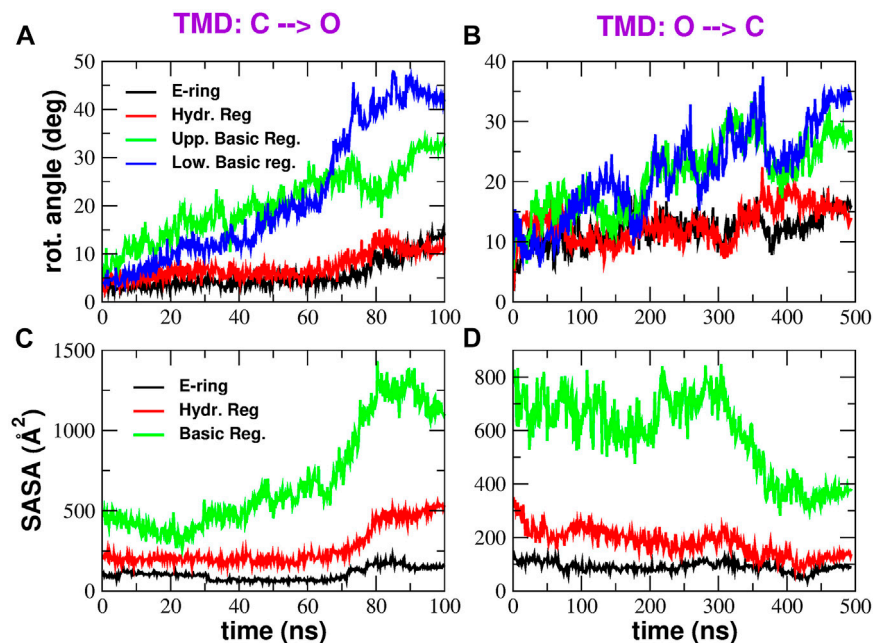


FIGURE 7 | Rotation and Solvent Accessible Surface Area of pore helices. Panels (A) and (B) show the time evolution of the rotation angles (averaged over the six pore helices) on the opening and closing transition respectively. Rotation angles were measured at four different axial levels: E-ring (black curve), hydrophobic region (red curve), upper basic region (green curve) and lower basic region (blue curve). Panels (C) and (D) show the Solvent Accessible Surface Area in the opening and closing TMD simulation respectively. The black curve represents the SASA of the E-ring, the red curve is the SASA of the hydrophobic region and the green curve shows the SASA of the basic region.

equilibrium simulations. This may be due to the fact that, even at equilibrium, the system transiently visits conformations relevant for its functional dynamics.

Finally, in the $C \rightarrow O$ transition it is possible to identify a change in slope of the rotation angles around 70 ns, just little before bubble destruction. This suggests that the rotation of pore

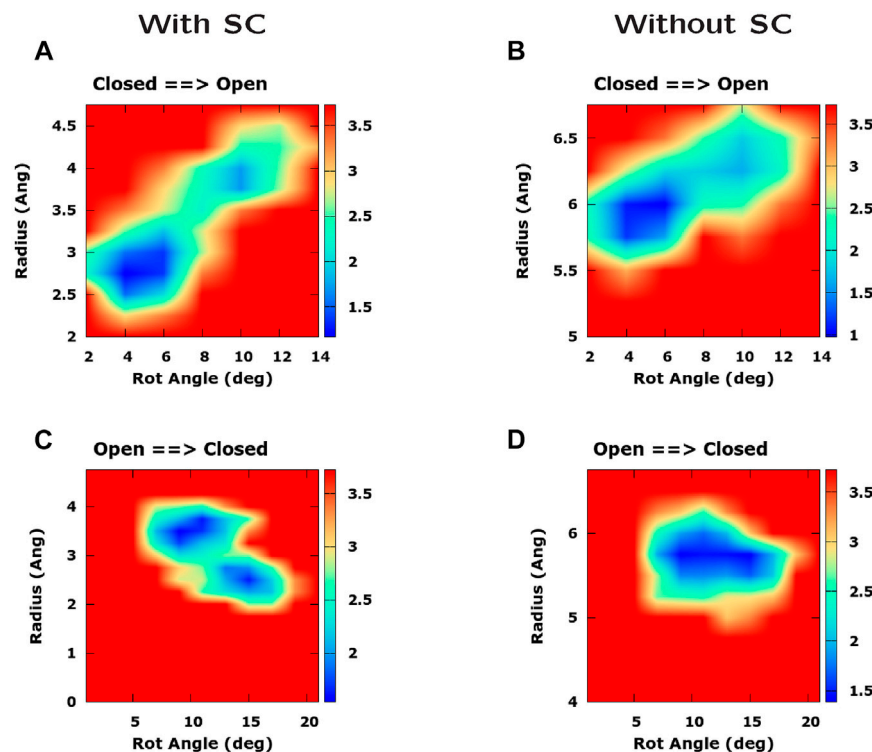


FIGURE 8 | Influence of pore helix rotation on pore radius. The four panels represent a Potential of Mean Force as a function of pore radius and pore helix rotation angle. In panels (A) and (C) the PMF was computed including the side chain in the calculation of pore radius, whereas in panels (B) and (D) side chains were excluded from the calculation. Panels (A) and (B) refer to the opening TMD simulation while panels (C) and (D) refer to the closing simulation. Free energies are expressed in kcal/mol.

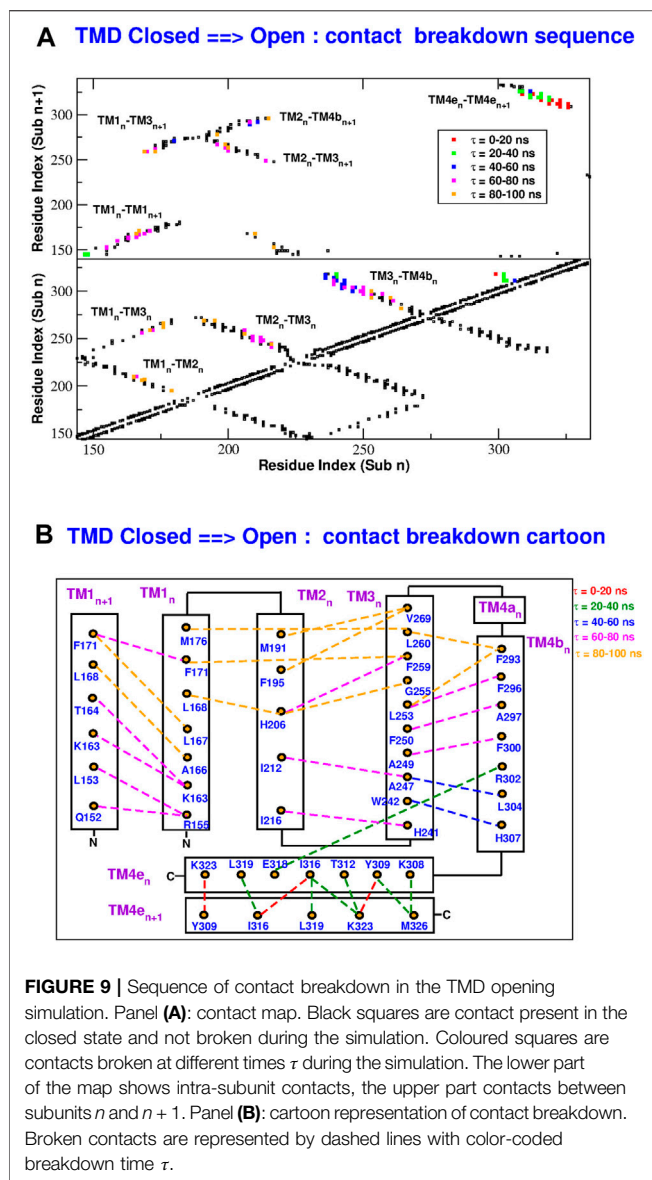
helices might be the trigger for bubble destruction. However, the time coincidence between the change in rotation angles and bubble formation is less evident in the closing transition.

After the rotation of pore helices is ascertained, it is important to investigate the functional role of this event. According to the thermodynamic model by Roth et al. (2008), hydrophobic gating is under the control of two key parameters: the hydrophobicity of pore wall and the pore radius. We therefore checked whether either of these parameters was affected by pore helix rotation. **Figures 7C,D** show the time evolution of the Solvent Accessible Surface Area (SASA) in the most important regions of the pore: the Glu-ring, the hydrophobic region, and the basic region. It can be noted that, both in the opening and closing transition, the SASA plot shows a change in slope approximately at the same time of the change in slope of rotation angles. However, while the SASA change of the basic region and E-ring favour the increase of water content expected during opening and the decrease expected during closing, the SASA change of the hydrophobic region tends to oppose the wetting expected during opening and the de-wetting of the closing process. These results therefore suggest that the rotation of pore helices is not finalized to the creation of a thermodynamically favourable environment for bubble formation or destruction.

We now explore the possibility that the rotation of pore helices might cause a change of the pore radius. In **Supplementary**

Figure S8, we consider two possible scenarios. In the first scenario, the rotation of pore helices is the main cause of the increase of the pore radius through a displacement of the bulky side chains of hydrophobic residues. In this case, if we compute a PMF as a function of rotation angle and pore radius, the low free energy region should be slanted. On the other hand, if we repeat the calculation after excluding the side chains from the calculation of pore radius, the low free energy region should be flat. In the second scenario, helix rotation and pore radius increase are simultaneous events but rotation is not the main cause of the growth of the pore radius. In this case, either performing the calculation with or without side chains, the low free energy region of the PMF should be sloped.

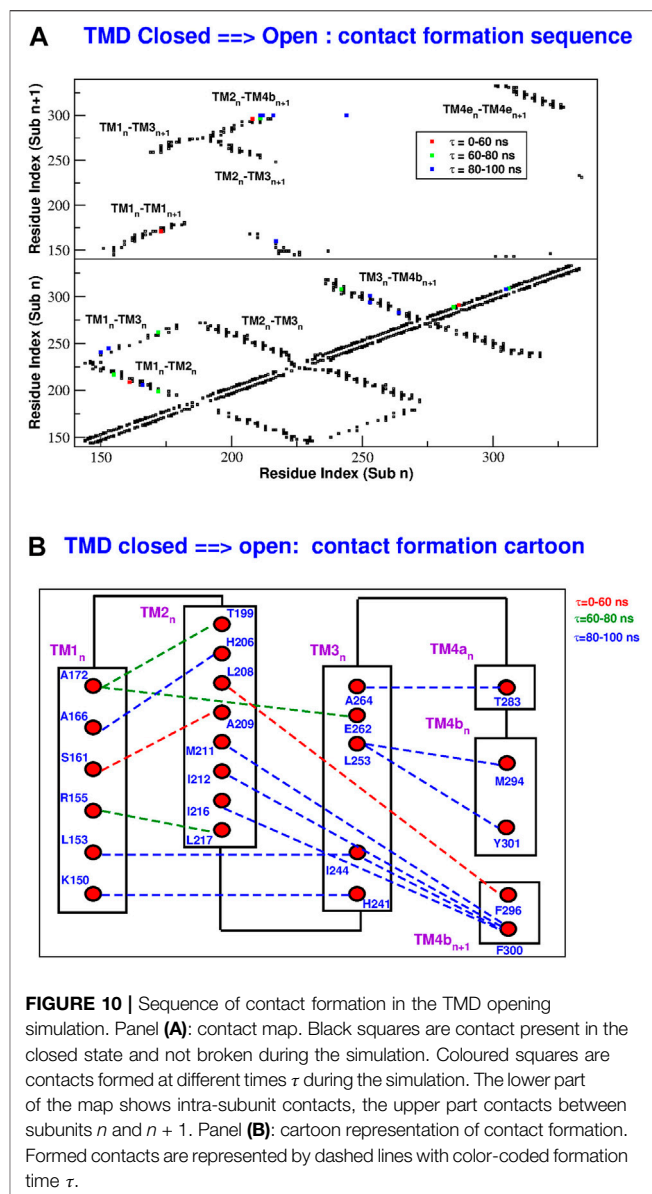
This strategy can be employed to analyze the PMFs derived from our TMD simulations and illustrated in **Figure 8**. In the opening simulations, both computing the PMF with (**Figure 8A**) and without side chains (**Figure 8B**), the minimal free energy region is inclined. This suggests that helix rotation and radius enlargement occur simultaneously but there is no causal link between the two phenomena. However, if we consider the closing simulation, we note that, when the PMF is computed using side chains (**Figure 8C**), the increase of the rotation angle is accompanied by a decrease in the pore radius while this effect is suppressed when removing the side chains (**Figure 8D**). The conclusion of these results is that rotation of pore helices might



play some role in the change of pore radius. However, this driving force is probably not the only one and the change of pore radius also depends on helix displacement.

2.3.2 Contact Analysis

In order to reconstruct the gating mechanism, for each frame of the TMD trajectories we built a contact map (two residues are considered to be in contact if at least two heavy atoms of the side chains are closer than 5.0 Å). In this way it is possible to determine the sequence of contact breakdown (Figure 9 and Supplementary Figure S9) and formation (Figure 10 and Supplementary Figure S10). The black squares in the maps represent contacts present in the initial conformation and not broken during the simulation. The coloured symbols represent contacts formed or broken at different times during the simulation. In particular, we only considered contacts formed or broken in at least 3 of the subunits and we averaged their



formation or breakdown times. In the contact maps, the elements on the diagonal represent contacts inside the same alpha helix. The elements orthogonal to the diagonal represent contacts between different alpha helices of the same subunit. Finally the islands of off-diagonal elements represent inter-subunit contacts. The maps show that all the broken and formed contacts are either intra-subunit or between neighbouring subunits n and $n + 1$.

During the opening simulation, the number of broken contacts is much higher than the number of formed contacts, consistent with the formation of a looser structure. As shown in Figure 9, the contact breakdown originates at the coiled coil between TM4-ext helices of neighbouring subunits and propagates towards the extracellular side through the TM3-TM4b interface. The contact breakdown then propagates towards the inner rings of helices. In particular we can

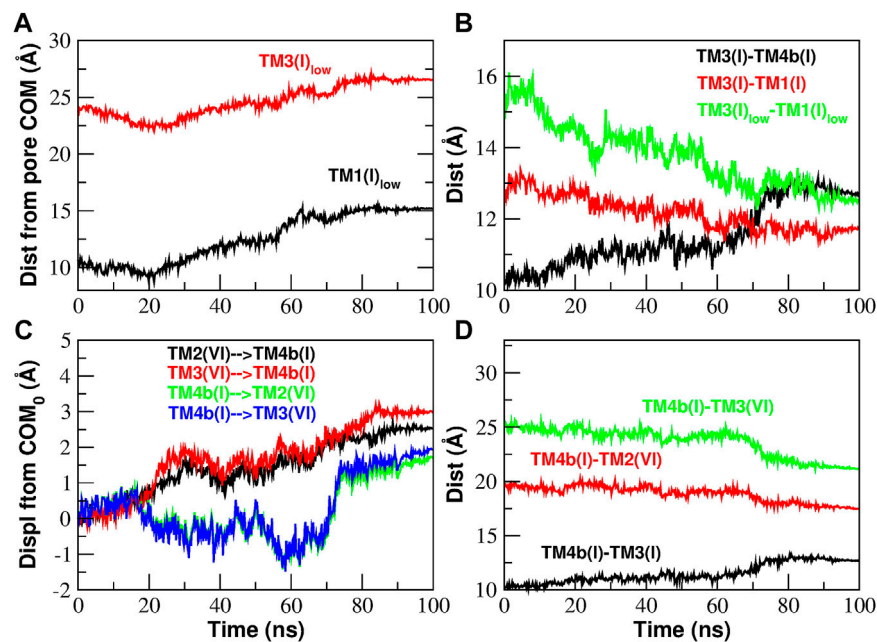


FIGURE 11 | Inter-helical distances involving helices TM3 and TM4b of Subunit I during the opening TMD simulation. Panel **(A)**: distance of the lower part of helices TM1 and TM3 from the Center of Mass (COM) of the pore. Panel **(B)**: the increase of the distance TM3-TM4b is paralleled by a decrease of the TM3-TM1 distance (more pronounced if considering only the lower part of the two helices). Panel **(C)**: displacement of the center of mass of helices TM4b(I), TM2(VI), TM3(VI) from its initial position. The displacement vector is projected such that a positive displacement represents an approach while a negative displacement a distancing between the helices. Panel **(D)**: the increase of the distance TM3(I)-TM4b(I) is paralleled by a decrease of the TM4b(I)-TM3(VI) and TM4b(I)-TM2(VI) distances.

observe the breakdown of contacts in the upper part of the TM2-TM3 and TM1-TM2 interface and a breakdown of contacts spanning the whole length of neighbouring TM1 helices. The few formed contacts (**Figure 10A**) are scattered throughout the contact map, but indeed they are very localized in space (**Figure 10B**). Most of them, indeed, involve the lower part of helices TM2(n)-TM4b(n + 1) and TM1(n)-TM3(n). This opening mechanism is consistent with the fact that activator STIM1 is known [Hou et al. (2012) and references therein] to break down the TM4e(n)-TM4e(n + 1) coiled-coil to form a new one. The conformational change is then expected to allosterically propagate (Yeung et al., 2018) to the innermost circle of helices where gating occurs.

The closing process, depicted in **Supplementary Figure S9** and **Supplementary Figure S10**, is basically the reverse of the opening one. In this case the number of formed contacts is much higher than that of the broken ones. As illustrated in **Supplementary Figure S10**, contact formation starts in the extracellular side of helices TM3-TM4b and propagates downwards to restore the coiled coil between neighbouring TM4e helices. Contact formation also propagates towards inner helices. In both the opening and closing processes, the last events involve H206 on helix TM2. As shown in **Figure 9B**, during opening H206 breaks its hydrogen bond with L202 (TM2) and breaks the hydrophobic contacts with L168 (TM1) to form new hydrophobic contacts with A166 (TM1). Other broken contacts are those with F259 and G255 of TM3 (**Figure 10B**). The fact that the contacts involving H206 are formed and broken

at the very end of the process, suggests that the whole mechanism is finalized to these events highlighting the importance of H206. This is consistent with the experimental evidence (Yeung et al., 2018) that most mutations of H206 create constitutively open mutants. Indeed our open structure was taken from the backmutated H206A mutant (Hou et al., 2018).

2.3.3 Analysis of Inter-helical Distances

The contact analysis has highlighted two main events during the gating process: the massive formation or breakdown of contacts between helices TM3 and TM4b and the final formation and breakdown of several contacts involving H206. We will now analyze more in depth these two events starting with the formation/destruction of contacts in the TM3/TM4b interface.

In the C → O transition, after the massive breakdown of contacts, helices TM3 and TM4b move apart (**Figure 11B**) and they face a different destiny. Helix TM3, in particular its lower part, moves centrifugally. The displacement of helix TM3 makes room for a corresponding centrifugal displacement of the lower part of helix TM1: this is the opening of the basic region of the pore. These motions are described in **Figure 11A** where we show the displacement of helices TM1 and TM3 from the center of mass of the pore. Both helices move centrifugally, but since TM1 takes a longer step, the TM1-TM3 distance decreases (**Figure 11B**) justifying the formation of contacts that we observed in the contact analysis (**Figure 10**).

We now turn to the fate of TM4b. In **Figure 11C** we show the displacement of TM4b(n + 1), TM3(n), and TM2(n) with respect

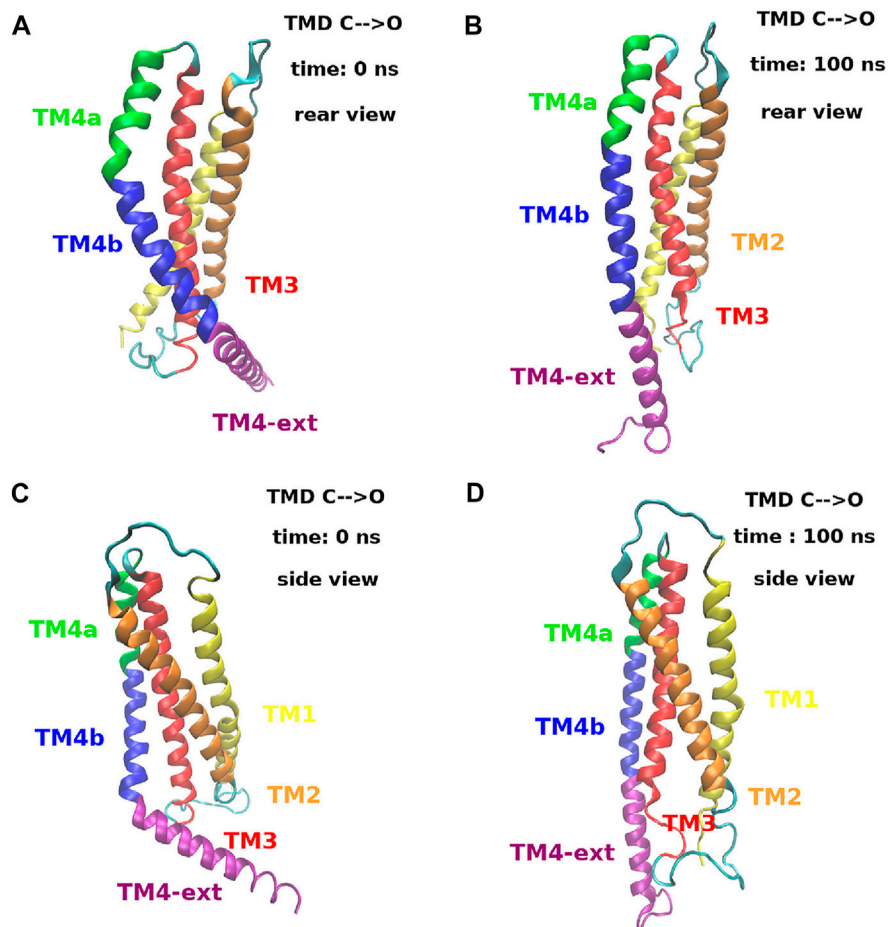


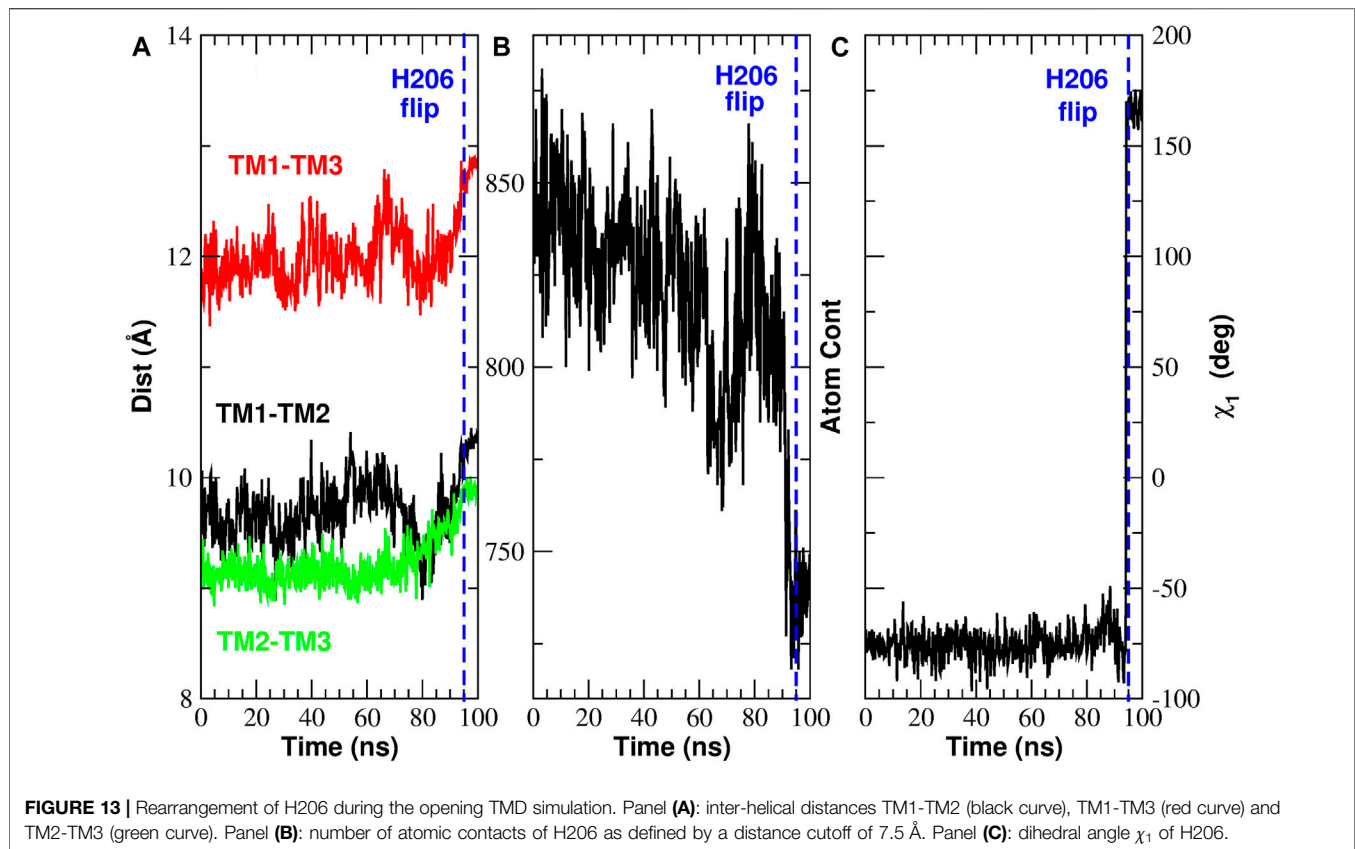
FIGURE 12 | Extension process of helix TM4 during the opening TMD simulation. Panels (A) and (B) show a rear view of a single subunit at time $t = 0$ ns and $t = 100$ ns. Panels (C) and (D) show a side view of the same subunit at the same simulation times. The color code is the following. Helix TM1: yellow, helix TM2: orange, helix TM3: red, helix TM4a: green, helix TM4b: blue and helix TM4-ext: purple. A dynamic view of this process can be seen in **Supplementary Movie S2**.

to the initial position of the centers of mass. The displacements have been projected on the vectors connecting the COMs of the three helices so that a positive displacement corresponds to an approach while negative displacements correspond to a distancing. Our plots show that, while TM4b($n + 1$) moves closer to TM2(n) and TM3(n), also TM2(n) and TM3(n) move towards TM4b($n + 1$) so that there is a decrease of distances TM4b($n + 1$)-TM3(n) and TM4b($n + 1$)-TM2(n) as illustrated in **Figure 11D**. This pattern is in agreement with the TM4b($n + 1$)-TM2(n) contact formation observed in the contact analysis (**Figure 10**).

As shown in **Supplementary Figure S11**, what happens during the closing transition is the reverse of what occurs during opening. The lower parts of helices TM1 and TM3 move towards the center of the pore (**Supplementary Figure S11A**) and since TM1 takes a longer step, the distance between the two helices increases (**Supplementary Figure S11B**) and we have breakdown of TM1-TM3 contacts (**Supplementary Figure S9**). We also note that, as helices TM4b($n + 1$), TM2(n)

and TM3(n) move apart from each other (**Supplementary Figure S11C**), their distance increases (**Supplementary Figure S11D**) and we have the breakdown of TM4b($n + 1$)-TM2(n) contacts highlighted in the contact analysis (**Supplementary Figure S9**).

The structural mechanism that underlies the distance plots in **Figure 11** is depicted in **Figure 12**. Panels (A) and (B) of **Figure 12** show a rear view of a single subunit at time zero and at 100 ns during the opening process. At time zero, in the closed state, helix TM4 has a double bend, one between TM4a and TM4b and one between TM4b and TM4-ext. In this particular arrangement it can be observed that helices TM4b and TM4-ext are behind helix TM3 that therefore is prevented from moving back. At time 100 ns, helix TM4 is fully extended. In this conformation, the space behind helix TM3 has been cleared and, since helix TM4b is no longer in the way, helix TM3 can move backwards. Panels (C) and (D) of **Figure 12** show a side view of the same process. What is notable here is that the extension of TM4b allows the backward movement of the



lower part of TM3. This motion, in turn, clears the space behind TM1 allowing a backward movement of the lower part of this helix that opens the basic region of the pore. This process is dynamically illustrated in **Supplementary Movie S2**.

As already discussed, the contact analysis has highlighted two key events. After analyzing the implications of the TM3-TM4b contact breakdown, we now turn to the events involving H206. In **Figure 11** and in **Supplementary Figure S11** we have observed a significant rearrangement of helices TM1, TM2, TM3. In particular, we have noted that, during the opening process, helix TM1 moves centrifugally while helices TM2 and TM3 of subunit n move towards helix TM4b of subunit $n + 1$. **Figure 13A** shows that these events cause an increase in the distances TM1-TM2, TM1-TM3, and TM2-TM3. Since the side-chain of H206 leans in the space between these three helices, their distancing causes a decrease in the atom density around H206, see **Figure 13B** showing the number of atom contacts of H206 as defined by a distance cutoff of 7.5 Å. Finally, **Figure 13C** shows that as soon as the atom density around H206 decreases, the side chain of this residue swings due to a rotation around dihedral angle χ_1 . **Supplementary Figure S12** shows that the reverse process occurs during closing. In this case there is a decrease of the distances, TM1-TM2, TM1-TM3, and TM2-TM3 (**Supplementary Figure S12A**). This causes an increase in the atom density around H206 (**Supplementary Figure S12B**) so that the side chain of this residue is pushed back (**Supplementary Figure S12C**) to the conformation typical of the closed state.

Figure 14 provides a structural view of the conformational transition involving H206. For the sake of clarity only a short stretch of helices TM1 and TM2 is shown. **Figures 14A,B** offer a view from the front while **Figures 14C,D** from the rear. In the closed state, as predicted by Yeung et al. (2018), H206 is hydrogen bonded with L202 also located on TM2. H206 is also close to S165, but differently from Frischauf et al. (2019), no hydrogen bond can be seen. Finally, in the closed state, H206 forms hydrophobic contacts with L168 on helix TM1. When opening occurs, H206 rotates around the χ_1 dihedral breaking the hydrogen bond with L202 and swinging from the contact with L168 to a hydrophobic contact with A166 (also located on TM1). It is important to note that this rearrangement of H206 creates a free space behind the hydrophobic region of TM1. A dynamic view of this process is provided by **Supplementary Movie S3**.

3 DISCUSSION

In this work we computationally characterized the closed and two putatively open conformations of CRAC channel to shed light on its gating mechanism. The assignment to the open or closed state of the available structures is not completely obvious. Indeed, the radius profile of structure 4HKR is always larger than the radius of a single water molecule. This means that, from a geometric standpoint, the pore is water-accessible and it should be assigned to the open state in disagreement with the results of the

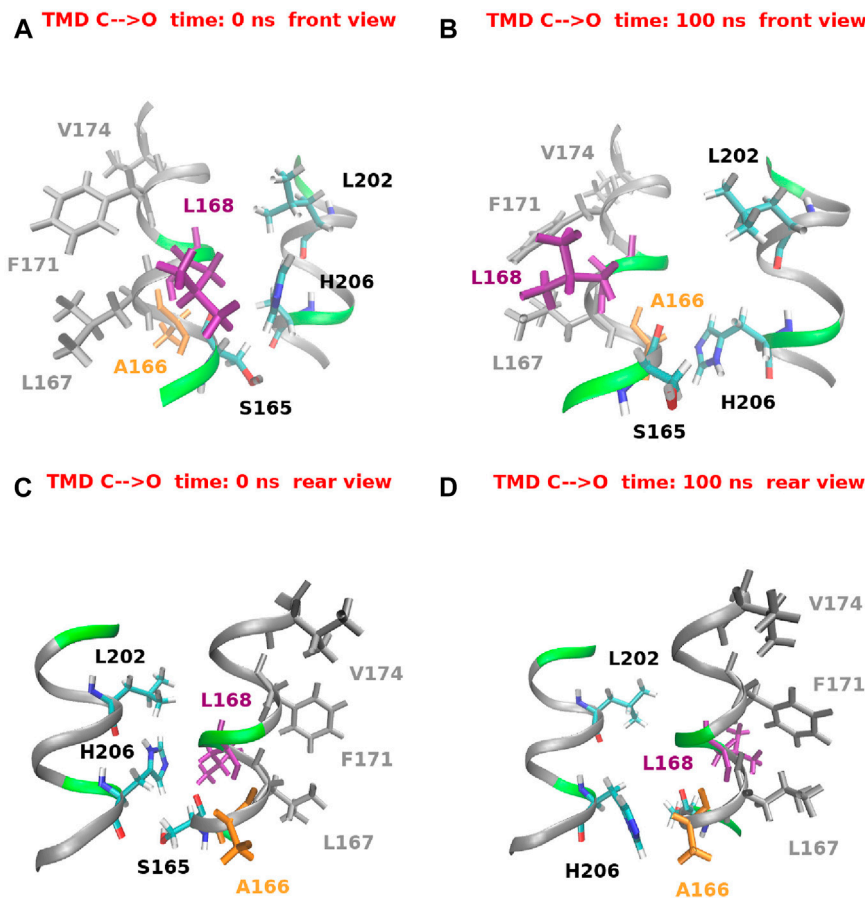


FIGURE 14 | Histidine 206 swing during the opening TMD simulation. For the sake of clarity only a small stretch of helices TM1 (residues 165–175) and TM2 (residues 200–208) is shown. Panels (A) and (B) show a front view at simulation time $t = 0$ ns and $t = 100$ ns respectively. Panels (C) and (D) show a rear view of the same helices at the same simulation times.

fluorescence-based flux measurements performed on the purified channel reconstituted in liposomes (Hou et al., 2012). This contradiction can be reconciled if the geometric analysis is integrated with a study of the chemical properties of the pore wall. Our equilibrium simulations show a peak of the hydrophobicity profile in correspondence of the hydrophobic region, where also the Potential of Mean Force of water has its maximum. This suggests a scenario of functional occlusion of the pore even in the absence of steric block, which is the hallmark of *hydrophobic gating* (Aryal et al., 2015). During our equilibrium simulations of the closed state 4HKR, a vacuum bubble appears early in the hydrophobic region and is stably maintained throughout the simulation. The bubble prevents the flow of liquid water and ions that would be obliged to release their hydration shells. In agreement with this pattern, during our TMD simulation the bubble forms in the O \rightarrow C transition and disappears in the C \rightarrow O transition. According to the thermodynamic theory by Roth et al. (2008), even in a geometry as complex as that of KcsA channel, hydrophobic gating is tuned by pore radius and wall hydrophobicity. The phenomenon is predicted to be highly cooperative and to occur

abruptly in a narrow range of values of the radius or hydrophobicity (in agreement with our **Figures 6C,D**). Roth et al. (2008) arrive as far as to say that all ion channels use hydrophobic gating, the only difference regarding the details of the conformational change adopted to tune radius and hydrophobicity of the pore. This statement probably overestimates the diffusion of hydrophobic gating. However, hydrophobic gating, originally discovered in simple model nanopores (Beckstein and Sansom, 2003), has recently been identified in an increasing number of biological ion channels (see Aryal et al. (2015) and references therein) including bacterial mechanosensitive channels, ligand-gated ion channels of the Cys-loop family (including the nicotinic acetylcholine receptor, GLIC, and 5-HT₃ receptor), and even members of the superfamily of tetrameric P-loop cation channels.

The functional assignment of the P288L mutant (PDB: 6AKI) is just as controversial. The dOrail P288L mutant is the equivalent of the P245L gain of function mutant (Nesin et al., 2014) of hOrail that causes tubular myopathy and congenital myosis. Moreover, when Liu et al. (2019) performed patch clamp measurements on HEK cells transfected with the P288L

mutant, they recorded an inward-rectified Ca^{2+} current that in the absence of calcium was replaced by a current of monovalent cations. However, Hou et al. (2020) were unable to detect ion permeation through purified P288L Orai in liposomes. Hou et al. (2020) also observed that the narrow pore radius profile of P288L made this structure similar to the non-conductive *unlatched-close* conformation discovered by their group. Another piece of evidence is represented by the scanning mutagenesis study by Yeung et al. (2018). This study revealed that P245C, along with many other mutants of Orai1, displays a basal level of constitutive activation that can be enhanced by STIM1 interaction. Indeed, the STIM1-induced increase of current shows an inverse relationship with constitutive activity. These results suggest that open mutants are not maximally active but rather adopt one or more states that can be further activated by STIM1. This scenario is consistent with our equilibrium simulations where 6AKI structure is conformationally unstable undergoing a spontaneous bending of TM4 helices and the disruption of a bubble initially present in the hydrophobic region. We thus suggest this structure represents an intermediate in the gating process rather than the open state conformation. The P288L structure resolved by Liu et al. (2019) is thus likely to represent one of the metastable states postulated by Yeung et al. (2018) whose activity can be enhanced by STIM1.

CRAC gating mechanism is a highly controversial issue. In a seminal work Yamashita et al. (2017), on the grounds of Cd^{2+} accessibility experiments on cysteine mutants of pore wall residues, proposed a mechanism based on a modest counter-clockwise rotation of pore helices aimed at displacing from the pore lumen the bulky side-chains of hydrophobic residues. This model was also supported by equilibrium MD simulations (Yamashita et al., 2017) of wild type and mutant channels revealing frequent spontaneous conformational fluctuations involving rotation of the pore helix relative to the crystallographic structure. The rotation of F99 was also observed in MD simulations performed by Bulla et al. (2019) on the H134C constitutively open mutant. The rotation of pore helices, however, was not observed in a number of subsequent computational and experimental works. Frischauf et al. (2019) in a molecular dynamics simulation study of a homology model of human CRAC channel did not observe any rotation of pore helices. Neither was any rotation observed in the crystal structure of the putatively open mutant P288L (Liu et al., 2019). Recently the crystal structure of another constitutively open mutant, H206A, has been resolved (Hou et al., 2018). The resolution (6.7 Å) however, was so low that side chains were not visible making it impossible to ascertain a possible rotation. When the structure was resolved again (Hou et al., 2020) at 3.3 Å resolution through cryo-electron microscopy, rotation was not observed and the data suggested a simple dilation of pore helices. However, it must be noted that, in order to increase the resolution of the cryo-EM structure, the mass of CRAC channel was increased through formation of a complex with the Fab fragment of a monoclonal antibody. The binding site of the antibody is the extra-cellular loop connecting helices TM2 and TM3 and the close proximity of the docking point with the pore helices might prevent their rotation. Even if Hou et al. (2020) showed that acute application of the

antibody does not alter Ca^{2+} influx, the short incubation time of the antibody-channel mixture may have led to a strained conformation limiting the mobility of pore helices.

Our Targeted Molecular Dynamics simulations showed a rotation of pore helices occurring as a twisting, rather than a rigid body rotation. Interestingly, the rotation angle plot exhibited a change in slope matching the time of formation or disruption of the bubble in the hydrophobic region. The rotation of the hydrophobic region however, induced a change of the Solvent Accessible Area that opposed rather than favouring the formation of the bubble. Further analysis revealed that helix rotation might play a role in the change of pore radius even if helix displacement is also important. In other words our work suggests that the purpose of pore helix rotation is not to create a thermodynamically favourable environment for bubble formation or disruption but it contributes to change the pore radius complementing the effect of helix displacement.

A fascinating feature of CRAC channel is the recently proposed (Zhou et al., 2019; Yeung et al., 2020) allosteric nature of its activation mechanism. The activator protein STIM1 is known to bind to the TM4-ext helices, the outermost ring of helices. This event then induces opening of the pore that is lined by helices TM1, the innermost ring of helices. The coupling between these two events occurring far away in space implies the propagation of a conformational wave.

The allosteric nature of CRAC gating is also suggested by a recent work of Bulla et al. (2019) on a homology model of human CRAC channel. In particular, it was shown that the tubular myopathy related mutation T184M, on helix TM3, favours channel opening but is strictly dependent on STIM1. The mutation thus, does not lock the pore in a permanently open state but favours the propagation of the conformational change triggered by STIM1 docking. This finding is consistent with our results. Indeed, residue T184 in human CRAC corresponds to residue L256 in the *Drosophila* variant and our contact analysis revealed that the neighbouring residue G255 is involved in the breakdown or formation of contacts with the critical H206 residue in the final stage of the process. In order to shed light on this mechanism, we systematically applied this approach and we thus determined the sequence of contact breakdown and formation during the C → O and O → C transitions. We discovered that in the opening process contact breakdown starts at the coiled-coil between TM4-ext helices (where STIM1 is expected to bind) and proceeds to the extracellular side across the TM3-TM4b interface. The breakdown wave then further proceeds to the inner helices. What is more interesting, both in the opening and closing processes, the final stage involves formation and breakdown of contacts of H206 suggesting that the whole mechanism might be finalized to this event. The importance of H206 is well documented in the literature (Yeung et al., 2018). Its mutations to smaller and/or hydrophilic residues (like Ala, Cys, Ser, Thr) generate Ca^{2+} selective, constitutively open mutants.

The analysis of our TMD simulations reveals that, in the opening process, the extension of helix TM4 causes a massive breakdown of contacts in the TM3-TM4b interface that leads to the separation of the two helices. In particular, helix TM4b moves

aside clearing the space behind TM3 that can move back. This event, in turn, clears the space behind the lower part of helix TM1 that also moves back, increasing the radius of the basic region and drawing water from the bulk. In this last stage, a number of TM1-TM3 contacts are established. The transduction pathway TM4b \rightarrow TM3 \rightarrow TM1 (basic region) was also predicted by Liu et al. (2019) based on the analysis of the structure of mutant P288L. The existence of this pathway was validated in patch-clamp and Ca^{2+} flow measurements of a series of mutants (Liu et al., 2019). For instance, the mutation of residues L153, S154, and K157 that are involved in the TM1-TM3 interactions, significantly reduced the extracellular Ca^{2+} influx.

The rearrangement of helices TM1, TM2, and TM3 determines in our opening TMD simulations an increase of the inter-helical distances TM1-TM2, TM1-TM3, and TM2-TM3. This results in a decrease of the atomic density around H206 whose side chain leans into the space delimited by the three helices. As soon as the atomic density around H206 is sufficiently low the side chain of H206 swings from a position in hydrophobic contact with L168 to a new position where it forms a hydrophobic contact with A166. It is important to note that the rearrangement of H206 creates a free space behind the hydrophobic region of helix TM1.

The functional role of H206 is object of debate in the literature. According to Frischauf et al. (2019) H206 plays its role by hydrogen bonding S165 and S169 on helix TM1 so as to stabilize the closed state. These bonds, however, can only be found in less than 5% of the frames of our simulations. In an alternative model proposed by Yeung et al. (2018), H206 is hydrogen bonded with the backbone carbonyl of L202, in agreement with our TMD simulations. Moreover, in a series of mutagenesis experiments, Yeung et al. (2018) showed that the ability of the residue in position 206 to stabilize the closed state does not depend on its hydrogen-bonding ability but rather on the side chain volume. In other words H206 would act as a *steric brake* pushing against helix TM1 and preventing its backward movement. In agreement with this model we speculate that the void space created by the flipping of H206 observed in our TMD simulations would allow the backward motion of the hydrophobic region of TM1. According to the thermodynamic theory by Roth et al. (2008) even a small increase in the pore radius could then be sufficient to break the bubble and open the pore.

Even if in our O \rightarrow C simulation the displacement of H206 takes place just before the formation of the bubble, in the C \rightarrow O simulation the H206 swing occurs at time $t \sim 95$ ns, after the bubble has already been destroyed. Moreover in neither simulation do we observe any change in the radius of the hydrophobic region after the H206 swing. This pattern however, may be due to an insufficiently long Targeted MD simulation or to the limitations of the TMD algorithm. A more accurate (albeit more computationally expensive) enhanced sampling approach like Transition Path Sampling (Bolhuis et al., 2002) might have reproduced a behaviour consistent with the steric brake model.

The mechanism of conformational transition from the closed to the open state emerging from our simulations, sheds some light

on the elusive role of the *unlatched-closed* conformations. These structures (PDB: 6BBG and 6BBH), featuring extended TM4 helices and a pore domain (TM1-TM4a) indistinguishable from that of the closed state (PDB: 4HKR) within the limits of the diffraction data (Hou et al., 2018), suggest that the unlatching of TM4 helices does not automatically lead to pore opening. Indeed, Hou et al. (2018) suggested that unlatching is a necessary but not sufficient condition for pore opening. This result significantly complicates the formulation of a convincing transition mechanism, but the problem may be solved by adopting a dynamic rather than a static view. Hou et al. (2018) put forward the idea that the unlatched-closed conformations may represent intermediates in the path from the closed to the open state. These authors suggested that, even in the closed state, a chemical equilibrium should exist between the bent and extended conformations of helix TM4. The interaction with the STIM1 activator would then shift the equilibrium to the extended state generating an unlatched-open conformation. The propagation of the conformational change to the inner rings of helices would then complete the transition to the closed state. The results of our equilibrium simulation of 6AKI perfectly fit within this scenario. As already discussed, 6AKI features extended TM4 helices and a pore radius profile similar to that of the closed state. The structure of 6AKI is therefore very similar to that of the unlatched-closed conformations resolved by Hou et al. (2018). The spontaneous bending of TM4 helices observed in our equilibrium simulations highlights the conformational instability of 6AKI supporting the idea that this structure, as conjectured for unlatched-closed conformations, is an intermediate, presumably very close to the quiescent state along the gating pathway. Our TMD simulations, on the other hand, highlight a sequence of events that causally link the unlatching of helix TM4 with the dissolution of the bubble *via* the backward motion of helices TM3 and TM1, the distancing of helices TM1, TM2, and TM3, the swinging of the side-chain of H206 and the increase of pore radius in the hydrophobic region. In short sum, our work confirms with dynamical data of MD simulations the sequence of channel activation proposed by Hou et al. (2018) on the grounds of static crystallographic pictures.

As already discussed, our work has been performed using as a closed state the X-ray structure of mutant H206A resolved by Hou et al. at 6.7 Å resolution. Recently however, a new high-resolution (3.2 Å) cryo-EM structure of mutant H206A has been published (Hou et al., 2020). This suggests the opportunity to discuss the relevance of our results in view of the new structural data. The main merit of the new structure is that it resolves the side-chains of pore-lining residues and its comparison to the closed structure (PDB: 4HKR) shows that the gating mechanism of Orai does not involve rotation of pore helices but just their translation. Our analysis of pore helix rotation was performed using a methodology that does not require knowledge of the exact position of side-chains in the experimental structures. In fact, we defined rotation angles only based on the position of α -Carbons. The modest main-chain RMSD (1.5 Å) between the new 7KR5 structure and the 6BBF structure employed in our study suggests that our C_α -based methodology should be appropriate. Moreover, our TMD simulations were not started from the experimental

structures, but from structures equilibrated for 100 ns where the position of pore helix side-chains is allowed to vary with respect to the initial crystallographic conformations. Our simulations did reveal pore helix rotation that, however, only provides a small contribution to the variation of the pore radius; this quantity mainly depends on helix displacement, in agreement with the cryo-EM structure 7KR5. It is possible that an alternative definition of the rotation angles, more dependent on the orientation of side-chains, would have led to smaller or even negligible rotation angles. However, it is also possible that the presence of antibody Fab fragments complexed with CRAC channel at the level of the TM1-TM2 loop (Hou et al., 2020), may have put helix TM1 under strain preventing its ability to rotate. Further studies will be needed to solve this problem.

Another important issue is related to the hydrophobic gating mechanism. Using an hydrophobic constriction with length similar to that of the hydrophobic region of CRAC channel, Aryal et al. (2015) observed a dewetting transition when the diameter of the construct falls below a cutoff of approximately 9 Å. When discussing the features of the 7KR5 structure, Hou et al. (2020) highlighted the fact that the diameter of CRAC hydrophobic region is 5–6 Å in the closed state (PDB: 4HKR) and 9–10 Å in the open state (PDB: 7KR5) and on this ground they predicted a hydrophobic gating mechanism. The fact that our TMD simulations showed formation and destruction of a bubble in the hydrophobic region, shows that our simulations based on the lower-resolution (6.7 Å) 6BBF H206A structure are also compatible with the higher resolution 7KR5 structure.

In short sum, our work, judiciously combining equilibrium and enhanced sampling MD simulations, highlighted the hydrophobic gating mechanism of CRAC channel and traced the allosteric coupling between the TM4 helices where the effector STIM1 binds, and the pore helices where the bubble forms and breaks. Many aspects of this mechanism require further investigation. The events following the H206 flip will have to be identified through longer or more accurate enhanced sampling simulations. Moreover, the role of a basic region in a cation channel will have to be clarified and the interplay between the electrostatic and hydrophobic gates accurately analyzed. These efforts will not only aid in the treatment of the diseases caused by mutations of this channel, but will also deepen our general understanding of hydrophobically-gated ion channels.

4 MATERIALS AND METHODS

4.1 Set-Up of the Systems

The conformation of the closed state of CRAC channel was taken from the Protein Data Bank (PDB ID: 4HKR) and the missing loops 181–190 and 220–235 were modelled with the MODELLER 9.21 software (Sali and Blundell, 1993). This structure contains mutations C224S, C283T introduced to prevent non specific disulfide formation and P276R, P277R (in the hypervariable TM3-TM4 loop) introduced to produce well ordered crystals (Hou et al., 2012). In order to better compare our computational results with the experimental data in the literature, these mutations were retained. The structures of the constitutively

open mutants H206A and P288L were also taken from the Protein Data Bank (PDB ID: 6BBF and 6AKI respectively). In order to prepare the systems for Targeted Molecular Dynamics simulations (Schlitter et al., 1994) that require the same number of atoms in the initial and final conformations, short N-terminal and C-terminal extensions have been added to both 6BBF (residues 144–147 and 328–334) and 6AKI (residues 144–149 and 331–334) to match the sequence length of 4HKR, using the MODELLER software (Sali and Blundell, 1993). The structures of 6BBF and 6AKI have been back-mutated to the wild type sequence (mutation A206H in 6BBF and L288P in 6AKI). In order to match the sequence of 4HKR mutations P276R and P277R have also been introduced. Protonation states have been assigned using the WHATIF server (Vriend, 1990). A number of open issues pertaining to the experimental structures of the closed state (PDB: 4HKR) and the putatively open states (PDB: 6BBF, 6AKI) is discussed in Supplementary Material section *Open issues on CRAC experimental structures*. The three channels were embedded in a lipid bilayer comprising 533 molecules of 1-palmitoyl-2-oleoyl-sn-glycero-3-phosphocholine (POPC) and solvated by 62,927 water molecules using the CHARMM Membrane Builder (Wu et al., 2014). We added 184 sodium ions and 172 chloride ions so as to neutralize the charge of the channel and reach a final concentration (NaCl) = 0.15 M. Overall, the system comprised 279,195 atoms and the simulation box had dimensions 145 × 145 × 130 Å.

4.2 Equilibrium MD Simulations

All simulations were performed with the NAMD 2.11b2 suite of programs (Phillips et al., 2005) using the ff15ipq force field (Debiec et al., 2016) for the protein, the Lipid17 force-field (Dickson et al., 2014) for the phospholipids and the SPC/E water model (Takemura and Kitao, 2012).

The three systems first underwent 10,000 steps of conjugate gradient minimization. During equilibration harmonic restraints were applied to nonhydrogen atoms of the protein backbone and side-chains as well as to the phospholipid heads. A harmonic restraint was also applied to the dihedral angle formed by carbons 8–11 of oleoyl acid and to the improper dihedral C₁-C₃-C₂-O₂ involving the three carbons of the glycerol unit and the hydroxyl oxygen linked to its central carbon. The equilibration was organized in 12 stages whereby the constraints were gradually released. The values of the force constants used in the 12 stages can be found in **Supplementary Table S1**.

The production run, following the restrained equilibration, was carried out in the isothermal isobaric ensemble for 100 ns. Pressure was kept at 1 atm by the Nosé-Hoover Langevin piston method, and the temperature was kept at 300 K by coupling to a Langevin thermostat with a damping coefficient of 1 ps⁻¹. Long-range electrostatic interactions were evaluated with the smooth particle mesh Ewald algorithm. For the short-range nonbonded interactions, we used a cutoff of 12 Å with a switching function at 10.0 Å. The integration time step was 2 fs, and the bonds between hydrogen and heavy atoms were fixed to eliminate the most rapid oscillatory motions.

Pore radius profiles have been computed using the HOLE program (Smart et al., 1996). The Potential of Mean Force (PMF)

of water and ions as a function of the axial position and of the distance from the pore axis was computed using equation (Im and Roux, 2002): $PMF(z, r) = -k_B T \log(\rho(z, r)/\rho_{bulk})$ where k_B is Boltzmann constant, T is the absolute temperature, ρ_{bulk} is the water or ion density in the bulk and $\rho(z, r)$ is the density in position (z, r) . In order to avoid a divergence of the PMF in ranges of z devoid of samples, we arbitrarily assign to these bins the maximal value of the free energy of the profile, *i.e.* the value of the free energy corresponding to the bin with the smallest non-zero water density. The assignment of this constant value to all the bins devoid of samples leads to the emergence of an artificially flat region near the maximum of the PMF as can be observed, *e.g.*, in **Figure 3C**; for this region the physical expectation is to find water molecules in the gas state. The electrostatic potential inside the pore has been computed using the PMEpot plugin (Aksimentiev and Schulten, 2005) of VMD as detailed in the *Supplementary Methods* section of the Supplementary Information. This section also provides information on our protocols to compute rotation angles, solvent accessible area and hydrophobicity profile.

4.3 Targeted MD Simulations

Targeted Molecular Dynamics (TMD) (Schlitter et al., 1994) is an enhanced sampling technique used to drive a system between given end states. The algorithm applies a harmonic biasing potential to the RMSD between the current conformation and the target conformation:

$$U_{TMD} = \frac{1}{2} \frac{k}{N} [RMSD(t) - \rho(t)]^2$$

where k is the force constant, N is the number of atoms where the biasing force will be applied and $\rho(t)$ is the target RMSD that during the simulation is linearly decreased from the RMSD between initial and final structure to zero. In our case the system was steered from the final frame of the equilibrium simulation of the closed state (PDB: 4HKR) to the final frame of the equilibrium simulation of the open state (PDB: 6BBF) and *vice versa*. We applied a biasing force constant of 100,000 kcal/mol/Å² and we chose a simulation length of 100 ns for the C → O transition and 500 ns for the O → C transition. Since the initial distance between closed and open state is 13.94 Å, this choice ensured a sufficiently slow transition with a variation of the RMSD of ~0.14 Å/ns in the C → O and of ~0.03 Å/ns in the O → C transition. This extremely slow protocol should allow the relaxation of the degrees of freedom that were not biased during the simulation. The good superposition between the time-

evolutions of the current and target RMSD (**Supplementary Figure S13**) is an indication that the TMD was run slowly enough to allow the system to follow the target RMSD schedule. Finally, in order to avoid unfolding events an harmonic constraint was applied on the α -helical content of TM4-ext helices (force constant 50,000 kcal/mol/Å²).

DATA AVAILABILITY STATEMENT

The datasets presented in this study can be found in online repositories. The names of the repository/repositories and accession number(s) can be found below: <https://zenodo.org/doi/10.5281/zenodo.5497661>.

AUTHOR CONTRIBUTIONS

CG and AG designed the research, DS ran and analyzed equilibrium simulations, CG ran and analyzed TMD simulations, CG drafted the paper, CG, DS and AG revised the manuscript.

FUNDING

This project has received funding from the European Research Council (ERC) under the European Union's Horizon 2020 research and innovation programme (grant agreement No. 803213).

ACKNOWLEDGMENTS

We thank Gerhard Thiel and Anna Moroni for thoughtful discussion. The authors acknowledge PRACE for awarding us access to Marconi100 at CINECA, Italy.

SUPPLEMENTARY MATERIAL

The Supplementary Material for this article can be found online at: <https://www.frontiersin.org/articles/10.3389/fmolb.2021.773388/full#supplementary-material>

REFERENCES

- Aksimentiev, A., and Schulten, K. (2005). Imaging α -Hemolysin with Molecular Dynamics: Ionic Conductance, Osmotic Permeability, and the Electrostatic Potential Map. *Biophysical J.* 88, 3745–3761. doi:10.1529/biophysj.104.058727
- Aryal, P., Sansom, M. S. P., and Tucker, S. J. (2015). Hydrophobic Gating in Ion Channels. *J. Mol. Biol.* 427, 121–130. doi:10.1016/j.jmb.2014.07.030
- Beckstein, O., and Sansom, M. S. P. (2003). Liquid-vapor Oscillations of Water in Hydrophobic Nanopores. *Proc. Natl. Acad. Sci.* 100, 7063–7068. doi:10.1073/pnas.1136844100
- Böhm, J., Bulla, M., Urquhart, J. E., Malfatti, E., Williams, S. G., O'Sullivan, J., et al. (2017). Orail Mutations with Distinct Channel Gating Defects in Tubular Aggregate Myopathy. *Hum. Mutat.* 38, 426–438. doi:10.1002/humu.23172
- Bolhuis, P. G., Chandler, D., Dellago, C., and Geissler, P. L. (2002). Transition Path Sampling: Throwing Ropes over Rough Mountain Passes, in the Dark. *Annu. Rev. Phys. Chem.* 53, 291–318. doi:10.1146/annurev.physchem.53.082301.113146
- Bulla, M., Gyimesi, G., Kim, J. H., Bhardwaj, R., Hediger, M. A., Frieden, M., et al. (2019). Orail Channel Gating and Selectivity Is Differentially Altered by Natural Mutations in the First or Third Transmembrane Domain. *J. Physiol.* 597, 561–582. doi:10.1113/JP277079
- Camisasca, G., Tinti, A., and Giacomello, A. (2020). Gas-induced Drying of Nanopores. *J. Phys. Chem. Lett.* 11, 9171–9177. doi:10.1021/acs.jpclett.0c02600

- Costa, F., Guardiani, C., and Giacomello, A. (2021). Gating Pathways in Herg Channel. *Submitted Commun. Biol.*
- Debiec, K. T., Cerutti, D. S., Baker, L. R., Gronenborn, A. M., Case, D. A., and Chong, L. T. (2016). Further along the Road Less Traveled: Amber Ff15ipq, an Original Protein Force Field Built on a Self-Consistent Physical Model. *J. Chem. Theor. Comput.* 12, 3926–3947. doi:10.1021/acs.jctc.6b00567
- Dickson, C. J., Madej, B. D., Skjevik, Å. A., Betz, R. M., Teigen, K., Gould, I. R., et al. (2014). Lipid14: The Amber Lipid Force Field. *J. Chem. Theor. Comput.* 10, 865–879. doi:10.1021/ct4010307
- Dong, H., Fiorin, G., Carnevale, V., Treptow, W., and Klein, M. L. (2013). Pore Waters Regulate Ion Permeation in a Calcium Release-Activated Calcium Channel. *Proc. Natl. Acad. Sci.* 110, 17332–17337. doi:10.1073/pnas.1316969110
- Dong, H., Klein, M. L., and Fiorin, G. (2014). Counterion-assisted Cation Transport in a Biological Calcium Channel. *J. Phys. Chem. B* 118, 9668–9676. doi:10.1021/jp5059897
- Feske, S., Prakriya, M., Rao, A., and Lewis, R. S. (2005). A Severe Defect in CRAC Ca²⁺ Channel Activation and Altered K⁺ Channel Gating in T Cells from Immunodeficient Patients. *J. Exp. Med.* 202, 651–662. doi:10.1084/jem.20050687
- Frenkel, D., and Smit, B. (2002). *Understanding Molecular Simulation*. San Diego, San Francisco, New York, Boston, London, Sydney, Tokyo: Academic Press, a Division of Harcourt Inc.
- Frischauf, I., Litviňuková, M., Schober, R., Zayats, V., Svobodová, B., Bonhenry, D., et al. (2017). Transmembrane helix Connectivity in Orai1 Controls Two gates for Calcium-dependent Transcription. *Sci. Signal.* 10, 1–38. doi:10.1126/SCISIGNAL.AAO0358
- Garibaldi, M., Fattori, F., Riva, B., Labasse, C., Brochier, G., Ottaviani, P., et al. (2017). A Novel Gain-Of-Function Mutation in Orai1 causes Late-Onset Tubular Aggregate Myopathy and Congenital Miosis. *Clin. Genet.* 91, 780–786. doi:10.1111/cge.12888
- Giacomello, A., and Roth, R. (2020). Bubble Formation in Nanopores: a Matter of Hydrophobicity, Geometry, and Size. *Adv. Phys. X* 5, 1817780. doi:10.1080/23746149.2020.1817780
- Hou, X., Burstein, S., and Long, S. (2018). Structures Reveal Opening of the Store-Operated Calcium Channel Orai. *eLife* 7, e36758. doi:10.7554/eLife.36758
- Hou, X., Outhwaite, I. R., Pedi, L., and Long, S. B. (2020). Cryo-em Structure of the Calcium Release-Activated Calcium Channel Orai in an Open Conformation. *eLife* 9, e62772. doi:10.7554/eLife.62772
- Hou, X., Pedi, L., Diver, M., and Long, S. (2012). Crystal Structure of the Calcium Release-Activated Calcium Channel Orai. *Science* 338, 1308–1313. doi:10.1126/science.1228757
- Im, W., and Roux, B. (2002). Ion Permeation and Selectivity in Ompf Porin: a Theoretical Study Based on Molecular Dynamics, Brownian Dynamics and Continuum Electrodiffusion Theory. *J. Mol. Biol.* 322, 851–869. doi:10.1016/s0022-2836(02)00778-7
- Lacruz, R., and Feske, S. (2015). Diseases Caused by Mutations in Orai1 and Stim1. *Ann. N. Y. Acad. Sci.* 1356, 45–79. doi:10.1111/nyas.12938
- Li, Y., Barbault, F., Delamar, M., Zhang, R., and Hu, R. (2013). Targeted Molecular Dynamics (Tmd) of the Full-Length Kcsa Potassium Channel: on the Role of the Cytoplasmic Domain in the Opening Process. *J. Mol. Model.* 19, 1651–1666. doi:10.1007/s00894-012-1726-3
- Liang, Q., Pang, C., Li, J., Zhang, S., Liu, H., Zhan, Y., et al. (2017). Allosteric Mechanism of Calmodulin Revealed by Targeted Molecular Dynamics Simulation. *Chin. Phys. Lett.* 34, 068701. doi:10.1088/0256-307x/34/6/068701
- Liu, X., Wu, G., Yu, Y., Chen, X., Ji, R., Lu, J., et al. (2019). Molecular Understanding of Calcium Permeation through the Open Orai Channel. *PLoS Biol.* 17, e3000096. doi:10.1371/journal.pbio.3000096
- Nesin, V., Wiley, G., Kousi, M., Ong, E.-C., Lehmann, T., Nicholl, D., et al. (2014). Activating Mutations in Stim1 and Orai1 Cause Overlapping Syndromes of Tubular Myopathy and Congenital Miosis. *Proc. Natl. Acad. Sci. USA* 111, 4197–4202. doi:10.1073/pnas.1312520111
- Park, C., Hoover, P., Mullins, F., Bachhawat, P., Covington, E., Raunser, S., et al. (2009). Stim1 Clusters and Activates Crac Channels via Direct Binding of a Cytosolic Domain to Orai1. *Cell* 136, 876–890. doi:10.1016/j.cell.2009.02.014
- Phillips, J., Braun, R., Wang, W., Gumbart, J., Tajkhorshid, E., Villa, E., et al. (2005). Scalable Molecular Dynamics with Namd. *J. Comput. Chem.* 26, 1781–1802. doi:10.1002/jcc.20289
- Prakriya, M., and Lewis, R. (2015). Store-operated Calcium Channels. *Physiol. Rev.* 95, 1383–1436. doi:10.1152/physrev.00020.2014
- Rao, S., Klesse, G., Stansfeld, P., Tucker, S., and Sansom, M. (2019). A Heuristic Derived from Analysis of the Ion Channel Structural Proteome Permits the Rapid Identification of Hydrophobic gates. *Proc. Natl. Acad. Sci. USA* 116, 13989–13995. doi:10.1073/pnas.1902702116
- Roth, R., Gillespie, D., Nonner, W., and Eisenberg, R. (2008). Bubbles, Gating and Anesthetics in Ion Channels. *Biophys. J.* 94, 4282–4298. doi:10.1529/biophysj.107.120493
- Sali, A., and Blundell, T. (1993). Comparative Protein Modelling by Satisfaction of Spatial Restraints. *J. Mol. Biol.* 234, 779–815. doi:10.1006/jmbi.1993.1626
- Schlitter, J., Engels, M., and Krueger, P. (1994). Targeted Molecular Dynamics: A New Approach for Searching Pathways of Conformational Transitions. *J. Mol. Graphics* 12, 84–89. doi:10.1016/0263-7855(94)80072-3
- Smart, O., Neduvilil, J., Wang, X., Wallace, B., and Sansom, M. (1996). Hole: a Program for the Analysis of the Pore Dimensions of Ion Channel Structural Models. *J. Mol. Graphics* 14, 354–360. doi:10.1016/s0263-7855(97)00009-x
- Takemura, K., and Kitao, A. (2012). Water Model Tuning for Improved Reproduction of Rotational Diffusion and Nmr Spectral Density. *J. Phys. Chem.* 116, 6279–6287. doi:10.1021/jp301100g
- Tinti, A., Giacomello, A., Grosu, Y., and Casciola, C. (2017). Intrusion and Extrusion of Water in Hydrophobic Nanopores. *Proc. Natl. Acad. Sci. USA* 114, E10266–E10273. doi:10.1073/pnas.1714796114
- Vriend, G. (1990). What if: A Molecular Modeling and Drug Design Program. *J. Mol. Graphics* 8, 52–56. doi:10.1016/0263-7855(90)80070-v
- Wu, E., Cheng, X., Jo, S., Rui, H., Song, K., Davila-Contreras, E., et al. (2014). Charmm-gui Membrane Builder toward Realistic Biological Membrane Simulations. *J. Comput. Chem.* 35, 1997–2004. doi:10.1002/jcc.23702
- Xiao, X., Zeng, X., Yuan, Y., Gao, N., Guo, Y., Pu, X., et al. (2015). Understanding the Conformation Transition in the Activation Pathway of β_2 Adrenergic Receptor via a Targeted Molecular Dynamics Simulation. *Phys. Chem. Chem. Phys.* 17, 2512–2522. doi:10.1039/c4cp04528a
- Yamashita, M., Yeung, P.-W., Ing, C., McNally, B., Pomes, R., and Prakriya, M. (2017). Stim1 Activates Crac Channels through Rotation of the Pore helix to Open a Hydrophobic Gate. *Nat. Commun.* 8, 1–13. doi:10.1038/ncomms14512
- Yeung, P.-W., Yamashita, M., Ing, C., Pomes, R., Freymann, D., and Prakriya, M. (2018). Mapping the Functional Anatomy of Orai1 Transmembrane Domains for Crac Channel Gating. *Proc. Natl. Acad. Sci. USA* 115, E5193–E5202. doi:10.1073/PNAS.1718373115/-DCSSupplemental
- Yeung, P.-W., Yamashita, M., and Prakriya, M. (2020). Molecular Basis of Allosteric Orai1 Channel Activation by Stim1. *J. Physiol.* 598, 1707–1723. doi:10.1113/JP276550
- Zhou, Y., Nwokoko, R., Baraniak, J. J., Trebak, M., Lee, K., and Gill, D. (2019). The Remote Allosteric Control of Orai Channel Gating. *Plos Biol.* 17, e3000413. doi:10.1371/journal.pbio.3000413

Conflict of Interest: The authors declare that the research was conducted in the absence of any commercial or financial relationships that could be construed as a potential conflict of interest.

Publisher's Note: All claims expressed in this article are solely those of the authors and do not necessarily represent those of their affiliated organizations, or those of the publisher, the editors and the reviewers. Any product that may be evaluated in this article, or claim that may be made by its manufacturer, is not guaranteed or endorsed by the publisher.

Copyright © 2021 Guardiani, Sun and Giacomello. This is an open-access article distributed under the terms of the Creative Commons Attribution License (CC BY). The use, distribution or reproduction in other forums is permitted, provided the original author(s) and the copyright owner(s) are credited and that the original publication in this journal is cited, in accordance with accepted academic practice. No use, distribution or reproduction is permitted which does not comply with these terms.



Exploring K_v1.2 Channel Inactivation Through MD Simulations and Network Analysis

Flavio Costa, Carlo Guardiani and Alberto Giacomello*

Dipartimento di Ingegneria Meccanica e Aerospaziale, Sapienza Università di Roma, Rome, Italy

OPEN ACCESS

Edited by:

Luca Maragliano,
Marche Polytechnic University, Italy

Reviewed by:

Fatemeh Khalili-Araghi,
University of Illinois at Chicago,
United States
Giulio Alberini,
Fondazione Istituto Italiano di
Tecnologia, Italy

*Correspondence:

Alberto Giacomello
alberto.giacomello@uniroma1.it

Specialty section:

This article was submitted to
Biological Modeling and Simulation,
a section of the journal
Frontiers in Molecular Biosciences

Received: 27 September 2021

Accepted: 12 November 2021

Published: 20 December 2021

Citation:

Costa F, Guardiani C and Giacomello A
(2021) Exploring K_v1.2 Channel
Inactivation Through MD Simulations
and Network Analysis.
Front. Mol. Biosci. 8:784276.
doi: 10.3389/fmolb.2021.784276

The KCNA2 gene encodes the K_v1.2 channel, a mammalian Shaker-like voltage-gated K⁺ channel, whose defections are linked to neuronal deficiency and childhood epilepsy. Despite the important role in the kinetic behavior of the channel, the inactivation remained hereby elusive. Here, we studied the K_v1.2 inactivation via a combined simulation/network theoretical approach that revealed two distinct pathways coupling the Voltage Sensor Domain and the Pore Domain to the Selectivity Filter. Additionally, we mutated some residues implicated in these paths and we explained microscopically their function in the inactivation mechanism by computing a contact map. Interestingly, some pathological residues shown to impair the inactivation lay on the paths. In summary, the presented results suggest two pathways as the possible molecular basis of the inactivation mechanism in the K_v1.2 channel. These pathways are consistent with earlier mutational studies and known mutations involved in neuronal channelopathies.

Keywords: Shaker, Kv1.2, C-type inactivation, molecular dynamics, network analysis

1 INTRODUCTION

The KCNA2 gene encodes the K_v1.2 channel, a mammalian voltage-gated K⁺ channel featuring up to 80% homology with the *Drosophila* Shaker channel (Suárez-Delgado et al., 2020). It is widely expressed in mammals by visceral smooth muscle cells (Wang et al., 1994) and neurons of the central and peripheral nervous system (Niday and Tzingounis, 2018). Its defections/malfunction are linked to neuronal deficiency inducing encephalopathies, ataxia, cerebellar atrophy (Morrison-Levy et al., 2020), and especially childhood epilepsy (Masnada et al., 2017).

Initially, this channel was studied using the structure solved by MacKinnon and colleagues of a modified rat K_v1.2 channel where the voltage sensor paddle, encompassing the S3 and S4 helices, was replaced by the voltage sensor paddle from the rat K_v2.1 channel, the so-called “paddle-chimera channel” (Long et al., 2007). Then, the structure of the K_v1.2 channel was experimentally solved (Chen et al., 2010), revealing that it is characterized by four identical subunits made of six *trans*-membrane alpha helices each. There are three functional domains: the T1 domain at the amino-terminus, the Voltage Sensor Domain (VSD) that encompasses helices S1 to helix L45 and is sensitive to the membrane potential variation triggering the channel to open, and the Pore Domain (PD) delimited by the S5 and S6 alpha helices with the P-Loop and the Selectivity Filter (SF) (Figure 1A).

Based on the protein architecture, the Kv1.2 channel is classified as a domain-swapped channel where the peripheral VSDs interact with the PDs of the *neighboring* subunit (dashed circles in Figure 1B). These channels are characterized by a long helical S4–S5 linker (also referred to as L45) that acts as a mechanical lever pushing onto helix S6 of the neighboring subunit and straightening it to close the pore. These are the main features of the domain-swapped channels canonical activation/

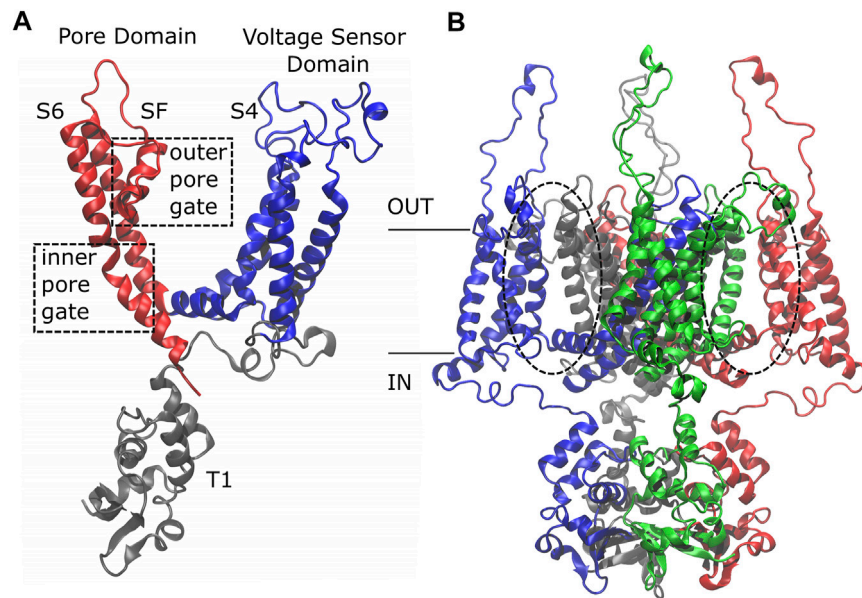


FIGURE 1 | Side view of the Kv1.2 channel. The single subunit **(A)** is colored by domain: in gray, the T1 domain at the N-term; in blue, the Voltage Sensor Domain (VSD) ranging from helix S1 to loop L45, including the positively charged helix S4; in red, the Pore Domain (PD), composed of helix S5, P-Loop, Selectivity Filter, and helix S6. The whole protein **(B)** is colored by subunit: the first subunit in blue, the second in red, the third in gray, and the fourth in green. Note that the color code has a different meaning in the two sub-figures.

deactivation mechanism. On the other hand, in non-domain-swapped channels, the linker L45 is non helical and so short that it is unlikely to exert a force on S6 (Barros et al., 2019).

In most K⁺ channels, the ion permeation is regulated by conformational changes occurring at least at opposite sites of the PD: the bending of the S6 alpha helices (at the bottom of S6) causes the inner gate to close, determining the transition from the Open (O) to the Closed (C) state of the channel (Liu et al., 1997; Doyle et al., 1998; del Camino and Yellen, 2001; Long et al., 2005; Jensen et al., 2012). On the other hand, structural rearrangement of the SF that forms the outer gate is the cause of the transition from the O to the Inactivated (I) state, a slow process defined as C-type inactivation (Hoshi et al., 1991; Baukowitz and Yellen, 1995; Ader et al., 2009). The I state plays a key role in the kinetic behavior of the channels because it is reached immediately after the inner gate opening and, likewise, it allows the channel to close leading the conformation of the inner gate towards the closed state (Monod et al., 1965; Cuello et al., 2010). Despite its central role in channel function, the molecular determinants of the inactivation remained quite elusive.

The transitions O → I and I → C and *vice versa* are regulated by the membrane potential variation, implying a functional connectivity between the VSD and the SF (Olcese et al., 1997; Loots and Isacoff, 1998). Previous computational studies on Shaker activation/deactivation revealed the existence of an alternative pathway that connected the VSD to the PD excluding the long loop L45 (Fernandez-Marino et al., 2018). Successively, experimental evidences supported the idea of a non-canonical activation/deactivation mechanism in the VSD-PD coupling that involved the S4\S5 and S5\P-Loop interfaces

(Carvalho-de Souza and Bezanilla, 2019). Moreover, a very similar non-canonical pathway involving the S1 and S5 helices was identified in hERG, a non-domain-swapped channel, where it contributed to the pore opening (Costa et al., 2021). Finally, Bezanilla and coworkers showed that this alternative pathway operates independent of the canonical coupling endowing the voltage dependence to the SF, suggesting a key role in the inactivation mechanism (Bassetto et al., 2021). In order to characterize the dynamic coupling between VSD and SF in Kv1.2 inactivation, in this work, we studied the motion propagation between these two regions analyzing equilibrium fluctuations of the open state. The rationale of this strategy is that the open state immediately precedes the inactivated state in the functional cycle of Kv1.2 with small conformational differences between the two states (Panyi and Deutsch, 2006); in particular, we used the SF as the final endpoint of our search, which is responsible for C-type inactivation (see below).

Based on the KcsA studies about the influence of the inner pore gate on the conformation of the outer pore gate (Cuello et al., 2010), it has been demonstrated that, in Shaker, the residue I470 at the bottom of S6 helix plays a critical role in the C-type inactivation: when the pore opens, this residue modifies its side-chain orientation and physically makes contact with the SF, inducing a constriction capable of stopping the ion flow (Peters et al., 2013). These experimental evidences support the idea of a different coupling mechanism implicated in the C-type inactivation driven by the modifications of the S6 helices after the channel opening and not by a direct coupling with the VSD. Then, it has been shown that the C-type inactivation in hERG, a non-domain-swapped channel, depends on residue F627 of the

SF that blocks rapidly the ion flux (Li et al., 2015); similarly, Shaker-like K^+ domain-swapped channels are characterized by this type of inactivation (Hoshi et al., 1991; Baukrowitz and Yellen, 1995; Ader et al., 2009). It is notable that this inactivation mechanism completely occurs within the PD so that a mechanism occurring in a non-domain-swapped channel like hERG may also apply to domain-swapped channels of the Shaker family. After the sequence alignment between hERG and Kv1.2 (shown in **Supplementary Figure S2**), it is evident that in the SF of Kv1.2, only Y377 has a side-chain characterized by a steric hindrance similar to that of the phenylalanine on hERG, which suggests that Y377 may have a similar role to F627 in hERG. For this reason, in addition to VSD-SF couplings, we studied in detail the pathways connecting the PD to the side-chain re-orientation of Y377 that was chosen to be the key residue of the sink region on the SF for the network analysis (for more details, see *Methods*).

The C-type inactivation in the Kv1.2 channel seemingly originates in VSD-SF and PD-SF couplings. Thus, characterizing microscopically this transition amounts to study how conformational changes of the S4 sensor helix and the pore-delimiting S6 helix propagate to the SF. Considering the long-range conformational re-arrangements of the channels occurring during the transitions from one functional state to another, ion channels can be classified as allosteric molecules (Changeux et al., 1984). A promising approach to study allosteric proteins examines how the fluctuations of residue pairs correlate over the course of an equilibrium simulation to reconstruct the propagation of motion across the protein network (Elbahnsi and Delemotte, 2021). This approach was successfully employed to study the long-range communication path in the E2 enzymes (Papaleo et al., 2012) and in the tRNA synthetase (Ghosh and Vishveshwara, 2007). It has recently been applied also to ion channels, in particular to the Kv1.2–2.1 chimera (Fernandez-Marino et al., 2018) and hERG (Costa et al., 2021) to clarify how motion propagation determines their activation and deactivation. Here, we applied this network theoretical approach to clarify the molecular determinants of inactivation in the Kv1.2 channel.

2 METHODS

The initial configuration of Kv1.2 was taken from the experimentally solved open structure (PDB ID 3LUT) (Chen et al., 2010). Using the CHARMM membrane builder (Jo et al., 2008, 2009), it was embedded in bilayers of 880 1-palmitoyl-2-oleoyl-sn-glycero-3-phosphocholine lipids with 65,408 TIP3P water molecules and 0.15 M of KCl to form a simulation box of ca. $150 \times 150 \times 175$ Å totaling 259,933 atoms. The APBS server (Baker et al., 2001) was used to analyze the protonation states of residues: all aspartates and glutamates were ionized; H271, H378, and H486 were predicted to be in the δ protonation state; H264 was assigned to the ϵ protonation state. Then, the channel was equilibrated in the NPT ensemble for 100 ns. Mutants were produced from the pre-equilibrated wild-type system. At first, they were equilibrated for 6.5 ns in the NPT ensemble applying a time-varying harmonic restraint on each mutated residue and on

its neighbors within a cutoff distance of 5.0 Å. The force constant, initially set to 10 kcal/mol/Å, was decreased by 2 units every 0.5 ns of this simulation and then they were equilibrated for 50 ns in the NPT ensemble. All simulations were run with NAMD (Phillips et al., 2005) using the ff14SB force field for the protein (Maier et al., 2015) and the Lipid17 force field for the lipids (Dickson et al., 2014). Pressure was kept at 1.01325 Bar by the Nosé-Hoover Langevin piston method (Martyna et al., 1994; Feller et al., 1995) and the temperature was maintained at 303.15 K by a Langevin thermostat with damping coefficient of 1 ps^{-1} . Long-range electrostatic interactions were evaluated with the smooth Particle Mesh Ewald algorithm with a grid space of 1 Å. For short-range non-bonded interactions, a cutoff of 12 Å with a switching function at 10.0 Å was used. The integration time step was 2 fs.

The contact map analysis was carried out computing for each couple of residues the probability to be in contact during the equilibrium simulations. Precisely, two residues were considered to be in contact when a pair of heavy atoms of the side chains was closer than 5.0 Å for at least 75% of the trajectory.

For the network analysis, the protein was represented as a graph (Bondy and Murty, 1976) where nodes correspond to residues and edges to interactions between pairs. Edge weights were calculated using: $d_{ij} = -\log|\text{Corr}_{ij}|$ where Corr_{ij} is the correlation coefficient, that is, the normalized covariance of C_α positions:

$$\text{Corr}_{ij} = \frac{\langle (\vec{r}_i - \langle \vec{r}_i \rangle) (\vec{r}_j - \langle \vec{r}_j \rangle) \rangle}{\sqrt{\langle (\vec{r}_i - \langle \vec{r}_i \rangle)^2 \rangle \langle (\vec{r}_j - \langle \vec{r}_j \rangle)^2 \rangle}} \quad (1)$$

where \vec{r}_i and \vec{r}_j are the position vectors of the i and j residues and Corr_{ij} assumes values in the interval $[-1, 1]$. Spheres of radius 6 Å were centered on two key residues on S4 and S6 helices and on SF of the neighboring subunit to identify all residues inside them for at least 75% of the trajectory defining the source and sink regions. Shortest pathways were computed using Dijkstra's algorithm (Dijkstra et al., 1959). The betweenness of each residue was computed with Brandes algorithm (Brandes, 2001) as implemented in the NetworkX library (Hagberg et al., 2008). For more details, see *Supporting Methods*.

3 RESULTS

3.1 Network Analysis: The Inactivation Pathways

Using the network-theoretical approach (see *Methods*), we identified two different families of pathways for the motion propagation (**Figure 2**) joining the VSD and SF and the PD and the SF, respectively. In the first case, the motion from the top of helix S4 went down and jumped onto helix S5 of the neighboring subunit at the level of the residues V301 and S344; at the same time, from the bottom of helix S4, it went up and passed to helix S5 of the neighboring subunit with I304 and L341. Then, through the P-Loop it reached the SF (red arrows in **Figure 2A**) where the motion of Y377 could affect the

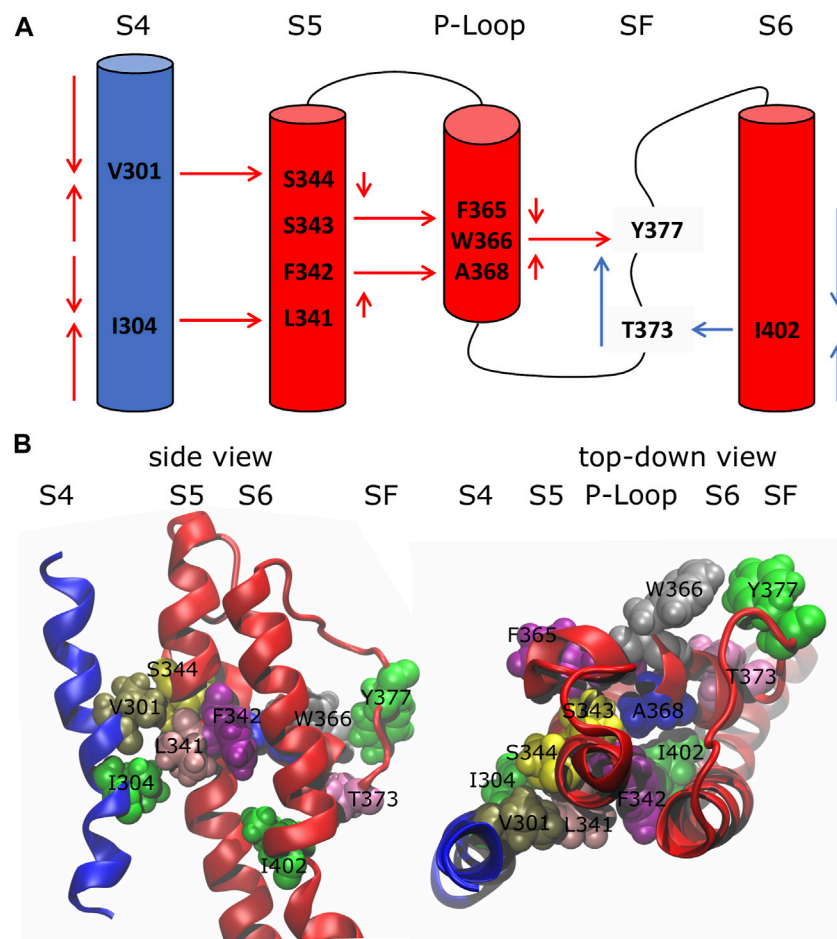


FIGURE 2 | Inactivation pathways of the wild-type Kv1.2 channel. **(A)** Arrows describe the preferred routes of motion propagation: red arrows refer to S4 → S5 → P-Loop → SF route; blue arrows refer to the S6 → SF route. **(B)** Side and top-down views of residues implicated in the paths at the interfaces S4\S5, S5\P-Loop, P-Loop\SF and S6\SF.

dynamics of its counterpart Y377 on the SF of the subunit where the pathway was originated. The VSD-SF path length averaged for the four subunits was ca. 1. This value is expressed by the sum of the arc lengths (weights) d_{ij} that are traversed along a path of minimal length connecting residues i and j . Arc weights are computed according to equation $d_{ij} = -\log|\text{Corr}_{ij}|$ where Corr_{ij} is the correlation coefficient that measured how efficiently the information was transferred from one residue to the other (see *Methods*). Considering the logarithmic nature of this metric, the length value is a pure number, which is zero only for perfect correlation. Values in the range $0 < d_{ij} < 2$ typically mean that there is a high correlation of the motion of each pair of residues on the path. In the same way, we saw a direct connection between the inner and the outer pore gates (PD-SF coupling) involving the residues I402 and T373 of the same subunit with an average path length of ca. 1.10 (blue arrows in **Figure 2A**).

The centrality index (CI) and the betweenness (B) of each residue implicated in the paths are shown

in **Table 1**: high values correspond to residues that act as hubs in the communication pathways and thus are expected to play a key role in the motion propagation.

3.2 Contact Map Analysis

The microscopic characterization of the inactivation pathways was done computing a contact map that highlighted all the conserved interactions formed between residues of the same or the neighboring subunits. **Figure 3** represents the contact map of the whole protein and of a single subunit where black dots are the formed interactions between residues for at least 75% of the equilibrium trajectory. The contact pattern shown in the whole protein map confirmed the presence of interactions between helices S4 and helices S5 of the neighboring subunit (red box in **Figure 3A**). Besides, the contacts formed between helices S5 and the P-Loop and helices S6 and the SF of the same subunit (blue box in **Figure 3B**) supported the second part of the paths that we identified in **Figure 2A**.

TABLE 1 | Centrality index (CI) and betweenness of each residue implicated in the paths. Legend Betweenness (B): low $0 < B \leq 1$; medium: $1 < B \leq 4$; high: $4 < B \leq B_{\max}$. Residues whose mutations are implied in epileptic encephalopathy are shown in bold.

Residue	Centrality index (CI)	Betweenness
L293	$0.10 \leq CI \leq 0.15$	Low
R294	$0.10 \leq CI \leq 0.15$	Low
V295	$0.10 \leq CI \leq 0.20$	Low
I296	$0.20 \leq CI \leq 0.25$	Low
R297	$0.30 \leq CI \leq 0.35$	Low
L298	$0.30 \leq CI \leq 0.45$	Medium
V299	$0.40 \leq CI \leq 0.55$	Medium
R300	$0.50 \leq CI \leq 0.60$	Medium
V301	$0.70 \leq CI \leq 0.80$	High
F302	$0.70 \leq CI \leq 0.80$	High
R303	$0.70 \leq CI \leq 0.80$	High
I304	$0.80 \leq CI \leq 0.90$	High
F305	$0.70 \leq CI \leq 0.85$	Medium
K306	$0.70 \leq CI \leq 0.80$	Medium
L307	$0.60 \leq CI \leq 0.70$	Medium
S308	$0.40 \leq CI \leq 0.55$	Medium
R309	$0.40 \leq CI \leq 0.55$	Medium
H310	$0.10 \leq CI \leq 0.20$	Low
S311	$0.10 \leq CI \leq 0.20$	Low
L341	$CI \geq 0.90$	High
F342	$CI \geq 0.90$	High
S343	$CI \geq 0.90$	Medium
S344	$0.50 \leq CI \leq 0.70$	Medium
F365	$0.75 \leq CI \leq 0.85$	High
W366	$CI \geq 0.95$	High
W367	$0.90 \leq CI \leq 0.95$	High
A368	$CI \geq 0.95$	High
T373	$CI \geq 0.95$	High
T374	$0.90 \leq CI \leq 0.95$	High
V375	$CI \geq 0.95$	High
G376	$0.80 \leq CI \leq 0.90$	Medium
Y377	$CI \geq 0.95$	High
C394	$0.10 \leq CI \leq 0.15$	Low
A395	$0.10 \leq CI \leq 0.20$	Low
I396	$0.20 \leq CI \leq 0.25$	Low
A397	$0.20 \leq CI \leq 0.30$	Medium
G398	$0.30 \leq CI \leq 0.45$	Medium
V399	$0.50 \leq CI \leq 0.60$	Medium
L400	$0.70 \leq CI \leq 0.85$	Medium
T401	$0.80 \leq CI \leq 0.90$	High
I402	$CI \geq 0.95$	High
A403	$0.80 \leq CI \leq 0.90$	High
L404	$0.70 \leq CI \leq 0.80$	Medium
P405	$0.40 \leq CI \leq 0.50$	Medium
V406	$0.20 \leq CI \leq 0.40$	Medium
P407	$0.20 \leq CI \leq 0.35$	Medium
V408	$0.10 \leq CI \leq 0.20$	Low
I409	$0.10 \leq CI \leq 0.20$	Low
V410	$0.10 \leq CI \leq 0.20$	Low

3.3 Mutants

The network approach allowed to identify two routes of the motion propagation as the molecular basis of a VSD-SF and PD-SF coupling mechanisms. The residues that connect the interfaces S4\S5, S5\P-Loop, P-Loop\SF, and S6\SF are strongly coupled in the equilibrium dynamics of the open state. Since they lie on paths that reached the SF excluding the L45 known to be involved in the activation/deactivation of the channel (Barros et al., 2019), it can be

hypothesized that they are involved in the channel inactivation. Many of them have been already demonstrated to influence the Shaker or Kv1.2 inactivation if mutated including L361R, L366H, and W366F (Perozo et al., 1993; Yang et al., 2007; Cuello et al., 2010; Cordero-Morales et al., 2011; Bassetto et al., 2021) but a microscopic interpretation of the effects of the mutation is still elusive. Moreover, it was hypothesized that the VSD-SF coupling depends on the volume of the residues that lay along the inactivation pathway (Bassetto et al., 2021). For this reason, in order to describe the microscopic role of each residue implicated in the paths, we applied the same network-theoretical approach to mutated channels and then we computed a contact map to identify the effects of the mutations on the contact formation. In some cases, we reproduced computationally experimental mutants whose effect on the inactivation was already characterized in Shaker channels, e.g., L361R, L366H, W434F. In order to further characterize the role of key residues lying along the pathways coupling the VSD and the PD to the SF and for which an experiment was not available, we produced a computational model of Kv1.2 with non-conservative mutations obtained by replacing individual residues by an alanine. All the mutated residues on the sequence of Shaker and Kv1.2 channels are shown in **Supplementary Figure S1** and the corresponding paths lengths are shown in **Table 2**.

At first we focused on the VSD-SF coupling path, starting from residues of the voltage sensor helix S4: L293R, L298H, V301A, I304A. In all cases the coupling paths for the inactivation were qualitatively similar to the wild type but with a different path length. The greatest effects were observed mutating L293 on the top of S4 helix, with the average path length reaching values of ca. 10 in the L293R mutant. It probably depended on the introduction of a new positively charged amino acid that influenced the sensitivity to the membrane potential variation. Considering the logarithmic nature of this metric, a difference of two units in the path length corresponds to a difference of one order of magnitude in terms of correlation, meaning that the pathway is effectively hindered in the mutant. These results are in agreement with the experiments on Shaker where L361R channels activated and inactivated at much more hyperpolarized membrane potentials, implying that the inactivation was not preserved (Yang et al., 2007).

In the L298H channel the VSD-SF coupling was extremely weak. The contact map analysis revealed the formation of new contacts between helix S4 and helices S1 and S2 (**Figure 4**). More precisely, in the mutant, the new histidine maintained the hydrophobic interaction with F348 on helix S5 but its larger steric clash induced a displacement of helix S4 by 3 Å towards helices S1 and S2. We hypothesize that the rearrangements of helix S4 is at the origin of the modification of the inactivation pathways. These computational evidences seem to be in agreement with the experimental Shaker double mutant L366H:W434F where the currents show a decay under sustained voltage-clamp depolarization reminiscent of C-type inactivation, suggesting this process has not been eliminated but rather mitigated. Indeed, L366H relieves the W434F effect of the inactivation increased speed, converting a non-conductive channel in a conductive one (Bassetto et al., 2021).

In the I304A channel the efficiency of the information transfer from VSD to SF became weaker than the wild type.

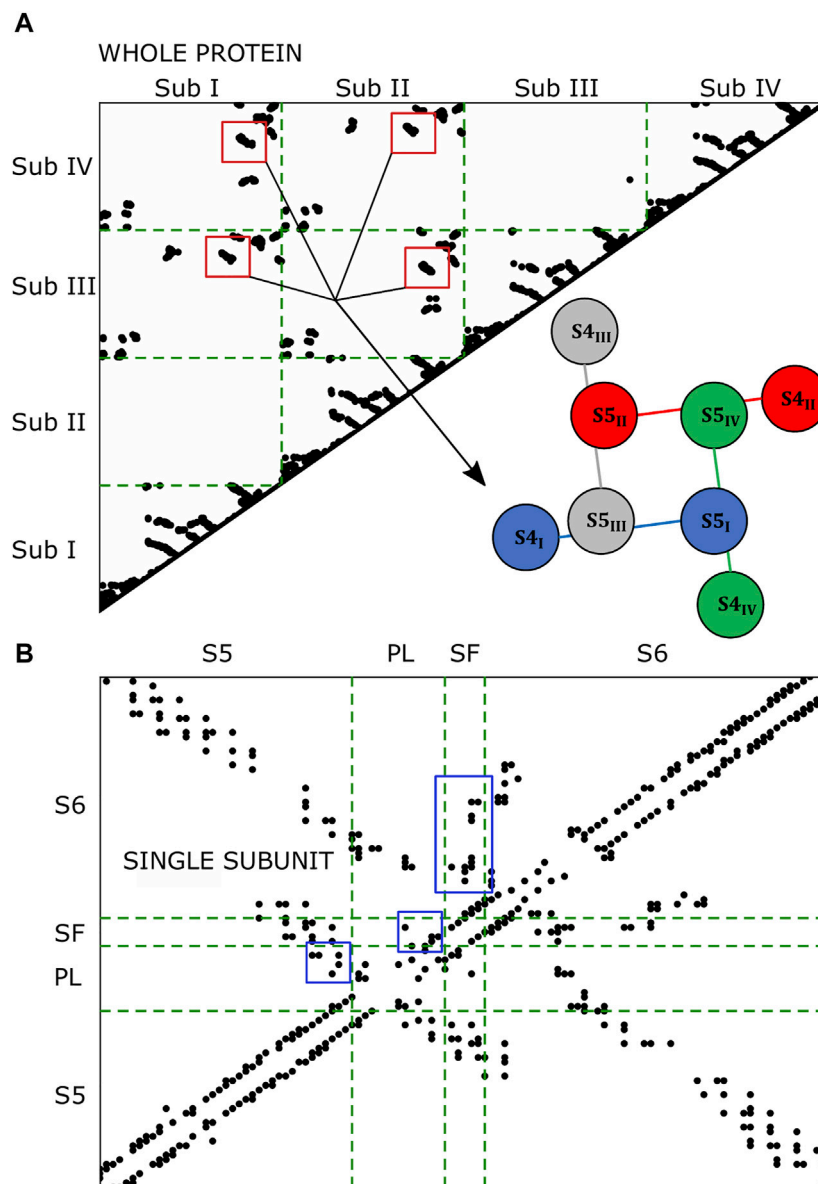


FIGURE 3 | Contact maps of the whole protein **(A)** and of the single subunit **(B)**. Black dots represent the formed interactions. In the single subunit map, the black dots are the interactions formed at least 75% of the trajectory in 3/4 subunits.

The missing hydrophobic interaction between A304 and L341 on helix S5 is probably the main cause of the loss of inactivation. Interestingly, we identified a new route that from helix S4 reached helix S5 jumping onto helix S1 of the same subunit at the level of R300-F180 contact but this path had a length greater of ca. 3 (see **Table 2**). Consequently, in I304A channel the inactivation seems to be delayed or completely abolished.

For both V301A and S344A mutants we saw a path qualitatively and quantitatively (length ca. 1) similar to the wild type, meaning that the inactivation would not be affected by the alanine substitutions. Indeed, the contact map analysis

revealed that the hydrophobic interactions at the S4/S5 interface were preserved. These results agree with the thesis that the VSD-SF coupling depends on the volume of the residues involved in the inactivation pathway (Bassetto et al., 2021).

Residue F342 on helix S5 plays a central role in the inactivation path connecting the VSD to the SF. Indeed, it is characterized by a very high CI. To further dissect its role in this path, we introduced an alanine substitution in each subunit. The mutated channel F342A had a loss of this coupling mechanism. Interestingly, we saw that the F342-A368 interaction was completely broken by the alanine replacement probably due to the smaller size of the hydrophobic region of the residue.

TABLE 2 | Comparison of the average path length between WT and mutants.

Mutation	VSD-SF path length	PD-SF path length
WT	0.97	1.12
L293R	9.79	2.78
L298H	5.44	1.36
V301A	1.72	1.31
I304A	3.01	1.50
F342A	5.61	1.49
S344A	1.58	1.37
W366F	0.62	1.71
T373A	1.06	2.32
I402A	1.37	4.77

On the other hand, in the W366F channel, we identified the same VSD-SF path as in the wild type but with a lower average length of ca. 0.60. Here, the efficiency of the information transfer was greater than the wild type, suggesting the presence of an enhanced and faster inactivation in agreement with the experimental results on the $K_v1.2$ channel (Cordero-Morales et al., 2011) and on the corresponding W434F of Shaker (Perozo et al., 1993). However, the contact map analysis did not reveal new broken or formed interactions.

Finally, we focused on the PD-SF coupling mechanism where we performed the mutations T373A and I402A. In both mutants there was an increase of the path length, meaning that the information transfer was generally less efficient than in the wild type. No interactions were detected between these residues in the contact map analysis, which suggests that the PD-SF coupling breaks. These results are supported by Cuello and coworkers where strong van der Waals interactions were observed between these residues in the pore-helix of the same subunit (Cuello et al., 2010).

It is noteworthy that the mutation of a residue implicated in one of the two pathways that defined the VSD-SF or the PD-SF couplings did not influence the other mechanism. However, the experimental studies showed that mutating a residue along one of the two paths (Perozo et al., 1993; Yang et al., 2007; Cuello et al., 2010; Cordero-Morales et al., 2011; Bassetto et al., 2021) determined the disruption only of that path which is sufficient to impair inactivation. This evidence suggests that the two communication pathways are not inter-changeable and both play a role in the C-type inactivation mechanism.

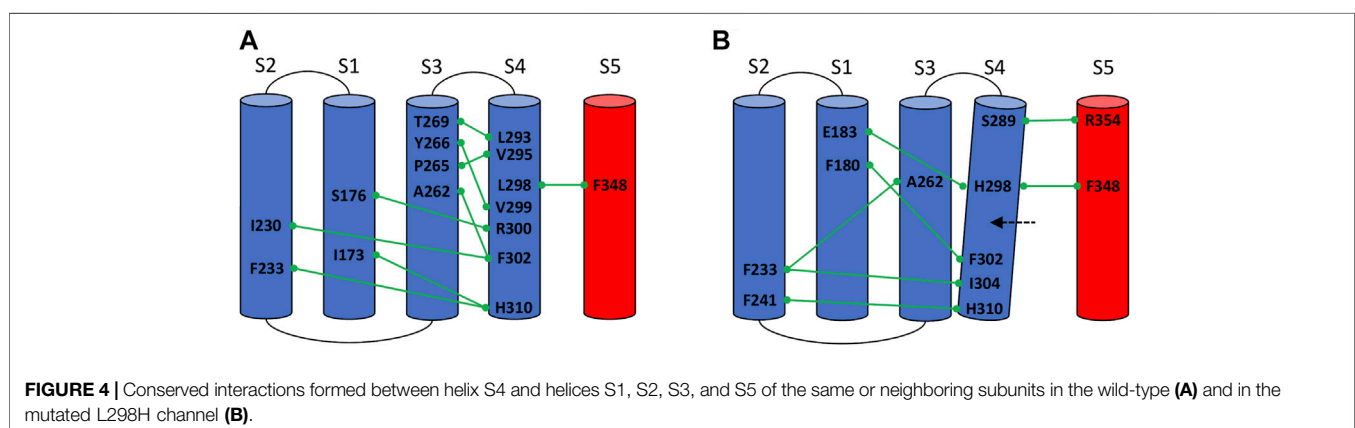
4 DISCUSSION AND CONCLUSION

In this study, a combined simulations/network theoretical approach was applied to identify dynamical pathways as the possible molecular basis of C-type inactivation in the $K_v1.2$ channel. This dynamic analysis allowed us to identify two routes of motion propagation that occur during this transition. In particular, our results revealed that the constriction of the SF is coupled to the VSD displacement (i) through helix S5 and the P-Loop and (ii) through a direct connection with the PD.

In the first path, the inactivation starts from helix S4, which is the only part of the channel that responds to changes in the membrane potential. From here, the motion propagates to helix S5 of the neighboring subunit using two bridges in the middle helix, corresponding to residues V301 and I304, respectively. By mutating residues on the top of the helix, we noticed an impairment of inactivation, in agreement with the experimental results obtained in Shaker channels (Yang et al., 2007; Bassetto et al., 2021). It is noteworthy that this pathway encompasses residues L293 and F302, whose mutations into histidine and leucine, respectively, are known to modify the inactivation of $K_v1.2$ leading to epileptic encephalopathy (Masnada et al., 2017; Pantazis et al., 2020).

Moreover, a second communication pathway was identified coupling the SF to the PD excluding the VSD. In this case, the starting point of the motion propagation is represented by the bending region on helix S6 whose movements, after the channel opening, are transferred to Y377 on the SF through the contact between I402 and T373. Interestingly, residue P405 lays on this path, and it is correlated to slight changes in the inactivation if mutated into a leucine: similar to L293H and F302L, mutation P405L has been shown to induce epilepsy (Syrbe et al., 2015).

Finally, in order to support our computational results, we mutated some residues implicated in the paths whose effects have been demonstrated to modify the inactivation in Shaker channels. The computed changes in the path lengths account for a delayed inactivation in the majority of cases while an acceleration occurs for W366F (see Table 2); these results yield microscopic insights into experimental results (Perozo et al., 1993; Yang et al., 2007; Cuello et al., 2010; Cordero-Morales et al., 2011; Bassetto et al., 2021), in particular on the allosteric mechanism of inactivation.



In summary, our work has unveiled the molecular determinants of C-type inactivation in the Kv1.2 channel through a novel approach combining molecular dynamics simulations and network theoretical techniques. Two pathways were found coupling the VSD and the inner pore gate with the SF providing a tentative explanation of the inactivation mechanism. Interestingly, some pathological mutants shown to impair the inactivation lay on the pathways that we identified, strengthening our computational results.

DATA AVAILABILITY STATEMENT

The datasets presented in this study can be found in online repositories. The names of the repository/repositories and accession number(s) can be found below: doi.org/10.5281/zenodo.5528762.

AUTHOR CONTRIBUTIONS

FC performed the research and wrote the paper. CG and AG designed the research and wrote the paper.

REFERENCES

- Ader, C., Schneider, R., Hornig, S., Velisetty, P., Vardanyan, V., Giller, K., et al. (2009). Coupling of Activation and Inactivation Gate in a K⁺-channel: Potassium and Ligand Sensitivity. *Embo J.* 28, 2825–2834. doi:10.1038/emboj.2009.218
- Baker, N. A., Sept, D., Joseph, S., Holst, M. J., and McCammon, J. A. (2001). Electrostatics of Nanosystems: Application to Microtubules and the Ribosome. *Proc. Natl. Acad. Sci.* 98, 10037–10041. doi:10.1073/pnas.181342398
- Barros, F., Pardo, L., Domínguez, P., Sierra, L., and de la Peña, P. (2019). New Structures and Gating of Voltage-dependent Potassium (Kv) Channels and Their Relatives: a Multi-Domain and Dynamic Question. *Ijms* 20, 248. doi:10.3390/ijms20020248
- Bassetto, C. A., Carvalho-de-Souza, J. L., and Bezanilla, F. (2021). Molecular Basis for Functional Connectivity between the Voltage Sensor and the Selectivity Filter Gate in Shaker K⁺ Channels. *Elife* 10, e63077. doi:10.7554/eLife.63077
- Baukrowitz, T., and Yellen, G. (1995). Modulation of K⁺ Current by Frequency and External [K⁺]: a Tale of Two Inactivation Mechanisms. *Neuron* 15, 951–960. doi:10.1016/0896-6273(95)90185-x
- Bondy, J. A., and Murty, U. S. R. (1976). *Graph Theory with Applications*, Vol. 290. Macmillan London.
- Brandes, U. (2001). A Faster Algorithm for Betweenness Centrality*. *J. Math. Sociol.* 25, 163–177. doi:10.1080/0022250x.2001.9990249
- Carvalho-de Souza, J. L., and Bezanilla, F. (2019). Noncanonical Mechanism of Voltage Sensor Coupling to Pore Revealed by Tandem Dimers of Shaker. *Nat. Commun.* 10, 1–12. doi:10.1038/s41467-019-11545-7
- Changeux, J.-P., Devillers-Thiéry, A., and Chemouilli, P. (1984). Acetylcholine Receptor: an Allosteric Protein. *Science* 225, 1335–1345. doi:10.1126/science.6382611
- Chen, X., Wang, Q., Ni, F., and Ma, J. (2010). Structure of the Full-Length Shaker Potassium Channel Kv1.2 by normal-mode-based X-ray Crystallographic Refinement. *Proc. Natl. Acad. Sci.* 107, 11352–11357. doi:10.1073/pnas.1000142107
- Cordero-Morales, J. F., Jogini, V., Chakrapani, S., and Perozo, E. (2011). A Multipoint Hydrogen-Bond Network Underlying KcsA C-type Inactivation. *Biophysical J.* 100, 2387–2393. doi:10.1016/j.bpj.2011.01.073
- Costa, F., Guardiani, C., and Giacomello, A. (2021). *Communications Biology Submitted COMMSBIO-21-1746-T*. Simulating Activation/deactivation Pathways in hERG Channel via Molecular Dynamics.

FUNDING

This project has received funding from the European Research Council (ERC) under the European Union's Horizon 2020 research and innovation programme (grant agreement No. 803213). The authors acknowledge PRACE for awarding us access to Marconi100 at CINECA, Italy.

ACKNOWLEDGMENTS

We thank Dr. Carlos AZ Bassetto for helpful suggested references on Shaker experimental works.

SUPPLEMENTARY MATERIAL

The Supplementary Material for this article can be found online at: <https://www.frontiersin.org/articles/10.3389/fmolb.2021.784276/full#supplementary-material>

- Cuello, L. G., Jogini, V., Cortes, D. M., Pan, A. C., Gagnon, D. G., Dalmás, O., et al. (2010). Structural Basis for the Coupling between Activation and Inactivation gates in K⁺ Channels. *Nature* 466, 272–275. doi:10.1038/nature09136
- del Camino, D., and Yellen, G. (2001). Tight Steric Closure at the Intracellular Activation Gate of a Voltage-Gated K⁺ Channel. *Neuron* 32, 649–656. doi:10.1016/s0896-6273(01)00487-1
- Dickson, C. J., Madej, B. D., Skjevik, Å. A., Betz, R. M., Teigen, K., Gould, I. R., et al. (2014). Lipid14: the Amber Lipid Force Field. *J. Chem. Theor. Comput.* 10, 865–879. doi:10.1021/ct4010307
- Dijkstra, E. W. (1959). A Note on Two Problems in Connexion with Graphs. *Numer. Math.* 1 (1), 269–271. doi:10.1007/bf01386390
- Doyle, D. A., Cabral, J. M., Pfuetzner, R. A., Kuo, A., Gulbis, J. M., Cohen, S. L., et al. (1998). The Structure of the Potassium Channel: Molecular Basis of K⁺ Conduction and Selectivity. *science* 280, 69–77. doi:10.1126/science.280.5360.69
- Elbahnsi, A., and Delemotte, L. (2021). Structure and Sequence-Based Computational Approaches to Allosteric Signal Transduction: Application to Electromechanical Coupling in Voltage-Gated Ion Channels. *J. Mol. Biol.* 433, 167095. doi:10.1016/j.jmb.2021.167095
- Feller, S. E., Zhang, Y., Pastor, R. W., and Brooks, B. R. (1995). Constant Pressure Molecular Dynamics Simulation: the Langevin Piston Method. *J. Chem. Phys.* 103, 4613–4621. doi:10.1063/1.470648
- Fernández-Mariño, A. I., Harpole, T. J., Oelstrom, K., Delemotte, L., and Chanda, B. (2018). Gating Interaction Maps Reveal a Noncanonical Electromechanical Coupling Mode in the Shaker K⁺ Channel. *Nat. Struct. Mol. Biol.* 25, 320–326. doi:10.1038/s41594-018-0047-3
- Ghosh, A., and Vishveshwara, S. (2007). A Study of Communication Pathways in Methionyl- tRNA Synthetase by Molecular Dynamics Simulations and Structure Network Analysis. *Proc. Natl. Acad. Sci.* 104, 15711–15716. doi:10.1073/pnas.0704459104
- Hagberg, A., Swart, P., and Schult, D. (2008). *Tech. rep., Los Alamos National Lab.(LANL)*. Los Alamos, NM (United States). Exploring Network Structure, Dynamics, and Function Using NetworkX.
- Hoshi, T., Zagotta, W. N., and Aldrich, R. W. (1991). Two Types of Inactivation in Shaker K⁺ Channels: Effects of Alterations in the Carboxy-Terminal Region. *Neuron* 7, 547–556. doi:10.1016/0896-6273(91)90367-9
- Jensen, M. Ø., Jogini, V., Borhani, D. W., Leffler, A. E., Dror, R. O., and Shaw, D. E. (2012). Mechanism of Voltage Gating in Potassium Channels. *Science* 336, 229–233. doi:10.1126/science.1216533

- Jo, S., Kim, T., Iyer, V. G., and Im, W. (2008). CHARMM-GUI: a Web-Based Graphical User Interface for CHARMM. *J. Comput. Chem.* 29, 1859–1865. doi:10.1002/jcc.20945
- Jo, S., Lim, J. B., Klauda, J. B., and Im, W. (2009). CHARMM-GUI Membrane Builder for Mixed Bilayers and its Application to Yeast Membranes. *Biophysical J.* 97, 50–58. doi:10.1016/j.bpj.2009.04.013
- Li, W., Cowley, A., Uludag, M., Gur, T., McWilliam, H., Squizzato, S., et al. (2015). The EMBL-EBI Bioinformatics Web and Programmatic Tools Framework. *Nucleic Acids Res.* 43, W580–W584. doi:10.1093/nar/gkv279
- Liu, Y., Holmgren, M., Jurman, M. E., and Yellen, G. (1997). Gated Access to the Pore of a Voltage-dependent K⁺ Channel. *Neuron* 19, 175–184. doi:10.1016/s0896-6273(00)80357-8
- Long, S. B., Campbell, E. B., and MacKinnon, R. (2005). Voltage Sensor of Kv1.2: Structural Basis of Electromechanical Coupling. *Science* 309, 903–908. doi:10.1126/science.1116270
- Long, S. B., Tao, X., Campbell, E. B., and MacKinnon, R. (2007). Atomic Structure of a Voltage-dependent K⁺ Channel in a Lipid Membrane-like Environment. *Nature* 450, 376–382. doi:10.1038/nature06265
- Loots, E., and Isacoff, E. Y. (1998). Protein Rearrangements Underlying Slow Inactivation of the Shaker K⁺ Channel. *J. Gen. Physiol.* 112, 377–389. doi:10.1085/jgp.112.4.377
- Maier, J. A., Martinez, C., Kasavajhala, K., Wickstrom, L., Hauser, K. E., and Simmerling, C. (2015). ff14SB: Improving the Accuracy of Protein Side Chain and Backbone Parameters from ff99SB. *J. Chem. Theor. Comput.* 11, 3696–3713. doi:10.1021/acs.jctc.5b00255
- Martyna, G. J., Tobias, D. J., and Klein, M. L. (1994). Constant Pressure Molecular Dynamics Algorithms. *J. Chem. Phys.* 101, 4177–4189. doi:10.1063/1.467468
- Masnada, S., Hedrich, U. B. S., Gardella, E., Schubert, J., Kaiwar, C., Klee, E. W., et al. (2017). Clinical Spectrum and Genotype-Phenotype Associations of KCNA2-Related Encephalopathies. *Brain* 140, 2337–2354. doi:10.1093/brain/awx184
- Monod, J., Wyman, J., and Changeux, J.-P. (1965). On the Nature of Allosteric Transitions: a Plausible Model. *J. Mol. Biol.* 12, 88–118. doi:10.1016/s0022-2836(65)80285-6
- Morrison-Levy, N., Borlot, F., Jain, P., and Whitney, R. (2020). Early-onset Developmental and Epileptic Encephalopathies of Infancy: An Overview of the Genetic Basis and Clinical Features. *Pediatr. Neurol.*
- Niday, Z., and Tzingounis, A. V. (2018). Potassium Channel Gain of Function in Epilepsy: an Unresolved Paradox. *Neuroscientist* 24, 368–380. doi:10.1177/1073858418763752
- Olcese, R., Latorre, R., Toro, L., Bezanilla, F., and Stefani, E. (1997). Correlation between Charge Movement and Ionic Current during Slow Inactivation in Shaker K⁺ Channels. *J. Gen. Physiol.* 110, 579–589. doi:10.1085/jgp.110.5.579
- Pantazis, A., Kaneko, M., Angelini, M., Steccanella, F., Westerlund, A. M., Lindström, S. H., et al. (2020). Tracking the Motion of the K V 1.2 Voltage Sensor Reveals the Molecular Perturbations Caused by a De Novo Mutation in a Case of Epilepsy. *J. Physiol.* 598, 5245–5269. doi:10.1113/jp280438
- Panyi, G., and Deutsch, C. (2006). Cross Talk between Activation and Slow Inactivation gates of Shaker Potassium Channels. *J. Gen. Physiol.* 128, 547–559. doi:10.1085/jgp.200609644
- Papaleo, E., Lindorff-Larsen, K., and De Gioia, L. (2012). Paths of Long-Range Communication in the E2 Enzymes of Family 3: a Molecular Dynamics Investigation. *Phys. Chem. Chem. Phys.* 14, 12515–12525. doi:10.1039/c2cp41224a
- Perozo, E., MacKinnon, R., Bezanilla, F., and Stefani, E. (1993). Gating Currents from a Nonconducting Mutant Reveal Open-Closed Conformations in Shaker K⁺ Channels. *Neuron* 11, 353–358. doi:10.1016/0896-6273(93)90190-3
- Peters, C. J., Fedida, D., and Accili, E. A. (2013). Allosteric Coupling of the Inner Activation Gate to the Outer Pore of a Potassium Channel. *Sci. Rep.* 3, 3025–3028. doi:10.1038/srep03025
- Phillips, J. C., Braun, R., Wang, W., Gumbart, J., Tajkhorshid, E., Villa, E., et al. (2005). Scalable Molecular Dynamics with NAMD. *J. Comput. Chem.* 26, 1781–1802. doi:10.1002/jcc.20289
- Suárez-Delgado, E., Rangel-Sandín, T. G., Ishida, I. G., Rangel-Yescas, G. E., Rosenbaum, T., and Islas, L. D. (2020). KV1. 2 Channels Inactivate through a Mechanism Similar to C-type Inactivation. *J. Gen. Physiol.* 152.
- Syrbe, S., Hedrich, U. B., Hedrich, U. B. S., Riesch, E., Djémié, T., Müller, S., et al. (2015). De Novo loss- or Gain-Of-Function Mutations in KCNA2 Cause Epileptic Encephalopathy. *Nat. Genet.* 47, 393–399. doi:10.1038/ng.3239
- Wang, H., Kunkel, D., Schwartzkroin, P., and Tempel, B. (1994). Localization of Kv1.1 and Kv1.2, Two K Channel Proteins, to Synaptic Terminals, Somata, and Dendrites in the Mouse Brain. *J. Neurosci.* 14, 4588–4599. doi:10.1523/jneurosci.14-08-04588.1994
- Yang, Y.-C., Own, C.-J., and Kuo, C.-C. (2007). A Hydrophobic Element Secures S4 Voltage Sensor in Position in Resting Shaker K⁺ Channels. *J. Physiol.* 582, 1059–1072. doi:10.1113/jphysiol.2007.131490

Conflict of Interest: The authors declare that the research was conducted in the absence of any commercial or financial relationships that could be construed as a potential conflict of interest.

Publisher's Note: All claims expressed in this article are solely those of the authors and do not necessarily represent those of their affiliated organizations, or those of the publisher, the editors, and the reviewers. Any product that may be evaluated in this article, or claim that may be made by its manufacturer, is not guaranteed or endorsed by the publisher.

Copyright © 2021 Costa, Guardiani and Giacomello. This is an open-access article distributed under the terms of the Creative Commons Attribution License (CC BY). The use, distribution or reproduction in other forums is permitted, provided the original author(s) and the copyright owner(s) are credited and that the original publication in this journal is cited, in accordance with accepted academic practice. No use, distribution or reproduction is permitted which does not comply with these terms.



From Acid Activation Mechanisms of Proton Conduction to Design of Inhibitors of the M2 Proton Channel of Influenza A Virus

Elnaz Aledavood^{1,2†}, Beatrice Selmi^{2†}, Carolina Estarellas^{1*}, Matteo Masetti^{2*} and F. Javier Luque^{1*}

OPEN ACCESS

Edited by:

Carla Molteni,
King's College London,
United Kingdom

Reviewed by:

Mercedes Alfonso-Prieto,
Helmholtz Association of German
Research Centres (HZ), Germany
Suman Chakrabarty,
S. N. Bose National Centre for Basic
Sciences, India
Giacomo Florin,
Temple University, United States

*Correspondence:

Carolina Estarellas
cestorellas@ub.edu
Matteo Masetti
matteo.masetti4@unibo.it
F. Javier Luque
fjluque@ub.edu

[†]These authors have contributed
equally to this work and share first
authorship

Specialty section:

This article was submitted to
Biological Modeling and Simulation,
a section of the journal
Frontiers in Molecular Biosciences

Received: 16 October 2021

Accepted: 24 December 2021

Published: 14 January 2022

Citation:

Aledavood E, Selmi B, Estarellas C,
Masetti M and Luque FJ (2022) From
Acid Activation Mechanisms of Proton
Conduction to Design of Inhibitors of
the M2 Proton Channel of Influenza
A Virus.
Front. Mol. Biosci. 8:796229.
doi: 10.3389/fmolb.2021.796229

¹Departament de Nutrició, Ciències de l'Alimentació i Gastronomia, Institut de Biomedicina and Institut de Química Teòrica i Computacional, University of Barcelona, Barcelona, Spain, ²Department of Pharmacy and Biotechnology, Alma Mater Studiorum – Università di Bologna, Bologna, Italy

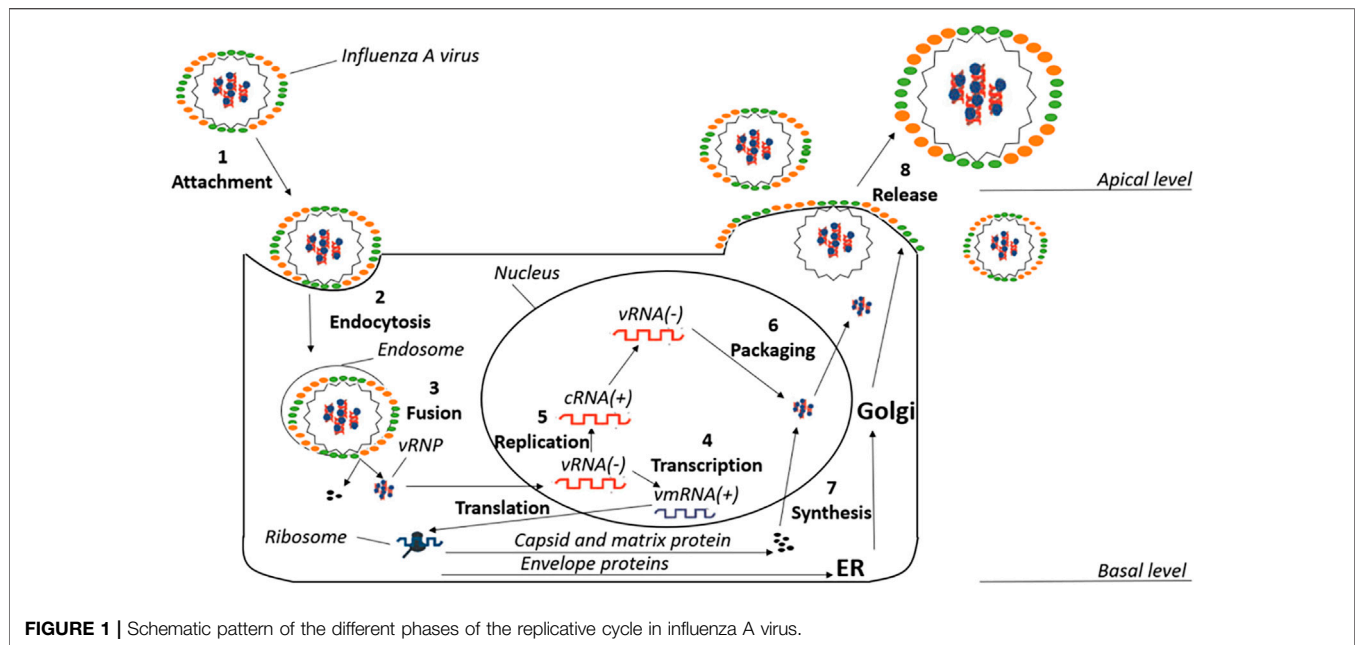
With an estimated 1 billion people affected across the globe, influenza is one of the most serious health concerns worldwide. Therapeutic treatments have encompassed a number of key functional viral proteins, mainly focused on the M2 proton channel and neuraminidase. This review highlights the efforts spent in targeting the M2 proton channel, which mediates the proton transport toward the interior of the viral particle as a preliminary step leading to the release of the fusion peptide in hemagglutinin and the fusion of the viral and endosomal membranes. Besides the structural and mechanistic aspects of the M2 proton channel, attention is paid to the challenges posed by the development of efficient small molecule inhibitors and the evolution toward novel ligands and scaffolds motivated by the emergence of resistant strains.

Keywords: M2 proton channel, influenza A virus, proton transport, inhibition, molecular mechanism, drug design

INTRODUCTION

Influenza A virus is an important pathogen that still causes the death of 290,000–650,000 people in seasonal outbreaks worldwide (Iuliano et al., 2018). It pertains to the Orthomyxoviridae family, which is characterized by the presence of a negative-sense, single-stranded, enveloped ribonucleic acid with a segmented genome (Cheung and Poon, 2007). There are four genera in the Orthomyxoviridae family: Influenza A, Influenza B, Influenza C, and Thogotovirus. Influenza A viruses are found in many different animals, and Influenza B viruses circulate widely only among humans. Influenza A viruses are divided into subtypes based on two proteins on the surface of the virus: hemagglutinin (HA), which is responsible for the receptor binding and membrane fusion, and neuraminidase (NA), which assists the release of the viral progeny (Cheung and Poon, 2007). Up to 18 variants of HA (from type H1 to H18) have been described till now, whereas 11 subtypes have been disclosed for NA. All known subtypes of influenza A viruses have been found among birds, except subtypes H17N10 and H18N11, which have only been found in bats. Only some subtypes (H1N1, H2N2, H3N2, H5N1, H7N7, and H9N2) have been isolated from humans, suggesting that there are restrictions to host viruses in humans.

While infections in humans directly from animals are unusual, sporadic infections and outbreaks caused by influenza A viruses have occurred in the past. The most severe pandemic was the “Spanish Flu” of 1918–1919, which caused 20–50 million deaths by influenza A H1N1 virus strain. The subsequent health challenges were the “Asian flu” in 1957 and the “Hong Kong flu” in 1968, which



were caused respectively by H2N2 and H3N2 strains, and more recently the 2009 swine influenza pandemics, which pertains to the H1N1 strain (Cox and Subbarao, 2000; Hayward et al., 2014; Watson et al., 2015; Saunders-Hastings and Krewski, 2016). The latent risk of facing future pandemics underlined the Global Influenza Strategy initiative launched by the World Health Organization in 2019, which has the goal of preventing seasonal influenza, controlling the spread of influenza from animals to humans, and preparing for the next influenza pandemic (World Health Organization, 2019). This threatening scenario underscores the urgency in developing better diagnostic tools and promoting the discovery of effective influenza treatments, including vaccines and antiviral drugs.

This review aims to discuss experimental and computational efforts invested in elucidating the structural basis of the proton conducting activity of the M2 protein channel and the discovery of antiviral compounds targeting the M2 transmembrane domain. To this end, the manuscript first describes the role of the M2 proton channel in the replicative life cycle of the influenza A virus. Then, attention is focused on the structure of the proton channel, which is directly implicated in the proton transfer across the viral membrane as a preliminary event leading to the fusion of viral and host membranes and the subsequent release of the viral genetic material. Emphasis is made on the molecular mechanisms that underlie the proton conduction through the lumen of the M2 proton channel. The discussion also highlights the role played by key residues located in the transmembrane region, and especially the efforts spent in the determination of the pKa of the imidazole rings present in the His37 tetrad. Finally, the manuscript examines the mechanism of action of selected inhibitors, and the evolution followed in the design of novel compounds introduced to increase the inhibition potency and to mitigate the emergence of resistance to current treatments.

THE INFLUENZA A VIRUS REPLICATIVE CYCLE

Influenza A virus replicates in the epithelial cells of the upper respiratory tract of humans, pigs, and horses. Regarding *in vitro* models, the virus can also affect different cells that contain targets decorated with sialic acid moieties (Julkunen et al., 2001; Sidorenko and Reichl, 2004), which act as the entrance anchor point into the cells.

Enclosed by a lipid-protein envelope, the genetic material of the influenza A virus contains 8 single-stranded RNA segments that encode the genetic information for viral proteins (Dou et al., 2018; Krammer et al., 2018; Jung and Lee, 2020): the membrane-bound hemagglutinin (HA) and neuraminidase (NA), the transmembrane M2 proton channel, the matrix protein M1, the non-structural proteins (NS1, NS2/NEP), and the heterotrimeric RNA-dependent RNA polymerase (RdRp), formed by three domains (PA, PB1, and PB2), and nucleoprotein (NP) components.

The replicative life cycle of the virus is schematically shown in **Figure 1**. The first step of the cycle is the entry of the virus inside the host cell (step 1). Viral entry into the cell occurs via HA, which recognizes and binds the sialic acid of the host cell receptors. The virions penetrate inside the host cell through clathrin-dependent receptor-mediated endocytosis (step 2). The acidification of the endosome is facilitated by the M2 proton channel, which transfers protons to the interior of the viral particles. This event promotes a large-scale conformational remodeling in HA that facilitates the release of the fusion peptide, and the concomitant structural rearrangement of HA triggers the fusion of the viral and host membranes, leading to conformational changes in the M1 protein that facilitate the release of the viral ribonucleoproteins (vRNPs) to the cellular cytoplasm (step 3) (Honda et al., 2002). These vRNPs comprise complexes formed by the individual viral RNA

segments and proteins, including the RNA-dependent RNA polymerase (RdRp), which is associated with the 3'- and 5'-ends of viral RNA segments, and nucleoproteins (NPs) that are coating the remainder of the viral RNA. The vRNP complexes are then transported into the nucleus to initiate transcription and replication by RdRp, which is formed by the polymerase basic protein 1 (PB1), polymerase basic protein 2 (PB2), and polymerase acidic protein (PA). The first step is known as cap-snatching, a process where RdRp (PB2 and PA subunits) interacts with the C-terminal domain of the host RNA polymerase II and removes the first 10–13 nucleotides of a nascent transcript, which is then used as a primer to initiate transcription from the viral RNA template by PB1 (De Vlugt et al., 2018). This is followed by a viral genome replication phase that involves the synthesis of full-length viral RNA and cRNA strands (steps 4 and 5) (Pielak and Chou, 2011). With a late stage of packaging, vRNPs are formed (step 6). The synthesis of M2 protein, HA and NA is carried out by ribosomes bound to the membranes of the endoplasmic reticulum, which are then glycosylated and transported to the Golgi apparatus (step 7) (Sidorenko and Reichl, 2004). Finally, a complex between the membrane-embedded proteins and vRNPs is formed and delivered to the cell membrane, leading to the assembly of new virions that will be released to the extracellular side of the host cell membrane (step 8).

The preceding discussion suffices to reveal the complexity encoded in the multi-step processes - cell entry, replication, intracellular trafficking, virion assembly, and release - involved in the generation of new virions. In this scenario, the search for effective antiviral treatments has been inspired by the identification of druggable viral targets with a relevant role in the life cycle of virus infection. Early drug discovery projects targeting the M2 proton channel primarily relied on adamantane-related compounds (Moorthy et al., 2014; Wang et al., 2015). However, the emergence of resistant strains motivated the search of novel therapeutic approaches, including the development of 1) NA inhibitors such as zanamivir and oseltamivir, although drug-resistant variants have also been reported, 2) HA inhibitors, as exemplified by the discovery of arbidol and JNJ7918, and, more recently, 3) RdRp inhibitors, such as pimodivir and baloxavir (Loregian et al., 2014; Wu et al., 2017; Han et al., 2018; Mifsud et al., 2019; Ginex and Luque, 2021). The discovery of small-molecule antiviral compounds against these targets has benefited from the progress made in disclosing the fine structural details of these proteins, the molecular mechanisms that underlie their biological function, and the characterization of the mode of action of inhibitory compounds.

STRUCTURE OF THE M2 PROTON CHANNEL

The M2 proton channel is a homotetrameric integral transmembrane (TM) protein located in the viral envelope of the influenza A virus. It is a selective, pH-dependent channel that regulates the acidification of the interior of the virion, leading to dissociation of the viral RNA from its bound matrix proteins and

release of the viral genetic material for replication (Pinto et al., 1992; Pielak and Chou, 2011; Manzoor et al., 2017).

From a structural point of view, the M2 channel is a homotetramer, each monomer consisting of 97 amino acids and can be divided into four main regions: 1) the highly conserved, unstructured N-terminal domain (residues 1–21) located in the viral exterior, which assists the incorporation of the M2 channel into the virion, 2) the TM domain (residues 22–46) (**Figure 2**), which assembles into a tetrameric domain and is involved in the proton flux, 3) an amphiphilic membrane-anchored helical domain (residues 47–67), which is located in the interface with the membrane and stabilizes the channel by inducing membrane curvature and mediates membrane scission, and 4) the C-terminal domain (residues 68–97), which is located in the viral interior and interacts with the matrix protein M1 and contributes to virus packaging and budding (McCown and Pekosz, 2006; Rossman et al., 2010; Wang and Hong, 2015a).

The TM region contains the binding site for M2 inhibitors in the interior of the pore, filling a pocket located between the tetrads formed by residues Val27, Ser31, Gly34, and His37 (Schnell and Chou, 2008; Acharya et al., 2010; Cady et al., 2010; Sharma et al., 2010). This pore is implicated in the proton conduction, and the proton current is regulated by the tetrads formed by His37 and Trp41. His37 is a pH sensor and can conduct the proton inside the channel by changing the protonation state of the imidazole side chain, whereas Trp41 acts as a gate of the channel. Accordingly, binding of compounds that fill the binding site in the interior of the M2 channel would sterically impede the passage of protons (**Figure 2**).

The pH-sensing gating mechanism regulates the proton flux through the channel, which is modulated by the transition from an open state at an acidic pH, where the imidazole rings of the His37 tetrad are protonated, to a closed state at alkaline pH environment, which promotes the deprotonated state of His37 residues. In the open state, the M2 channel is also permeable to some cations, such as Na⁺ and K⁺, through an antiporter-like mechanism, carrying out the metal cation efflux in conjunction to proton influx, but the permeability to protons has been estimated to be 10⁶–10⁷ higher than the conduction of alkaline cations (Chizhnikov et al., 1996; Shimbo et al., 1996; Mould et al., 2000a; Manzoor et al., 2017). There is an asymmetric conductance as the proton flux is higher when the pH outside the virus is low, consistently with an acidic endosome. This behavior has been attributed to the presence of the Trp41 gate, which reduces the conduction in the reverse direction (Ma et al., 2013). Thus, when the His37 tetrad is protonated by protons coming from the endosome, the indole moiety of Trp41 undergoes a conformational change and the channel enters an open state that would allow the passage of protons to the interior of the virus.

The functional relevance of His37 and Trp41 is revealed by the drastic effects triggered by mutations in these positions, which cause a reduction in the pH sensitivity of the channel, and a disruption in the proton conduction (Wang et al., 1995; Tang et al., 2002; Venkataraman et al., 2005). Thus, mutations in His37 have a drastic effect on the functional properties of the M2

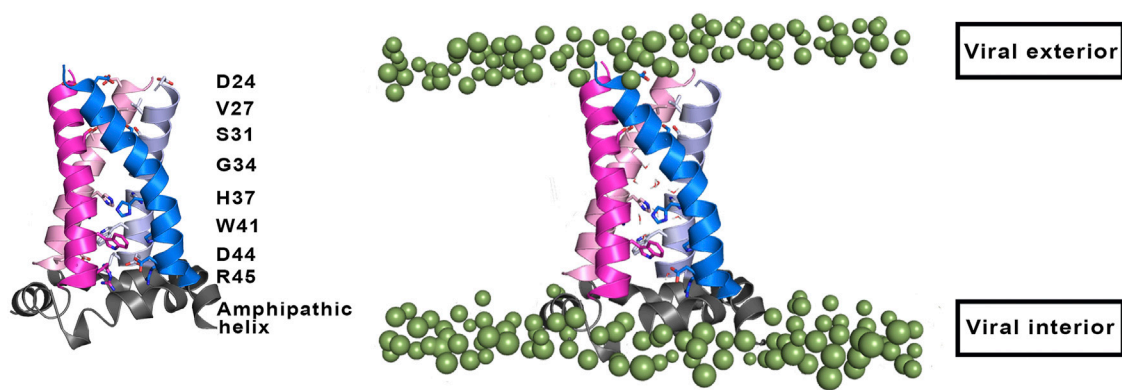


FIGURE 2 | (Left) Representation of selected residues that shape the inner pore of the M2 proton channel (shown as sticks). (Right) Representation of the four transmembrane helices (residues 22–46; shown as cartoon in magenta, blue, pink and violet), where the amphipathic helices (residues 47–67) that are located near the inner side of the membrane are shown as grey cartoon. Polar heads of membrane lipids in both outer and inner sides of the viral membrane are shown as green spheres (adapted from a Molecular Dynamics simulations of the membrane-embedded M2 proton channel).

channel, since the mutated proteins not only increase the proton conduction of the channel, but also suppress the selectivity for proton conduction. As an example, the specific activity determined for the voltage-independent component of the conductance at pH 6.2 for the wild type channel was $0.16 \mu\text{A}/\text{ng}$, but increased to 1.36 and $30 \mu\text{A}/\text{ng}$ for the H37G and H37E mutated channels, respectively (Holsinger et al., 1994). Furthermore, the mutated ion channels H37G, H37S, and H37T were found to be deficient in ion selectivity (Venkataraman et al., 2005). On the other hand, the expression of the M2 protein in oocytes leads to an inward H^+ current upon bathing in acidic media (pH 5.9), which is lost upon return to alkaline conditions (pH 8.5). However, whereas no currents were observed for mutated channels containing Phe41, Cys41, or Ala41 prior to acidification, outward H^+ currents were detected by changing acidic conditions to alkaline solution.

Mechanism of Proton Conduction

The specific role played by His37 and Trp41 in assisting the proton flux through the pore of the M2 channel has been the subject of intense efforts, mainly focused on the TM domain, which reproduces most of the biophysical, site-directed mutagenesis and electrophysiological features of the full-length protein. These studies, further assisted by X-ray crystallography of structures solved in membrane-mimetic solvents at different pH and temperature, solution NMR, solid-state NMR (ss-NMR) spectroscopy (see below), in conjunction with computational simulations, have crystallized in several models of proton conduction.

An early mechanistic hypothesis was the water wire model, also known as the shutter mechanism (**Figure 3**), which assumes the presence of a discontinuous water column when the His37 tetrad is in the deprotonated state, where the channel adopts a

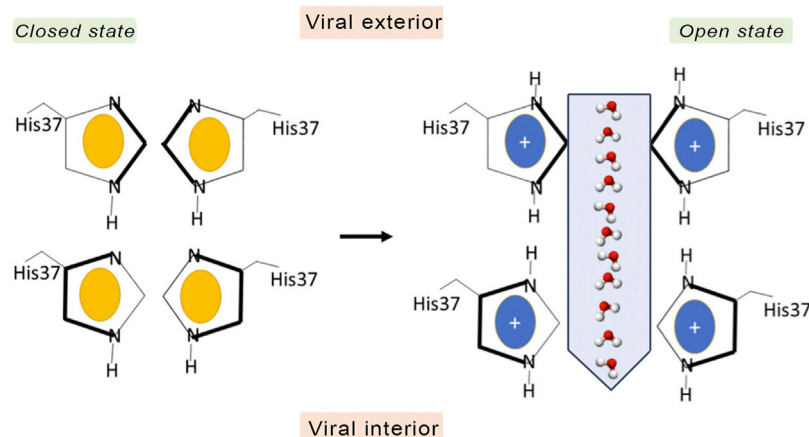


FIGURE 3 | Schematic representation of the shutter mechanism. In the closed state the channel is in the neutral state (imidazole ring in yellow), and there is not an electrostatic repulsion between the imidazole rings of His37. However, when His37 are fully protonated (coloured in blue), the electrostatic repulsion between imidazole rings triggers a conformational change that allows water and protons to pass through the gate.

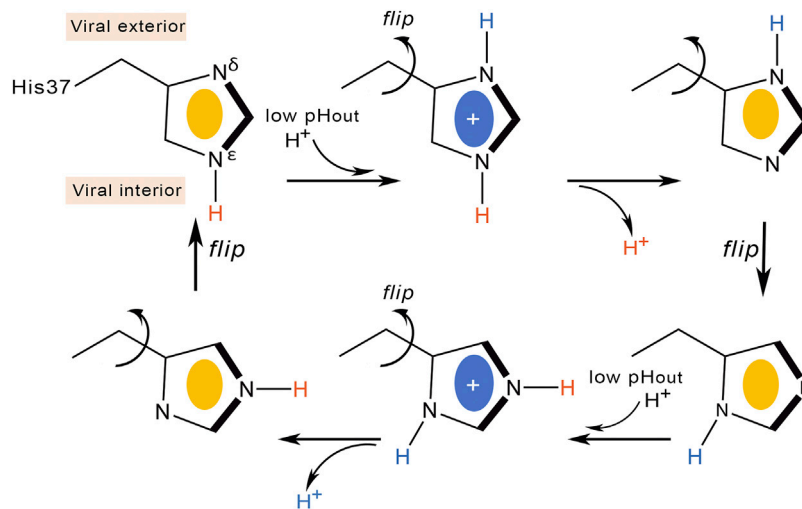


FIGURE 4 | Schematic representation of the proton transfer flow associated to conformational rearrangement of the His37 imidazole ring.

closed conformation that would be populated at alkaline pH (Sansom et al., 1997). When the pH decreases, protonation of the His37 tetrad leads to electrostatic repulsion between the charged imidazole rings. This would facilitate the conformational transition to an open state, which enables the diffusion of excess proton through the pore by means of a Grotthuss-type mechanism (Agmon, 1995). By merely working as a gatekeeper, in this model, the His37 tetrad would play a passive role as long as it is not directly involved in the proton transfer.

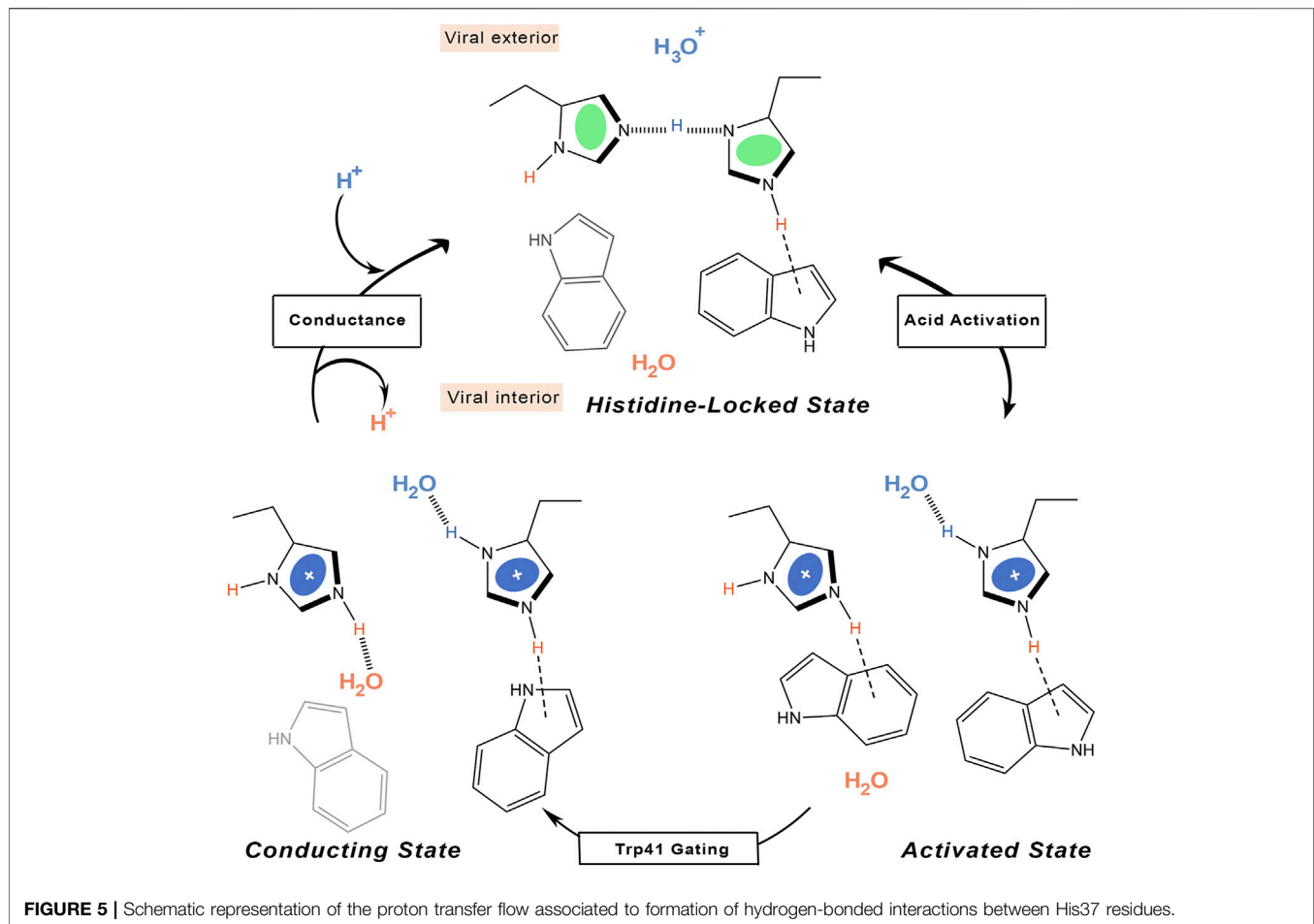
In contrast to the shutter model, the currently accepted proton conduction mechanism assumes a proton relay model (**Figure 4**). According to this model, protons diffuse along a water wire until reaching the tetrad formed by His37, generating an imidazolium intermediate, which in turn releases a proton to the inner side (Pinto et al., 1997; Okada et al., 2001). This mechanism was first proposed by Pinto et al. on the basis of conductance measurements in conjunction with Cys scanning mutagenesis (Pinto et al., 1997). However, a number of questions remained to be elucidated, such as the number of His residues required to be protonated for proton conduction, the stabilization of the protonated imidazolium via interactions with other residues in the channel or with water molecules filling the inner pore, and whether translocation of the proton into the viral interior would be mediated by prototropic tautomerism of the imidazole ring or through conformational flip of the His37 side chain.

Deeper knowledge into the molecular events implicated in proton conduction has been gained from ss-NMR studies. Hu et al. refined the proton relay model suggesting that proton conduction is concomitant with His37 conformational changes (**Figure 4**) (Hu et al., 2010). At high external pH the His37 imidazole are tightly packed through CH- π interactions, preventing the formation of hydrogen-bonded water chains in the pore. Acidification protonates the imidazole ring at position N δ 1, and the electrostatic repulsion between protonated histidines would widen the pore (Khurana et al., 2009), enabling the reorientation of the imidazolium ring at the

microsecond time scale. Proton conduction would involve imidazolium deprotonation facilitated by C ϵ 1-He1 hydrogen bonding and continuous ring flips, which would contribute to the proper alignment of the charged imidazolium with C-terminal water molecules and rearrangement of the neutral imidazole to the N-terminal side of the pore to start another protonation cycle.

This proton transfer model dynamically couples the interaction of His37 with water molecules, which are required for delivering protons to the imidazole ring, with the conformational flips of His37 side chains. The barrier of the conformational rearrangement of the His37 residues was estimated to be close to 14 kcal mol⁻¹, which would justify the temperature dependence of proton transport, though possibly this value may contain a contribution arising from the barrier for proton transfer (Lin and Schroeder, 2001). This model is consistent with the deuterium isotope effects (Mould et al., 2000b), and support comes from ¹⁵N NMR data, which yielded an estimated rate of 10⁵ s⁻¹ for the protonation and deprotonation of the imidazole nitrogens (Hu et al., 2012). This rate was consistent with the ring reorientation rate estimated from motionally averaged dipolar couplings, supporting the proposal that ring reorientation is synchronized with, and facilitates, proton transfer. Notably, only a single histidine residue is required to be actively involved in proton transfer according to this mechanism.

Other ssNMR studies suggested that proton conduction may also involve the formation and breaking of hydrogen bonds between adjacent pairs of histidines, in conjunction with the assistance of tryptophan residues, to guide the proton through the channel (**Figure 5**) (Sharma et al., 2010). Thus, two His37 residues are protonated, each proton being shared with an adjacent His residue through a strong hydrogen bond. Accordingly, the His37 tetrad can be viewed as a pair of imidazole-imidazolium dimer (also denoted dimer-of-dimers). This would define the so-called histidine-locked state, which is



further stabilized by a cation- π interaction of the protonated histidine with a tryptophan residue. When the pH decreases, a proton is transferred from the hydronium cation to the interresidue hydrogen bond formed between N δ 1 and N ϵ 2 of the hydrogen-bonded histidines, leading to the activated state that contains a third protonated His37. The two imidazolium rings can then rotate, so that a protonated histidine may form a hydrogen bond with water in the N-terminal pore, while a conformational change in the other histidine enables the formation of a cation- π interaction with an indole of Trp41, which would block water access from the C-terminal pore. The conducting state is obtained when this indole moves aside to expose the N ϵ 2 proton to a water molecule in the C-terminal pore. Finally, the histidine-locked state is recovered after the release of the N ϵ 2 proton to a water molecule in the C-terminus. Recent studies have also suggested that the hydrogen bonding between imidazole rings could be formed even at a pH of 7.8 in the neutral charge state (Movellan et al., 2020), and that a water molecule is hydrogen-bonded to the deprotonated nitrogen of the histidine imidazole (Movellan et al., 2021).

According to this mechanism, the His37 tetrad would only sense acidification in the N-terminal side, reflecting previous observations obtained upon application of a voltage to drive protons outward in M2-transformed cells (Chizhnikov et al.,

2003). The selectivity of proton selective transport is also justified as long as the proton must bind to and unbind from the histidine imidazole ring, which would explain the saturation attained at a moderate pH close to the histidine-tetrad pK_a on the N-terminal side (Yi et al., 2009). In fact, the proton flux determined for the H37A mutant exhibits no pH dependence (Venkataraman et al., 2005). Finally, the low conductance would reflect the conformational transition of the Trp41 gate, which opens occasionally to form the conducting state that enables the proton to be released to the C-terminal pore.

More recently, measurement of ¹⁵N-¹⁵N J-couplings of ¹⁵N His37-labeled full-length M2 proton channel have been used to examine the occurrence of various imidazolium-imidazole hydrogen-bonding arrangements in the channel at low pH (Miao et al., 2015; Fu et al., 2020). According to these results, the proton conduction takes place through a dynamical process where low-barrier hydrogen bonds between pairs of His37 residues are broken and reformed.

From a computational point of view, the translocation of the proton has been examined by Carnevale et al. by combining classical Molecular Dynamics (MD) simulations and hybrid quantum mechanics/molecular mechanics (QM/MM) methods. MD simulations were performed using methylammonium cation to examine the response of water molecules lying in the pore to an

incoming positively charged moiety for the +2 state of the M2 channel (Carnevale et al., 2010). The results disclosed a broad minimum in the free energy landscape in the region below Val27 side chains, and the existence of a second local minimum in the region near Ala34, where the positive charge is stabilized by interactions with water molecules located above the His37 tetrad, and with the local dipoles of the backbone carbonyl groups. QM/MM computations aimed to determine the energetics of proton transport through the set of water molecules located above His37. In this case, the results supported a nearly free diffusion of the excess proton, as the transport of the proton from the water molecules to a neutral His37 occurs through several local minima separated by small barriers. Therefore, these findings suggest that the confining environment in the pore has little impact on the kinetics of proton diffusion, which should resemble proton transport in bulk water.

As a final remark, it is worth noting the computational study of proton conduction reported by Liang et al. (2016), which resorted to mutiscale simulations to follow the proton translocation through the channel considering distinct protonation states (fully deprotonated, +1 and +2) of the channel in models containing the TM region without (M2TM) and with (M2CD) the amphipathic helix, which together define the conductance domain. To this end, the free energy profile for proton migration was determined by combining multiscale reactive molecular dynamics (MS-RMD) and QM/MM MD simulations, which enabled to follow the proton diffusion from the N-terminal and C-terminals ends of the pore as well as (de)protonation of His37 tetrad. The free energy profile determined for the fully neutral and +1 states reveal a high barrier ($>15 \text{ kcal mol}^{-1}$) for His37 deprotonation to the viral interior, leading to a predicted conductance well below the experimental value, suggesting that the ion channel is inactive at high pH conditions. In the +2 state, however, although the electrostatic repulsion between the incoming proton increases the barrier from viral exterior to His37, deprotonation of His37 is facilitated by the increased electrostatic repulsion between the leaving proton and the His37 tetrad, this process being further assisted by larger exposure to water molecules and increased flexibility of Trp41 residues. Thus, the His37 deprotonation barrier is decreased to $\sim 12 \text{ kcal mol}^{-1}$, and the predicted conductance (1.0 and 7.7 for the M2CD and M2TM models, respectively) is in agreement with the measured values (ranging from 0.4 to 4.0; Mould et al., 2000b; Leiding et al., 2010; Sharma et al., 2010).

The whole of these studies illustrate the complexity of gaining a detailed knowledge of the mechanism of proton conduction in spite of the apparent simplicity encoded in the four-helix bundle of the M2 proton channel. The proton conductance determined from electrophysiological assays encompass a variety of molecular events that take place at different spatiotemporal scales, including the formation and breaking of hydrogen-bond complexes implicated in the proton transfer between water molecules and to/from the His37 imidazole-imidazolium ring, the coupling with conformational changes in the side chains

of specific residues, and the structural rearrangements observed in the TM helices depending on the protonation state of the His37 tetrad.

The pKa of Histidines

The mechanistic models described above emphasize the relevance of the microscopic pKa of the His37 tetrad (Table 1) in assisting the proton flow through the inner pore of the M2 channel, which in turn would be associated with the pH-dependent equilibrium between open and closed states of the channel.

Using ultraviolet Resonance Raman spectroscopy and the transmembrane domain of the M2 proton channel (residues 22–46), Okada et al. reported that the proton channel is activated by low pH with a transition midpoint at pH 5.7 (Okada et al., 2001). Using the same construct, studies by Hu et al. measured pKa values of <5.0, 6.3, 8.2, and 8.2, leading to a +2 protonation state at neutral pH (Hu et al., 2006). Recent studies by Hu et al. supported pKa values of 4.0, 4.2, 6.8, and 7.6, which would support a +3 state at neutral pH, revealing the difficulty of elucidating the protonation preferences of the His37 tetrad and the influence of the experimental conditions used in these assays (Hu et al., 2012). On the other hand, NMR studies performed for a larger construct consisting of residues 21–97, which include the transmembrane helix but also the full cytoplasmic domain, led to pKa values of 7.1 and 5.4 for the second and third protonation (Liao et al., 2015). Likewise, a construct formed by residues 18–60, which encompass both the TM helix and the amphipathic helix that interacts with the interfacial region of the lipid bilayer, yielded estimated pKa values of 7.6 and 4.5 for the second and third protonations (Colvin et al., 2014), whereas pKas of 6.3 and 5.5 for the second and third protonations were determined by Miao et al. for the full-length protein (Miao et al., 2015). Even though the first two pKas are lower than the values estimated for shorter constructs, the authors indicate that at pH 6.2, where the channel should become activated, the M2 channel should be primarily in the +2 state. Moreover, the authors point out that there is little opportunity for a singly charged His37 tetrad.

The differences found in the pKas reported in Table 1 can be ascribed to the usage of different constructs, membrane-mimetic lipid environments, and conformational heterogeneity of the tetrameric helical bundle. In spite of these differences, there is consensus that the first two pKas appear to be above the endosomal pH that activates the M2 channel (pH ~ 6) (Mould et al., 2000b), suggesting that the physiologically active state for the early activation of the M2 channel corresponds to the protonation state of +2 for the His tetrad.

Computational studies have also been performed with the aim to estimate the pKa of the His37 tetrad, while providing atomistic details of the pH-dependent protonation process. In this regard, Dong et al. performed QM/MM calculations to characterize the structural features of the +3 state and its subsequent deprotonation to the +2 species (Dong et al., 2013; Dong et al., 2014). Calculations were performed considering both a 4-fold symmetric arrangement of the His37 residues (histidine-box) and a 2-fold symmetric configuration (i.e., the dimer-of-dimers arrangement). The results showed that in the triply

TABLE 1 | Estimated pKa values determined for the His37 tetrad in different constructs of the M2 channel.

Construct	His37 pKas	Lipid environment ^a	References
(22–46)	8.2, 8.2, 6.3, <5.0	DMPC, DMPCG	Hu et al. (2006)
(22–46)	7.6, 6.8, 4.9, 4.2	DPPC, DPPE, SM, Chol	Hu et al. (2012)
(21–97)	7.1, 5.4	POPC, POPE, SM, Chol	Liao et al. (2015)
(18–60)	7.6, 4.5	DPhPC	Colvin et al. (2014)
Full length	6.3, 6.3, 5.5	DOPC/DOPE	Miao et al. (2015)

^aDMPC: 1,2-dimyristoyl-sn-3-phosphocholine; DMPCG: 1,2-dimyristoyl-sn-glycero-3-phosphoglycerol; DPPC: 1,2-dipalmitoyl-sn-glycero-3-phosphocholine; DPPE: 1,2-dipalmitoyl-sn-glycero-3-phosphoethanolamine; SM: egg sphingomyelin; POPC: 1-palmitoyl-2-oleoyl-sn-glycero-3-phosphocholine; POPE: 1-palmitoyl-2-oleoyl-sn-glycero-3-phosphoethanolamine; DPhPC: 1,2-diphytanoyl-sn-glycerol-3-phosphocholine; DOPC: dioleoylphosphatidylcholine; DOPE: dioleoylphosphatidylethanolamine.

protonated state the two alternative models (histidine-box and dimer-of-dimers arrangements) converge to a single deprotonation mechanism, and exhibit similar free energy profiles with a barrier height of ~6.5 kcal/mol to release a proton, supporting deprotonation as a mechanism for proton conduction.

Chen et al. have used constant pH replica-exchange MD simulations to determine the pKa values using a simulation model consisting of the TM helix (Chen et al., 2016). In this study, the simulated system consisted of the TM helix embedded in an explicit DMPC lipid bilayer and surrounded by an explicit solvent model (CHARM22 force field). However, the forces on titration coordinates were determined using the Generalized Born model in conjunction with an implicit membrane. Furthermore, a high-dielectric cylinder that encompass the channel was used to account for the continuous water wire in the pore. Finally, 12 replicas were used in simulations, covering a pH range of 3.5–9.0. The pKa values were estimated to be 8.3, 7.1, 6.2, and 5.7, which are in general close to the first three pKa's obtained in previous ssNMR studies (see Table 1). The largest deviation is limited to the pKa of the last protonation, likely reflecting limitations arising from the Generalized Born model employed in the hybrid-solvent CpHMD, and to the conformational sensitivity of helices related to differences in the lipid environment used in simulations and experiments.

More recently, Torabifard *et al.* have used CpHMD simulations performed using explicit solvent and the multisite λ -dynamics to estimate the pKa values of the His37 tetrad (Torabifard et al., 2020). They used two models consisting of the TM helix alone (M2TM) and another one that combines the TM region with the amphipatic helix at the interface of the cytoplasmic domain (M2CD). These models were inserted in bilayers composed of a 4:1 ratio of DOPC:DOPE and solvated by water with an ionic force of 0.15 M (CHARMM36 force field). CpHMD simulations were performed using the multisite λ -dynamics approach (Knight and Brooks, 2011). This computational strategy yielded pKa values of 12.5, 10.5, 7.0, and 5.4 for the M2CD model, which are within the range of uncertainty for measured pKa values, especially regarding the first and second pKa values (larger deviations from the experimental data, however, were observed for the M2TM model).

Although the deviations observed between predicted and experimental pKa values may be likely ascribed to inaccuracies in the biomolecular force field, the approximated nature of the physical models used in calculations, incomplete convergence of

the CpHMD simulations, and differences in the nature of lipid environments used in simulations and experiments, the results are encouraging and should provide a basis for gaining insight into the molecular factors that underlie the proton conduction in the M2 channel.

Other Factors That Influence the Proton Conduction of the M2 Channel

Besides the protonation state of the imidazole rings of the His37 tetrad, the efficiency of the M2 channel to perform the proton conduction may be influenced by a number of factors related to both the global structure of the ion channel and to the role of key residues other than His37 and Trp41. In this regard, Asp44 (see Figure 2) may contribute to modulate the proton conduction mechanism, as this residue forms direct or water-mediated hydrogen bonds with the indole moiety of Trp41 in the closed state (Acharya et al., 2010). In fact, Asp44 mutants tend to increase the population of the open state, as there is a loss of a stabilizing interaction of the closed state (Ma et al., 2013).

The influence exerted by the N-terminal ectodomain has been examined by Hong and coworkers (Kwon and Hong, 2016). The ectodomain is highly dynamic, although the motional flexibility is reduced for residues closer to the TM domain, possibly reflecting a tethering effect of the TM helix and the influence of lipid headgroups on the membrane surface. Furthermore, the electrostatic repulsion experienced by acidic residues (i.e., the ectodomain contains four acidic residues and only two cationic residues) appear to promote the adoption of TM conformations that would favor the binding of drugs in the inner pore (see below) even in the absence of the drug. This may be a factor that justifies the lower inhibitory concentration of full-length M2 compared to that of the ectodomain-truncated M2.

In this context, the potential role of Asp21 (see Figure 2) has also been recently highlighted by Jeong and Dyer (2017). Thus, by using a laser-induced pH jump coupled with time-resolved Trp fluorescence spectroscopy, protonation of His37 was estimated to occur in an unusually fast process, as reflected in a protonation rate of $1.6 \pm 0.4 \times 10^{10} \text{ M}^{-1} \text{ s}^{-1}$, suggesting that Asp21 at the end of the ectodomain and Asp24 at the beginning of the TM helix may act synergistically as proton-collecting antenna residues. The electrostatic field created by these residues would thus create a proton-capturing funnel at the entrance of the ion channel, enhancing proton harvesting from the surrounding aqueous phase. Protons would then be captured by hydrogen-bonded

TABLE 2 | X-ray structures containing chloride anions at the C-terminus of the M2 proton channel.

PDB ID	Resolution (Å)	Construct (mutant)	Experimental conditions	References
5C02	1.59	22–46 (S31N)	pH: 8.0 T: 283/100 K ^a LCP (OG) ^b	Thomaston and DeGrado, (2016)
6BMZ	2.63	22–46	pH: 7.0 T: 293/100 K LCP (MNG-3-C8) ^b	Thomaston et al. (2018)
6NV1	2.50	22–46 (V27A)	pH: 7.5 T: 293/100 K LCP (MNG-3-C8)	Thomaston et al. (2020)
6US8	1.70	22–46	pH: 7.5 T: 293/100 K LCP (MNG-3-C8)	Thomaston et al. (2021)
6US9	2.00	22–46	pH: 8.5 T: 293/100 K LCP (MNG-3-C8)	Thomaston et al. (2021)

^aTemperature of crystallization/temperature of data collection (values in Kelvin).

^bObtained considering a lipidic cubic phase (LPC) formed by monoolein and octyl glucopyranoside (OG) or maltose neopentyl glycol analogue (MNG-3-C8).

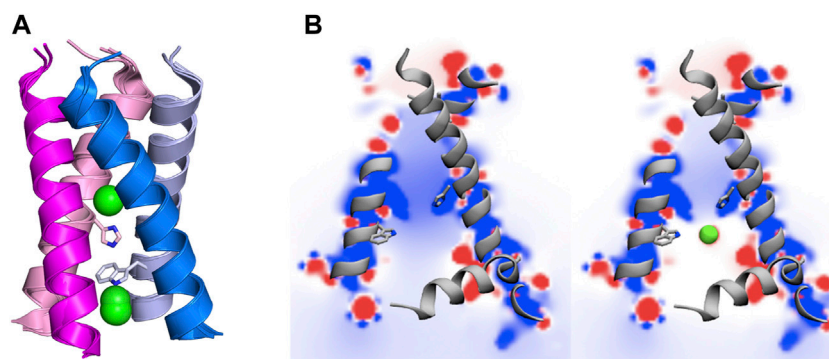


FIGURE 6 | (A) Representation of chloride anions (green spheres) in selected X-ray crystallographic structures of the transmembrane region of the M2 proton channel (adapted from PDB entries 5C02, 6BMZ, 6NV1, 6US8 and 6US9). (B) Representation of the electrostatic potential (kcal mol^{-1}) in a plane passing through the interior of the M2 channel in (left) absence and (right) presence of chloride anions. Isocontours range from +12 (blue) to -12 kcal/mol (red). His37 and Trp41 residues are shown as sticks. Adapted with permission from (Lladrés et al., 2016) (Copyright 2016 American Chemical Society). For the sake of clarity one of the helices is not shown.

wires of water molecules within the pore, and the hydronium cation could be stabilized by interactions with pore-lining carbonyl groups as well as through bridging water molecules (Thomaston et al., 2015). Furthermore, they concluded that protonation of the His37 tetrad promotes opening of the C-terminal region, enhancing the solvent-exposure of Trp41, with a rate of $(4 \pm 2) \times 10^3 \text{ s}^{-1}$. The temporal decoupling between His37 protonation and this conformational change suggests that probably each proton transport cycle does not require a further conformational change after M2 activation.

Additional studies have examined the effect of the cytoplasmic tail on the conformational properties of the TM domain (Chizhnikov et al., 2003). The results obtained for the cytoplasmic-containing M2 channel reveal that even at neutral pH cationic histidines are present in the interior of the pore, which is in contrast to the results obtained for the TM peptide alone. This effect might be attributed to the acidic character of the cytoplasmic domain, which could facilitate opening of the TM pore at the His37 constriction. Furthermore, the presence of the cytoplasmic domain favors the adoption of a more helical conformation in the His37 backbone, suggesting an ordering effect on the four-helix bundle. Overall, these results provide a

basis for the higher proton conductance of full-length M2 channel compared to the TM peptide.

Finally, the stability of the protonated states of the His37 tetrad may be affected by the presence of chloride anions in the interior of the pore. Inspection of the X-ray crystallographic data available for the M2 proton channel in the Protein Data Bank (Berman et al., 2000; Burley et al., 2021) reveals the occurrence of a subset of structures where chloride anions are found in the interior of the pore (this subset is collected in Table 2) (Thomaston and DeGrado, 2016; Thomaston et al., 2018; Thomaston et al., 2020; Thomaston et al., 2021). In four out of the five cases, the chloride anion occupies a well-defined position close to the plane formed by the Trp41 residues. Indeed, the chloride anion is stabilized by hydrogen-bond interaction with the indole NH groups, as well as by electrostatic interactions with the positive charge of Arg45 residues, though this latter effect is counterbalanced by the repulsion with the negative charge of Asp44 (Figure 6A). More strikingly, a chloride anion was observed along the four-fold axis in the plane defined by Gly34 residues in the X-ray structure of the S31N mutated variant (PDB entry 5C02).

MD simulations have also revealed the presence of chloride anions in the interior of the channel pore, though the presence of chloride anions depends on the protonation state of the M2 proton channel. Thus, Mustafa et al. reported the occurrence of chloride anions at the level of the Trp41 tetrad for the +2 and +3 states in short simulations performed for the 22–46 construct (Mustafa et al., 2009). Wei and Pohorille also indicated that chloride anions penetrate the pore in all charged states of the M2 channel, but not for the fully unprotonated form (Wei and Pohorille, 2013). The position of the chloride anions was also affected by the charge state, as they were located in the space defined by the His37 and Trp41 planes for the diprotonated form of the channel. Gleed and Busath (2015), Gkeka et al. (2013) and Llabrés et al. (2016) also reported the presence of chloride anions close to the protonated His37 residues.

The presence of chloride anions in the pore may contribute to modulate the structural stability of the helical bundle, as suggested by Wei and Pohorille (2013). The MD simulations performed in presence of chloride ions revealed that they reside near Trp41, but their presence in this location of the pore depends on the charged state of the channel. Thus, anions do penetrate the pore, but to different degree, in all charged states, and they were absent only in the unprotonated form of M2 channel. Furthermore, simulations performed in the presence of phosphate anions confirmed their presence in the pore, suggesting that the size and specific chemical nature of counterions are not essential for the structural stabilization of the channel. Remarkably, additional simulations carried out in the presence of a uniform electrostatic field instead of explicit ions revealed a destabilization of the helical bundle in the +3 and +4 states, reflecting the electrostatic stabilization afforded by counterions that would balance the electrostatic repulsion between protonated His37 residues.

Besides the structural stabilization, the presence of anions in the pore has a strong influence on the nature of the electrostatic potential in the interior of the channel, which is highly positive in the absence of anions, but only slightly positive when chloride anions are present near the His37 sites, according to the MD simulations reported for the channel in the +2 state (**Figure 6B**) (Llabrés et al., 2016). Keeping in mind the functional relevance of electric fields in enzyme catalysis as well as in (un)binding of ligands to their macromolecular targets (Tan et al., 1993; Dillon et al., 2006; Fried and Boxer, 2017; Vaissier Welborn and Head-Gordon, 2019), the presence of negatively charged ions in the interior of the pore might be valuable to facilitate the diffusion of the proton from the bulk solvent along the N-terminal side of the luminal pore, and hence the transition from the +2 charged species to the triply protonated state. Furthermore, counterions may also facilitate the binding of Amt and related inhibitors by screening the electrostatic repulsion of the protonated amine of inhibitors with the charged His37 residues in the +2 state.

Finally, it is unclear whether the presence of counterions may have a functional role in assisting the translocation of the proton from the protonated His37 residues to the interior of the virion. At this point, it is worth noting that previous QM/MM calculations have suggested that the presence of chloride anions may increase the barrier for deprotonation (Dong

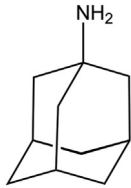
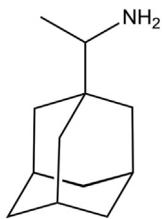
et al., 2014), which would reduce the proton conduction. This effect, however, can be largely dependent upon the precise location of the chloride anions relative to the His37-Trp41 pair. Moreover, the functional impact might also be alleviated if the residence time of the chloride anion is affected by the structural fluctuations of the C-terminus in the triply charged state of the channel due to the larger electrostatic repulsion between the imidazolium rings. In particular, one can speculate that a fast exchange of chloride anions might transiently induce an electric field that would ease the transfer of the proton from the protonated His37 tetrad to the C-terminal side, thus facilitating the restoration of the +2 state and hence enabling the entry of new protons to the interior of the virion. In our view, this is an issue that deserves more attention.

INHIBITION OF THE M2 PROTON CHANNEL

Beyond the definition of the molecular events implicated in proton conduction, a major challenge has been the identification of small molecules that can block the proton flow through the inner pore, and hence be used for therapeutic treatments against flu. Amantadine (Amt) and its ethyl analog, rimantadine (Rmt), were patented in 1961 and 1963, respectively (Du Pont Patent, 1961; Prichard, 1967), but they are no longer recommended for the treatment of flu infection. This obeys to several reasons, such as the limited effectiveness against influenza B virus, unwanted side effects, and the emergence of adamantane-resistant influenza A viral strains, primarily single mutated variants V27A, L26F and S31N. These mutations are found in a specific area facing the interior of the pore, suggesting therefore the location of the binding site in the M2 channel (Grambas et al., 1992; Hoyden, 2006; Deyde et al., 2007). For instance, in contrast to the large and widespread chemical shifts observed upon binding of Rmt to the M2 channel, only minor changes in chemical shifts were detected upon addition of a 4-fold molar excess of Rmt to the S31N mutated channel (Cady et al., 2009; Andreas et al., 2010; Andreas et al., 2012). For our purposes here, the discussion of the molecular determinants implicated in drug binding will be limited to the subset of structures available in the Protein Data Bank that contains drug-like inhibitors (see **Tables 3, 4**).

As noted above, the binding site for M2 inhibitors is located in the interior of the pore, filling a pocket shaped by residues Val27, Ser31, Gly34, and His37. Early neutron diffraction (Duff et al., 1994) and computational (Samson and Kerr, 1993) studies already identified this pocket as the binding site that mediates the blockade of proton conduction by Amt. Detailed information about the binding mode of Amt and Rmt has subsequently been gained from structural studies based on X-ray diffraction, solution NMR and ss-NMR (**Table 3**; Schnell and Chou, 2008; Stouffer et al., 2008; Cady et al., 2009; Cady et al., 2010; Thomaston et al., 2018). The inspection of these structures reveals the existence of two binding sites (**Figure 7**). In most cases the drug is located in the interior of the pore filling the space located between Val27 and Gly34 (pore-binding model), but in two structures (PDB ID 2RLF and 6US8) the drug is also found

TABLE 3 | X-ray and ss-NMR structures of the complexes formed by the wild type M2 proton channel and mutated variants with Amt and Rmt.

PDB ID	Construct (mutant)	Method	Experimental conditions	References
<p style="text-align: center;">Amantadine</p> 				
2KAD	22–46 (L40A)	ss-NMR	pH: 7.5 T: 243 K DLPC bilayer ^a	Cady et al. (2009)
3C9J	22–46 (G34A)	X-ray (3.50 Å)	pH 5.3 T: 298/100 K ^b OG ^c	Stouffer et al. (2008)
2KQT	22–46	ss-NMR	pH 7.5 T: 243 K DMPC bilayer ^d	Cady et al. (2010)
6BKK	22–46	X-ray (2.00 Å)	pH 5.6 T: 293/100 K LCP (MNG-3-C8) ^e	Thomaston et al. (2018)
<p style="text-align: center;">Rimantadine</p> 				
2RLF (R-Rmt)	18–60	NMR	pH: 7.5 T: 303 K DHPC ^f	Schnell and Chou, (2008)
6BKL (R,S-Rmt)	22–46	X-ray (2.00 Å)	pH 4.5 T: 293/100 K LCP (MNG-3-C8)	Thomaston et al. (2018)
6BOC	22–46	X-ray (2.25 Å)	pH 3.5 T: 293/100 K LCP (MNG-3-C8)	Thomaston et al. (2018)
6US8 (S-Rmt)	22–46	X-ray (1.70 Å)	pH: 7.5 T: 293/100 K LCP (MNG-3-C8)	Thomaston et al. (2021)
6US9 (R-Rmt)	22–46	X-ray (2.00 Å)	pH: 8.5 T: 293/100 K LCP (MNG-3-C8)	Thomaston et al. (2021)

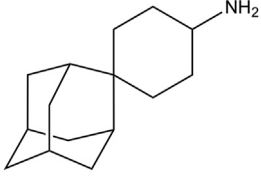
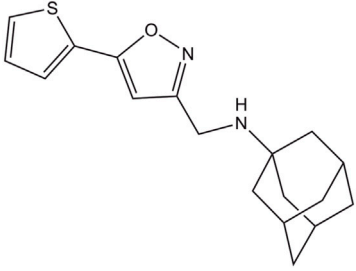
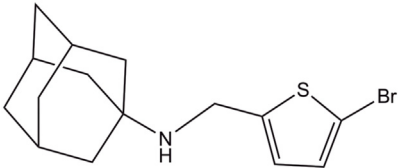
^a1,2-Dilauroyl-sn-glycero-3-phosphatidylcholine.^bTemperature of crystallization/temperature of data collection in Kelvin.^cOctyl-β-D-glucopyranoside.^dDimyristoylphosphatidylcholine.^eStructures obtained considering a lipidic cubic phase (LCP) formed by monoolein and maltose neopentyl glycol analogue (MNG-3-C8).^fDihexanoylphosphocholine.

outside the channel located in a peripheral site close to Leu43 and Asp44 in the C-terminus of the TM helical region (interface-binding model). The high-affinity site lies in the pore, as revealed from the analysis of REDOR dipolar dephasing between ¹³C-labeled M2TM and perdeuterated Amt in ss-NMR studies performed in a lipid bilayer (Cady et al., 2010). From a computational point of view, free energy calculations also pointed out that binding of Rmt to the pore-binding site is ~7 kcal/mol more favorable relative to the interface-binding site, leading to more stable drug binding and channel inhibition (Li et al., 2008). The presence of the peripheral binding site can be attributed to the partitioning of the drug in the membrane-like lipidic environment (Duff et al., 1994; Gu et al., 2011). The studies reported by Cady et al. (2010) showed that the highest affinity binding site of amantadine is the N-terminal pore lumen, which is consistent

with the known stoichiometry of binding (1:1 drug:channel) and the location of resistant mutations, such as V27A and S31N. However, increasing the drug:channel concentration up to 4:1, the drug contributes ~7% of the amphiphiles composing the DMPC bilayer, and binding to the low-affinity, peripheral site is observed in NMR studies. Thus, when free amantadine is a major component of the membrane, Amt contacts the C-terminus of the protein, though the affinity for the peripheral site has been estimated to be ~40-fold lower (see (Wang et al., 2015) for a detailed discussion of biophysical, computational and functional assays that addressed the binding mode of Amt and Rmt).

Inspection of these structures shows that in the pore the drug is oriented along the axis of the channel. Drug binding causes a dehydration of the channel, thus preventing the formation of a water wire from the N-terminus, although the amino group of

TABLE 4 | X-ray and solution NMR structures of the complexes formed by the wild type M2 proton channel and mutated variants with adamantane-related compounds.

PDB ID	Construct (mutant)	Method	Experimental conditions	References
(1<i>r</i>,1'<i>S</i>,3<i>S</i>,5'<i>S</i>,7'<i>S</i>)-spiro [cyclohexane-1,2'-tricyclo [3.3.1.1~3,7~]decan]-4-amine				
				
6BMZ	22–46	X-ray (2.63 Å)	pH: 7.0 T: 293/100 K ^a LCP (MNG-3-C8) ^b	Thomaston et al. (2018)
6NV1	22–46 (V27A)	X-ray (2.50 Å)	pH: 7.5 T: 293/100 K LCP (MNG-3-C8)	Thomaston et al. (2020)
6OUG	21–61 (V27A)	X-ray (3.01 Å)	pH: 8.0 T: 293/100 K LCP (MNG-3-C8)	Thomaston et al. (2020)
(3<i>S</i>,5<i>S</i>,7<i>S</i>)-N-[[5-(thiophen-2-yl)-1,2-oxazol-3-yl]methyl]tricyclo[3.3.1.1~3,7~]decan-1-aminium (M2WJ332)				
				
2LYO	19–49 (S31N)	NMR	pH: 6.8 T: 313 K DPC ^c	Drakopoulos et al. (2018)
(3<i>S</i>,5<i>S</i>,7<i>S</i>)-N-[[5-bromothiophen-2-yl]methyl]tricyclo[3.3.1.1~3,7~]decan-1-aminium				
				
2MUW	19–49	NMR	pH: 7.5 T: 313 K DPC	Wang et al. (2013)
2MUV	19–49 (S31N)	NMR	pH: 7.5 T: 313 K DPC	Wang et al. (2013)

^aTemperature of crystallization/temperature of data collection in Kelvin.^bStructures obtained considering a lipidic cubic phase (LPC) formed by monoolein and maltose neopentyl glycol analogue (MNG-3-C8).^c*n*-Dodecylphosphocholine.

Amt and Rmt is bound to water molecules that fill the space located between the drug and the His37 tetrad. In the specific case of Rmt, the two enantiomers bind to the pore with only slight differences in the hydration pattern, and exhibit similar values for association and dissociation kinetic rate constants and binding affinities, which was in agreement with the small differences in the relative binding free energy (around 0.3 kcal mol⁻¹) determined from free energy calculations (Thomaston et al., 2020). Furthermore, Rmt was found to be more potent than Amt, as noted in a ~14-fold ratio of their binding affinities to the M2 channel. On the other hand, it has been shown that binding of Amt reduces the pKa of His37 and alters the propensity to form

hydrogen-bond interactions in the His37 tetrad (Hu et al., 2007; Cady et al., 2011).

From a computational standpoint, fine details of the binding mode of adamantane blockers have been extensively investigated. Yi et al. paid attention to the changes in conformational states of the M2 channel upon binding of Amt through comparison of the ensembles collected for both apo and bound forms (Yi et al., 2008; Yi et al., 2009). In particular, they observed a reduction in the conformational heterogeneity upon Amt binding, as reflected in a narrower distribution of kink angles around Gly34 in the transmembrane helices compared to the apo species, which agrees with the broadened resonances observed from ssNMR

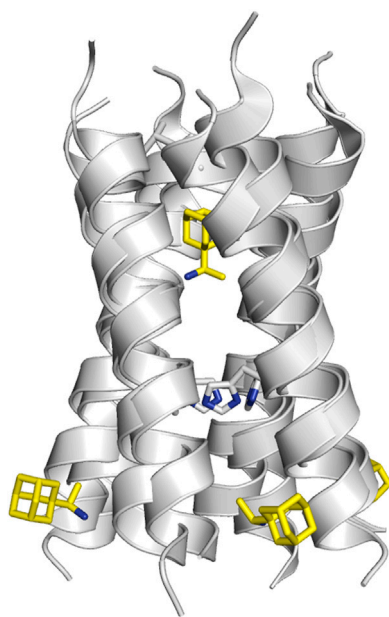


FIGURE 7 | Representation of the binding mode of Rmt (shown as sticks with C-atoms in pink and yellow, respectively) to the TM helical region of the M2 proton channel (residues Val27 and His37 are shown as sticks; obtained from superposition of PDB structures 2RLF and 6BKL).

studies of this latter form. In contrast, large-kink angles were not observed in simulations. The occurrence of kinks also allows the access of water molecules that may stabilize the kinked helices via hydrogen bonds with the backbone carbonyl and amide groups around the kink, which in turn may also influence the proton conduction.

On the other hand, efforts have been conducted to predict the differences in binding affinity for adamantane inhibitors using free energy calculations, including implicit solvent/implicit membrane molecular mechanics Poisson-Boltzmann surface area (MM-PBSA) approach (Homeyer et al., 2016) and free energy perturbation techniques (Gkeka et al., 2013; Ioannidis et al., 2016). Gratifyingly, alchemical free energy calculations performed for a set of 10 adamantane ligands reproduced satisfactorily the binding potency determined experimentally using isothermal titration calorimetry (ITC) against the M2 channel at high pH (pH = 8), especially keeping in mind that they cover a binding affinity range of only ~ 2 kcal mol⁻¹. Nevertheless, it is worth noting that the agreement between computational and experimental data was affected by the nature of the lipids used to model the membrane. In particular, a higher correlation between experimental and computed relative binding free energies was obtained when calculations were performed for the tetramer in a 1,2-dimyristoyl-*sn*-glycero-3-phosphocholine bilayer, possibly due to a larger mimetic resemblance with the dodecylphosphocholine micelles used for ITC measurements.

Furthermore, the entire recognition process of Amt to the M2 channel has been explicitly explored using multiple-walkers

well-tempered metadynamics calculations (Llabrés et al., 2016). The results suggested that Amt retains some degree of conformational motion in the pore allowing the adoption of two main orientations where the amino group is oriented to the N-terminus and C-terminus (denoted *up* and *down*, respectively). Binding of Amt would follow a sequential mechanism that would involve trapping of the protonated Amt by the negative electrostatic field created by the tetrad of Asp24, followed by the adoption of a transiently populated intermediate with Amt in the *up* state, and finally the reorientation in the interior of the pore to the *down* state, which is the thermodynamically favored orientation (Figure 8). Release of Amt from the *down* state to the channel mouth is destabilized by ~ 12 kcal mol⁻¹. The agreement with the experimental binding affinity (~ 8 – 9 kcal mol⁻¹) is reasonable, since the theoretical estimate omits the free energy contribution due to the release of Amt to the aqueous solvent, and the fact that the apparent K_i might not properly correspond to an equilibrium measurement of the inhibitory constant (Wang et al., 1993; Ma et al., 2009; Rosenberg and Casarotto, 2010). As a particular remark, this study also pointed out that the *down* \rightarrow *up* transition depends on the presence of chloride anions in the C-terminus of the channel, since the stabilization of the *down* state can be enhanced by ~ 6 kcal mol⁻¹ due to the modulation of the electrostatic field in the interior of the pore. Finally, the barrier from Amt dissociation was estimated to be ~ 19 kcal mol⁻¹, which compares a value of 22 kcal mol⁻¹ determined from electrophysiological assays (Wang et al., 1993).

Mutation of Val27 to Ala causes a drastic alteration in the free energy surface for Amt binding, as noted in a stabilization of the *up* state less than 1 kcal mol⁻¹, which agrees with the experimentally observed lack of inhibitory potency for the Amt-resistant V27A channel. This effect can be attributed to the increased accessible volume in the inner pore due to the V27A mutation, which encouraged the search of compounds with an expanded hydrophobic cage (Duque et al., 2011; Wang et al., 2011; Rey-Carrizo et al., 2014; Rey-Carrizo et al., 2015; Thomaston et al., 2018). In the case of the spiroadamantane **1** ((1*r*,1'*s*,3'*s*,5'*s*,7'*s*)-spiro[cyclohexane-1,2'-tricyclo[3.3.1.1^{3,7}~]decan]-4-amine) shown in Table 4 (Thomaston et al., 2018; Thomaston et al., 2020), comparison of the X-ray structures solved for the wild type and the V27A mutant shows that the compound exhibits a similar arrangement in the ion channel, which is found in the closed conformation (Figure 9) (Thomaston et al., 2020). The ligand exhibits only a slight shift depending on the nature of the residue at position 27. In the V27A complex, the amino group of **1** occupies approximately the same position as the ammonium group of Amt in complex with the wild type channel (PDB entry 6BKK) (Thomaston et al., 2018). This is facilitated by the larger free volume enabled by the presence of Ala27. Nevertheless, in the complex with the wild type channel, the adamantyl group of **1** and Amt overlap, but the ammonium group binds deeper in the pore at the expense of displacing few water molecules. MD simulations performed for the V27A complex with **1** reflected the shift of the ligand toward the N-terminus.

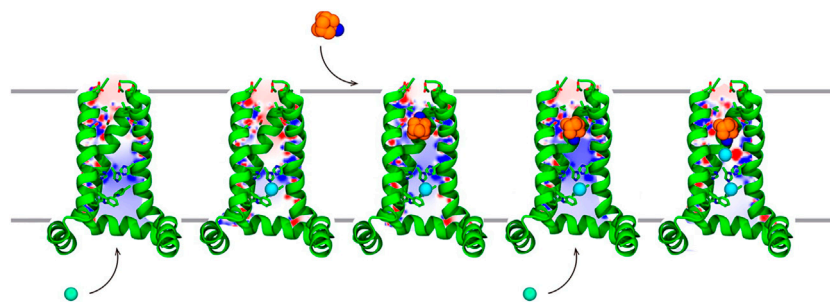


FIGURE 8 | Representation of the stepwise mechanism for Amt (carbon/nitrogen atoms shown as orange/blue-colored spheres.) binding to the M2 proton channel. (i) Amt is trapped by electrostatic interactions with Asp24. (ii) Thermal fluctuations of the helices facilitate crossing through the Val27 filter, and Amt fills the channel lumen in the *up* binding mode (iii) Finally, rotation of Amt leads to the *down* state, which is further stabilized by chloride anions. Chloride anions are shown as green spheres. For the sake of clarity, only three helices of the tetrameric channel are shown as green cartoon embedded in the lipid membrane. Reprinted with permission from (Lladrés et al., 2016) (Copyright 2016 American Chemical Society).

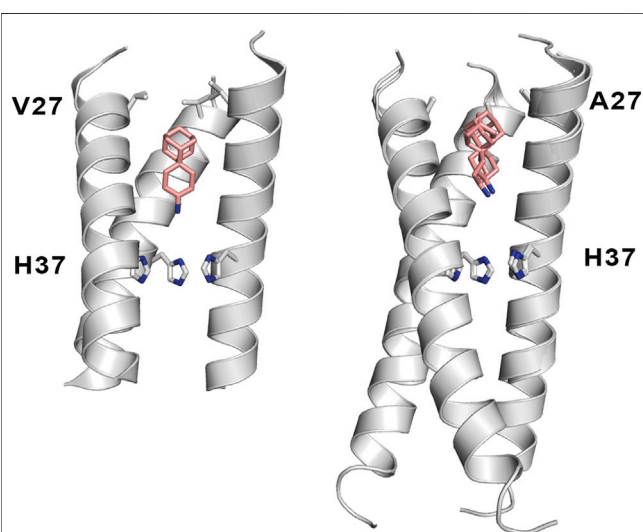


FIGURE 9 | Representation of the binding mode of the spiroadamantane **1** bound to (left) the wild type M2 proton channel (construct 22–46; PDB ID 6BMZ) and (right) the V27A mutant (construct 21–61; PDB ID 6NV1 and 6OUG). The ligand is shown as sticks with C-atoms in pink, and the TM helical region of the M2 proton channel as cartoon (residues Val27, Ala27 and His37 are shown as sticks). For the sake of clarity one of the helices is not shown.

A combination of computational techniques, biophysical studies, functional assays and classical medicinal chemistry approaches has been used also to design potent inhibitors of V27A. This mutation imposes a reduction in the steric constraint found in the wild type channel, suggesting the compounds with a size-expanded hydrophobic cage would be better suited to fit the larger volume of the pocket in the V27A channel (Wang et al., 2011). An example is the spiroadamantane **4**, which has an IC_{50} value of $18.7 \mu M$ against the wild type channel and of $0.3 \mu M$ against the V27A species. MD simulations showed that the ammonium group occupies the lower aqueous site forming solvent-mediated hydrogen bonds with the His37 residues in both wild type and V27A, but in this latter case the compound

was slight shifted toward the N-terminus due to the extra space afforded by Ala27.

Other efforts to develop size-expanded analogs have led to the pyrrolidine derivative **5** reported by Vázquez and coworkers (Figure 10) (Duque et al., 2011; Rey-Carrizo et al., 2014). This compound inhibits the wild type M2 channel with an IC_{50} of $18 \mu M$, while being *ca.* 26-fold more potent against the V27A mutant. MD simulations revealed an orientation consistent with the *down* state of Amt, with the amine nitrogen pointing toward the His37 tetrad with an average tilt angle (i.e., the deviation of the amine nitrogen from the pore axis) of 16° . Nevertheless, in the V27A complex **5** adopted the *down* orientation, but was also found in a *up*-like arrangement, presumably facilitated not only by the larger volume in the pore, but also by the widening of the helices at the location of Ala27, as the cross-diagonal distance between Ca atoms at position 27 was enlarged by 1.1 \AA compared to the wild type channel. The effect of including other polycyclic scaffolds as the hydrophobic cage have led to analogs **6** and **7** (Figure 10), which exhibit a micromolar potency against the wild type channel ($IC_{50} \sim 2 \mu M$), but a lower inhibition in the V27A mutant ($IC_{50} \sim 17.2$ and $184.6 \mu M$ for **7** and **6**, respectively) (Rey-Carrizo et al., 2015), suggesting a limiting effect in the size of the hydrophobic cage even for the V27A channel. At this point, MD simulations suggested that even the center-of-mass of **6** and **7** was located between the planes formed by S31 and A27 tetrads, the protonated amine was pointing to the N-terminus in five out of six MD simulations.

The resistance of the S31N channel, which is the most prevalent in currently circulating influenza viruses, to inhibition by Amt is reflected in the more variable motion and orientation of the ligand in the mutated channel. Thus, whereas Amt occupies a stable position in the wild type channel, it showed larger positional fluctuations in the pore of the mutated channel. This trait is reflected in a decreased energetic stability of the ligand in the proximity to the Asn31 side chains, as reflected in potential of mean force calculations. Finally, this destabilization was accompanied by an increase in the density of water molecules around and above Amt in the S31N channel compared to the wild type species, enabling water molecules to fill laterally the available

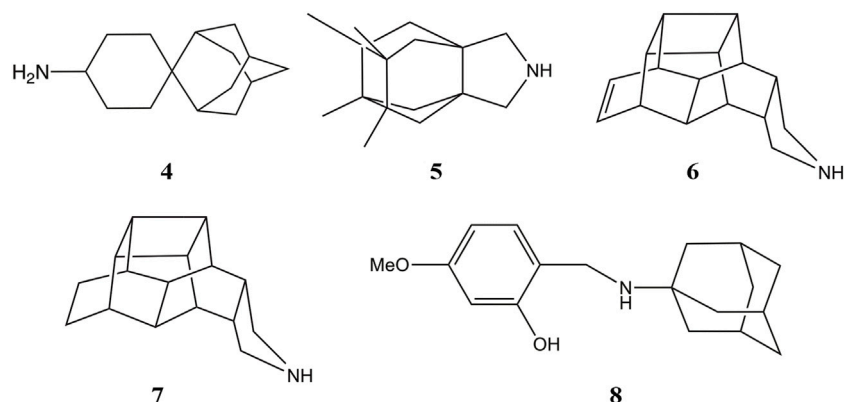


FIGURE 10 | Representation of selected size-expanded analogs of Amt.

space in the channel pore (Gleed and Busath, 2015). Furthermore, studies conducted for the binding of Rmt to the wild type M2 channel and the S31N variant have related the resistance with the higher dissociation rate constant determined for the mutated channel (Drakopoulos et al., 2018). In turn, this effect was attributed to the reduction in van der Waals interactions due to the shift of the ligand toward the C-terminus due to due to enhanced repulsive forces of the Asn side chains with the adamantyl ring in the mutated channel, and the concomitant weakening of the stabilizing contacts with Val27.

While these features reveal the challenges for developing inhibitors against the M2 S31N variant, significant progresses have been made in the last years. An example is compound **2** ((3S,5S,7S)-N-([5-(thiophen-2-yl)-1,2-oxazol-3-yl]methyl} tricyclo [3.3.1.1~3,7~]decan-1-aminium), also denoted M2WJ332, **Table 4**). This compound inhibits the proton conduction in electrophysiological assays of the S31N channel with an IC_{50} of 16 μ M, being however much less effective against the wild type ion channel (Rey-Carrizo et al., 2014). Remarkably, the NMR structure reveals that the compound binds the S31N channel in a different orientation compared to Amt and Rmt (**Figure 10**), since the adamantyl ring is located facing the His37 tetrad, whereas the thienyl group is located at the level of the Val27 tetrad. This arrangement is facilitated by the slight expansion (~ 1.0 Å) observed at the N-terminus of the TM helices relative to the wild type M2 channel. As noted in the analysis of MD simulations performed for the complex with **2**, this binding mode is reinforced by hydrogen-bonds formed by the protonated amine and the isoxazole ring with three Asn31 residues (Wang et al., 2013).

Starting from compound **2**, a successful rational design led to compound **3** ((3s,5s,7s)-N-[(5-bromothiophen-2-yl)methyl] tricyclo [3.3.1.1~3,7~]decan-1-aminium; **Table 4**) (Drakopoulos et al., 2018), which exhibits a similar potency in inhibiting both the wild type and the S31N channel (around 77% inhibition in two-electrode voltage clamp assays, and EC_{50} values of 4.6 and 1.8 μ M, respectively). The chemical scaffold of compound **3** combines an adamantane moiety with a bromothiophene unit. However, the most remarkable

structural feature is that **3** adopts completely flipped arrangements in the wild type and mutated channels (**Figure 11A**). Thus, the bromothiophene unit of the ligand faces the His37 tetrad in the wild type channel, but it is pointing toward the N-terminus in the S31N variant. MD simulations confirmed the structural stability of the flipped orientations in the wild type and mutated channels, enabling an interpretation of the structure-activity relationships (Wu et al., 2014). Inspection of the NMR structures (2MUW and 2MUV) does not support the involvement of halogen bonding, as this noncovalent interaction requires specific geometric features between the halogen atom and an electron-rich atom that are not fulfilled in these structures (see Kolár and Hobza, 2016 for details of halogen bonding). Furthermore, MD simulations revealed the formation of weak interactions between the bromine atom and water molecules, supplemented with transient, nonspecific contacts with the imidazole ring of His37 and the carbonyl group of Gly34 in the wild type channel, and with the Val27 side chains in the S31N channel (Wu et al., 2014).

It is also interesting to highlight the synthesis of aminoadamantane- CH_2 -aryl derivatives (**8** in **Figure 10**) designed as sensitive probes for blockage of the wild type and S31N ion channels (Tzitzoglaki et al., 2020). These compounds retain the aminoadamantane unit present in **2**, but the isoxazole ring has been replaced by a substituted phenyl ring. MD simulations have shown that compound **8** exhibits a stable binding in the S31N mutated channel. The binding mode locates the adamantyl group between Val27 and Gly34, and the phenyl unit fills the space between the side chains of Val27 residues. The results obtained from electrophysiological assays in oocytes evidence that blockage of the proton conduction in the wild type channel is relatively insensitive to chemical changes in the scaffold of **8**, such as the insertion of a methylene between the adamantane and amino units or the replacement of adamantane by diamantane or triamantane. However, these changes have a drastic effect on the current blockage of the S31N channel, leading to lower association and higher dissociation rate constants relative to the parent

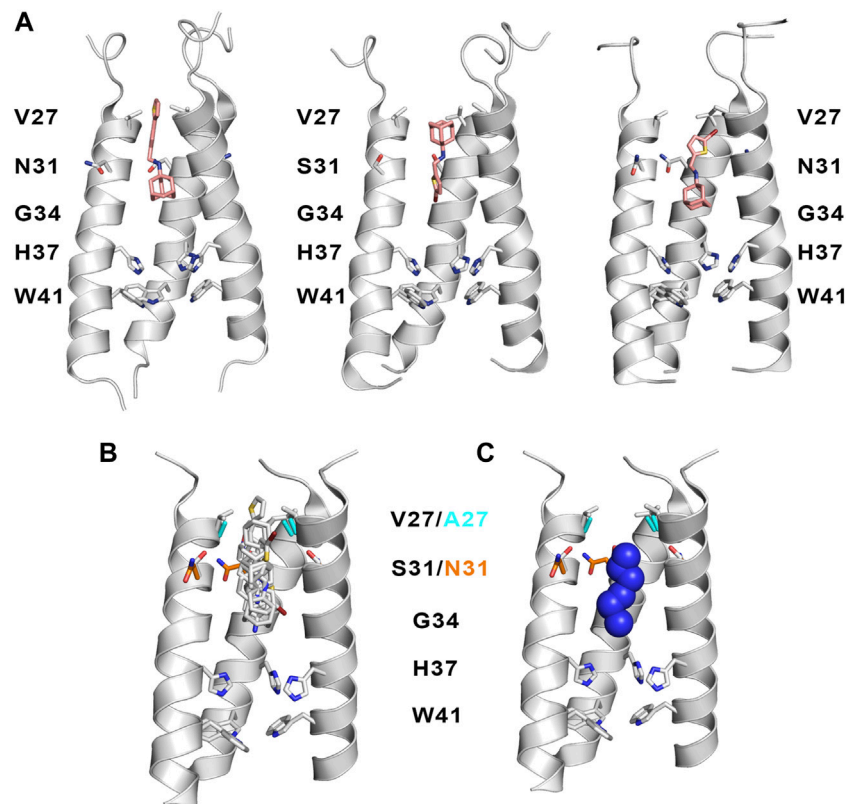


FIGURE 11 | (A) Representation of the binding mode of (left) compound **2** bound to the S31N channel (construct 19–49; PDB ID 2LYO), and compound **3** bound to (middle) the wild type M2 proton channel (construct 19–49; PDB ID 2MUW) and (right) the S31N mutant (construct 19–49; PDB ID 2MUV). The ligand is shown as sticks with C-atoms in pink, and the TM helical region of the M2 proton channel as cartoon (residues Val27, Ala27 and His37 are shown as sticks). For the sake of clarity one of the helices is not shown. **(B)** Superposition of selected inhibitors of wild type M2 ion channel and its V27A and S31N variants (taken from PDB ID 2KQT, 6US8, 6BMZ, 6NV1, 2LYO, 2MUW, and 2MUV). **(C)** Representation of the location of the protonated amine nitrogen atom along the channel axis taken from the previous subset of structures. For the sake of simplicity, only three helices of the tetrameric bundle are shown using the backbone skeleton of PDB ID 2KQT as cartoon is shown in plots **(B,C)**.

compound **8**. These results point out the larger sensitivity of the S31N ion channel to the chemical features of inhibitors upon binding to the pore.

Superposition of the compounds shown in **Tables 3, 4** is useful to exemplify the ability of the inhibitors to exploit different sites and binding modes along the interior of the pore in order to prevent proton transport in the wild type M2 channel and the V27A and S31N mutated species. (**Figures 11B,C**). This feature has been highlighted in previous studies that combined the structural analysis of bound channels with metadynamics calculations (Wang et al., 2013; Gianti et al., 2015), which pointed out the existence of distinct locations that can be occupied by the protonated amine along the axis of the channel. These studies also remarked the role played by water molecules inside the pore, as they contribute to stabilize the inhibitor by facilitating hydrogen-bond bridges with carbonyl groups of the transmembrane helices as well as with the His37 tetrad. From a practical perspective, the presence of multiple interaction sites for the protonated amine and the structure of water clusters that stabilize the inhibitor can be useful hallmarks for guiding the design of new drugs. In this regard, recent studies have

indicated that the ammonium group of these inhibitors can act as a hydronium mimic upon binding to the channel pore, suggesting that the adamantane-like compounds function as mechanism-based inhibitors as long as they exploit structural features of the channel implicated in proton transport (Watkins et al., 2020).

As a final remark, it is worth noting a very recent study by Kolokouris and coworkers where a systematic analysis of setup conditions and methodological details, covering from docking calculations to MD simulations, is presented for the M2 channel (Kolokouris et al., 2021). This study examines distinctive traits, such as the usage of M2 (22–46) and M2 (22–62) constructs, lipid content in the bilayer (1,2-dimyristoyl-sn-glycero-3-phosphocholine, 1-palmitoyl-2-oleoyl-sn-glycero-3-phosphocholine, and 1-palmitoyl-2-oleoyl-sn-glycero-3-phosphoethanol-amine), and the effect of cholesterol, paying particular attention to the location of channel blockers and water structure, the presence of chloride anions, structural properties of the helical bundle, and the binding site of cholesterol. While this study deserves practical interest for the choice of parameters in simulations of the M2 proton channel (and related viroporins), we limit ourselves to highlight three

findings. First, the results obtained for M2 complexes with Amt at pH 8 revealed that chloride anions approached Arg45 and occupied a position located between Trp41 and Arg45 (at a distance close to 15.5–17.5 Å from the Amt nitrogen atom) presence of chloride anions stabilized in the interior of the pore. The anions approached in the C-terminus. The anions approached Arg45. Second, the simulations with CHARMM36 preserved the structure of the amphipathic helices, providing a correct description for the wedge shape geometry that might be required to modulate the saddle-shape curvature of the membrane for the release of virions (Wang and Hong, 2015b; Martyna et al., 2017). Finally, the ability of cholesterol to interact with the tetrameric channel, forming van der Waals interactions with Ile39, Leu40, Leu43, Leu46, Phe47, Ile51 and Phe54, and a hydrogen bond with Ser50, which is in agreement with previous experimental evidence (Ekanayake et al., 2016; Elkins et al., 2017; Elkins et al., 2018), paving the way to future studies about the role of cholesterol in mediating the M2 protein function.

CONCLUSION

Resistance to current pharmacological treatments is a severe health challenge, as illustrated by the emergence of viral strains resistant to drugs interfering with the M2 proton channel, such as Amt and Rmt, but also to antiviral agents targeting neuraminidase, such as oseltamivir, as noticed in a resistant strain associated to the His275Tyr mutation in this protein (Meijer et al., 2009; Ginex and Luque, 2021). Currently circulating seasonal H1N1 and H3N2 strains are now resistant to adamantanes, and oseltamivir is no longer effective against the pandemic H1N1 subtypes (Hussain et al., 2017).

Finding new active antiviral compounds is an urgent need, which may be explored resorting to the application of a combinatorial therapy that should potentiate the effect of two or three drugs endowed with distinct mechanisms of action, hopefully being less susceptible to inactivating mutations (Dunning et al., 2014). A long-term strategy is the identification and characterization of the molecular mechanisms associated to the activity of proteins relevant for the life cycle of the virus, as this knowledge may disclose novel strategies for the design of antiviral compounds.

This approach is illustrated by the research efforts invested in the M2 proton channel. In spite of the apparent simplicity posed by the membrane-embedded four-helix bundle, the flow of protons reflects a complex synergy between different molecular events, involving the acidity of the His37 residues,

the structural coupling between His37 and the gating Trp41 residue, the structure of the hydrating water molecules in the pore, the pH-dependent conformational arrangement of the TM helices, the electrostatic funnel created by acidic residues in the N-terminus of the channel, and the influence of the amphiphilic helix and cytoplasmic tail on the flexibility of the TM domain, in addition to the potential influence exerted by other factors such as the nature of the lipid environment in the viral capsid.

Although a full understanding of the interplay between these factors, which encompass a diverse range of spatial and time processes, has not yet been achieved, the progress consolidated in the last decades through the combined use of structural, biophysical, physiological and computational techniques is impressive, and the successful development of compound 3 is encouraging. This scientific background defines the framework to address novel questions about the mechanisms of drug resistance and the guidance to novel antiviral and treatment approaches, such as the potential dependence between drug resistance and the nature of the viral strain or the infected cell type, which have been the subject of recent studies (Musharrafieh et al., 2019; Musharrafieh et al., 2020). Hopefully, the outcome will be valuable to enrich our current anti-influenza therapeutic arsenal in the form of effective antivirals less susceptible to drug resistance.

AUTHOR CONTRIBUTIONS

All authors contributed to conception, design and writing of the manuscript. EA and BS wrote the draft of the manuscript and prepared Figures and Tables. CE, MM and FJL revised and completed the draft and prepared the final version of the manuscript.

FUNDING

We thank the Spanish Ministerio de Ciencia e Innovación (PID2020-117646RB-I00 MCIN/AEI/10.13039/501100011033, and Maria de Maetzu MDM-2017-0767 AEI/FEDER) for financial support and the Barcelona Supercomputing Center (BCV-2019-1-0009) and the Consorci de Serveis Universitaris de Catalunya (CSUC; Molecular Recognition project) for computational resources. E.A. thanks AGAUR (Generalitat of Catalunya; 2018FI-B1-00001) for a fellowship.

REFERENCES

- Acharya, R., Carnevale, V., Fiorin, G., Levine, B. G., Polishchuk, A. L., Balannik, V., et al. (2010). Structure and Mechanism of Proton Transport through the Transmembrane Tetrameric M2 Protein Bundle of the Influenza A Virus. *Proc. Natl. Acad. Sci.* 107, 15075–15080. doi:10.1073/pnas.1007071107
- Agmon, N. (1995). The Grotthuss Mechanism. *Chem. Phys. Lett.* 244, 456–462. doi:10.1016/0009-2614(95)00905-j
- Andreas, L. B., Eddy, M. T., Pielak, R. M., Chou, J., and Griffin, R. G. (2010). Magic Angle Spinning NMR Investigation of Influenza A M218–60: Support for an Allosteric Mechanism of Inhibition. *J. Am. Chem. Soc.* 132, 10958–10960. doi:10.1021/ja101537p
- Andreas, L. B., Eddy, M. T., Chou, J. J., and Griffin, R. G. (2012). Magic-angle-spinning NMR of the Drug Resistant S31N M2 Proton Transporter from Influenza A. *J. Am. Chem. Soc.* 134, 7215–7218. doi:10.1021/ja3003606

- Berman, H. M., Westbrook, J., Feng, Z., Gilliland, G., Bhat, T. N., Weissig, H., et al. (2000). The Protein Data Bank. *Protein Data Bank Nucleic Acids Res.* 28, 235–242. doi:10.1093/nar/28.1.235
- Burley, S. K., Bhikadiya, C., Bi, C., Bittrich, S., Chen, L., Crichlow, G., et al. (2021). RCSB Protein Data Bank: Powerful New Tools for Exploring 3D Structures of Biological Macromolecules for Basic and Applied Research and Education in Fundamental Biology, Biomedicine, Biotechnology, Bioengineering and Energy Sciences. *Nuc. Acids Res.* 49, 437–451. doi:10.1093/nar/gkaa1038
- Cady, S. D., Mishanina, T. V., and Hong, M. (2009). Structure of Amantadine-Bound M2 Transmembrane Peptide of Influenza A in Lipid Bilayers from Magic-Angle-Spinning Solid-State NMR: The Role of Ser31 in Amantadine Binding. *J. Mol. Biol.* 385, 1127–1141. doi:10.1016/j.jmb.2008.11.022
- Cady, S. D., Schmidt-Rohr, K., Wang, J., Soto, C. S., DeGrado, W. F., and Hong, M. (2010). Structure of the Amantadine Binding Site of Influenza M2 Proton Channels in Lipid Bilayers. *Nature* 463, 689–692. doi:10.1038/nature08722
- Cady, S. D., Wang, J., Wu, Y., DeGrado, W. F., and Hong, M. (2011). Specific Binding of Adamantane Drugs and Direction of Their Polar Amines in the Pore of the Influenza M2 Transmembrane Domain in Lipid Bilayers and Dodecylphosphocholine Micelles Determined by NMR Spectroscopy. *J. Am. Chem. Soc.* 133, 4274–4284. doi:10.1021/ja102581n
- Carnevale, V., Fiorin, G., Levine, B. G., DeGrado, W. F., and Klein, M. L. (2010). Multiple Proton Confinement in the M2 Channel from the Influenza A Virus. *J. Phys. Chem. C* 114, 20856–20863. doi:10.1021/jp107431g
- Chen, W., Huang, Y., and Shen, J. (2016). Conformational Activation of a Transmembrane Proton Channel from Constant pH Molecular Dynamics. *J. Phys. Chem. Lett.* 7, 3961–3966. doi:10.1021/acs.jpclett.6b01853
- Cheung, T. K. W., and Poon, L. L. M. (2007). Biology of Influenza A Virus. *Ann. N. Y. Acad. Sci.* 1102, 1–25. doi:10.1196/annals.1408.001
- Chizhmakov, I. V., Geraghty, F. M., Ogden, D. C., Hayhurst, A., Antoniou, M., and Hay, A. J. (1996). Selective Proton Permeability and pH Regulation of the Influenza Virus M2 Channel Expressed in Mouse Erythroleukemia Cells. *J. Physiol.* 494, 329–336. doi:10.1113/jphysiol.1996.sp021495
- Chizhmakov, I. V., Ogden, D. C., Geraghty, F. M., Hayhurst, A., Skinner, A., Betakova, T., et al. (2003). Differences in Conductance of M2 Proton Channels of Two Influenza Viruses at Low and High pH. *J. Physiol.* 546, 427–438. doi:10.1113/jphysiol.2002.028910
- Colvin, M. T., Andreas, L. B., Chou, J. J., and Griffin, R. G. (2014). Proton Association Constants of His 37 in the Influenza-A M218–60 Dimer-Of-Dimers. *Biochemistry* 53, 5987–5994. doi:10.1021/bi5005393
- Cox, N. J., and Subbarao, K. (2000). Global Epidemiology of Influenza: Past and Present. *Annu. Rev. Med.* 51, 407–421. doi:10.1146/annurev.med.51.1.407
- De Vlucht, C., Sikora, D., and Pelchat, M. (2018). Insight into Influenza: A Virus Cap-Snatching. *Viruses* 10, 641. doi:10.3390/v10110641
- Deyde, V. M., Xu, X., Bright, R. A., Shaw, M., Smith, C. B., Zhang, Y., et al. (2007). Surveillance of Resistance to Adamantanes Among Influenza A(H₃N₂) and A(H₁N₁) Viruses Isolated Worldwide. *J. Infect. Dis.* 196, 249–257. doi:10.1086/518936
- Dillon, P. F., Root-Bernstein, R. S., and Lieder, C. M. (2006). Molecular Shielding of Electric Field Complex Dissociation. *Biophysical J.* 90, 1432–1438. doi:10.1529/biophysj.105.071969
- Dong, H., Fiorin, G., Degrado, W. F., and Klein, M. L. (2013). Exploring Histidine Conformations in the M2 Channel Lumen of the Influenza A Virus at Neutral pH via Molecular Simulations. *J. Phys. Chem. Lett.* 4, 3067–3071. doi:10.1021/jz401672h
- Dong, H., Fiorin, G., Degrado, W. F., and Klein, M. L. (2014). Proton Release from the Histidine-Tetrad in the M2 Channel of the Influenza A Virus. *J. Phys. Chem. B* 118, 12644–12651. doi:10.1021/jp5102225
- Dou, D., Revol, R., Östbye, H., Wang, H., and Daniels, R. (2018). Influenza A Virus Cell Entry, Replication, Virion Assembly and Movement. *Front. Immunol.* 9, 1581. doi:10.3389/fimmu.2018.01581
- Drakopoulos, A., Tzitzoglaki, C., McGuire, K., Hoffmann, A., Konstantinidi, A., Kolokouris, D., et al. (2018). Unraveling the Binding, Proton Blockage, and Inhibition of Influenza M2 WT and S31N by Rimantadine Variants. *ACS Med. Chem. Lett.* 9, 198–203. doi:10.1021/acsmchemlett.7b00458
- Du Pont Patent (1961). *Pharmaceutical Compositions and Methods Utilizing 1-aminoadamantane and its Derivatives*. US3310469A. United States Patent and Trademark Office. Available at: <https://www.uspto.gov>. (Accessed September 14, 2021).
- Duff, K. C., Gilchrist, P. J., Saxena, A. M., and Bradshaw, J. P. (1994). Neutron Diffraction Reveals the Site of Amantadine Blockade in the Influenza A M2 Ion Channel. *Virology* 202, 287–293. doi:10.1006/viro.1994.1345
- Dunning, J., Baillie, J. K., Cao, B., and Hayden, F. G. (2014). International Severe Acute Respiratory and Emerging Infection Consortium (ISARIC) Antiviral Combinations for Severe Influenza. *Lancet Infect. Dis.* 14, 1259–1270. doi:10.1016/s1473-3099(14)70821-7
- Duque, M. D., Ma, C., Torres, E., Wang, J., Naesens, L., Juárez-Jiménez, J., et al. (2011). Exploring the Size Limit of Templates for Inhibitors of the M2 Ion Channel of Influenza A Virus. *J. Med. Chem.* 54, 2646–2657. doi:10.1021/jm101334y
- Ekanayake, E. V., Fu, R., and Cross, T. A. (2016). Structural Influences: Cholesterol, Drug, and Proton Binding to Full-Length Influenza A M2 Protein. *Biophysical J.* 110, 1391–1399. doi:10.1016/j.bpj.2015.11.3529
- Elkins, M. R., Williams, J. K., Gelenter, M. D., Dai, P., Kwon, B., Sergeyev, I. V., et al. (2017). Cholesterol-binding Site of the Influenza M2 Protein in Lipid Bilayers from Solid-State NMR. *Proc. Natl. Acad. Sci. USA* 114, 12946–12951. doi:10.1073/pnas.1715127114
- Elkins, M. R., Sergeyev, I. V., and Hong, M. (2018). Determining Cholesterol Binding to Membrane Proteins by Cholesterol 13C Labeling in Yeast and Dynamic Nuclear Polarization NMR. *J. Am. Chem. Soc.* 140, 15437–15449. doi:10.1021/jacs.8b09658
- Fried, S. D., and Boxer, S. G. (2017). Electric Fields and Enzyme Catalysis. *Annu. Rev. Biochem.* 86, 387–415. doi:10.1146/annurev-biochem-061516-044432
- Fu, R., Miao, Y., Qin, H., and Cross, T. A. (2020). Observation of the Imidazole-Imidazolium Hydrogen Bonds Responsible for Selective Proton Conductance in the Influenza A M2 Channel. *J. Am. Chem. Soc.* 142, 2115–2119. doi:10.1021/jacs.9b09985
- Gianti, E., Carnevale, V., DeGrado, W. F., Klein, M. L., and Fiorin, G. (2015). Hydrogen-Bonded Water Molecules in the M2 Channel of the Influenza A Virus Guide the Binding Preferences of Ammonium-Based Inhibitors. *J. Phys. Chem. B* 119, 1173–1183. doi:10.1021/jp506807y
- Ginex, T., and Luque, F. J. (2021). Searching for Effective Antiviral Small Molecules against Influenza A Virus: A Patent Review. *Expert Opin. Ther. Patents* 31, 53–66. doi:10.1080/13543776.2020.1831471
- Gkeka, P., Eleftheratos, S., Kolocouris, A., and Cournia, Z. (2013). Free Energy Calculations Reveal the Origin of Binding Preference for Aminoadamantane Blockers of Influenza A/M2TM Pore. *J. Chem. Theor. Comput.* 9, 1272–1281. doi:10.1021/ct300899n
- Gleed, M. L., and Busath, D. D. (2015). Why Bound Amantadine Fails to Inhibit Proton Conductance According to Simulations of the Drug-Resistant Influenza A M2 (S31N). *J. Phys. Chem. B* 119, 1225–1231. doi:10.1021/jp508545d
- Grambas, S., Bennett, M. S., and Hay, A. J. (1992). Influence of Amantadine Resistance Mutations on the pH Regulatory Function of the M2 Protein of Influenza A Viruses. *Virology* 191, 541–549. doi:10.1016/0042-6822(92)90229-i
- Gu, R.-X., Liu, L. A., Wei, D.-Q., Du, J.-G., Liu, L., and Liu, H. (2011). Free Energy Calculations on the Two Drug Binding Sites in the M2 Proton Channel. *J. Am. Chem. Soc.* 133, 10817–10825. doi:10.1021/ja1114198
- Han, J., Perez, J., Schäfer, A., Cheng, H., Peet, N., Rong, L., et al. (2018). Influenza Virus: Small Molecule Therapeutics and Mechanisms of Antiviral Resistance. *Curr. Med. Chem.* 25, 5115–5127. doi:10.2174/0929867324666170920165926
- Hayward, A. C., Fragsz, E. B., Bermingham, A., Wang, L., Copas, A., Edmunds, W. J., et al. (2014). Comparative Community burden and Severity of Seasonal and Pandemic Influenza: Results of the Flu Watch Cohort Study. *Lancet Respir. Med.* 2, 445–454. doi:10.1016/s2213-2600(14)70034-7
- Holsinger, L. J., Nichani, D., Pinto, L. H., and Lamb, R. A. (1994). Influenza A Virus M2 Ion Channel Protein: A Structure-Function Analysis. *J. Virol.* 68, 1551–1563. doi:10.1128/jvi.68.3.1551-1563.1994
- Homeyer, N., Ioannidis, H., Kolarov, F., Gauglitz, G., Zikos, C., Kolocouris, A., et al. (2016). Interpreting Thermodynamic Profiles of Aminoadamantane Compounds Inhibiting the M2 Proton Channel of Influenza A by Free Energy Calculations. *J. Chem. Inf. Model.* 56, 110–126. doi:10.1021/acs.jcim.5b00467
- Honda, A., Mizumoto, K., and Ishihama, A. (2002). Minimum Molecular Architectures for Transcription and Replication of the Influenza Virus. *Proc. Natl. Acad. Sci.* 99, 13166–13171. doi:10.1073/pnas.152456799

- Hoyden, F. G. (2006). Antiviral Resistance in Influenza Viruses - Implications for Management and Pandemic Response. *N. Eng. J. Med.* 354, 785–788. doi:10.1056/NEJMp068030
- Hu, J., Fu, R., Nishimura, K., Zhang, L., Zhou, H.-X., Busath, D. D., et al. (2006). Histidines, Heart of the Hydrogen Ion Channel from Influenza A Virus: Toward an Understanding of Conductance and Proton Selectivity. *Proc. Natl. Acad. Sci.* 103, 6865–6870. doi:10.1073/pnas.0601944103
- Hu, J., Fu, R., and Cross, T. A. (2007). The Chemical and Dynamical Influence of the Anti-viral Drug Amantadine on the M2 Proton Channel Transmembrane Domain. *Biophys. J.* 93, 276–283. doi:10.1529/biophysj.106.102103
- Hu, F., Luo, W., and Hong, M. (2010). Mechanisms of Proton Conduction and Gating in Influenza M2 Proton Channels from Solid-State NMR. *Science* 330, 505–508. doi:10.1126/science.1191714
- Hu, F., Schmidt-Rohr, K., and Hong, M. (2012). NMR Detection of pH-Dependent Histidine-Water Proton Exchange Reveals the Conduction Mechanism of a Transmembrane Proton Channel. *J. Am. Chem. Soc.* 134, 3703–3713. doi:10.1021/ja2081185
- Hussain, M., Galvin, H., Haw, T. Y., Nutsford, A., and Husain, M. (2017). Drug Resistance in Influenza A Virus: The Epidemiology and Management. *Idr* 10, 121–134. doi:10.2147/idr.s105473
- Ioannidis, H., Drakopoulos, A., Tzitzoglaki, C., Homeyer, N., Kolarov, F., Gkeka, P., et al. (2016). Alchemical Free Energy Calculations and Isothermal Titration Calorimetry Measurements of Aminoamantanes Bound to the Closed State of Influenza A/M2TM. *J. Chem. Inf. Model.* 56, 862–876. doi:10.1021/acs.jcim.6b00079
- Iuliano, A. D., Roguski, K. M., Chang, H. H., Muscatello, D. J., Palekar, R., Tempia, S., et al. (2018). Estimates of Global Seasonal Influenza-Associated Respiratory Mortality: A Modelling Study. *Lancet* 391, 1285–1300. doi:10.1016/S0140-6736(17)33293-2
- Jeong, B.-S., and Dyer, R. B. (2017). Proton Transport Mechanism of M2 Proton Channel Studied by Laser-Induced pH Jump. *J. Am. Chem. Soc.* 139, 6621–6628. doi:10.1021/jacs.7b00617
- Julkunen, T., Sareneva, T., Pirhonen, J., Ronni, T., Melén, K., and Matikainen, S. (2001). Molecular Pathogenesis of Influenza A Virus Infection and Virus-Induced Regulation of Cytokine Gene Expression. *Cytokine Growth Factor. Rev.* 12, 171–180. doi:10.1016/s1359-6101(00)00026-5
- Jung, H. E., and Lee, H. K. (2020). Host Protective Immune Responses against Influenza A Virus Infection. *Viruses* 12, 504. doi:10.3390/v12050504
- Khurana, E., Peraro, M. D., DeVane, R., Vemparala, S., DeGrado, W. F., and Klein, M. L. (2009). Molecular Dynamics Calculations Suggest a Conduction Mechanism for the M2 Proton Channel from Influenza A Virus. *Proc. Natl. Acad. Sci.* 106, 1069–1074. doi:10.1073/pnas.0811720106
- Knight, J. L., and Brooks, C. L., 3rd. (2011). Multisite λ Dynamics for Simulated Structure-Activity Relationship Studies. *J. Chem. Theor. Comput.* 7, 2728–2739. doi:10.1021/ct200444f
- Kolár, M. H., and Hobza, P. (2016). Computer Modeling of Halogen Bonds and Other σ -hole Interactions. *Chem. Rev.* 116, 5155–5187. doi:10.1021/acs.chemrev.5b00560
- Kolocouris, D., Kalenderoglou, I. E., and Kolocouris, A. (2021). Inside and Out of the Pore: Comparing Interactions and Molecular Dynamics of Influenza A M2 Viroprotein Complexes in Standard Lipid Bilayers. *J. Chem. Inf. Model.* 61, 5550–5568. doi:10.1021/acs.jcim.1c00264
- Krammer, F., Smith, G. J. D., Fouchier, R. A. M., Peiris, M., Kedzierska, K., Doherty, P. C., et al. (2018). Influenza. *Nat. Rev. Dis. Primers* 4, 3. doi:10.1038/s41572-018-0002-y
- Kwon, B., and Hong, M. (2016). The Influenza M2 Ectodomain Regulates the Conformational Equilibria of the Transmembrane Proton Channel: Insights from Solid-State Nuclear Magnetic Resonance. *Biochemistry* 55, 5387–5397. doi:10.1021/acs.biochem.6b00727
- Leiding, T., Wang, J., Martinsson, J., DeGrado, W. F., and Arsköld, S. P. (2010). Proton and Cation Transport Activity of the M2 Proton Channel from Influenza A Virus. *Proc. Natl. Acad. Sci.* 107, 15409–15414. doi:10.1073/pnas.1009997107
- Li, C., Yi, M., Hu, J., Zhou, H.-X., and Cross, T. A. (2008). Solid-state NMR and MD Simulations of the Antiviral Drug Amantadine Solubilized in DMPC Bilayers. *Biophysical J.* 94, 1295–1302. doi:10.1529/biophysj.107.112482
- Liang, R., Swanson, J. M. J., Madsen, J. J., Hong, M., DeGrado, W. F., and Voth, G. A. (2016). Acid Activation Mechanism of the Influenza A M2 Proton Channel. *Proc. Natl. Acad. Sci. U. S. A.* 113, E6955–E6964. doi:10.1073/pnas.1615471113
- Liao, S. Y., Yang, Y., Tietze, D., and Hong, M. (2015). The Influenza M2 Cytoplasmic Tail Changes the Proton-Exchange Equilibria and the Backbone Conformation of the Transmembrane Histidine Residue to Facilitate Proton Conduction. *J. Am. Chem. Soc.* 137, 6067–6077. doi:10.1021/jacs.5b02510
- Lin, T.-I., and Schroeder, C. (2001). Definitive Assignment of Proton Selectivity and Attoampere Unitary Current to the M2 Ion Channel Protein of Influenza A Virus. *J. Virol.* 75, 3647–3656. doi:10.1128/jvi.75.8.3647-3656.2001
- Llabrés, S., Juárez-Jiménez, J., Masetti, M., Leiva, R., Vázquez, S., Gazzarrini, S., et al. (2016). Mechanism of the Pseudoirreversible Binding of Amantadine to the M2 Proton Channel. *J. Am. Chem. Soc.* 138, 15345–15358. doi:10.1021/jacs.6b07096
- Loregian, A., Mercorelli, B., Nannetti, G., Compagnin, C., and Palù, G. (2014). Antiviral Strategies against Influenza Virus: Towards New Therapeutic Approaches. *Cel. Mol. Life Sci.* 71, 3659–3683. doi:10.1007/s00018-014-1615-2
- Ma, C., Polishchuk, A. L., Ohigashi, Y., Stouffer, A. L., Schön, A., Magavern, E., et al. (2009). Identification of the Functional Core of the Influenza A Virus A/M2 Proton-Selective Ion Channel. *Proc. Natl. Acad. Sci.* 106, 12283–12288. doi:10.1073/pnas.0905726106
- Ma, C., Fiorin, G., Carnevale, V., Wang, J., Lamb, R. A., Klein, M. L., et al. (2013). Asp44 Stabilizes the Trp41 Gate of the M2 Proton Channel of Influenza A Virus. *Structure* 21, 2033–2041. doi:10.1016/j.str.2013.08.029
- Manzoor, R., Igarashi, M., and Takada, A. (2017). Influenza A Virus M2 Protein: Roles from Ingress to Egress. *Int. J. Mol. Sci.* 18, 1–16. doi:10.3390/ijms18122649
- Martyna, A., Bahsoun, B., Badham, M. D., Srinivasan, S., Howard, M. J., and Rossman, J. S. (2017). Membrane Remodeling by the M2 Amphipathic helix Drives Influenza Virus Membrane Scission. *Sci. Rep.* 7, 44695. doi:10.1038/srep44695
- McCown, M. F., and Pekosz, A. (2006). Distinct Domains of the Influenza A Virus M2 Protein Cytoplasmic Tail Mediate Binding to the M1 Protein and Facilitate Infectious Virus Production. *J. Virol.* 80, 8178–8189. doi:10.1128/jvi.00627-06
- Meijer, A., Lackenby, A., Hungnes, O., Lina, B., van der WerfSchweiger, S. B., Schweiger, B., et al. (2009). Oseltamivir-resistant Influenza Virus A (H1N1), Europe, 2007–08 Season. *Emerg. Infect. Dis.* 15, 552–560. doi:10.3201/eid1504.181280
- Miao, Y., Fu, R., Zhou, H.-X., and Cross, T. A. (2015). Dynamic Short Hydrogen Bonds in Histidine Tetrad of Full-Length M2 Proton Channel Reveal Tetrameric Structural Heterogeneity and Functional Mechanism. *Structure* 23, 2300–2308. doi:10.1016/j.str.2015.09.011
- Mifsud, E. J., Hayden, F. G., and Hurt, A. C. (2019). Antivirals Targeting the Polymerase Complex of Influenza Viruses. *Antiviral Res.* 169, 104545. doi:10.1016/j.antiviral.2019.104545
- Moorthy, N. S., Poongavanam, V., and Pratheepa, V. (2014). Viral M2 Ion Channel Protein: A Promising Target for Anti-influenza Drug Discovery. *Mini Rev. Med. Chem.* 14, 819–830. doi:10.2174/138955751410141020150822
- Mould, J. A., Drury, J. E., Frings, S. M., Kaupp, U. B., Pekosz, A., Lamb, R. A., et al. (2000). Permeation and Activation of the M2 Ion Channel of Influenza A Virus. *J. Biol. Chem.* 275, 31038–31050. doi:10.1074/jbc.m003663200
- Mould, J. A., Li, H.-C., Dudlak, C. S., Lear, J. D., Pekosz, A., Lamb, R. A., et al. (2000). Mechanism for Proton Conduction of the M2 Ion Channel of Influenza A Virus. *J. Biol. Chem.* 275, 8592–8599. doi:10.1074/jbc.275.12.8592
- Movellan, K. T., Wegstroth, M., Overkamp, K., Leonov, A., Becker, S., and Andreas, L. B. (2020). Imidazole-imidazole Hydrogen Bonding in the pH-Sensing Histidine Side Chains of Influenza A M2. *J. Am. Chem. Soc.* 142, 2704–2708. doi:10.1021/jacs.9b10984
- Movellan, K. T., Dervişoğlu, R., Becker, S., and Andreas, L. B. (2021). Pore-Bound Water at the Key Residue Histidine 37 in Influenza A M2. *Angew. Chem. Int. Ed.* 60, 24075–24079. doi:10.1002/anie.202103955
- Musharrafieh, R., Lagarias, P. I., Ma, C., Tan, G. S., Kolocouris, A., and Wang, J. (2019). The L46P Mutant Confers a Novel Allosteric Mechanism of Resistance toward the Influenza A Virus M2 S31N Proton Channel Blockers. *Mol. Pharmacol.* 96, 148–157. doi:10.1124/mol.119.116640
- Musharrafieh, R., Lagarias, P., Ma, C., Hau, R., Romano, A., Lambrinidis, G., et al. (2020). Investigation of the Drug Resistance Mechanism of M2-S31N

- Channel Blockers through Biomolecular Simulations and Viral Passage Experiments. *ACS Pharmacol. Transl. Sci.* 3, 666–675. doi:10.1021/acspstci.0c00018
- Mustafa, M., Henderson, D. J., and Busath, D. D. (2009). Free-Energy Profiles for Ions in the Influenza M2-TMD Channel. *Proteins* 76, 794–807. doi:10.1002/prot.22376
- Okada, A., Miura, T., and Takeuchi, H. (2001). Protonation of Histidine and Histidine–Tryptophan Interaction in the Activation of the M2 Ion Channel from Influenza A Virus. *Biochemistry* 40, 6053–6060. doi:10.1021/bi0028441
- Pielak, R. M., and Chou, J. J. (2011). Influenza M2 Proton Channels. *Biochim. Biophys. Acta (Bba) - Biomembr.* 1808, 522–529. doi:10.1016/j.bbamem.2010.04.015
- Pinto, L. H., Holsinger, L. J., and Lamb, R. A. (1992). Influenza Virus M2 Protein Has Ion Channel Activity. *Cell* 69, 517–528. doi:10.1016/0092-8674(92)90452-i
- Pinto, L. H., Dieckmann, G. R., Gandhi, C. S., Papworth, C. G., Braman, J., Shaughnessy, M. A., et al. (1997). A Functionally Defined Model for the M2 Proton Channel of Influenza A Virus Suggests a Mechanism for its Ion Selectivity. *Proc. Natl. Acad. Sci.* 94, 11301–11306. doi:10.1073/pnas.94.21.11301
- Prichard, W. W. (1967). *Adamantanes and tricyclo[4.3.1.13.8] Undecanes*. US3352912A.
- Rey-Carrizo, M., Barniol-Xicota, M., Ma, C., Frigolé-Vivas, M., Torres, E., Naesens, L., et al. (2014). Easily Accessible Polycyclic Amines that Inhibit the Wild-type and Amantadine-Resistant Mutants of the M2 Channel of Influenza A Virus. *J. Med. Chem.* 57, 5738–5747. doi:10.1021/jm5005804
- Rey-Carrizo, M., Gazzarrini, S., Llabrés, S., Frigolé-Vivas, M., Juárez-Jiménez-Font-Bardia, J. M., Font-Bardia, M., et al. (2015). New Polycyclic Dual Inhibitors of the Wild Type and the V27A Mutant M2 Channel of the Influenza A Virus with Unexpected Binding Mode. *Eur. J. Med. Chem.* 96, 318–329. doi:10.1016/j.ejmech.2015.04.030
- Rosenberg, M. R., and Casarotto, M. G. (2010). Coexistence of Two Adamantane Binding Sites in the Influenza A M2 Ion Channel. *Proc. Natl. Acad. Sci.* 107, 13866–13871. doi:10.1073/pnas.1002051107
- Rossman, J. S., Jing, X., Leser, G. P., and Lamb, R. A. (2010). Influenza Virus M2 Protein Mediates ESCRT-independent Membrane Scission. *Cell* 142, 902–913. doi:10.1016/j.cell.2010.08.029
- Samson, M. S., and Kerr, I. D. (1993). Influenza Virus M2 Protein: A Molecular Modelling Study of the Ion Channel. *Protein Eng.* 6, 65–74.
- Sansom, M. S. P., Kerr, I. D., Smith, G. R., and Son, H. S. (1997). The Influenza A Virus M2 Channel: A Molecular Modeling and Simulation Study. *Virology* 233, 163–173. doi:10.1006/viro.1997.8578
- Saunders-Hastings, P., and Krewski, D. (2016). Reviewing the History of Pandemic Influenza: Understanding Patterns of Emergence and Transmission. *Pathogens* 5, 66. doi:10.3390/pathogens5040066
- Schnell, J. R., and Chou, J. J. (2008). Structure and Mechanism of the M2 Proton Channel of Influenza A Virus. *Nature* 451, 591–595. doi:10.1038/nature06531
- Sharma, M., Yi, M., Dong, H., Qin, H., Peterson, E., Busath, D. D., et al. (2010). Insight into the Mechanism of the Influenza A Proton Channel from a Structure in a Lipid Bilayer. *Science* 330, 509–512. doi:10.1126/science.1191750
- Shimbo, K., Brassard, D. L., Lamb, R. A., and Pinto, L. H. (1996). Ion Selectivity and Activation of the M2 Ion Channel of Influenza Virus. *Biophys. J.* 70, 1335–1346. doi:10.1016/S0006-3495(96)79690-X
- Sidorenko, Y., and Reichl, U. (2004). Structured Model of Influenza Virus Replication in MDCK Cells. *Biotechnol. Bioeng.* 88, 1–14. doi:10.1002/bit.20096
- Stouffer, A. L., Acharya, R., Salom, D., Levine, A. S., Di Costanzo, L., Soto, C. S., et al. (2008). Structural Basis for the Function and Inhibition of an Influenza Virus Proton Channel. *Nature* 451, 596–599. doi:10.1038/nature06528
- Tan, R. C., Truong, T. N., McCammon, J. A., and Sussman, J. L. (1993). Acetylcholinesterase: Electrostatic Steering Increases the Rate of Ligand Binding. *Biochemistry* 32, 401–403. doi:10.1021/bi00053a003
- Tang, Y., Zaitseva, F., Lamb, R. A., and Pinto, L. H. (2002). The Gate of the Influenza Virus M2 Proton Channel Is Formed by a Single Tryptophan Residue. *J. Biol. Chem.* 277, 39880–39886. doi:10.1074/jbc.m206582200
- Thomaston, J. L., and DeGrado, W. F. (2016). Crystal Structure of the Drug-Resistant S31N Influenza M2 Proton Channel. *Protein Sci.* 25, 1551–1554. doi:10.1002/pro.2937
- Thomaston, J. L., Alfonso-Prieto, M., Woldeyes, R. A., Fraser, J. S., Klein, M. L., Fiorin, G., et al. (2015). High-resolution Structures of the M2 Channel from Influenza A Virus Reveal Dynamic Pathways for Proton Stabilization and Transduction. *Proc. Natl. Acad. Sci. USA* 112, 14260–14265. doi:10.1073/pnas.1518493112
- Thomaston, J. L., Polizzi, N. F., Konstantinidi, A., Wang, J., Kolocouris, A., and DeGrado, W. F. (2018). Inhibitors of the M2 Proton Channel Engage and Disrupt Transmembrane Networks of Hydrogen-Bonded Waters. *J. Am. Chem. Soc.* 140, 15219–15226. doi:10.1021/jacs.8b06741
- Thomaston, J. L., Konstantinidi, A., Liu, L., Lambrinidis, G., Tan, J., Caffrey, M., et al. (2020). X-ray crystal Structures of the Influenza M2 Proton Channel Drug-Resistant V27A Mutant Bound to a spiro-adamantyl Amine Inhibitor Reveal the Mechanism of Adamantane Resistance. *Biochemistry* 59, 627–634. doi:10.1021/acs.biochem.9b00971
- Thomaston, J. L., Samways, M. L., Konstantinidi, A., Ma, C., Hu, Y., Bruce Macdonald, H. E., et al. (2021). Rimantadine Binds to and Inhibits the Influenza A M2 Proton Channel without Enantiomeric Specificity. *Biochemistry* 60, 2471–2482. doi:10.1021/acs.biochem.1c00437
- Torabifard, H., Panahi, A., and Brooks, C. L., III (2020). M2 Amphipathic Helices Facilitate pH-dependent Conformational Transition in Influenza A Virus. *Proc. Natl. Acad. Sci. USA* 117, 3583–3591. doi:10.1073/pnas.1913385117
- Tzitzoglaki, C., McGuire, K., Lagarias, P., Konstantinidi, A., Hoffmann, A., Fokina, N. A., et al. (2020). Chemical Probes for Blocking of Influenza A M2 Wild-type and S31N Channels. *ACS Chem. Biol.* 15, 2331–2337. doi:10.1021/acscchembio.0c00553
- Vaissier Welborn, V., and Head-Gordon, T. (2019). Computational Design of Synthetic Enzymes. *Chem. Rev.* 119, 6613–6630. doi:10.1021/acs.chemrev.8b00399
- Venkataraman, P., Lamb, R. A., and Pinto, L. H. (2005). Chemical rescue of Histidine Selectivity Filter Mutants of the M2 Ion Channel of Influenza A Virus. *J. Biol. Chem.* 280, 21463–21472. doi:10.1074/jbc.m412406200
- Wang, T., and Hong, M. (2015). Investigation of the Curvature Induction and Membrane Localization of the Influenza Virus M2 Protein Using Static and Off-Magic-Angle Spinning Solid-State Nuclear Magnetic Resonance of Oriented Bicelles. *Biochemistry* 54, 2214–2226. doi:10.1021/acs.biochem.5b00127
- Wang, C., Takeuchi, K., Pinto, L. H., and Lamb, R. A. (1993). Ion Channel Activity of Influenza A Virus M2 Protein: Characterization of the Amantadine Block. *J. Virol.* 67, 5585–5594. doi:10.1128/jvi.67.9.5585-5594.1993
- Wang, C., Lamb, R. A., and Pinto, L. H. (1995). Activation of the M2 Ion Channel of Influenza Virus: A Role for the Transmembrane Domain Histidine Residue. *Biophys. J.* 69, 1363–1371. doi:10.1016/s0006-3495(95)80003-2
- Wang, J., Ma, C., Fiorin, G., Carnevale, V., Wang, T., Hu, F., et al. (2011). Molecular Dynamics Simulation Directed Rational Design of Inhibitors Targeting Drug-Resistant Mutants of Influenza A Virus M2. *J. Am. Chem. Soc.* 133, 12834–12841. doi:10.1021/ja204969m
- Wang, J., Wu, Y., Ma, C., Fiorin, G., Wang, J., Pinto, L. H., et al. (2013). Structure and Inhibition of the Drug-Resistant S31N Mutant of the M2 Ion Channel of Influenza A Virus. *Proc. Natl. Acad. Sci. USA* 110, 1315–1320. doi:10.1073/pnas.1216526110
- Wang, J., Li, F., and Ma, C. (2015). Recent Progress in Designing Inhibitors that Target the Drug-Resistant M2 Proton Channels from the Influenza A Viruses. *Biopolymers* 104, 291–309. doi:10.1002/bip.22623
- Watkins, L. C., DeGrado, W. F., and Voth, G. A. (2020). Influenza A M2 Inhibitor Binding Understood through Mechanisms of Excess Proton Stabilization and Channel Dynamics. *J. Am. Chem. Soc.* 142, 17425–17433. doi:10.1021/jacs.0c06419
- Watson, S. J., Langat, P., Reid, S. M., Lam, T. T.-Y., Cotten, M., Kelly, M., et al. (2015). Molecular Epidemiology and Evolution of Influenza Viruses Circulating within European Swine between 2009 and 2013. *J. Virol.* 89, 9920–9931. doi:10.1128/jvi.00840-15

- Wei, C., and Pohorille, A. (2013). Activation and Proton Transport Mechanism in Influenza A M2 Channel. *Biophysical J.* 105, 2036–2045. doi:10.1016/j.bpj.2013.08.030
- World Health Organization (2019). *Global Influenza Strategy 2019–2030*. Geneva: World Health Organization. Available at: <https://apps.who.int/iris/handle/10665/311184> (Accessed September 14, 2021).
- Wu, Y., Canturk, B., Jo, H., Ma, C., Gianti, E., Klein, M. L., et al. (2014). Flipping in the Pore: Discovery of Dual Inhibitors that Bind in Different Orientations to the Wild-type versus the Amantadine-Resistant S31N Mutant of the Influenza A Virus M2 Proton Channel. *J. Am. Chem. Soc.* 136, 17987–17995. doi:10.1021/ja508461m
- Wu, X., Wu, X., Sun, Q., Zhang, C., Yang, S., Li, L., et al. (2017). Progress of Small Molecular Inhibitors in the Development of Anti-influenza Virus Agents. *Theranostics* 7, 826–845. doi:10.7150/thno.17071
- Yi, M., Cross, T. A., and Zhou, H.-X. (2008). A Secondary Gate as a Mechanism for Inhibition of the M2 Proton Channel by Amantadine. *J. Phys. Chem. B* 112, 7977–7979. doi:10.1021/jp800171m
- Yi, M., Cross, T. A., and Zhou, H.-X. (2009). Conformational Heterogeneity of the M2 Proton Channel and a Structural Model for Channel Activation. *Proc. Natl. Acad. Sci.* 106, 13311–13316. doi:10.1073/pnas.0906553106
- Conflict of Interest:** The authors declare that the research was conducted in the absence of any commercial or financial relationships that could be construed as a potential conflict of interest.
- Publisher's Note:** All claims expressed in this article are solely those of the authors and do not necessarily represent those of their affiliated organizations, or those of the publisher, the editors and the reviewers. Any product that may be evaluated in this article, or claim that may be made by its manufacturer, is not guaranteed or endorsed by the publisher.

Copyright © 2022 Aledavood, Selmi, Estarellas, Masetti and Luque. This is an open-access article distributed under the terms of the Creative Commons Attribution License (CC BY). The use, distribution or reproduction in other forums is permitted, provided the original author(s) and the copyright owner(s) are credited and that the original publication in this journal is cited, in accordance with accepted academic practice. No use, distribution or reproduction is permitted which does not comply with these terms.



Molecular Insights Into Binding and Activation of the Human KCNQ2 Channel by Retigabine

Barbara Garofalo¹, Alexandre M.J.J. Bonvin², Andrea Bosin³, Francesco P. Di Giorgio¹, Rosella Ombrato^{1*} and Attilio V. Vargiu^{3*}

¹Angelini Pharma S.p.A., Rome, Italy, ²Faculty of Science—Chemistry, Bijvoet Center for Biomolecular Research, Utrecht University, Utrecht, Netherlands, ³Department of Physics, University of Cagliari, Cagliari, Italy

OPEN ACCESS

Edited by:

Matteo Masetti,
University of Bologna, Italy

Reviewed by:

Harley Takatsuna Kurata,
University of Alberta, Canada
Ekaterina Lyukmanova,
Institute of Bioorganic Chemistry
(RAS), Russia

*Correspondence:

Rosella Ombrato
rosella.ombrato@
angelinipharma.com
Attilio V. Vargiu
vargiu@dsf.unica.it

Specialty section:

This article was submitted to
Biological Modeling and Simulation,
a section of the journal
Frontiers in Molecular Biosciences

Received: 19 December 2021

Accepted: 11 February 2022

Published: 03 March 2022

Citation:

Garofalo B, Bonvin AMJJ, Bosin A,
Di Giorgio FP, Ombrato R and
Vargiu AV (2022) Molecular Insights
Into Binding and Activation of the
Human KCNQ2 Channel
by Retigabine.
Front. Mol. Biosci. 9:839249.
doi: 10.3389/fmolb.2022.839249

Voltage-gated potassium channels of the Kv7.x family are involved in a plethora of biological processes across many tissues in animals, and their malfunctioning could lead to several pathologies ranging from diseases caused by neuronal hyperexcitability, such as epilepsy, or traumatic injuries and painful diabetic neuropathy to autoimmune disorders. Among the members of this family, the Kv7.2 channel can form heterotetramers together with Kv7.3, forming the so-called M-channels, which are primary regulators of intrinsic electrical properties of neurons and of their responsiveness to synaptic inputs. Here, prompted by the similarity between the M-current and that in Kv7.2 alone, we perform a computational-based characterization of this channel in its different conformational states and in complex with the modulator retigabine. After validation of the structural models of the channel by comparison with experimental data, we investigate the effect of retigabine binding on the two extreme states of Kv7.2 (resting-closed and activated-open). Our results suggest that binding, so far structurally characterized only in the intermediate activated-closed state, is possible also in the other two functional states. Moreover, we show that some effects of this binding, such as increased flexibility of voltage sensing domains and propensity of the pore for open conformations, are virtually independent on the conformational state of the protein. Overall, our results provide new structural and dynamic insights into the functioning and the modulation of Kv7.2 and related channels.

Keywords: voltage-gated potassium channels, Kv7.2, retigabine, homology modelling, docking, molecular dynamics

INTRODUCTION

Potassium channels (K⁺ channels) are primary regulators of intrinsic electrical properties of neurons and their responsiveness to synaptic inputs (Ashcroft, 2000; Jentsch, 2000; Miller, 2000; Hille, 2001). An increase in the membrane conductance to K⁺ ions causes neuronal hyperpolarization and, in most cases, reduces firing frequency, exerting a strong inhibitory function on neuronal excitability. On the other hand, reduction in conductance seems to be a hallmark of the hyperexcitability seen in many pain syndromes ranging from traumatic injuries and painful diabetic neuropathy to autoimmune disorders (Shieh et al., 2000; Villa and Combi, 2016; Nikitin and Vinogradova, 2021).

The Kv7.x subfamily of voltage-gated K⁺ channels, encoded by the KCNQ gene family, consists of five members (Kv7.1–Kv7.5 or KCNQ1–KCNQ5), each showing distinct tissue distribution and subcellular localization, as well as biophysical, pharmacological, and pathophysiological properties

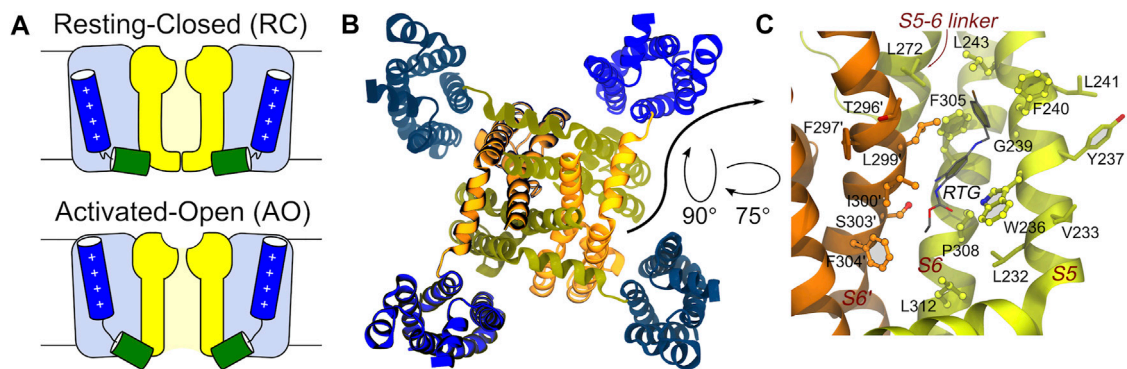


FIGURE 1 | Main conformational states, overall tetrameric structure, and RTG binding site of the KCNQ2 channel. **(A)** Schematic view of the RC and AO conformational states of the channel. The Pore and VSD domains are colored yellow and blue, respectively. The S4 and S4-S5 linker helices are shown as blue and green cylinders, respectively. **(B)** Top view of the tetrameric channel in the AC conformational state (PDB ID: 7CR0). **(C)** Zoom on the RTG binding site on the Pore domain of the KCNQ2 channel. The site is a crevice between two adjacent channel monomers (shown as orange and greenish yellow ribbons). Residues in contact with the drug in the experimental structure 7CR2 (Li et al., 2021) are shown using a CPK model with bright surfaces, while residues identified in this work based on previous knowledge are shown as sticks. Residues on the second monomer are labelled by primed numbers.

(Jentsch, 2000; Robbins, 2001; Brown and Passmore, 2009; Barrese et al., 2018; Abd-Elseyed et al., 2019; Jepps et al., 2021). All these channels assemble into membrane-embedded tetramers. Heteromeric assembly of KCNQ2 and KCNQ3, originally termed the “M-channels”, are primary regulators of intrinsic electrical properties of neurons and of their responsiveness to synaptic inputs (Jentsch, 2000; Robbins, 2001). The M-type potassium current is a slowly activating, non-inactivating voltage-gated current, which occurs at subthreshold potentials. It is named after the proposed pathway of its inhibition, i.e., activation of the muscarinic (M) acetylcholine receptor, which leads to the closure of the channel (Brown and Adams, 1980; Marrion, 1997; Delmas and Brown, 2005; Brown and Passmore, 2009; Hernandez et al., 2009). M-currents contribute to the afterhyperpolarization of the action potentials, the spike frequency adaptation, the shaping of the action potential firing properties, the setting of the resting membrane potential and the regulation of presynaptic functions (Bordas et al., 2015). Studies have shown that the current detected across homo-tetrameric KCNQ2 channels is very similar to the M-current, while KCNQ3 channels are rarely able to generate recordable currents (Maljevic et al., 2003).

KCNQ2 shows a topological arrangement with six transmembrane segments (S1–S6), and intracellular NH2 and COOH termini. The region encompassing segments S1–S4 forms the voltage sensing domain (VSD), with positively charged residues in S4 comprising the main voltage sensor. The S5–S6 region forms the pore domain that contains a P-loop that imparts K⁺ ion selectivity; the carboxylic tail contains four helices (A–D), which contain regions important for tetramerization or binding to regulatory factors including phosphatidylinositol-4,5-bisphosphate (PIP2), ankyrin G, and Calmodulin CaM (Soldovieri et al., 2011). The central pore domain is surrounded by four voltage-sensing domains that respond to membrane depolarization by undergoing a conformational change. This in turn triggers structural rearrangements in the

pore domain via electromechanical coupling, ultimately opening the channel gate to allow ion conduction (Bezaniila and Stefani, 1994; Jensen et al., 2012). VSD activation occurs stepwise due to the depolarization and proceeds from an initial resting VSD conformation in which the pore is closed (resting/closed, RC) to an activated VSD with an open pore (activated/open, AO) (Bezaniila, 2000; Wu et al., 2010), passing through a conformational change of the VSD into an activated conformation and the pore still closed (activated/closed, AC) as caught by cryo-electron microscopy (cryo-EM) solved structure of KCNQ2 (PDB ID: 7CR0) (Li et al., 2021) (Figure 1).

Functional studies in heterologous expression systems revealed that mutations in KCNQ2 (and KCNQ3) genes are related to the onset of diseases such as epilepsy, benign familial neonatal convulsions (BFNC) or neonatal epileptic encephalopathy (Miceli et al., 2013), peripheral nerve hyperexcitability (PNH or myokymia or neuromyotonia) (Maljevic et al., 2008), neuropathic pain (Di Cesare Mannelli et al., 2017), osteoarthritis or cancer pain, migraine, anxiety, dystonia and dyskinesia, bipolar disorder, bladder hypersensitive disorder, addiction, sensory deficits, stroke (Miceli et al., 2008; Zwierzyńska et al., 2017; Du et al., 2018), mania (Kristensen et al., 2012) and tinnitus (Li et al., 2013). These channels were early identified as pharmacological targets, and M-channel enhancers such as retigabine (hereafter RTG) were developed and approved in humans [with indications and antiepileptic drug (Brown and Passmore, 2009)].

Unfortunately, RTG was withdrawn from the market due to safety issues associated with retina and skin discoloration (Clark et al., 2015). Nonetheless, this compound remains an excellent tool to investigate the mechanism of action related to KCNQ2-opener activity, which is not yet fully unveiled. In particular, while studies have shown that RTG can bind to the hydrophobic pocket located near the channel gate of the subunit of KCNQ2, thereby stabilizing the open conformation of the channel (Gunthorpe et al., 2012), Wang et al. recently suggested that the interaction

with KCNQ2 is not gated by channel opening and closing, and that RTG could also interact with the resting states of the protein (Wang et al., 2018).

The binding mode of RTG onto KCNQ2 (featuring an activated VSD and a closed pore—AC) was confirmed by the determination of a cryo-EM structure (Li et al., 2021). The drug sits in a hydrophobic pocket formed by S5, pore helix, and S6 from the neighbouring subunit at the inter-subunit interface in the pore domain (**Figure 1**). The drug binds to KCNQ2 mainly by hydrogen bonds with the side chain of Trp236, Ser303, and the main chain carbonyls of Leu299, Phe305, as well as the hydrophobic interactions with residues Trp236, Phe240, Leu243, Leu272, Leu299, Phe304 and Phe305. To date there are no KCNQ2 structures available in the RC and AO states and when we performed this work the cryo-EM structure of AC KCNQ2, alone and in complex with RTG (Li et al., 2021), had not yet been published. For this reason, to investigate the structural features underlying the three different conformations, we resorted to using atomistic molecular dynamics (MD) simulations. Here, we report the development and structural validation of new homology models of the human KCNQ2 channel in the RC, AC and AO states. The models turned out to be highly accurate, thus allowing to investigate not only the structural and dynamical features of the channel, but also the binding of RTG to different pore states. By performing ensemble docking and multi-replica MD simulations of the RTG-KCNQ2 complexes in the RC and AO states, we show that this ligand can form stable interactions at the same channel site in both states. Moreover, we reproduce several experimental findings and trends underlying the molecular mechanism behind RTG action, such as a higher flexibility of the VSD domains and an increased tendency to pore opening upon ligand binding.

Overall, our work confirms the high potential of computational methods in this field (Khalili-Araghi et al., 2010; Jensen et al., 2012; Yarov-Yarovoy et al., 2012; Kim et al., 2015; Kasimova et al., 2018; DeMarco et al., 2019; Kuenze et al., 2019; Alberini et al., 2021; Şterbuleac 2021) and provides new insightful data that might help drug design efforts.

METHODS

Homology Modelling and Validation

We aimed to model the AO, AC, and RC states of the KCNQ2 tetramer. The sequence of KCNQ2 was taken from the UNIPROT website (identifying code: O43526), and the modelling was restricted to the transmembrane region of the channel (residue ARG75 to GLN323 in each monomer), amounting to 249 aminoacids per monomer and including helices S0 to S6. The models were generated using the Prime tool (Jacobson et al., 2004) of the Maestro software package (Prime, Schrödinger, LLC, New York, NY, 2019). Namely, the AC model was generated using as (single) template structure the cryo-EM structure of the homologous KCNQ1 channel (PDB ID: 5VMS) (Sun and MacKinnon, 2017), sharing 58% identity and 75% homology with the sequence of KCNQ2 (**SupplementaryTable S1**). The sequence alignment was performed with Clustal Omega 1.2.4

(<https://www.ebi.ac.uk/Tools/msa/clustalo/>). Regarding the AO and RC states, as no experimental structure of KCNQ2 in these conformations was available at the time of this investigation, we used as templates the corresponding structures of the KCNQ1 channel previously published by Kuenze et al. (2019). Validation of the structural models was performed by submitting them to the MOLPROBITY webserver (<http://molprobity.biochem.duke.edu/>) (Williams et al., 2018).

Molecular Dynamics Simulations

Apo proteins. MD simulations of the AO, RC, and AC models of KCNQ2 in explicit phospholipid membranes at 310 K were performed using Amber18 (Case et al., 2018) and the Lipid17 force field (Gould, I.R., Skjevik A.A., Dickson, C.J., Madej, B.D., Walker, R.C., "Lipid17: A Comprehensive AMBER Force Field for the Simulation of Zwitterionic and Anionic Lipids", 2018, in preparation). We employed a protocol similar to that recently used by Kuenze et al. to simulate the transmembrane region of the tetrameric KCNQ1 channel (Kuenze et al., 2019). Namely, the models generated by Prime were used as starting conformations for MD simulations after alignment to the membrane normal using the PPM webserver (Lomize et al., 2012) and embedded into bilayers of POPC (palmitoyl-oleoyl-phosphatidylcholine; ~250 phospholipids per leaflet) using the membrane builder tool of the CHARMM-GUI website (Wu et al., 2014). A TIP3P water layer ~30 Å thick and containing 0.15 M of KCl was added on each side of the membrane. In addition, four K⁺ ions were placed in the channel selectivity filter at positions inferred from the X-ray structure coordinates of PDB 2R9R. The bilayer contained 26 PIP2 (phosphatidyl-4,5-bisphosphate) molecules in the inner leaflet, consisting of an equal number of C4-PO₄⁻ and C5-PO₄⁻ mono-protonated PIP2 molecules with stearoyl and arachidonoyl conjugations at the sn-1 and sn-2 position. The PIP2 parameters were taken from (Kuenze et al., 2019). No PIP2 was added to the MD system of the AC model because the decoupled state seen in the cryo-EM structure of KCNQ1 is assumed to be due to the absence of PIP2 and the inability of that membrane composition to induce conformational changes. SHAKE bond length constraints were applied to all bonds involving hydrogen. Nonbonded interactions were evaluated with a 10 Å cut-off, and electrostatic interactions were calculated by the particle-mesh Ewald method. Each MD system was first minimized for 15,000 steps using steepest descent for the first 100 steps, followed by conjugate gradient minimization. With protein and ions restrained to their initial coordinates, the lipid and water were heated to 50 K over 1,000 steps with a step size of 1 fs in the NVT ensemble using Langevin dynamics with a rapid collision frequency of 10 ns⁻¹. The system was then heated to 100 K over 50,000 steps with a collision frequency of 1,000 ps⁻¹ and finally to 310 K over 200,000 steps and a collision frequency of 100 ps⁻¹. After switching to the NPT ensemble, restraints on ions were gradually removed over 500 ps and the system was equilibrated for another 25 ns at 310 K with weak positional restraints (force constant of 1 kcal mol⁻¹ Å⁻²) applied to protein C_α atoms. The protein restraints were then gradually removed over 50 ns, and 9 replicas of production MD, each of 100 ns in length, were conducted for each model (yielding

1 μ s for each state) using a step size of 2 fs, constant pressure periodic boundary conditions, anisotropic pressure scaling and Langevin dynamics. Note that, as in (Kuenze et al., 2019), production runs were performed in the presence of soft restraints ($k = 2 \text{ kcal mol}^{-1} \text{ \AA}^{-2}$) between each K^+ ion and the 8, 4, 4, and 4 oxygen atoms of residues T277, I278, G279 and Y280 respectively. On top of these runs, for each model and each replica we performed 100 ns additional MD simulations in the absence of restraints. Therefore, for each state we generated a production trajectory corresponding to $\sim 2 \mu$ s of simulated time.

RTG-KCNQ2 complexes. Multicopy simulations of the RTG-KCNQ2 complexes derived from docking calculations (*vide infra*) were performed using the same settings as for the simulations of the unbound channel. Force field parameters of the ligand were derived from the GAFF (Wang et al., 2004) force field or generated using the antechamber module of AMBER when missing. In particular, atomic restrained electrostatic potential charges were derived after a structural optimization performed with Gaussian09 (Frisch et al., 2016). For complexes in both the AO and RC conformations, the top eight unique (that is, non-identical) docking poses (selected by visual inspection) were selected as starting conformations for MD simulations. Initial structures of the complexes in a model membrane and water solution were generated by superposing these structures to the conformation extracted the MD trajectory of the apo KCNQ2 channel and corresponding to the cluster representative used in docking calculations. Next, three independent MD simulations, each of 1 μ s in length, were performed for each complex structure, amounting to 24 replicas for each system and 48 μ s of cumulative time.

Molecular Docking of RTG on AO and RC States of KCNQ2

In order to assess the possibility of RTG binding to the AO and RC states of the potassium channel KCNQ2, ensemble docking calculations were performed using Autodock4.2 (Morris et al., 2009). Namely, a cluster analysis was performed on the equilibrium trajectories extracted from the cumulative MD simulations of the apo protein, using as a metric the distance RMSD matrix (dRMSD) calculated on the non-hydrogenous atoms of the putative RTG binding site (that is the enlarged binding site in **Figure 1**) and a 2 \AA cut-off. The analysis was performed separately on each of these four binding sites present on the KCNQ2 tetramer and resulted in an overall number of 42 and 17 clusters for AO and RC states, respectively. The default settings of Autodock were used, except for the grid space, which was set to 0.25 (default 0.375), and for the grid volume, which was automatically set so as to cover all residues lining the binding site, following the automated protocol described in (Basciu et al., 2019b). 7 out of the 8 rotatable bonds of RTG were activated during docking; up to 10 poses per channel structure were saved, resulting in 390 poses onto the AO state and 151 onto the RC state.

Analysis of the MD Trajectories

Stability of the models. The stability of our MD simulations was evaluated in terms of the RMSD of the heavy atoms of the protein along the trajectory with respect to the initial structure (i.e., the homology model) as well as to the experimental structures of the KCNQ2 channel in the AC state, as well as of its complex with RTG [PDB IDs 7CR0 and 7CR2, respectively (Li et al., 2021)].

Root Mean Square Fluctuations (RMSF). The flexibility of the protein was evaluated in terms of RMSF calculations, performed on each trajectory with the *atomicfluct* command of the AmberTools. The fluctuations were evaluated after alignment of the Pore domain to the average conformation extracted from the corresponding MD trajectory.

Identification of the putative binding site of retigabine. Since no experimental structure of RTG in complex with KCNQ2 was available when this investigation was performed, the putative (lately largely confirmed, see Results) binding site of RTG on the Pore-forming domain of the channels was identified based on the findings in (Lange et al., 2009; Kim et al., 2015). In KCNQ2, the residue W236 was shown to be crucial for the interaction of the channel with retigabine and its analogues (Kim et al., 2015). In particular, the presence of an H-bond donor in this residue was shown to be crucial for binding. Therefore, we identified as putative binding site of retigabine on KCNQ2 the crevice formed by W236 and all the residues within 3.5 \AA from it (**Figure 1**).

Cluster analysis. To perform some of the analyses described below within a reasonable time, and to select a tractable number of (maximally different) structures for molecular docking, a cluster analysis was performed on the cumulative trajectory generated by concatenating the 10 independent trajectories generated for each state. We performed two different cluster analyses, using either the C_α atoms of the protein or all heavy atoms of the residues around each of the four putative binding sites of retigabine. In this way, we obtained structures differing both in their overall architecture and as well as in the conformations of the putative binding site of retigabine. As metric, we used the dRMSD calculated over the selections above (which were also used for structural alignment), with cut off set to 2 \AA . These structural clusters were further analysed as described below.

Volume and druggability calculations. Druggability calculations were performed using the *f-pocket* (Le Guilloux et al., 2009) software as described in previous publications (Basciu et al., 2019b; Basciu et al., 2019a). For each conformation of the protein extracted from the cluster analysis described above, we evaluated its druggability score D, a descriptor ranging from 0 to 1 with higher values identifying more druggable geometries (Schmidtke and Barril, 2010). It is customary to associate scores >0.5 to putative binding sites. We also estimated the approximate volume of the retigabine binding sites by using the software VOIDOO (Kleywegt and Jones, 1994) with the following settings: grid spacing 0.5 \AA ; probe radius 1.4 \AA , growth factor for van der Waals radii 1.05, number of cavity refinement cycles 100. The coordinates of the centres of the cavity were set to the geometrical centre of the sites.

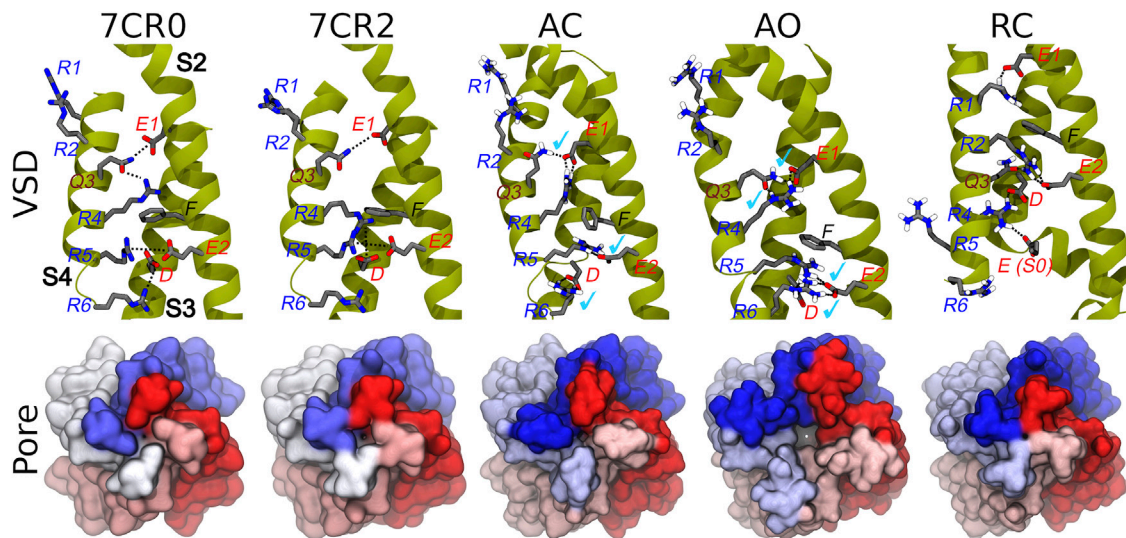


FIGURE 2 | Conformations of the VSD domain. Top row: Key interactions established between charged/polar residues of the S1–S4 helices in the apo and RTG-bound experimental structures, followed by the three models described in this work. Helices S2, S3, and S4 are shown in dark yellow ribbons, while the sidechains of key residues are represented by sticks colored by atom type. H-bonds/salt bridges are indicated by black dotted lines. Light blue check marks identify interactions present in the apo experimental structure (7CR0) and reproduced in the homology models. Bottom row: Comparison among the molecular surfaces (bottom view from the intracellular side; monomers colored differently) of the channel in the experimental and modelled structures generate in this work.

Interaction network. The intra- and inter-molecular interactions involving the retigabine binding sites were calculated using the *cptraj* tool of the AMBER18 package (Case et al., 2018, p. 18) and the PLATON software package (Spek, 2009). Namely, the first software was used to characterize the network of H-bonds (given the importance of W236 as H-bond donor), using a cut-off of 3.5 Å for the donor-acceptor distance and of 145° for the donor-hydrogen-acceptor angle. The second software was used to detect stacking interactions, given that a change in the network of residues involved in π - π interactions was suggested to occur upon switch of the channel from a closed to an open state (Syeda et al., 2016). The default parameters were used to detect interactions involving aromatic rings.

Pore morphology. For each simulated system, the presence of—and the morphology of putative tunnels leading from the cytoplasmic entrance to the center of the protein (beneath the selectivity filter) were evaluated using CAVER3.0 (Chovancova et al., 2012) on representative structures extracted from the cluster analysis performed on the C_{α} atoms of the whole protein, as described above. The probe radius, shell radius, shell depth, and clustering threshold were set to 0.9 Å, 5.0 Å, 3.0 Å, and 3.5 Å, respectively. Tunnel calculations were started for each conformation at the center between residues 276 and 306 on each monomer.

Binding free energy estimation. Free energies of binding for RTG-KCNQ2 complexes were estimated using the molecular mechanics generalized Born surface area (MM-GBSA) approach (Genheden and Ryde, 2015) through the formula:

$$\Delta G_{\text{bind}} = G_{\text{com}} - (G_{\text{rec}} + G_{\text{lig}})$$

G_{com} , G_{rec} , and G_{lig} are the absolute free energies of the complex, receptor, and ligand, respectively, averaged over the equilibrium trajectory. According to these schemes, the free energy difference can be decomposed as:

$$\Delta G_{\text{bind}} = \Delta E_{\text{MM}} + \Delta G_{\text{solv}} - T\Delta S_{\text{conf}}$$

where ΔE_{MM} is the difference in the molecular mechanics energy, ΔG_{solv} is the solvation free energy, and $T\Delta S_{\text{conf}}$ is the conformational entropy. The first two terms were calculated with the following equations:

$$\begin{aligned} \Delta E_{\text{MM}} &= \Delta E_{\text{bond}} + \Delta E_{\text{angle}} + \Delta E_{\text{torsion}} + \Delta E_{\text{vdw}} + \Delta E_{\text{elec}} \\ \Delta G_{\text{solv}} &= \Delta G_{\text{solv,p}} + \Delta G_{\text{solv,np}} \end{aligned}$$

E_{MM} includes the molecular mechanics energy contributed by the bonded (E_{bond} , E_{angle} , and E_{torsion}) and non-bonded (E_{vdw} and E_{elec} , calculated with no cutoff) terms of the force field. As customary, we employed the single-trajectory approach, in which only simulations of the complex are employed to generate the ensemble of conformations of the receptor and of the ligand by simply removing the appropriate atoms (Genheden and Ryde, 2015). This corresponds to setting ΔE_{bond} , ΔE_{angle} , and $\Delta E_{\text{torsion}}$ to zero. ΔG_{solv} is the solvation free energy, which can be modeled as the sum of an electrostatic contribution ($\Delta G_{\text{solv,p}}$, evaluated using the MM-GBSA or MM-PBSA approach) and a non-polar one ($\Delta G_{\text{solv,np}} = \gamma\Delta S_A + b$, proportional to the difference in solvent-exposed surface area, ΔS_A).

The electrostatic solvation free energy was calculated using the implicit solvent model developed by Nguyen et al. (Nguyen et al., 2013) (igb = 8 option in AMBER) in combination with mbondi2 (for H, C, N, O, S elements) and intrinsic radii. Partial charges were taken from the AMBER/GAFF force fields, and relative

[illegible]

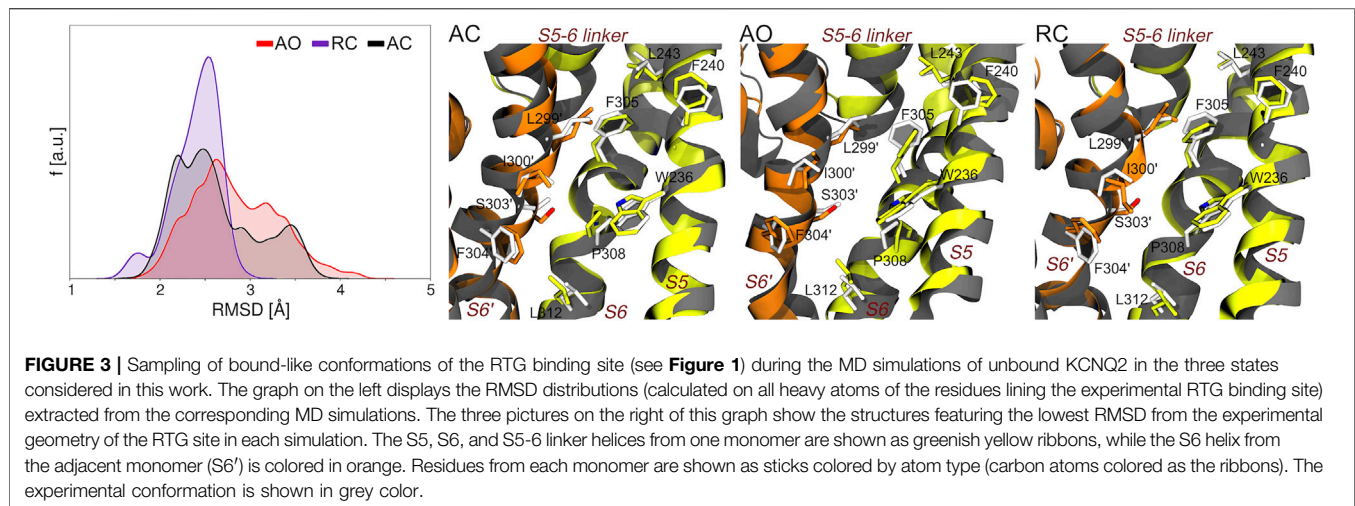


FIGURE 3 | Sampling of bound-like conformations of the RTG binding site (see **Figure 1**) during the MD simulations of unbound KCNQ2 in the three states considered in this work. The graph on the left displays the RMSD distributions (calculated on all heavy atoms of the residues lining the experimental RTG binding site) extracted from the corresponding MD simulations. The three pictures on the right of this graph show the structures featuring the lowest RMSD from the experimental geometry of the RTG site in each simulation. The S5, S6, and S5-6 linker helices from one monomer are shown as greenish yellow ribbons, while the S6 helix from the adjacent monomer (S6') is colored in orange. Residues from each monomer are shown as sticks colored by atom type (carbon atoms colored as the ribbons). The experimental conformation is shown in grey color.

dielectric constants of 1 for solute and 78.4 for the solvent were used. The non-polar contribution is approximated by the LCPO method (Weiser et al., 1999).

The solute conformational entropy contribution ($T\Delta S_{\text{conf}}$) was not evaluated as it is notoriously difficult to evaluate with accuracy (Genheden and Ryde, 2015). The estimates were performed on up to 100 different equally spaced conformations extracted from each of the ten most populated clusters calculated from the cumulative trajectories of AO-RTG and RC-RTG complexes.

RESULTS AND DISCUSSION

Model Building and Validation

The homology models of the AC, AO, and RC conformational states of the transmembrane region of the tetrameric KCNQ2 channel were generated according to the protocol described in the Methods section. When building the models, the recently published structure of the human KCNQ2 ion channel in the AC state (PDB ID: 7CR0) was unavailable, and the more reliable template was the AC cryo-EM structure of the KCNQ1 ion channel (PDB ID: 5VMS), featuring a high sequence similarity with KCNQ2 (**Supplementary Table S1**). The AC tetramer resulting from this modelling displays a closed pore and an activated VSD domain: the C_{α} -RMSDs values calculated for these domains taking the KCNQ2 structure 7CR0 as reference were 1.0 and 1.6 Å respectively (**Supplementary Figure S1**), indicating a good agreement between our model and the experimental structure. Moreover, characteristic interactions between E1 on helix S2 with Q3(S4), E2(S2) with R5(S4), and D(S3) with R6(S4), present in the experimental structure, are reproduced in our model (**Figure 2**). As expected, the access to the pore through the activation gate, lined by residues A306, A309 and S314, is closed.

The AO and RC states were built using as templates the new and refined models of the KCNQ1 channel in the corresponding structures (Kuenze et al., 2019). Also in this case, the resulting models are overall reasonable (**Figure 2** and **Supplementary Figure S1**). In particular, in the AO state the VSD domain reproduces all the

TABLE 2 | Druggability index D calculated with fpocket on each of the four binding sites of RTG in the three different states of the KCNQ2 ion channel. For each site, the average value (weighted by the relative cluster population) of D and its standard deviation are reported, together with the normalized frequency f_N of conformations identified as druggable (calculated as sum of normalized fractions of cluster population).

Site	Channel state					
	AO		RC		AC	
	D	f_N	D	f_N	D	f_N
1	0.97 (0.03)	0.23	0.70 (0.19)	0.59	-	-
2	-	-	-	-	-	-
3	0.92 (0.10)	0.17	0.66 (0.02)	0.40	0.71 (0.17)	0.40
4	-	-	0.83 (0.03)	0.44	0.92 (0.05)	0.40

key interactions between R and E/D aminoacids sitting on helices S4 and S2, respectively. In contrast, in the resting state the VSD domain features interactions between E1(S2) and R1(S4), E2(S2) and R2(S4), which imply a downward shift of S4 by about 3 helical turns compared to the conformation assumed in the activated state. The pore is clearly closed also in the RC state (**Figure 2**), while it features a channel leading from the intracellular side to the central cavity (bottleneck radius of 2.46 Å near A309) in the AO state. All models were validated using the MOLPROBITY webserver, with scores of 1.48 (AO), 1.59 (RC), and 1.84 (AC), placing them respectively in the 96th, 93rd, and 84th percentiles (out of 27,675 structures). These values are comparable to that of 1.57 and 1.59 (93rd percentile) obtained respectively for the same region extracted from the cryo-EM structure of KCNQ1 (5VMS) used as structural template and for the cryo-EM structure of KCNQ2 in the AC state (7CR0).

Characterization of Channel Dynamics in the AC, AO, and RC States

Using the homology models discussed in the previous section as starting structures, we performed 9 independent MD simulations for each state, for a total production trajectory of ~6 μs in length.

TABLE 3 | Pseudo binding free energies and structural deviations from the experimental pose calculated for the top 10 clusters of the complexes between RTG and KCNQ2 in AO and RC conformational states. Standard deviations are reported in parentheses.

State Cluster	RTG-AO		RTG-RC	
	ΔG [kcal/mol]	RMSD ^{RTG} _{7CR2} [Å]	ΔG [kcal/mol]	RMSD ^{RTG} _{7CR2} [Å]
0	-30.8 (3.9)	1.5 (0.4)	-28.6 (3.1)	4.6 (0.3)
1	-22.2 (2.9)	4.5 (0.4)	-22.0 (3.8)	5.3 (0.4)
2	-26.4 (2.5)	4.8 (0.3)	-26.2 (2.4)	9.2 (0.1)
3	-36.2 (3.2)	9.0 (0.2)	-25.3 (3.9)	9.7 (0.6)
4	-33.7 (3.5)	4.7 (0.5)	-21.5 (3.4)	3.5 (0.3)
5	-28.1 (2.6)	11.4 (0.5)	-16.0 (2.2)	9.6 (0.5)
6	-25.9 (2.5)	4.5 (0.4)	-24.3 (3.5)	5.9 (0.4)
7	-22.1 (2.9)	7.1 (0.3)	-22.5 (3.3)	5.0 (0.5)
8	-30.7 (2.6)	4.7 (0.3)	-26.5 (3.8)	7.8 (0.3)
9	-29.2 (2.3)	9.1 (0.3)	-22.1 (2.7)	5.6 (0.3)

In all cases the trajectories were relatively stable, with C_{α} -RMSDs from the initial structure stable around 4 Å (**Supplementary Figure S2**). These values are very similar to that found by Kuenze et al. in their recent computational work on KCNQ1 (Kuenze et al., 2019). Note that, in the absence of soft restraints between K^+ ions and residues of the Pore-forming region, the number of ions simultaneously present within that region oscillates between 2 and 4. In this work we will not discuss further this aspect, while noting that the removal of the restraints had a limited impact on the overall stability of the protein (**Supplementary Figure S2**).

Given the recent availability of the experimental structure of the apo form of the channel in the AC state, we compared the structural features of the three simulated systems taking that structure (7CR0, PDB code) as a reference. The distribution of the protein C_{α} -RMSDs across the cumulative production trajectories is sharply peaked around 3 Å for the AC model. This confirms that our model is not only stable during μ s long MD trajectories, but samples conformations close to the experimental structure resolved for this state (**Supplementary Figure S3**). As expected, the RC and the AO states sample conformations that are more distant from the AC experimental structure (peaks around 6 and 8 Å, respectively; **Supplementary Figure S3**, upper panel). Similar distributions plots calculated separately for each VSD domain and for the Pore confirm the overall good reproduction of the structural features at the level of key regions in every conformational state (**Supplementary Figure S3**, middle and lower panel, respectively). Consistently with these results, the interactions characterizing the active and resting states of the VSD domain, reproduced in the homology models from which the MD simulations began, are well conserved in at least one domain of all (66%) replicas of the AO/C (RC) states (**Table 1** and **Supplementary Tables S2–S4**). Note that up to three VSD domains assumed simultaneously an active state conformation along the simulations of the AO state (**Table 1**). To obtain further structural insights into the KCNQ2 channel in the different states, we performed a cluster analysis on the cumulative production trajectory, using as metric the distance-RMSD among the C_{α} atoms of the protein.

The results indicate a decreasing structural variability for the AO, AC, and RC states (**Supplementary Table S5**) and confirmed

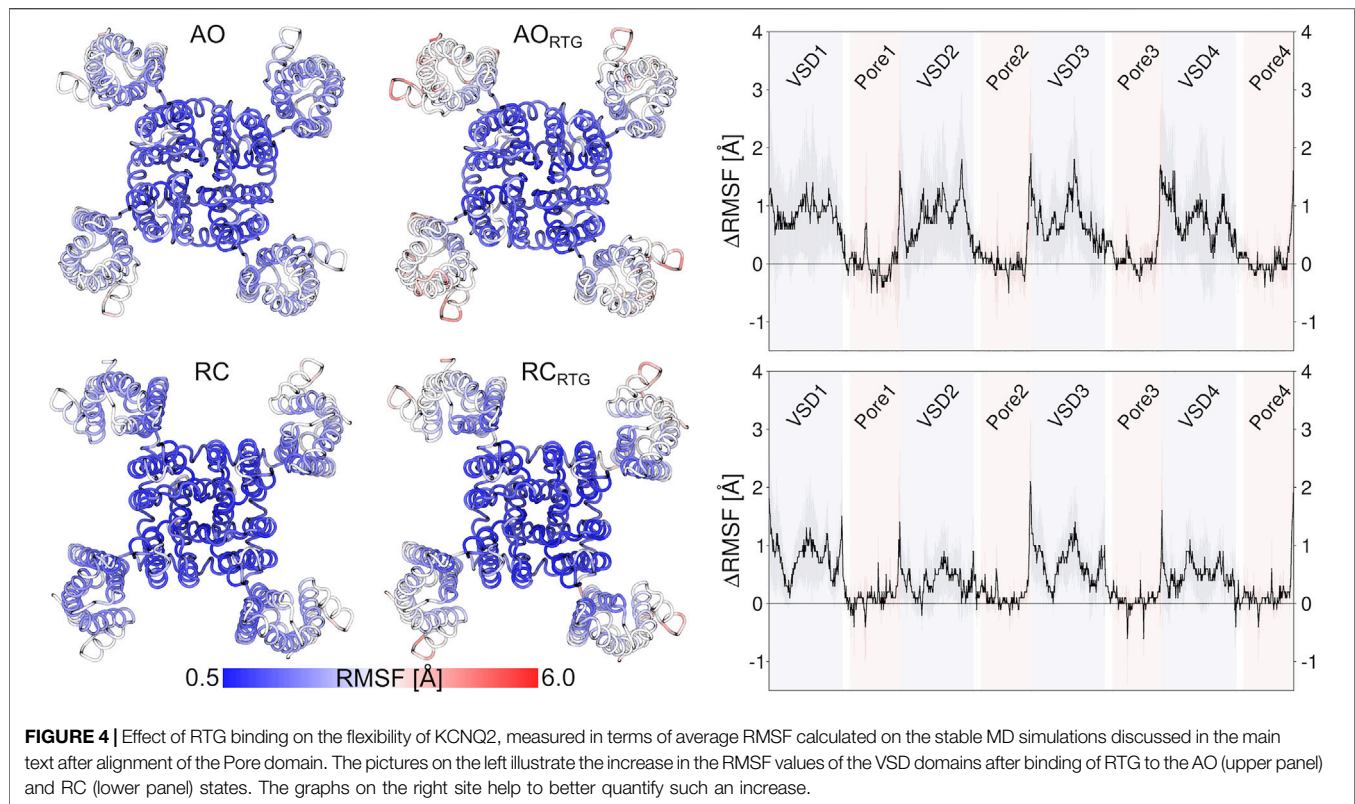
that each simulation maintains the intended state without evolving to any of the other ones. Indeed, the conformations within each simulation are markedly closer to the initial model of the corresponding state than to the two other ones (**Supplementary Figure S4**).

Next, we analysed the features of the binding site of the anticonvulsant drug RTG, targeting KCNQ2-5 channels (Kim et al., 2015). Since the structure of RTG bound to the KCNQ2 channel in the AC state (Li et al., 2021) was not published when this study was designed, we identified the putative residues lining this binding site in KCNQ2 based on the information available from literature (see Methods section). Importantly, that region compares very well with the experimental binding site reported by Li et al. with 8 out of 11 residues lining that site being also included in our selection. This essentially expands in this work by a few residues the true binding site for RTG (**Figure 1**). Moreover, while the binding of RTG has been characterized for the AC state of KCNQ2, no structural information is available regarding the binding of the modulator to the RC and AO states. Therefore, studying the dynamical features of this site on all conformational states of this channel could provide additional insights into the mechanism of action of RTG.

Along this line, we first assessed if and to what extent the precise geometry of the binding site hosting RTG in the experimental structure is reproduced during the MD simulations of the AC, AO, and RC conformational states of KCNQ2. As can be seen in **Figure 3**, bound-like conformations are sampled along all simulations with the RMSD calculated at the RTG site reaching values as low as 1.3, 1.5, and 1.7 Å for the RC, AC, and AO conformational states, respectively. A significant fraction of conformations with RMSD values lower than 2 Å were sampled in the RC and, to a slightly lower extent, AC states.

However, it is worth noticing that also the AO state, starting from a conformation distant 3.6 Å from the experimental geometry (2.3 and 2.4 Å for RC and AC, respectively), also assumed a non-negligible fractions of bound-like conformations.

To further assess the possibility of drug binding at this site in all KCNQ2 conformational states, we estimated the fraction of druggable geometries sampled along the trajectories of each of them. Namely, we calculated the druggability score D on a set of structures obtained from an additional cluster analysis performed on



the putative RTG binding site identified in **Figure 1** (see **Supplementary Table S5**). Such analysis was justified not only because of the larger conformational variability of the RTG site in the AO state (**Figure 3**), but also in view of: 1) previous findings by Kim and co-workers (Kim et al., 2015), reporting two possible orientations assumed by the residue W265 of the KCNQ3 channel—equivalent to W236 in KCNQ2—when in complex with RTG; 2) the change in the network of residues involved in interactions with RTG, which was suggested to occur upon switch of the channel from a closed to an open state (Syeda et al., 2016). According to the software *fpocket* (Le Guilloux et al., 2009), see Methods section), a site is defined as druggable (that is, likely to accommodate a drug-like molecule) if *D* is larger than 0.5. The results of this analysis (**Table 2**) show that: 1) for each state there are at least two druggable RTG binding sites; 2) in the RC state, three out of four RTG binding sites sample druggable conformations, and their relative population is the highest among the three states; 3) the AO state features the lowest relative population of druggable conformations, although their scores are on average the highest among the series. The occurrence of druggable conformations of the RTG binding sites in all states of the channel could have implications for the action mechanism of RTG and other modulators.

Characterization of RTG Binding Onto Putative Binding Site

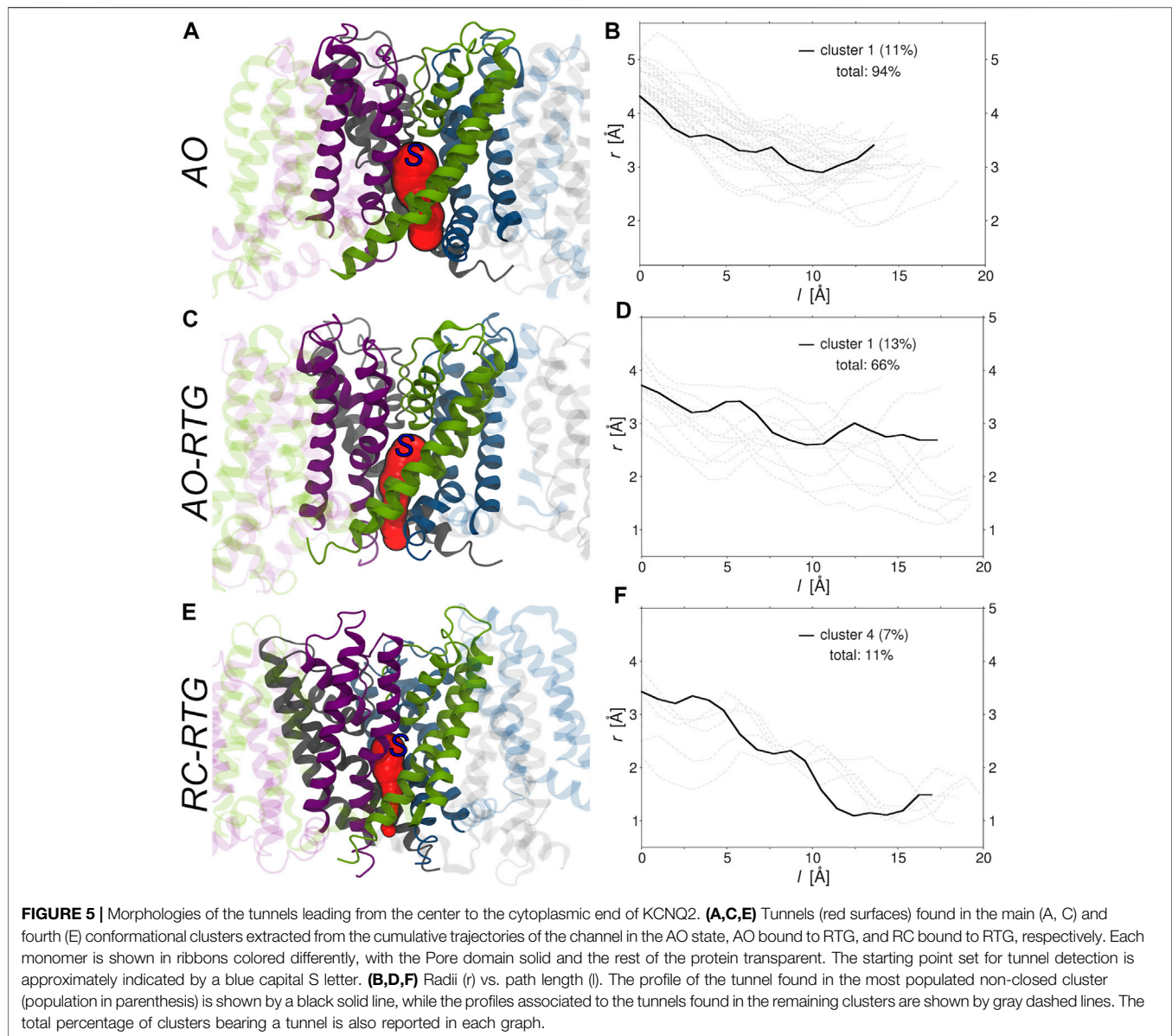
To identify possible binding modes of RTG on KCNQ2 in the AO and RC conformational states, we performed molecular docking calculations on different conformations of the four putative

binding sites located on the Pore domain of the channel. Namely, ensemble docking was performed on 42 and 16 structures in the AO and RC states, respectively (see **Supplementary Table S5** and the Methods section). At least one pose resembling the experimental binding mode was reproduced for both states, although the orientation of the residues lining the experimental binding site was virtually reproduced only in the AO state (**Supplementary Figures S5, S6**). Note that the docking score appears to be relatively insensitive to the conformation assumed by the channel, which points to the possibility of stable RTG binding to the protein bearing an open Pore. To further assess this possibility, starting from the top eight non-overlapping docking poses within each site (selected by visual inspection), we performed 24 1 μ s-long simulations for the AO-RTG and for the RC-RTG complexes (three replicas for each pose, for a cumulative time of 48 μ s). Given the unavailability of an experimental pose of RTG at the time of running our simulations, we relied on usual criteria (high docking score and pose occurrence) to select plausible conformations of the complexes.

Among the poses selected as starting structures for MD simulations, the ones resembling more closely the experimental structure of RTG featured RMSD values of 4.7 Å and 3.5 Å for the RC and AO states, respectively (**Supplementary Figures S5, S6**). Out of the 24 MD simulations performed for each of the AO and RC states, respectively 12 and 20 resulted in stable complexes between RTG and the channel, confirming the possibility of complex formation in different KCNQ2 states. Remarkably, in a few (one) simulations of the AO(RC)-RTG complex, the RTG molecule evolved towards a binding conformation closely

TABLE 4 | Key interactions characterizing the active and resting states of the four VSD domains of the KCNQ2 channel reproduced during the MD simulations of the RTG-channel complexes. See **Table 1** for details.

System		VSD domain	Key interactions in active state																				Interactions per VSD domain (# activated domains)	Key interactions in resting state																				Interactions per VSD domain (# resting domains)																																																																																																																																																																																																																																																																																																																																																																																																																																																																																																																																																																																																																																																																																																																																																																																																																																																																																																																																																																																																																																																																																																																																																																																																																																																																												
			D-R5				E1-Q3				E1-R4				E2-R5				E2-R6					D-R4				E-R4				E1-R1				E2-R2				R2-Q3																																																																																																																																																																																																																																																																																																																																																																																																																																																																																																																																																																																																																																																																																																																																																																																																																																																																																																																																																																																																																																																																																																																																																																																																																																																																																
			1	2	3	4	1	2	3	4	1	2	3	4	1	2	3	4	1	2	3	4		1	2	3	4	1	2	3	4	1	2	3	4	1	2	3	4																																																																																																																																																																																																																																																																																																																																																																																																																																																																																																																																																																																																																																																																																																																																																																																																																																																																																																																																																																																																																																																																																																																																																																																																																																																																																	
RTG-AO	Replica	1																																																																																																																																																																																																																																																																																																																																																																																																																																																																																																																																																																																																																																																																																																																																																																																																																																																																																																																																																																																																																																																																																																																																																																																																																																																																																																																						



resembling the experimental one (minimum RMSD values amounting to 0.8 and 0.7 Å from starting values of 4.4 and 4.8 Å, respectively; see **Supplementary Figures S7, S8**).

More importantly, the most populated cluster of the RTG-AO complex is the one featuring a RTG binding mode essentially equivalent to the experimental one, associated with a relatively high affinity compared to most clusters (**Table 3**). This nicely validates our overall modelling and simulation strategy, and points to the possibility for this modulator to interact with states other than AC without the need to significantly alter its contact network.

To assess more quantitatively the sampling of conformations of RTG resembling the experimental geometry in the RTG-AC complex, we performed a cluster analysis on the cumulative trajectory of each simulated system. In addition, we estimated the stability of the binding poses corresponding to the 10 most populated

clusters via MM/GBSA calculations (see Methods section). We notice that, on average, the affinity of the ligand is higher towards the channel in the AO state than the RC one (although the differences are minor and should be taken as a qualitative indication about binding propensity of RTG). While experimental binding geometries were recovered also in the simulations of the RTG-RC complexes (**Supplementary Figure S8**), they were not picked up in the top 10 conformational clusters (the lowest RMSD being 3.5 Å for the 5th cluster representative, see **Table 3**).

As we don't know if the binding mode of RTG is fully conserved across the different states of the channel, in the following we discuss our results in terms of average structural and dynamical properties across the stable trajectories of the complexes. This allows evaluating our findings on the effect of RTG binding on KCNQ2 free of any experimental bias. First, we found that binding

of RTG alters the dynamics of the channel; namely, it slightly rigidifies the Pore domain, and moreover, it increases the flexibility of the VSD domains with respect to the unbound protein, particularly in the AO state (**Figure 4**). This result is in agreement with the findings reported in (Li et al., 2021), showing an increase in the values of the B-factor of the VSD domains upon binding of four RTG molecules. Our data suggest that such an increase represents a general consequence of RTG binding to any conformational state of the channel. Next, to assess if the enhanced flexibility of the VSD domains resulting from RTG binding affects their propensity towards active conformations, we analysed the occurrence of specific interactions characterizing VSD active and resting (**Table 4**, **Supplementary Tables S6, S7**). Interestingly, binding of RTG to the RC state induces a decrease from 66 to 50% in the percentage of MD simulations featuring at least one VSD domain in the resting state (although no active VSD domain was detected, possibly due to the longer timescales of this event compared to the length of our simulations, and to the presence of only one compound instead of four as in the cryo-EM structures). In contrast, binding of the modulator to the AO state does not significantly alter the relative occurrence of activated vs. resting conformations, consistently with the proposed mechanism of action (Gunthorpe et al., 2012; Li et al., 2021).

Finally, we investigated if and to what extent the binding of RTG alters the morphology of tunnels leading from the center of KCNQ2 (beneath the selectivity filter) to its cytoplasmic gate. To this end, we run the software CAVER (Chovancova et al., 2012) on the representative structures of all the conformational clusters extracted from the cumulative trajectory of each simulated system (**Supplementary Table S5**). Consistently with experiments, in the absence of RTG virtually all conformations of the protein bear a tunnel in the AO state; in contrast, only closed conformations were found for the AC and RC states. Tunnel bottlenecks were found near the cytoplasmic end of the protein, with radii ranging from 1.9 to 3.5 Å (2.9 Å for the representative of the most populated cluster; see **Figure 5**). Binding of RTG to the channel in the AO state did not induce large structural changes in the morphology of the Pore, with 2/3 of the conformations still bearing a tunnel. More relevantly, binding of just one RTG molecule to the RC state seems to alter the conformational equilibrium of KCNQ2 in favour of conformations bearing an open Pore. Indeed, about 1/10 of the cluster representatives feature a tunnel with a bottleneck radius ranging between 1 and 1.2 Å.

While the limitations of our approach do not allow to assess the long-term effects of RTG binding on KCNQ2, the early steps of channel opening induced by ligand binding caught by our analysis shed light on the mechanism of action by this compound. Overall, our findings support an allosteric mechanism in which binding of RTG to the channel would promote its transition towards the AO conformational state. Such conformational transition could occur, according to our data, without the need for drastic rearrangements of RTG within the binding site recently validated by Li and co-workers (Li et al., 2021).

CONCLUDING REMARKS

KCNQ2 is a main molecular determinant of the M-current, a widespread K^+ current regulating neuronal excitability. Because of their fundamental role in regulating cellular excitability, this channel in its heterotetrameric form with KCNQ3 is implicated in several human disease conditions, including epilepsy, pain, migraine, arrhythmias, sensory dysfunction, and metabolic illnesses. The KCNQ2/KCNQ3 opener retigabine represents an attractive compound for the treatment of these diseases. Structural information about the molecular interactions of this compound with KCNQ2 along the conformational cycle (the various states) of the channel can be highly informative to drug design efforts.

However, apart the recent cryo-EM structure of AC KCNQ2, alone and in complex with RTG (unavailable when this work was undertaken), to date there are no KCNQ2 structures available in the RC and AO states. For these reasons our efforts were aimed at generating models of all three states and characterise their dynamics and interaction with RTG. Conformations extracted from the molecular dynamics simulations were used to dock RTG into the AO and RC states and compared with the experimental structure of the KCNQ2 in the AC state complexed with RTG. All the generated models of both the apo structures in various states as well as the complexes with RTG were subjected to MD simulations, for a total simulated time of ~50 μ s. The analysis of the trajectories confirmed the stability of the apo structures as well as the AO and RC structures complexed with RTG. Our results on the effect of binding of one RTG molecule to the AO and RC states are in line with experimental findings on the channel in the AC state bound to four drug molecules. Overall, our data suggest that RTG can bind to the same site of the channel, and maintaining the same orientation, independently of the KCNQ2 (and thus Pore domain) conformation/state. Furthermore, our simulations of the RTG-bound states unveil a tendency of the channel towards increased flexibility of the VSD domains and sampling of conformations corresponding to an open Pore, which are also in line with experiments. The excellent agreement of our simulations with the experimental AC state structure gives trust into our modelling approach and confidence that the new models of the AO and RC states of this channel are reliable, allowing to uncover new insightful details on the interaction of this channel with RTG.

DATA AVAILABILITY STATEMENT

The original contributions presented in the study are included in the article/**Supplementary Material**, further inquiries can be directed to the corresponding authors.

AUTHOR CONTRIBUTIONS

BG, AMB, RO, and AV designed research; AV performed research; BG, AB and AV analysed the data; BG and AV wrote the manuscript with contributions from all authors; AMB and AV obtained fundings for this work.

FUNDING

AMB and AV acknowledge financial support from the from the European Union Horizon 2020 project BioExcel (823830).

REFERENCES

- Abd-Elseyed, A., Jackson, M., Gu, S. L., Fiala, K., and Gu, J. (2019). Neuropathic Pain and Kv7 Voltage-Gated Potassium Channels: The Potential Role of Kv7 Activators in the Treatment of Neuropathic Pain. *Mol. Pain* 15, 174480691986425. doi:10.1177/1744806919864256
- Alberini, G., Benfenati, F., and Maragliano, L. (2021). Structural Mechanism of ω -Currents in a Mutated Kv7.2 Voltage Sensor Domain from Molecular Dynamics Simulations. *J. Chem. Inf. Model.* 61, 1354–1367. doi:10.1021/acs.jcim.0c01407
- Ashcroft, F. M. (2000). *Ion Channels and Disease*. Oxford, UK: Elsevier.
- Barrese, V., Stott, J. B., and Greenwood, I. A. (2018). KCNQ-Encoded Potassium Channels as Therapeutic Targets. *Annu. Rev. Pharmacol. Toxicol.* 58, 625–648. doi:10.1146/annurev-pharmtox-010617-052912
- Basciu, A., Koukos, P. I., Mallocci, G., Bonvin, A. M. J. J., and Vargiu, A. V. (2019a). Coupling Enhanced Sampling of the Apo-Receptor with Template-Based Ligand Conformers Selection: Performance in Pose Prediction in the D3R Grand Challenge 4. *J. Comput. Aided Mol. Des.* 34, 149–162. doi:10.1007/s10822-019-00244-6
- Basciu, A., Mallocci, G., Pietrucci, F., Bonvin, A. M. J. J., and Vargiu, A. V. (2019b). Holo-Like and Druggable Protein Conformations from Enhanced Sampling of Binding Pocket Volume and Shape. *J. Chem. Inf. Model.* 59, 1515–1528. doi:10.1021/acs.jcim.8b00730
- Bezanilla, F., and Stefani, E. (1994). Voltage-Dependent Gating of Ionic Channels. *Annu. Rev. Biophys. Biomol. Struct.* 23, 819–846. doi:10.1146/annurev.bb.23.060194.004131
- Bezanilla, F. (2000). The Voltage Sensor in Voltage-Dependent Ion Channels. *Physiol. Rev.* 80, 555–592. doi:10.1152/physrev.2000.80.2.555
- Bordas, C., Kovacs, A., and Pal, B. (2015). The M-Current Contributes to High Threshold Membrane Potential Oscillations in a Cell Type-specific Way in the Pedunculopontine Nucleus of Mice. *Front. Cel. Neurosci.* 9, 121. doi:10.3389/fncel.2015.00121
- Brown, D. A., and Adams, P. R. (1980). Muscarinic Suppression of a Novel Voltage-Sensitive K⁺ Current in a Vertebrate Neurone. *Nature* 283, 673–676. doi:10.1038/283673a0
- Brown, D. A., and Passmore, G. M. (2009). Neural KCNQ (Kv7) Channels. *Br. J. Pharmacol.* 156, 1185–1195. doi:10.1111/j.1476-5381.2009.00111.x
- Case, D. A., Ben-Shalom, I. Y., Brozell, S. R., Cerutti, D. S., Cheatham, T. E., Cruzeiro, V. W. D., et al. (2018). *AMBER18*. San Francisco: University of California.
- Chovancova, E., Pavelka, A., Benes, P., Strnad, O., Brezovsky, J., Kozlikova, B., et al. (2012). CAVER 3.0: A Tool for the Analysis of Transport Pathways in Dynamic Protein Structures. *Plos Comput. Biol.* 8, e1002708. doi:10.1371/journal.pcbi.1002708
- Clark, S., Antell, A., and Kaufman, K. (2015). New Antiepileptic Medication Linked to Blue Discoloration of the Skin and Eyes. *Ther. Adv. Drug Saf.* 6, 15–19. doi:10.1177/2042098614560736
- Delmas, P., and Brown, D. A. (2005). Pathways Modulating Neural KCNQ/M (Kv7) Potassium Channels. *Nat. Rev. Neurosci.* 6, 850–862. doi:10.1038/nrn1785
- DeMarco, K. R., Bekker, S., and Vorobyov, I. (2019). Challenges and Advances in Atomistic Simulations of Potassium and Sodium Ion Channel Gating and Permeation. *J. Physiol.* 597, 679–698. doi:10.1113/JP277088
- Di Cesare Mannelli, L., Lucarini, E., Micheli, L., Mosca, I., Ambrosino, P., Soldovieri, M. V., et al. (2017). Effects of Natural and Synthetic Isothiocyanate-Based H₂S-Releasers against Chemotherapy-Induced Neuropathic Pain: Role of Kv7 Potassium Channels. *Neuropharmacology* 121, 49–59. doi:10.1016/j.neuropharm.2017.04.029
- Du, X., Gao, H., Jaffe, D., Zhang, H., and Gamper, N. (2018). M-Type K⁺ Channels in Peripheral Nociceptive Pathways: M Channels in Peripheral Nociceptive Pathways. *Br. J. Pharmacol.* 175, 2158–2172. doi:10.1111/bph.13978
- Frisch, M. J., Trucks, G. W., Schlegel, H. B., Scuseria, G. E., Robb, M. A., Cheeseman, J. R., et al. (2016). *Gaussian-09 Revision E.01*. Wallingford, CT: Gaussian, Inc.
- Genheden, S., and Ryde, U. (2015). The MM/PBSA and MM/GBSA Methods to Estimate Ligand-Binding Affinities. *Expert Opin. Drug Discov.* 10, 449–461. doi:10.1517/17460441.2015.1032936
- Gunthorpe, M. J., Large, C. H., and Sankar, R. (2012). The Mechanism of Action of Retigabine (Ezogabine), a First-In-Class K⁺ Channel Opener for the Treatment of Epilepsy. *Epilepsia* 53, 412–424. doi:10.1111/j.1528-1167.2011.03365.x
- Hernandez, C. C., Falkenburger, B., and Shapiro, M. S. (2009). Affinity for Phosphatidylinositol 4,5-bisphosphate Determines Muscarinic Agonist Sensitivity of Kv7 K⁺ Channels. *J. Gen. Physiol.* 134, 437–448. doi:10.1085/jgp.200910313
- Hille, B. (2001). *Ion Channels of Excitable Membranes*. Sunderland, Massachusetts: Sinauer, 3.
- Jacobson, M. P., Pincus, D. L., Rapp, C. S., Day, T. J. F., Honig, B., Shaw, D. E., et al. (2004). A Hierarchical Approach to All-Atom Protein Loop Prediction. *Proteins* 55, 351–367. doi:10.1002/prot.10613
- Jensen, M. Ø., Jogini, V., Borhani, D. W., Leffler, A. E., Dror, R. O., and Shaw, D. E. (2012). Mechanism of Voltage Gating in Potassium Channels. *Science* 336, 229–233. doi:10.1126/science.1216533
- Jentsch, T. J. (2000). Neuronal KCNQ Potassium Channels: physiology and Role in Disease. *Nat. Rev. Neurosci.* 1, 21–30. doi:10.1038/35036198
- Jepps, T. A., Barrese, V., and Miceli, F. (2021). Editorial: Kv7 Channels: Structure, Physiology, and Pharmacology. *Front. Physiol.* 12, 679317. doi:10.3389/fphys.2021.679317
- Kasimova, M. A., Lindahl, E., and Delemotte, L. (2018). Determining the Molecular Basis of Voltage Sensitivity in Membrane Proteins. *J. Gen. Physiol.* 150, 1444–1458. doi:10.1085/jgp.201812086
- Khalili-Araghi, F., Jogini, V., Yarov-Yarovsky, V., Tajkhorshid, E., Roux, B., and Schulten, K. (2010). Calculation of the Gating Charge for the Kv1.2 Voltage-Activated Potassium Channel. *Biophysical J.* 98, 2189–2198. doi:10.1016/j.bpj.2010.02.056
- Kim, R. Y., Yau, M. C., Galpin, J. D., Seeböhm, G., Ahern, C. A., Pless, S. A., et al. (2015). Atomic Basis for Therapeutic Activation of Neuronal Potassium Channels. *Nat. Commun.* 6, 8116. doi:10.1038/ncomms9116
- Kleywegt, G. J., and Jones, T. A. (1994). Detection, Delineation, Measurement and Display of Cavities in Macromolecular Structures. *Acta Cryst. D* 50, 178–185. doi:10.1107/S0907444993011333
- Kristensen, L. V., Sandager-Nielsen, K., and Hansen, H. H. (2012). Kv7 (KCNQ) Channel Openers Normalize central 2-Deoxyglucose Uptake in a Mouse Model of Mania and Increase Prefrontal Cortical and Hippocampal Serine-9 Phosphorylation Levels of GSK3 β : Anti-Manic Efficacy of Kv7 Channel Openers. *J. Neurochem.* 121, 373–382. doi:10.1111/j.1471-4159.2012.07704.x
- Kuenze, G., Duran, A. M., Woods, H., Brewer, K. R., McDonald, E. F., Vanoye, C. G., et al. (2019). Upgraded Molecular Models of the Human KCNQ1 Potassium Channel. *PLoS ONE* 14, e0220415. doi:10.1371/journal.pone.0220415
- Lange, W., Geißendörfer, J., Schenzer, A., Grötzinger, J., Seeböhm, G., Friedrich, T., et al. (2009). Refinement of the Binding Site and Mode of Action of the Anticonvulsant Retigabine on KCNQ K⁺ Channels. *Mol. Pharmacol.* 75, 272–280. doi:10.1124/mol.108.052282
- Le Guilloux, V., Schmidtke, P., and Tuffery, P. (2009). Fpocket: An Open Source Platform for Ligand Pocket Detection. *BMC Bioinformatics* 10, 168. doi:10.1186/1471-2105-10-168
- Li, S., Choi, V., and Tzounopoulos, T. (2013). Pathogenic Plasticity of Kv7.2/3 Channel Activity Is Essential for the Induction of Tinnitus. *Proc. Natl. Acad. Sci.* 110, 9980–9985. doi:10.1073/pnas.1302770110

SUPPLEMENTARY MATERIAL

The Supplementary Material for this article can be found online at: <https://www.frontiersin.org/articles/10.3389/fmolb.2022.839249/full#supplementary-material>

- Li, X., Zhang, Q., Guo, P., Fu, J., Mei, L., Lv, D., et al. (2021). Molecular Basis for Ligand Activation of the Human KCNQ2 Channel. *Cell Res* 31, 52–61. doi:10.1038/s41422-020-00410-8
- Lomize, M. A., Pogozheva, I. D., Joo, H., Mosberg, H. I., and Lomize, A. L. (2012). OPM Database and PPM Web Server: Resources for Positioning of Proteins in Membranes. *Nucleic Acids Res.* 40, D370–D376. doi:10.1093/nar/gkr703
- Maljevic, S., Lerche, C., Seeböhm, G., Alekov, A. K., Busch, A. E., and Lerche, H. (2003). C-Terminal Interaction of KCNQ2 and KCNQ3 K⁺ Channels. *J. Physiol.* 548, 353–360. doi:10.1113/jphysiol.2003.040980
- Maljevic, S., Wuttke, T. V., and Lerche, H. (2008). Nervous System K_v 7 Disorders: Breakdown of a Subthreshold Brake: Nervous System K_v 7 Disorders. *J. Physiol.* 586, 1791–1801. doi:10.1113/jphysiol.2008.150656
- Marrion, N. V. (1997). Control of M-Current. *Annu. Rev. Physiol.* 59, 483–504. doi:10.1146/annurev.physiol.59.1.483
- Miceli, F., Soldovieri, M. V., Ambrosino, P., Barrese, V., Migliore, M., Cilio, M. R., et al. (2013). Genotype–Phenotype Correlations in Neonatal Epilepsies Caused by Mutations in the Voltage Sensor of K_v 7.2 Potassium Channel Subunits. *Proc. Natl. Acad. Sci. USA* 110, 4386–4391. doi:10.1073/pnas.1216867110
- Miceli, F., Soldovieri, M. V., Hernandez, C. C., Shapiro, M. S., Annunziato, L., and Tagliatela, M. (2008). Gating Consequences of Charge Neutralization of Arginine Residues in the S4 Segment of Kv7.2, an Epilepsy-Linked K⁺ Channel Subunit. *Biophysical J.* 95, 2254–2264. doi:10.1529/biophysj.107.128371
- Miller, C. (2000). An Overview of the Potassium Channel Family. *Genome Biol.* 1 (4), REVIEWS0004. doi:10.1186/gb-2000-1-4-reviews0004
- Morris, G. M., Huey, R., Lindstrom, W., Sanner, M. F., Belew, R. K., Goodsell, D. S., et al. (2009). AutoDock4 and AutoDockTools4: Automated Docking with Selective Receptor Flexibility. *J. Comput. Chem.* 30, 2785–2791. doi:10.1002/jcc.21256
- Nguyen, H., Roe, D. R., and Simmerling, C. (2013). Improved Generalized Born Solvent Model Parameters for Protein Simulations. *J. Chem. Theor. Comput.* 9, 2020–2034. doi:10.1021/ct3010485
- Nikitin, E., and Vinogradova, L. (2021). Potassium Channels as Prominent Targets and Tools for the Treatment of Epilepsy. *Expert Opin. Ther. Targets* 25, 1–13. doi:10.1080/14728222.2021.1908263
- Robbins, J. (2001). KCNQ Potassium Channels: Physiology, Pathophysiology, and Pharmacology. *Pharmacol. Ther.* 90, 1–19. doi:10.1016/S0163-7258(01)00116-4
- Schmidtke, P., and Barril, X. (2010). Understanding and Predicting Druggability. A High-Throughput Method for Detection of Drug Binding Sites. *J. Med. Chem.* 53, 5858–5867. doi:10.1021/jm100574m
- Shieh, C. C., Coghlan, M., Sullivan, J. P., and Gopalakrishnan, M. (2000). Potassium Channels: Molecular Defects, Diseases, and Therapeutic Opportunities. *Pharmacol. Rev.* 52, 557–594.
- Soldovieri, M. V., Miceli, F., and Tagliatela, M. (2011). Driving with No Brakes: Molecular Pathophysiology of Kv7 Potassium Channels. *Physiology* 26, 365–376. doi:10.1152/physiol.00009.2011
- Spek, A. L. (2009). Structure Validation in Chemical Crystallography. *Acta Crystallogr. D Biol. Cryst.* 65, 148–155. doi:10.1107/S090744490804362X
- Šterbuleac, D. (2021). Molecular Dynamics: A Powerful Tool for Studying the Medicinal Chemistry of Ion Channel Modulators. *RSC Med. Chem.* 12, 1503–1518. doi:10.1039/D1MD00140J
- Sun, J., and MacKinnon, R. (2017). Cryo-EM Structure of a KCNQ1/CaM Complex Reveals Insights into Congenital Long QT Syndrome. *Cell* 169, 1042–1050. e9. doi:10.1016/j.cell.2017.05.019
- Syeda, R., Santos, J. S., and Montal, M. (2016). The Sensorless Pore Module of Voltage-Gated K⁺ Channel Family 7 Embodies the Target Site for the Anticonvulsant Retigabine. *J. Biol. Chem.* 291, 2931–2937. doi:10.1074/jbc.M115.683185
- Villa, C., and Combi, R. (2016). Potassium Channels and Human Epileptic Phenotypes: An Updated Overview. *Front. Cel. Neurosci.* 10, 81. doi:10.3389/fncel.2016.00081
- Wang, C. K., Lamothe, S. M., Wang, A. W., Yang, R. Y., and Kurata, H. T. (2018). Pore- and Voltage Sensor-Targeted KCNQ Openers Have Distinct State-Dependent Actions. *J. Gen. Physiol.* 150, 1722–1734. doi:10.1085/jgp.201812070
- Wang, J., Wolf, R. M., Caldwell, J. W., Kollman, P. A., and Case, D. A. (2004). Development and Testing of a General Amber Force Field. *J. Comput. Chem.* 25, 1157–1174. doi:10.1002/jcc.20035
- Weiser, J. r., Shenkin, P. S., and Still, W. C. (1999). Approximate Atomic Surfaces from Linear Combinations of Pairwise Overlaps (LCPO). *J. Comput. Chem.* 20, 217–230. doi:10.1002/(SICI)1096-987X(19990130)20:2<217::AID-JCCA>3.0.CO;2-A
- Williams, C. J., Headd, J. J., Moriarty, N. W., Prisant, M. G., Videau, L. L., Deis, L. N., et al. (2018). MolProbity: More and Better Reference Data for Improved All-Atom Structure Validation: Protein Science. *Protein Sci.* 27, 293–315. doi:10.1002/pro.3330
- Wu, D., Delaloye, K., Zaydman, M. A., Nekouzadeh, A., Rudy, Y., and Cui, J. (2010). State-Dependent Electrostatic Interactions of S4 Arginines with E1 in S2 during Kv7.1 Activation. *J. Gen. Physiol.* 135, 595–606. doi:10.1085/jgp.201010408
- Wu, E. L., Cheng, X., Jo, S., Rui, H., Song, K. C., Dávila-Contreras, E. M., et al. (2014). CHARMM-GUIMembrane Buildertoward Realistic Biological Membrane Simulations. *J. Comput. Chem.* 35, 1997–2004. doi:10.1002/jcc.23702
- Yarov-Yarovoy, V., DeCaen, P. G., Westenbroek, R. E., Pan, C.-Y., Scheuer, T., Baker, D., et al. (2012). Structural Basis for Gating Charge Movement in the Voltage Sensor of a Sodium Channel. *Proc. Natl. Acad. Sci.* 109, E93–E102. doi:10.1073/pnas.1118434109
- Zwierzyńska, E., Krupa-Burtnik, A., and Pietrzak, B. (2017). The Possibility of Adverse Effect of Kv7-Channel Opener Retigabine on Memory Processes in Rats. *Epilepsy Behav.* 75, 170–175. doi:10.1016/j.yebeh.2017.08.004

Conflict of Interest: BG, FD, and RO are employees of Angelini Pharma S.p.A., which funded this research under the project “In silico characterization of the open and closed structures of the KV7.2 potassium channel.”

The remaining authors declare that the research was conducted in the absence of any commercial or financial relationships that could be construed as a potential conflict of interest.

Publisher’s Note: All claims expressed in this article are solely those of the authors and do not necessarily represent those of their affiliated organizations, or those of the publisher, the editors and the reviewers. Any product that may be evaluated in this article, or claim that may be made by its manufacturer, is not guaranteed or endorsed by the publisher.

Copyright © 2022 Garofalo, Bonvin, Bosin, Di Giorgio, Ombrato and Vargiu. This is an open-access article distributed under the terms of the Creative Commons Attribution License (CC BY). The use, distribution or reproduction in other forums is permitted, provided the original author(s) and the copyright owner(s) are credited and that the original publication in this journal is cited, in accordance with accepted academic practice. No use, distribution or reproduction is permitted which does not comply with these terms.



Unifying Single-Channel Permeability From Rare-Event Sampling and Steady-State Flux

Yi-Chun Lin and Yun Lyna Luo*

Department of Pharmaceutical Sciences, Western University of Health Sciences, Pomona, CA, United States

OPEN ACCESS

Edited by:

Matteo Masetti,
University of Bologna, Italy

Reviewed by:

Fatemeh Khalili-Araghi,
University of Illinois at Chicago,
United States
Grazia Cottone,
University of Palermo, Italy

*Correspondence:

Yun Lyna Luo
luoy@westernu.edu

Specialty section:

This article was submitted to
Biological Modeling and Simulation,
a section of the journal
Frontiers in Molecular Biosciences

Received: 24 January 2022

Accepted: 07 March 2022

Published: 13 April 2022

Citation:

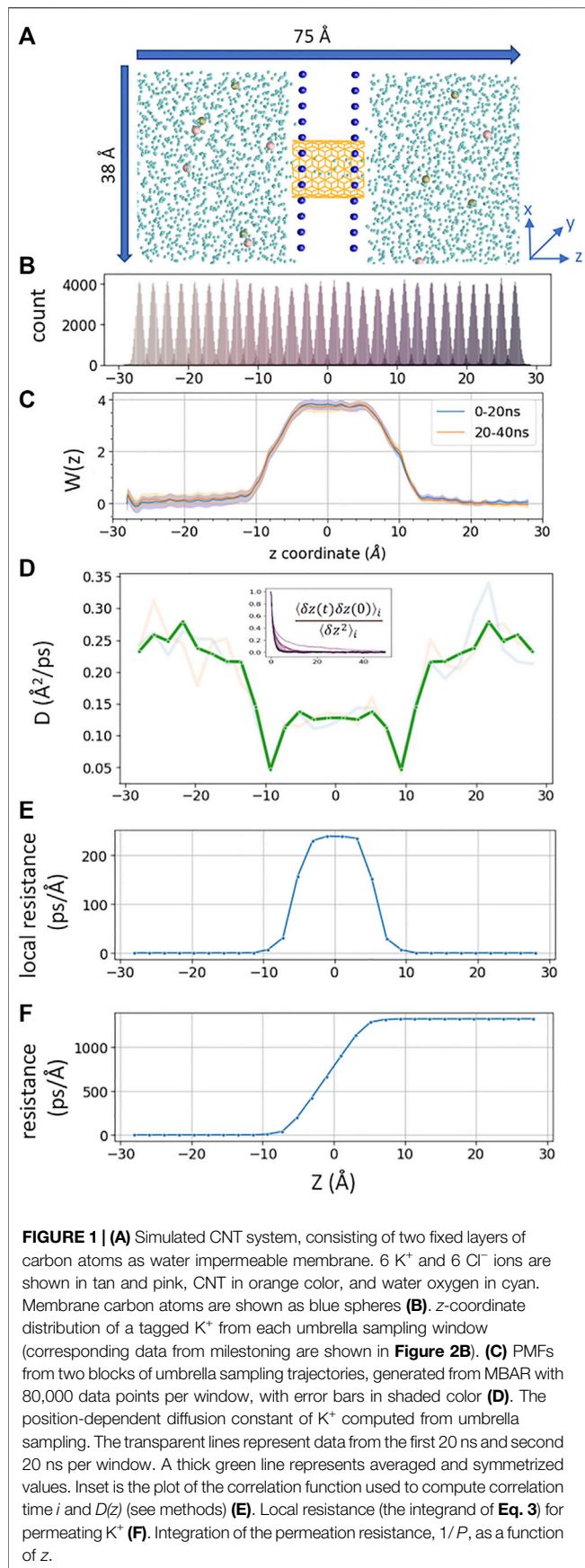
Lin Y-C and Luo YL (2022) Unifying
Single-Channel Permeability From
Rare-Event Sampling and Steady-
State Flux.
Front. Mol. Biosci. 9:860933.
doi: 10.3389/fmolb.2022.860933

Various all-atom molecular dynamics (MD) simulation methods have been developed to compute free energies and crossing rates of ions and small molecules through ion channels. However, a systemic comparison across different methods is scarce. Using a carbon nanotube as a model of small conductance ion channel, we computed the single-channel permeability for potassium ion using umbrella sampling, Markovian milestoning, and steady-state flux under applied voltage. We show that a slightly modified inhomogeneous solubility-diffusion equation yields a single-channel permeability consistent with the mean first passage time (MFPT) based method. For milestoning, applying cylindrical and spherical bulk boundary conditions yield consistent MFPT if factoring in the effective bulk concentration. The sensitivity of the MFPT to the output frequency of collective variables is highlighted using the convergence and symmetry of the inward and outward MFPT profiles. The consistent transport kinetic results from all three methods demonstrated the robustness of MD-based methods in computing ion channel permeation. The advantages and disadvantages of each technique are discussed, focusing on the future applications of milestoning in more complex systems.

Keywords: ion channel, permeability, milestoning, molecular dynamics simulations, carbon nanotube

INTRODUCTION

Ion channels are complex biological nanopores that perform vital physiological functions with high sensitivity and precision. Over the decades, molecular dynamics (MD) simulation has become an indispensable tool for computing the functional properties of ion channels directly from their dynamic structures. Various MD-based methods were developed for investigating the thermodynamics and kinetics of ions or small-molecules permeation at the single-channel level. Many pioneering atomistic MD simulations on ion channels have focused on computing ion permeation from equilibrium free energy profiles, or potential of mean force (PMF), in conjunction with electro-diffusion theory (Bernèche and Roux, 2001; Allen et al., 2004; Domene et al., 2008; Fowler et al., 2013). The increased computing power and performance of MD engines have also enabled researchers to simulate single-channel conduction explicitly under a constant external electric field (Khalili-Araghi et al., 2006; Roux, 2008) or an asymmetric ionic concentration across the channel (Kutzner et al., 2011; Khalili-Araghi et al., 2013). If the system reaches a steady-state under voltage or concentration gradient, a mean flux rate and a steady-state density profile can be obtained from the ensemble of nonequilibrium processes. These equilibrium and nonequilibrium MD simulations have significantly deepened our understanding of the ion channel permeation process at the high temporal and spatial resolution (Roux, 1998; Zheng and Trudeau, 2015; Flood et al., 2019; Carnevale et al., 2021).



Unlike the steady-state flux under voltage, the equilibrium MD approaches can be generally applied to any small-molecule permeation (neutral or charged). Several theoretical frameworks can be used to compute crossing rates from PMF profiles obtained from enhanced sampling simulations. Particularly, if the PMF is dominated by a single large barrier and the permeant diffusion is constant at the barrier region, the crossing rate can be estimated *via* Kramer's theory or transition state theory (TST) borrowed from reaction kinetics. However, for complex biological ion channels, the aforementioned assumptions may be far from satisfied. Alternatively, molecule permeation may be considered a one-dimensional nonreactive diffusive process that can be described using the fluctuation-dissipation theorem. For instance, PMF can be used together with the position-dependent diffusion coefficient to estimate permeability using the inhomogeneous solubility-diffusion (ISD) equation (Diamond and Katz, 1974). ISD equation has been applied successfully in studying solute permeation across the membrane (Awoonor-Williams and Rowley, 2016; Venable et al., 2019). Herein, we show that a slightly modified ISD equation yields a single-channel permeability consistent with a mean first passage time (MFPT) based method, which extracts detailed kinetics along the molecular permeation pathway directly from rare-event sampling methods. Recent examples of such rare-event sampling applied on ion channels include milestone (Alberini et al., 2018; Cottone et al., 2020; Jiang et al., 2021a), weighted ensemble sampling (Adelman and Grabe, 2015), and Markov state models (Teo and Schulten, 2013; Choudhary et al., 2014; Domene et al., 2021; Hempel et al., 2021). In theory, the PMF-based method, MFPT-based method, and steady-state flux under voltage should converge to the same single-channel permeability for the same studied system. However, a systemic comparison between different methods is still lacking.

In this work, we use a carbon nanotube (CNT) as a model (Figure 1A) of small conductance (~ 2 pS) ion channel to compare K^+ permeability from milestone, umbrella sampling (US), and voltage simulations. This CNT system has been used to compute K^+ permeability using a transition path approach similar to the reactive flux method (Zhou and Zhu, 2019). We chose this system because its free energy barrier height (~ 4 kcal/mol) and microsecond-timescale crossing rate are physiologically relevant. Such a system requires nontrivial sampling (beyond the capability of brute-force MD), but the rigidity of the CNT still allows good convergence and unambiguous comparison of all methods tested here.

The original milestone simulation requires running short trajectories in each milestone until they reach another milestone (Faradjian and Elber, 2004). Here, we use the "soft-walls" Voronoi-tessellated Markovian milestone, which confines the sampling within the Voronoi cells using flat-bottom harmonic restraining potentials (Maragliano et al., 2009). The implementation of this "soft-walls" version (referred to as milestone thereafter) resembles, to a large degree, the conventional umbrella sampling setup. A detailed comparison of the sampling, PMF, and MFPT results from milestone and umbrella sampling is the focus of this study. In addition, we tested two bulk boundary conditions, namely the cylindrical and

TABLE 1 | Summary of the three methods for computing single-channel permeability.

Method	Umbrella sampling	Markovian milestoning	Steady-state flux
Permeability equation	$P = \pi r^2 \left(\int_{z_1}^{z_2} \frac{e^{\beta w(z)}}{D(z)} dz \right)^{-1}$	$P = \frac{\pi r^2 \int_{z_1}^{z_2} e^{-w(z)/k_B T} dz}{2 \times \text{MFPT}}$	$P = \frac{\gamma k_B T}{q^2 C}$
Effective bulk conc.	0.77 M	0.77 M	0.52 M
Biasing potential	Harmonic	Flat-bottom harmonic	Voltage ± 0.4 V
Biasing force constant	2.5 kcal/mol	100 kcal/mol	—
Lateral restraint in bulk	6 Å	6 Å	—
PMF barrier (kcal/mol)	3.8 ± 0.17	4.1 ± 1.7	—
Key parameters	$D(z)$ 0.004 ~0.028 Å ² /ps	MFPT: 2.6 μs	Conductance 2.3 ± 1.2 pS
Permeability (cm ³ /s)	$(8.96 \pm 0.02) \times 10^{-16}$	2.92×10^{-16}	$(11.7 \pm 6.3) \times 10^{-16}$
Total sampling time (μs)	1.12	4.98	0.60

spherical boundaries, that are particularly useful for conducting milestoning on ion channels.

The CNT system chosen here is designed to satisfy the symmetric single barrier requirement, thus allowing us to check the robustness of the milestoning method by computing both inward and outward permeation rates. We also show that the MFPT from milestoning is extremely sensitive to the frequency of recording the relevant collective variables (e.g., the coordinates of the tagged ion). All physical quantities and the obtained results are summarized in **Table 1**. The overall consistent single-channel permeability demonstrated the robustness of the theoretical and computational framework tested here. The limitation and strengths of each method are discussed and compared.

THEORY AND METHODS

Relation Between Single-Channel Permeability, Mean First Passage Time, and Conductance

Assuming permeating molecules do not interact under sufficient low concentration, under physiological conditions, single-channel permeability P (cm³/s) can be related linearly to the rate of crossing k or mean first passage time (MFPT) $\langle t \rangle$ under equilibrium, $P = k/c = 1/\langle t \rangle$, in which c is the symmetric solute concentrations. Here, we use the number of molecules per second for k , seconds per molecule for MFPT, and molecule/cm³ for c .

For ionic permeation under voltage and/or concentration gradient, Goldman–Hodgkin–Katz (GHK) flux equation describes the ionic flux across a homogenous membrane as a function of a constant electric field (voltage) and an ionic concentrations gradient. Under symmetric concentration and constant voltage, the current (I) and the permeability (P) can be related by the GHK flux equation, $I = P z^2 \frac{V_m F^2}{RT} c$, where z is the charge of the permeant, V_m is the voltage, F is the Faraday constant, R is the gas constant, T is the absolute temperature, and c is the concentration (Hille, 2001). When applied to a membrane-embedded single-channel model and ions only cross the membrane through the channel, P in the GHK equation corresponds to the single-channel permeability. GHK

flux equation thus relates single-channel conductance γ , a nonequilibrium property, to the equilibrium property P .

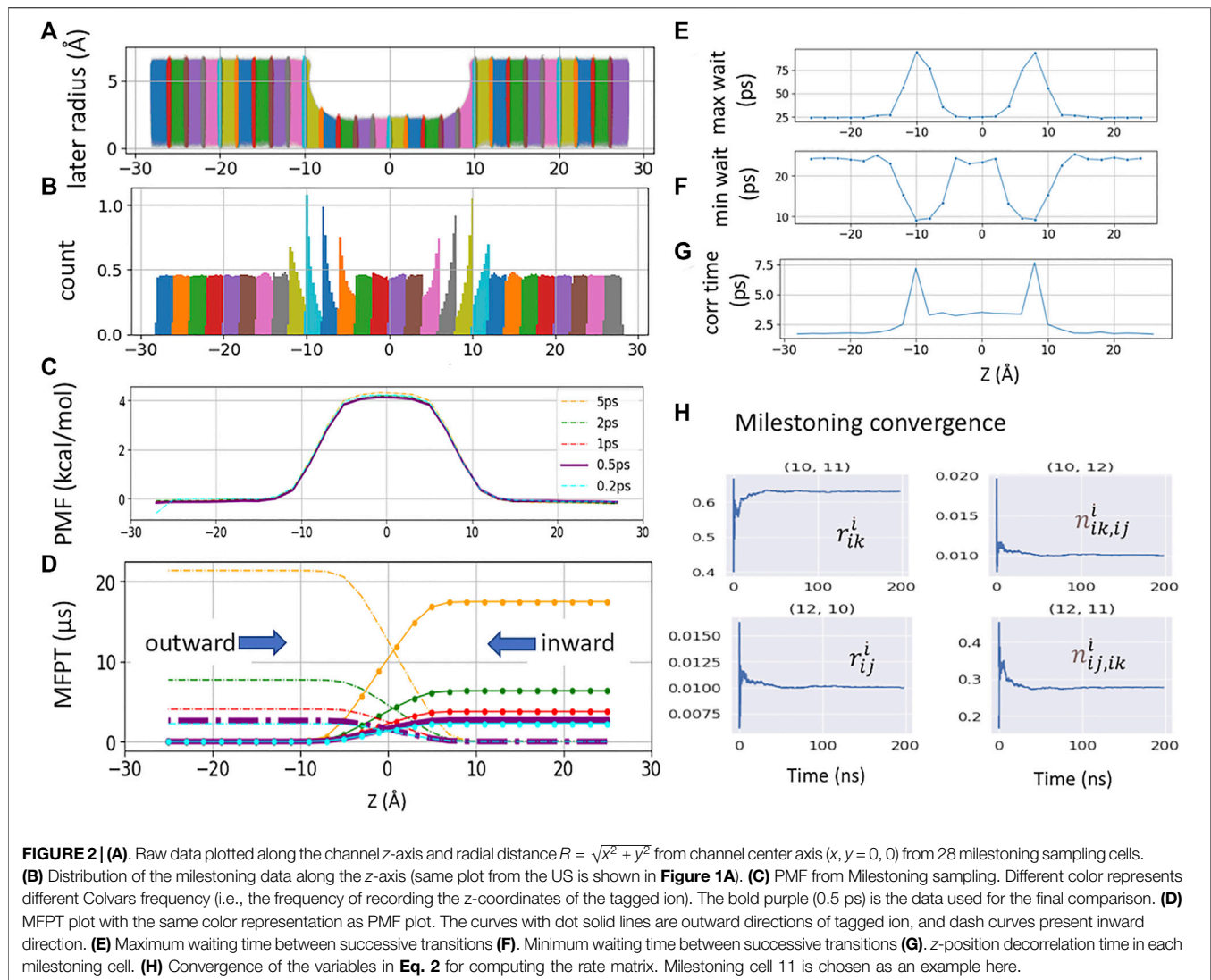
It can be seen from the equations above that the crossing rate k , MFPT, and conductance γ are all concentration-dependent; only P is independent of concentration. Experimentally, P is usually measured relative to the potassium ion permeability, thus representing an intrinsic property of each channel. It is hence an ideal quantity for rigorous comparison between different computational methods.

System Setup and Equilibrium Protocols

The coordinates of the carbon tube (CNT) were taken from Zhou and Zhu (2019). Briefly, it is an uncapped armchair CNT with 13.5 Å in length and 5.4 Å in radius. Two carbon sheets form an artificial membrane to separate the solution (**Figure 1A**). Constraints were applied to all carbon atoms to keep the system rigid. The CHARMM36 force field was used (MacKerell et al., 1998; Mackerell et al., 2004). After solvation, the box size was $38 \times 38 \times 75$ Å³, which contained 2503 TIP3P water molecules, six K⁺, and six Cl[−]. All MD simulations were performed using 1 fs time step using NAMD2.13 package under NVT ensemble, with 1 atm and 300 K temperature using Langevin thermostat (Hoover et al., 1982; Evans, 1983). Cutoff for calculating vdW interaction and short-range electrostatic interaction was set at 12 Å and force-switched at 10 Å. Long-range electrostatic interactions were calculated using the particle mesh Ewald algorithm (Darden et al., 1993). The system was equilibrium for 100 ns before conducting umbrella sampling, milestoning, and voltage simulations.

Umbrella Sampling Simulations

A total of 28 windows ($-27 \text{ Å} < z < +27 \text{ Å}$) were sampled. Each window was separated by 2 Å apart. The tagged K⁺ was restraint by a harmonic restraint on z and a flat-bottom harmonic cylindrical restraint. The force constant for harmonic restraint was 2.5 kcal/mol/Å, and that for cylindrical restraint was 10 kcal/mol/Å within 6 Å on the X - Y radius plane. The reference dummy atom to pull the K⁺ was set at (0, 0, 0). The harmonic distance restraint was determined by the projected vector along z between the dummy atom and tagged K⁺. The cylindrical restraint was determined by the center of mass of all carbon atoms from CNT. Each window was run for 40 ns (**Figure 1B**). The PMF (**Figure 1C**) was computed using Pymbar 3.0.3 (Chodera



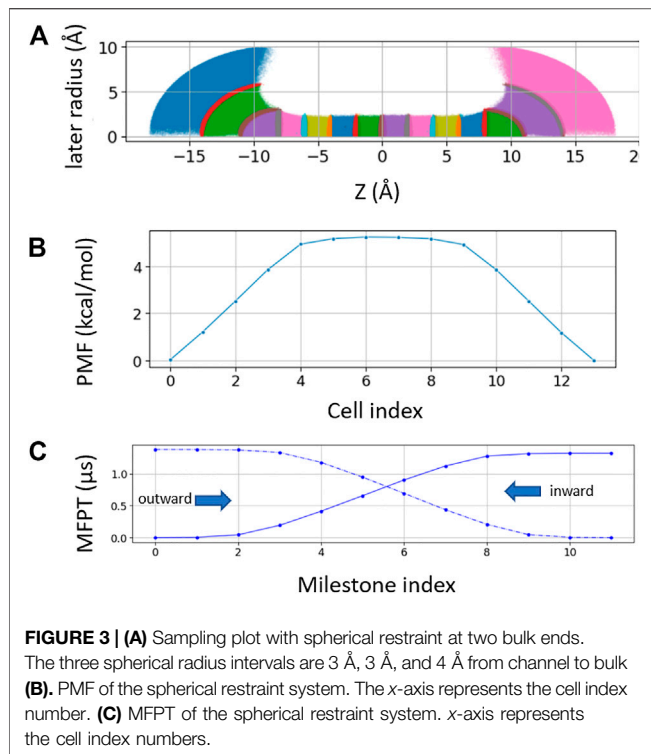
et al., 2007; Shirts and Chodera, 2008). The output frequency was 0.5 ps per frame.

Position-Dependent Diffusion Coefficient $D(z)$

$D(z)$ of K^+ inside the CNT was calculated from umbrella sampling trajectories (**Figure 1D**). The correlation time was extracted from each umbrella window i using $\tau_i = \int_0^\infty \frac{\langle \delta z(t) \delta z(0) \rangle_i}{\langle \delta z^2 \rangle_i} dt$, where $\delta z(t) = z(t) - \langle z \rangle$ is the deviation of the z -position of the ion at time t , $z(t)$, from the time-averaged position z in each window. $\langle \delta z^2 \rangle_i = \langle z^2 \rangle_i - \langle z \rangle_i^2$ is the variance. Following the formulation of Berne et al. (1988), Woolf and Roux (1994), Hummer (2005), the Laplace transformation of the velocity autocorrelation function along the reaction coordinate z in the harmonically restrained umbrella sampling gives $D(z_i) = \frac{\langle \delta z^2 \rangle_i}{\tau_i}$.

Markovian Milestoning With Cylindrical Bulk Restraint

The same as in umbrella sampling, the z -coordinate of the tagged ion was used to define a set of Voronoi cells along the channel pore and identify the milestones as the boundaries between the cells. To facilitate the comparison in analysis, we kept the Voronoi cell setup (28 cells and 2 Å apart) and the bulk cylindrical restraint (6 Å radius) identical to our umbrella sampling windows (**Figure 2A**). The only difference is that a flat-bottom harmonic restraint of force constant 100 kcal/mol/Å, instead of the weak harmonic restraint, was used to confine the sampling within each cell (**Figure 2B** vs. **Figure 1B**). We then ran 28 local simulations confined in each cell and collected the kinetics of transitions between milestones. More specifically, let us introduce a set of M Voronoi cells B_i , $i = 1, \dots, M$. Since the total flux in and out of each cell is zero at statistical equilibrium, the rate of attempted escape from cells B_j to B_i , $k_{j \rightarrow i}$,



and the equilibrium probability π_i for the tagged ion to be in cell B_i satisfies a balance equation:

$$\sum_{j=1, j \neq i} \pi_j k_{j \rightarrow i} = \sum_{j=1, j \neq i} \pi_i k_{i \rightarrow j}, \quad \sum_{i=1} \pi_i = 1 \quad (1)$$

The free energy of each cell can be obtained from the solution of Eq. 1 as $-k_B T \ln(\pi_i)$ (Figure 2C). By defining a milestone S_{ij} as the boundary between two adjacent Voronoi cells B_i and B_j , the dynamics of the system is reduced to that of a Markov chain in the state space of the milestone indices (Vanden-Eijnden and Venturoli, 2009). The MFPT between any pair of milestones S_{ij} and S_{ik} can hence be calculated from the rate matrix whose elements $q_{ij,ik}$, the rate of moving from milestone S_{ij} to S_{ik} , are given by

$$q_{ij,ik} = \frac{\pi_i n_{ij,ik}^i}{\pi_i r_{ij}^i + \pi_j r_{ij}^j} \quad (2)$$

where $n_{ij,ik}^i$ is the number of transitions from S_{ij} to S_{ik} , normalized by the time spent in cell B_i . r_{ij}^i is the time passed in cell B_i after having hit S_{ij} before hitting any other milestone, normalized by the total time spent in cell B_i . The inward and outward MFPT profiles were obtained by reversing the milestone indices when constructing the rate matrix (Figure 2D). The $n_{ij,ik}^i$ and r_{ij}^i can be used to monitor the convergence of the rate matrix (Figure 2H).

The total sampling time of all 28 cells was 4.9 μ s, where each cell was sampled between 150 and 300 ns. The NAMD Colvars output frequency was 0.5 ps. The PMF and MFPT were computed using a set of in-house python scripts https://github.com/yichunlin79/CNT_milestoning_method with different frame

sizes. In order to check whether the Colvars output frequency has any effect on MFPT, additional milestoning simulations were conducted with the Colvars output frequency of 0.2 ps and a total sampling time of 2.74 μ s.

Markovian Milestoning With Spherical Bulk Restraint

For spherical bulk restrained milestoning, a total of 14 Voronoi cells were used, including eight cells inside the channel (identical to the milestoning above) and three layers of spherical shell on each side of the channel (Figure 3A). The distance between the tagged K^+ ion and two dummy atoms fixed at the Cartesian coordinates of (0, 0, -8) and (0, 0, 8) are used to set up the spherical shells in bulk with radius increments of 3, 3, and 4 Å. Additional $z > |8|$ Å restraint is applied to keep the ion outside the channel. All restraint force constant is 100 kcal/mol/Å. The length of each bulk window is 150 ns with Colvars output frequency of 0.5 ps⁻¹.

Voltage Simulations

After 100 ns equilibrium simulation, constant electric fields corresponding to the transmembrane potential of ± 0.3 and ± 0.4 V were applied perpendicular to the membrane to all the atoms using NAMD2.13. In order to be consistent with the umbrella sampling and milestoning, a cylinder restraint of 6 Å radius was applied to a tagged K^+ in bulk with 10 kcal/mol/Å force constant for ± 0.4 V systems. All other ions moved freely beyond the cylinder restraint region. The K^+ conductance was computed by counting the total number of crossing events and computing the charge displacement along the z-axis (Figure 4). Error bar was computed from three independent replicas of 200 ns. For ± 0.3 V systems, all six K^+ were restrained inside the same cylindrical bulk boundary, and a single replica of 60 ns was conducted. The time step was 1 fs, and the output frequency was 5 ps for all voltage systems.

RESULTS AND DISCUSSION

Single-Channel Permeability From Inhomogeneous Solubility-Diffusion (ISD) Equation

Molecular permeation through ion channel can be described by ISD if the one-dimensional free energy and diffusion along channel normal is sufficient to describe the diffusion process (relaxation of orthogonal degrees of freedom is fast relative to the reaction coordinate) and the permeant velocity relaxation time is instantaneous (on the scale of integration time step). The only difference with the ISD equation used for membrane permeation is that a flat-bottom lateral potential $u(x, y)$ is often used to confine a single tagged ion in a cylindrical bulk region outside the ion channel. The effective cross-sectional area due to the lateral restraint is thus $\iint e^{-\beta u(x, y)} dx dy$, which can be approximated to πr^2 in a homogenous bulk, where r is the radius of the cylinder. Hence, πr^2 defines the effective bulk concentration in the

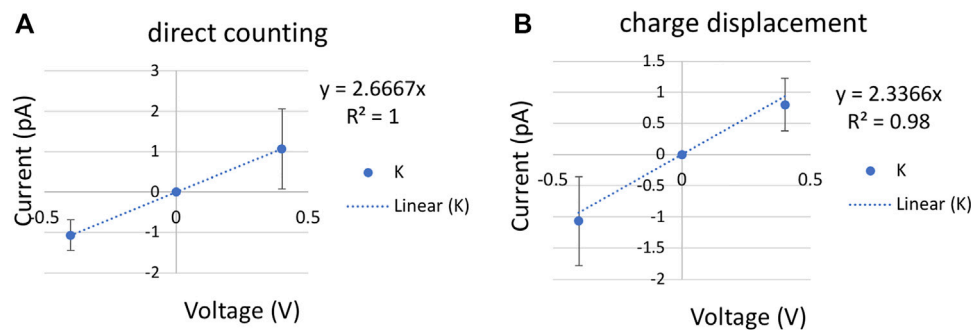


FIGURE 4 | Current-voltage (I-V) plot for a single K⁺ with a cylinder restraint of radius 6 Å in bulk. The slope of the linear fitting defines the conductance **(A)**. K⁺ current computed using direct counting method. **(B)**. K⁺ current computed using charge displacement method. The error bars are calculated from three replicas of 200 ns at each voltage.

simulated region, which led the probability of the ion inside the channel $p(z)$ over the true bulk density ρ to be $\frac{p(z)}{\rho} = \pi r^2 e^{-\beta w(z)}$, where $w(z)$ is the PMF with the bulk value set to zero at the cylindrical region and $\beta = 1/k_B T$ (Allen et al., 2004; Zhu and Hummer, 2012). T is the temperature, and k_B is Boltzmann's constant. Therefore, at low ionic concentration, single-channel permeability can be estimated using a slightly modified ISD equation:

$$P = \pi r^2 \left(\int_{z_1}^{z_2} \frac{e^{\beta w(z)}}{D(z)} dz \right)^{-1} \quad (3)$$

In Eq. 3, $D(z)$ is the position-dependent diffusion constant of the studied permeant along the z -axis (Figure 1D). The interval of the integration, $[z_1, z_2]$, is the lower and upper boundaries of the channel pore, beyond which PMF reaches the bulk value. r is the radius of the cylindrical restraint when the ion is outside of the $[z_1, z_2]$ interval. It is necessary to set r larger than the maximum pore radius so that it has no energetic contribution inside the pore. The radius of the cylindrical restraint defines the effective bulk concentration. Thus, it offsets the bulk PMF value and ensures that the single-channel permeability from Eq. 3 is concentration-independent.

In both umbrella sampling and milestoning, the same cylindrical restraint with $r = 6$ Å is applied in the bulk region, and the same window size of 2 Å was used. The only difference is that a weak harmonic restraint with a force constant of 2.5 kcal/mol is applied for all umbrella windows to ensure sufficient overlapping between neighboring samplings, but a strong flat-bottom harmonic restraint with a force constant of 100 kcal/mol is applied for all milestoning cells to confine the sampling within each cell. Figure 1B and Figure 2B illustrate the biased sampling distribution imposed by these two types of restraints. The PMFs from the US are shown in Figure 1C. With bulk value offset to zero, a broad energy barrier of 3.8 kcal/mol located inside the channel region is consistent with a previously reported PMF (Zhou and Zhu, 2019).

Using the PMF or $w(z)$ in Figure 1C and $D(z)$ in Figure 1D, the permeability estimated from Eq. 3 is $(8.96 \pm 0.02) \times 10^{-16} \text{ cm}^3/\text{s}$. We can also plot local resistance (the integrand of Eq. 3) for permeating K⁺ through CNT (Figure 1E) and the integration of the permeation resistance, $1/P(z)$, as a function of the z -axis (Figure 1F). It is not surprising that the $1/P(z)$ bears the same feature as the outward MFPT in Figure 2D.

Permeability Computed From Mean First Passage Time

The MFPT of a single K⁺ crossing the CNT is computed from Voronoi-tessellated Markovian milestoning simulations (see Methods). The distributions of the tagged K⁺ confined in each 2 Å cell by flat-bottom harmonic restraint are shown in Figures 2A,B. Milestoning simulation yields a consistent PMF profile with the highest energy barrier of 4.1 kcal/mol at the center of the CNT (Figure 2C). As the CNT used here is symmetric by design, a rigorous check of sampling convergence is the perfect symmetry (mirror image) of the inward and outward MFPT profiles (Figure 2D). The inward and outward MFPT profiles can be obtained by reversing the milestone indices when constructing the transition rate matrix.

We found that while PMF is nearly insensitive to the Colvars frequency (i.e., the frequency of recording the z -coordinates of the tagged ion) tested here, MFPT is susceptible to this frequency. In the current study, the frequency of 5 ps^{-1} severely overestimates the MFPT due to the missing transition events. Lower frequency also yields less data, which leads to asymmetric MFPTs. Here, the MFPT from the sampling saved per 5 ps has ten times fewer data points than the one from 0.5 ps. Thus, it failed to converge even after 18 μs of sampling. The ideal frequency has to be system-dependent (local diffusion and shape of the underlying free energy landscape). For our CNT system, the Colvars frequencies of 0.2 ps^{-1} and 0.5 ps^{-1} yield an identical and symmetric MFPT of $2.6 \pm 0.03 \mu\text{s}$ for K⁺ permeation.

Using the PMF, $w(z)$, and MFPT, t , from the milestoning (with 0.5 ps^{-1} Colvars frequency), the single-channel permeability computed from Eq. 4, derived from Eq. 3 and Eq. 5, (Votapka et al., 2016) is $2.92 \times 10^{-16} \text{ cm}^3 \text{ s}^{-1}$, in fairly good agreement with the permeability

of $8.96 \times 10^{-16} \text{ cm}^3 \text{ s}^{-1}$ computed from ISD equation (Eq. 3) using umbrella sampling data:

$$P = \frac{\pi r^2 \int_{z_1}^{z_2} e^{-\beta w(z)} dz}{2 \langle t \rangle} \quad (4)$$

Decorrelation Time Versus Waiting Time in Milestoning

Vanden-Eijnden et al. have shown that Markovian milestoning yields exact MFPTs if the milestones are chosen such that successive transitions between them are statistically independent (Vanden-Eijnden et al., 2008; Vanden-Eijnden and Venturoli, 2009) and thus no definition of lag time is needed. To check this assumption for transitions between two neighboring milestones, in each cell, the maximum and minimum waiting time between two neighboring milestones is extracted and plotted in Figures 2E,F. The mirror image-like relation between these two plots manifests that the transition down the slope of PMF is the fastest, and the one against the slope is the slowest. Hence, the longest waiting time of 94.0 ps and the shortest waiting time of 9.0 ps are in the same cell where the PMF is steepest. The velocity decorrelation time is less than the smallest frame size (0.2 ps). The z -position decorrelation time for the tagged K^+ in each cell is plotted in Figure 2G. The maximum positional decorrelation time (7.6 ps) is also located at the steepest PMF region. Hence, for all pairs of milestones, the velocity decorrelation time and position decorrelation time are both less than the minimum waiting time for successive transitions between milestones.

Mean First Passage Time Computed From Spherical Boundary Condition

Laterally confining the ion in the bulk region (cylindrical restraint) is convenient for describing the thermodynamics and kinetics of the ions across the channel along the channel pore axis (z -axis). However, the geometries of ion channels are diverse. For funnel-shaped channel pores [e.g., connexin hemichannel (Jiang et al., 2021a)] or pores connected with lateral fenestration [e.g., Piezo1 channel (Jiang et al., 2021b)], a spherical boundary may be a better choice to capture the distribution and dynamics of ions near the channel entrance. Hence, we further tested milestoning simulation using spherical restraint for ions in the bulk region (Figure 3A). Unlike the cylindrical restraint, which yields constant ionic concentration along the z -axis, the effective ionic concentration in the current spherical bulk cells decreases as the radius of the sphere increases. Thus, the PMF and MFPT are plotted against the milestoning cell index rather than the z -axis (Figures 3B,C).

At low concentration, single-channel permeability (cm^3/s) can be related linearly to the mean first passage time (MFPT) $\langle t \rangle$ under equilibrium $p = 1/c \langle t \rangle$, in which c is the symmetric solute concentrations. Because single-channel permeability is an intrinsic property of a channel, independent of solute concentration or the shape of the bulk cells, the ratio of MFPT from spherical restraint

over cylindrical restraint should be equal to the reciprocal bulk concentration ratio. The concentration of a single ion in a hemisphere with a radius of 10 Å is 1.26 M and in a cylinder with a radius of 6 Å and length of 10 Å is 0.68 M. Therefore, the concentration ratio of ~ 2 is indeed consistent with the MFPT of 2.6 μs from cylindrical restraint (Figure 2E) and 1.3 μs from spherical restraint (Figure 3C).

Mean First Passage Time Computed From Umbrella Sampling

In the high diffusion limit, the MFPT of diffusive motion of K^+ from the lower to upper boundaries of the channel pore, $[z_1, z_2]$, can be written as

$$\text{MFPT} = \int_{z_1}^{z_2} \frac{e^{\beta w(z)}}{D(z)} dz \int_{z_1}^z e^{-\beta w(z')} dz' \quad (5)$$

Eq. 5 was originally developed for computing the average reaction time for diffusion processes governed by a Smoluchowski-type diffusion equation (Szabo et al., 1980). It is also used to derive Eq. 4 from Eq. 3 (Votapka et al., 2016). To cross-validate our results, we apply the $w(z)$ and $D(z)$ from umbrella sampling to Eq. 5 and obtain an MFPT of $2.2 \pm 0.02 \mu\text{s}$, fairly similar to the 2.6 μs MFPT computed directly from milestoning. This consistency further demonstrated the robustness of the tested MD methods for computing transport kinetics.

Permeability Computed From Steady-State Flux

As mentioned above, under low concentration and constant electric field, we can simplify the GHK flux equation for computing the single-channel permeability P from conductance measurement. Under symmetric concentration, the GHK flux equation can be written as

$$P = \frac{\gamma RT}{q^2 F^2 C} = \frac{\gamma k_B T}{q^2 C} \quad (6)$$

where γ is the unitary conductance of a single channel, R is the gas constant, q is the charge of the permeating ion, F is the Faraday constant, C is the bulk concentration of the ion, and $k_B T$ has the same meaning above, except that the unit is eV here (0.026 eV at 300 K). At sufficiently small voltage, the current-voltage (I-V) relation is expected to be linear, and the slope defines the conductance.

Ionic conductance from MD simulations can be computed using two approaches. The most commonly used is a direct counting method, in which the currents were computed from the number of permeation events (N) over a simulation period (τ), $I = N/\tau$. In our code (see Github link in Methods), the channel is split into upper, inner, and lower regions. A positive permeation event of K^+ is counted if the time evolution of ion coordinates follows a lower-inner-upper sequence, and a negative permeation event is in reverse order. The carbon nanotube is applied with positive and negative 0.4 V voltage with 200 ns per replica. Each voltage simulation was repeated three times with

different initial velocities. A least-square fitting of the I/V curve gave the conductance of 2.7 ± 0.94 pS by the direct counting method (Figure 4A).

A more efficient approach that does not rely on completed permeation events is to compute the instantaneous ionic current from charge displacement along the z -axis, $I(t) = \sum_{i=1}^n q_i [z_i(t + \Delta t) - z_i(t)] / \Delta t L$, in which q_i and z_i are the charge and z coordinate of ion i and L is the length of the channel pore (Aksimentiev and Schulten, 2005). This charge displacement method yielded a similar conductance of 2.3 ± 1.2 pS, indicating a good convergence of the voltage simulations (Figure 4B).

With an ionic concentration of 0.52 M (one single K^+ in a cylinder bulk of radius 6 Å and length 28 Å), the permeability is $(11.9 \pm 6.36) \times 10^{-16}$ cm³/s by the charge displacement method, and $(13.6 \pm 4.81) \times 10^{-16}$ cm³/s by the direct counting method. In addition to ± 0.4 V simulations, ionic current calculated from 60 ns of ± 0.3 V with sixfold higher concentration yields a similar permeability of 10.9×10^{-16} cm³/s. Only the results from low concentration are reported in Table 1.

DISCUSSIONS

In this study, we used a carbon nanotube (CNT) as a toy model of a small conductance ion channel and computed the single-channel permeability from umbrella sampling, Markovian milestoning, and steady-state flux under voltage (Table 1). The PMF and MFPT for a single K^+ permeating through the CNT produced from Markovian milestoning and umbrella sampling are in good agreement. Milestoning with cylindrical bulk restraint and spherical bulk restraint were tested and yielded consistent MFPTs when the effective bulk concentration is accounted. The single-channel permeability from voltage simulation is also within the same order-of-magnitude as those obtained from PMF-based and MFPT-based methods. These results are also in the same range as the previously reported K^+ permeability of $(25 \pm 7) \times 10^{-16}$ cm³/s computed using a transition path approach with the CHARMM22 force field (Zhou and Zhu, 2019).

It should also be noted that the current CNT model is chosen because it reproduces macroscopic properties (e.g., free energy, conductance) similar to common small-conductance ion channels. However, two carbon sheets were used as an artificial membrane to separate the solution. In the absence of a dielectric medium surrounding the channel transmembrane region, this toy model is unsuitable for investigating detailed electrostatic interaction between the ions and the channel.

In terms of computational resources, umbrella sampling has the advantage because PMF converges much faster than MFPT. However, MFPT allows extracting the kinetics directly from

sampling. Thus, it does not rely on the assumption of ISD formalism and does not require additional calculations of position-dependent diffusion coefficient. Steady-state flux is straightforward to apply if the permeant is charged and sufficient sampling is achievable under reasonable voltages. However, if the permeant is not charged, a constant concentration gradient needs to be applied. Furthermore, the effect of an unphysiologically large voltage bias or electrochemical gradient on channel property is likely system-dependent and difficult to predict over a long simulation time. Compared with the steady-state flux approaches, the milestoning approach does not depend on the charge of the permeant. Thus, it can be used to study any type of small molecular permeation, such as the transport of a second messenger, cAMP, through a connexin26 hemichannel (Jiang et al., 2021a). Therefore, the use of milestoning has a significant promise for future applications on complex systems that are challenging to extract kinetics from unbiased MD or PMF-based enhanced sampling approaches.

DATA AVAILABILITY STATEMENT

The datasets presented in this study can be found in online repositories. The names of the repository/repositories and accession number(s) can be found in the article/Supplementary Material.

AUTHOR CONTRIBUTIONS

Y-CL performed all MD simulations. YL designed and supervised the project. Y-CL and YL analyzed data and wrote the paper together.

FUNDING

This work was supported by NIH Grants GM130834. Computational resources were provided via the Extreme Science and Engineering Discovery Environment (XSEDE) allocation TG-MCB160119, supported by NSF grant number ACI-154862.

ACKNOWLEDGMENTS

We are grateful to Dr. Fangqiang Zhu for sharing the coordinates of the CNT model and Drs. Luca Maragliano and Andrew Harris for inspiring discussions.

REFERENCES

- Adelman, J. L., and Grabe, M. (2015). Simulating Current-Voltage Relationships for a Narrow Ion Channel Using the Weighted Ensemble Method. *J. Chem. Theor. Comput.* 11, 1907–1918. doi:10.1021/ct501134s
- Aksimentiev, A., and Schulten, K. (2005). Imaging α -Hemolysin with Molecular Dynamics: Ionic Conductance, Osmotic Permeability, and the Electrostatic Potential Map. *Biophysical J.* 88, 3745–3761. doi:10.1529/biophysj.104.058727
- Alberini, G., Benfenati, F., and Maragliano, L. (2018). Molecular Dynamics Simulations of Ion Selectivity in a Claudin-15 Paracellular Channel. *J. Phys. Chem. B* 122, 10783–10792. doi:10.1021/acs.jpcc.8b06484
- Allen, T. W., Andersen, O. S., and Roux, B. (2004). Energetics of Ion Conduction through the Gramicidin Channel. *Proc. Natl. Acad. Sci. U.S.A.* 101, 117–122. doi:10.1073/pnas.2635314100
- Awoonor-Williams, E., and Rowley, C. N. (2016). Molecular Simulation of Nonfacilitated Membrane Permeation. *Biochim. Biophys. Acta (Bba) - Biomembranes* 1858, 1672–1687. doi:10.1016/j.bbame.2015.12.014
- Berne, B. J., Borkovec, M., and Straub, J. E. (1988). Classical and Modern Methods in Reaction Rate Theory. *J. Phys. Chem.* 92, 3711–3725. doi:10.1021/j100324a007
- Bernèche, S., and Roux, B. (2001). Energetics of Ion Conduction through the K⁺ Channel. *Nature* 414, 73–77. doi:10.1038/35102067
- Carnevale, V., Delemotte, L., and Howard, R. J. (2021). Molecular Dynamics Simulations of Ion Channels. *Trends Biochem. Sci.* 46, 621–622. doi:10.1016/j.tibs.2021.04.005
- Chodera, J. D., Swope, W. C., Pitera, J. W., Seok, C., and Dill, K. A. (2007). Use of the Weighted Histogram Analysis Method for the Analysis of Simulated and Parallel Tempering Simulations. *J. Chem. Theor. Comput.* 3, 26–41. doi:10.1021/ct0502864
- Choudhary, O. P., Paz, A., Adelman, J. L., Colletier, J.-P., Abramson, J., and Grabe, M. (2014). Structure-Guided Simulations Illuminate the Mechanism of Atp Transport through Vdac1. *Nat. Struct. Mol. Biol.* 21, 626–632. doi:10.1038/nsmb.2841
- Cottone, G., Chiodo, L., and Maragliano, L. (2020). Thermodynamics and Kinetics of Ion Permeation in Wild-type and Mutated Open Active Conformation of the Human $\alpha 7$ Nicotinic Receptor. *J. Chem. Inf. Model.* 60, 5045–5056. doi:10.1021/acs.jcim.0c00549
- Darden, T., York, D., and Pedersen, L. (1993). Particle Mesh Ewald: AnN Log(N) Method for Ewald Sums in Large Systems. *J. Chem. Phys.* 98, 10089–10092. doi:10.1063/1.464397
- Diamond, J. M., and Katz, Y. (1974). Interpretation of Nonelectrolyte Partition Coefficients between Dimyristoyl Lecithin and Water. *J. Membr. Biol.* 17, 121–154. doi:10.1007/bf01870176
- Domene, C., Klein, M. L., Branduardi, D., Gervasio, F. L., and Parrinello, M. (2008). Conformational Changes and Gating at the Selectivity Filter of Potassium Channels. *J. Am. Chem. Soc.* 130, 9474–9480. doi:10.1021/ja801792g
- Domene, C., Ocello, R., Masetti, M., and Furini, S. (2021). Ion Conduction Mechanism as a Fingerprint of Potassium Channels. *J. Am. Chem. Soc.* 143, 12181–12193. doi:10.1021/jacs.1c04802
- Evans, D. J. (1983). Computer “experiment” for Nonlinear Thermodynamics of Couette Flow. *J. Chem. Phys.* 78, 3297–3302. doi:10.1063/1.445195
- Faradjian, A. K., and Elber, R. (2004). Computing Time Scales from Reaction Coordinates by Milestoning. *J. Chem. Phys.* 120, 10880–10889. doi:10.1063/1.1738640
- Flood, E., Boiteux, C., Lev, B., Vorobyov, I., and Allen, T. W. (2019). Atomistic Simulations of Membrane Ion Channel Conduction, Gating, and Modulation. *Chem. Rev.* 119, 7737–7832. doi:10.1021/acs.chemrev.8b00630
- Fowler, P. W., Abad, E., Beckstein, O., and Sansom, M. S. P. (2013). Energetics of Multi-Ion Conduction Pathways in Potassium Ion Channels. *J. Chem. Theor. Comput.* 9, 5176–5189. doi:10.1021/ct4005933
- Hempel, T., del Razo, M. J., Lee, C. T., Taylor, B. C., Amaro, R. E., and Noe, F. (2021). Independent Markov Decomposition: Toward Modeling Kinetics of Biomolecular Complexes. *P Natl. Acad. Sci. USA* 118, e2105230118. doi:10.1073/pnas.2105230118
- Hille, B. (2001). *Ion Channels of Excitable Membranes*. 3rd ed. Sunderland, MA: Sinauer, p xviii, 814 p.
- Hoover, W. G., Ladd, A. J. C., and Moran, B. (1982). High-Strain-Rate Plastic Flow Studied via Nonequilibrium Molecular Dynamics. *Phys. Rev. Lett.* 48, 1818–1820. doi:10.1103/physrevlett.48.1818
- Hummer, G. (2005). Position-Dependent Diffusion Coefficients and Free Energies from Bayesian Analysis of Equilibrium and Replica Molecular Dynamics Simulations. *New J. Phys.* 7, 34. doi:10.1088/1367-2630/7/1/034
- Jiang, W., Del Rosario, J. S., Botello-Smith, W., Zhao, S., Lin, Y.-c., Zhang, H., et al. (2021b). Crowding-Induced Opening of the Mechanosensitive Piezo1 Channel In Silico. *Commun. Biol.* 4, 84. doi:10.1038/s42003-020-01600-1
- Jiang, W., Lin, Y.-C., Botello-Smith, W., Contreras, J. E., Harris, A. L., Maragliano, L., et al. (2021a). Free Energy and Kinetics of Camp Permeation through Connexin26 via Applied Voltage and Milestoning. *Biophysical J.* 120, 2969–2983. doi:10.1016/j.bpj.2021.06.024
- Khalili-Araghi, F., Tajkhorshid, E., and Schulten, K. (2006). Dynamics of K⁺ Ion Conduction through Kv1.2. *Biophys. J.* 91, L72–L74. doi:10.1529/biophysj.106.091926
- Khalili-Araghi, F., Ziervogel, B., Gumbart, J. C., and Roux, B. (2013). Molecular Dynamics Simulations of Membrane Proteins under Asymmetric Ionic Concentrations. *J. Gen. Physiol.* 142, 465–475. doi:10.1085/jgp.201311014
- Kutzner, C., Grubmüller, H., de Groot, B. L., and Zachariae, U. (2011). Computational Electrophysiology: The Molecular Dynamics of Ion Channel Permeation and Selectivity in Atomistic Detail. *Biophysical J.* 101, 809–817. doi:10.1016/j.bpj.2011.06.010
- MacKerell, A. D., Jr, Bashford, D., Bellott, M., Dunbrack, R. L., Jr, Evanseck, J. D., Field, M. J., et al. (1998). All-Atom Empirical Potential for Molecular Modeling and Dynamics Studies of Proteins. *J. Phys. Chem. B* 102, 3586–3616. doi:10.1021/jp973084f
- Mackerell, A. D., Jr, Feig, M., and Brooks, C. L., III (2004). Extending the Treatment of Backbone Energetics in Protein Force fields: Limitations of Gas-phase Quantum Mechanics in Reproducing Protein Conformational Distributions in Molecular Dynamics Simulations. *J. Comput. Chem.* 25, 1400–1415. doi:10.1002/jcc.20065
- Maragliano, L., Vanden-Eijnden, E., and Roux, B. (2009). Free Energy and Kinetics of Conformational Transitions from Voronoi Tessellated Milestoning with Restraining Potentials. *J. Chem. Theor. Comput.* 5, 2589–2594. doi:10.1021/ct900279z
- Roux, B. (1998). Molecular Dynamics Simulations of Ion Channels: How Far Have We Gone and where Are We Heading? *Biophysical J.* 74, 2744–2745. doi:10.1016/s0006-3495(98)77981-0
- Roux, B. (2008). The Membrane Potential and its Representation by a Constant Electric Field in Computer Simulations. *Biophysical J.* 95, 4205–4216. doi:10.1529/biophysj.108.136499
- Shirts, M. R., and Chodera, J. D. (2008). Statistically Optimal Analysis of Samples from Multiple Equilibrium States. *J. Chem. Phys.* 129, 124105. doi:10.1063/1.2978177
- Szabo, A., Schulten, K., and Schulten, Z. (1980). First Passage Time Approach to Diffusion Controlled Reactions. *J. Chem. Phys.* 72, 4350–4357. doi:10.1063/1.439715
- Teo, I., and Schulten, K. (2013). A Computational Kinetic Model of Diffusion for Molecular Systems. *J. Chem. Phys.* 139, 121929. doi:10.1063/1.4820876
- Vanden-Eijnden, E., Venturoli, M., Ciccotti, G., and Elber, R. (2008). On the Assumptions Underlying Milestoning. *J. Chem. Phys.* 129, 174102. doi:10.1063/1.2996509
- Vanden-Eijnden, E., and Venturoli, M. (2009). Markovian Milestoning with Voronoi Tessellations. *J. Chem. Phys.* 130, 194101. doi:10.1063/1.3129843
- Venable, R. M., Krämer, A., and Pastor, R. W. (2019). Molecular Dynamics Simulations of Membrane Permeability. *Chem. Rev.* 119, 5954–5997. doi:10.1021/acs.chemrev.8b00486
- Votapka, L. W., Lee, C. T., and Amaro, R. E. (2016). Two Relations to Estimate Membrane Permeability Using Milestoning. *J. Phys. Chem. B* 120, 8606–8616. doi:10.1021/acs.jpcc.6b02814
- Woolf, T. B., and Roux, B. (1994). Conformational Flexibility of O-Phosphorylcholine and O-Phosphorylethanolamine: A Molecular Dynamics Study of Solvation Effects. *J. Am. Chem. Soc.* 116, 5916–5926. doi:10.1021/ja00092a048
- Zheng, J., and Trudeau, M. C. (2015). *Handbook of Ion Channels*. 2nd Edition. Boca Raton: CRC Press.
- Zhou, X., and Zhu, F. (2019). Calculating Single-Channel Permeability and Conductance from Transition Paths. *J. Chem. Inf. Model.* 59, 777–785. doi:10.1021/acs.jcim.8b00914

Zhu, F., and Hummer, G. (2012). Theory and Simulation of Ion Conduction in the Pentameric Glic Channel. *J. Chem. Theor. Comput.* 8, 3759–3768. doi:10.1021/ct2009279

Conflict of Interest: The authors declare that the research was conducted in the absence of any commercial or financial relationships that could be construed as a potential conflict of interest.

Publisher's Note: All claims expressed in this article are solely those of the authors and do not necessarily represent those of their affiliated organizations or those of

the publisher, the editors, and the reviewers. Any product that may be evaluated in this article, or claim that may be made by its manufacturer, is not guaranteed or endorsed by the publisher.

Copyright © 2022 Lin and Luo. This is an open-access article distributed under the terms of the Creative Commons Attribution License (CC BY). The use, distribution or reproduction in other forums is permitted, provided the original author(s) and the copyright owner(s) are credited and that the original publication in this journal is cited, in accordance with accepted academic practice. No use, distribution or reproduction is permitted which does not comply with these terms.



Exploring the Conformational Impact of Glycine Receptor TM1-2 Mutations Through Coarse-Grained Analysis and Atomistic Simulations

Anil Ranu Mhashal, Ozge Yoluk and Laura Orellana *

Protein Dynamics and Cancer Lab, Department of Oncology-Pathology, Karolinska Institute, Solna, Sweden

OPEN ACCESS

Edited by:

Matteo Masetti,
University of Bologna, Italy

Reviewed by:

Jianzhong Chen,
Shandong Jiaotong University, China
Fangqiang Zhu,
Lawrence Livermore National
Laboratory (DOE), United States

*Correspondence:

Laura Orellana
laura.orellana@ki.se
doble.helix@gmail.com

Specialty section:

This article was submitted to
Biological Modeling and Simulation,
a section of the journal
Frontiers in Molecular Biosciences

Received: 06 March 2022

Accepted: 05 May 2022

Published: 28 June 2022

Citation:

Mhashal AR, Yoluk O and Orellana L
(2022) Exploring the Conformational
Impact of Glycine Receptor TM1-2
Mutations Through Coarse-Grained
Analysis and Atomistic Simulations.
Front. Mol. Biosci. 9:890851.
doi: 10.3389/fmolb.2022.890851

Pentameric ligand-gated ion channels (PLGICs) are a family of proteins that convert chemical signals into ion fluxes through cellular membranes. Their structures are highly conserved across all kingdoms from bacteria to eukaryotes. Beyond their classical roles in neurotransmission and neurological disorders, PLGICs have been recently related to cell proliferation and cancer. Here, we focus on the best characterized eukaryotic channel, the glycine receptor (GlyR), to investigate its mutational patterns in genomic-wide tumor screens and compare them with mutations linked to hyperekplexia (HPX), a Mendelian neuromotor disease that disrupts glycinergic currents. Our analysis highlights that cancer mutations significantly accumulate across TM1 and TM2, partially overlapping with HPX changes. Based on 3D-clustering, conservation, and phenotypic data, we select three mutations near the pore, expected to impact GlyR conformation, for further study by molecular dynamics (MD). Using principal components from experimental GlyR ensembles as framework, we explore the motions involved in transitions from the human closed and desensitized structures and how they are perturbed by mutations. Our MD simulations show that WT GlyR spontaneously explores opening and re-sensitization transitions that are significantly impaired by mutations, resulting in receptors with altered permeability and desensitization properties in agreement with HPX functional data.

Keywords: glycine receptor (GlyR), mutations, hyperekplexia, cancer, molecular dynamics, coarse-grained (CG) methods

INTRODUCTION

Pentameric ligand-gated ion channels (PLGICs) form a large family of integral membrane proteins with a central role in signal transduction from prokaryotes to eukaryotes (Dacosta and Baenziger, 2013; Changeux, 2014; Taly et al., 2014). Their ring-like pentamer architecture, with a fivefold symmetry axis centered on the ion-conducting pore, is conserved from bacteria to humans and mediates an incredibly sophisticated mechanism to allosterically propagate signals from the extracellular binding site to an ionic gate situated up to 50 Å away. In animals, PLGICs share a conserved extracellular cysteine bridge, which gives its name to the so-called Cys-loop family of ionotropic receptors. Given their key role in chemical synapses, Cys-loop receptors are major drug targets in neurological conditions from Alzheimer to rare genetic diseases. Mostly expressed at post-synaptic neurons, upon pre-synaptic neurotransmitter release, they mediate passive ion fluxes that shift the membrane potential. Depending on pore-lining residues, PLGICs are selective for cations

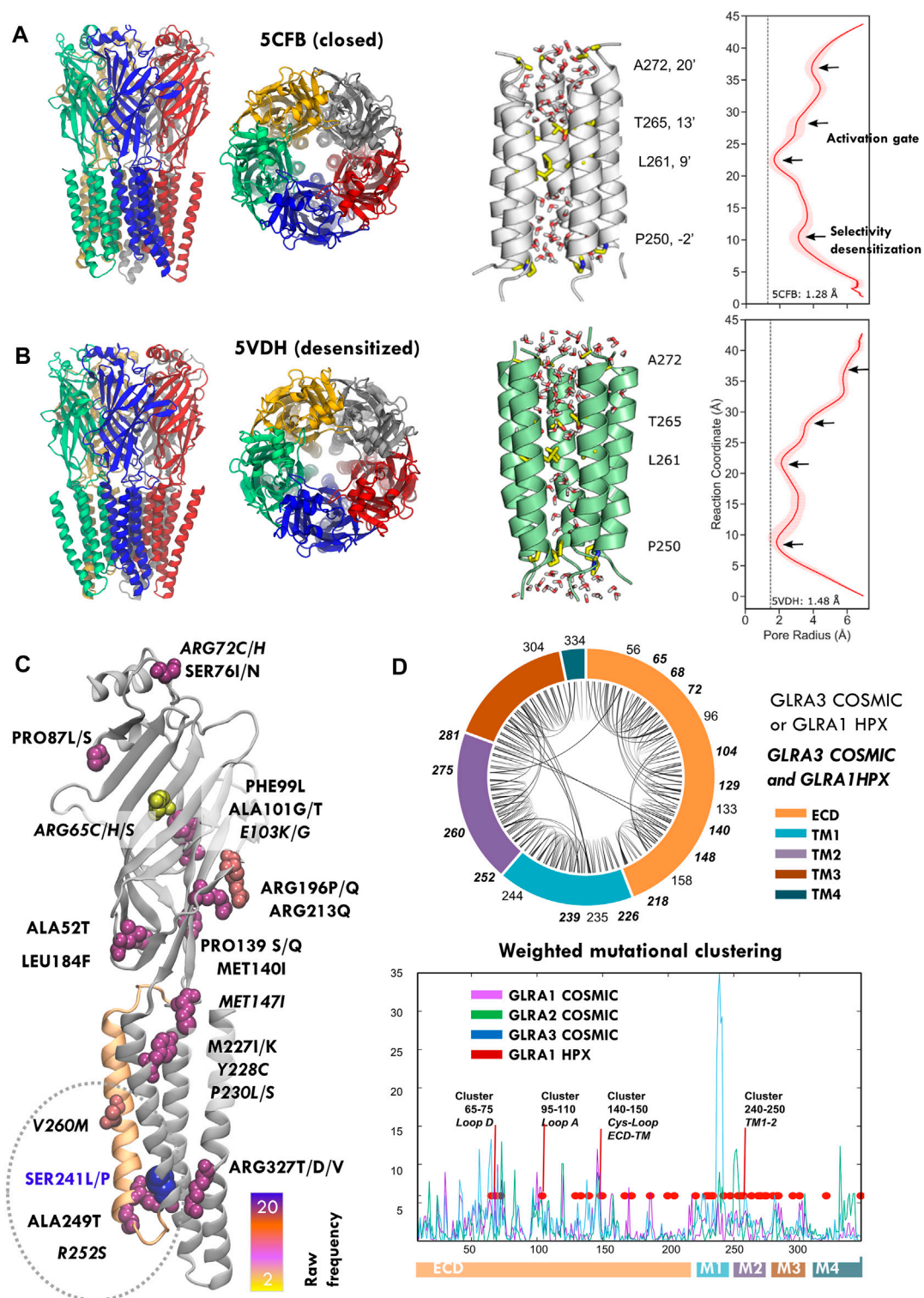


FIGURE 1 | Structure and mutations of the glycine receptor (GlyR). **(A,B)** Human GlyR closed (5cfb) and desensitized (5vdh) structures used as reference in this study (left), zoom onto TM2 pore helices with key pore residues highlighted with licorice representation (center) and corresponding profile of pore radii calculated by HOLE (right). **(C)** COSMIC GLRA3 mutations colored by frequency; note the top mutation in blue (S241L) at the end of pore lining TM2 (orange). **(D)** Chord plot of the network of conserved contacts from 5CFB, with doubly HPX-COSMIC mutated residues in bold (top) and mutational clustering across GLRA1-3 genes weighted by conservation score (bottom). Note how multiple peaks overlap with positions mutated in startle disease (red) and the highest one corresponds to the TM1-2 region where HPX changes concentrate. See related **Supplementary Figure S1**, **Supplementary Table S1**.

like sodium ions (Na^+) and result in excitatory effects, e.g. the nicotinic acetylcholine receptor (nACh-R) or the serotonin type-3 receptor ($5\text{-HT}_3\text{-R}$), or are selective for anions like chloride ions (Cl^-) resulting in inhibitory effects, e.g., the α -aminobutyric acid receptor ($\text{GABA}_\text{A}\text{-Rs}$) or the glycine receptor (Gly-Rs) (**Figure 1**).

Whether prokaryotic or eukaryotic, PLGICs share a topology characterized by a large N-terminal ligand-binding extracellular domain (ECD), followed by four transmembrane domains (TM1–4). Monomers assemble into a pentameric cylinder, with the five orthosteric ligand binding sites (LBS) located at ECD subunit interfaces, TM2 helices shaping the ion channel pore across the central symmetry axis, and TM4 helices facing the plasma membrane (**Figures 1A,B**, left). This universal topology is linked to incredibly conserved functional mechanisms to regulate ion gating (Gielen and Corringer, 2018). Classically, PLGIC activation was interpreted with simple two-state models like the MWC (Monod et al., 1965), in which receptors spontaneously sample resting/shut and active/open states until agonist binding shifts the equilibrium. Nevertheless, single-channel studies and growing structural data show a far more complex conformational cycle, with striking similarities across species. In the initial pre-activation or “priming” step, agonist binding stabilizes the ECD in a contracted higher-affinity conformation (“*un-blooming*”), triggering a key revolving motion of TM2–3 loop at the ECD–TMD interface and subsequent ECD–TMD rotation in opposite directions (“quaternary twist”) (Nemecz et al., 2016). This sequence of events is captured by the so-called “locally closed” conformations, where the ECD has undergone the transition toward the active state-like conformation, but the TMD still remains in a resting conformation (Prevost et al., 2012). In the activation step, global twisting couples to cooperative tilting of pore-lining helices (“iris-like gating”) (Martin et al., 2017), which widens the upper part of the channel (“activation gate”, TM2 9' and 13'; see **Figures 1A,B** right), formed by two or three rings of hydrophobic residues that create a barrier to ion permeation (Althoff et al., 2014; Du et al., 2015). Once the gate is open, ions flow according to their electrochemical gradient and channel selectivity, determined by the “selectivity filter” at the cytoplasmic end of the pore (TM2 -1' or -2'). Remarkably, this “unbloom-and-twist” allosteric mechanism that propagates a signal (ligand) from the ECD to a remote TMD pore gate is encoded in the PLGIC fold, as predicted by elastic network models (ENMs) (Bahar et al., 2010), and it has been further confirmed by molecular dynamics (MD) (Calimet et al., 2013) and coarse-grained eBDIMS simulations (Orellana et al., 2016). Apart from agonist-elicited activation, PLGICs also share another key physiological property: desensitization, in which the sustained agonist presence causes the channels to transit from the active to an agonist-bound inactive state (Katz and Thesleff, 1957) to prevent over-activation. Once the agonist disappears, receptors slowly recover, although the detailed transitions from agonist-unbound desensitized states to unbound resting or open states are still unclear. Desensitization mainly involves pore closure at its

intracellular end (TM1–2 loop), which therefore also acts as the main “desensitization gate” (Hibbs and Gouaux, 2011).

Among Cys-loop receptors, strychnine-sensitive GlyR, the major inhibitory ionotropic receptor in the brainstem and spinal cord, has become by far the better characterized (Howard, 2021): there are over 40 structures deposited in the Protein Data Bank, mostly in open, closed and desensitized-like states (Du et al., 2015; Huang et al., 2015, 2017b, 2017a; Kumar et al., 2020; Yu J. et al., 2021, Yu et al., 2021 H.); a few are trapped in a super-open states, whose physiological significance has been questioned, specially by MD (Cerdan et al., 2018; Cerdan and Cecchini, 2020; Dämgen and Biggin, 2020; Dämgen et al., 2020). Apart from these rich structural data, GlyR stands out among the eukaryotic PLGICs due to its role in neurological diseases and particularly in a rare Mendelian condition known as hyperekplexia (HPX) or “startle disease” (Lynch et al., 2017). Similar to the way the alkaloid strychnine antagonizes glycine binding, hyperekplexia disrupts glycinergic neurotransmission, resulting in exaggerated “startle” responses and muscle stiffness. Analysis of hyperekplexia patients has resulted in an exceptional amount of information on GlyR mutations and their phenotypic impact being gathered during the past two decades (Lewis et al., 1998; Chung et al., 2010; Bode et al., 2013; Bode and Lynch, 2014). As the GABA receptor, GlyR usually functions as a heteropentamer of alpha and beta subunits, but only alpha subunits form functional homopentamers. Over 50 mutations have been linked to hyperekplexia, mostly targeting the alpha1 subunit (GLRA1), thus providing an exhaustive mutational scanning map in terms of structural areas where missense changes result in GlyR disruption (Chung et al., 2010; Bode et al., 2013; Bode and Lynch, 2013, 2014). In general, HPX mutations (**Supplementary Table S1, Figure 1D**) are either recessive and typically associated with low surface expression (loss-of-function), or dominant, mostly located around TM2 and causing prolonged desensitization and/or spontaneous activation (gain-of-function), which leads to reduced maximal currents.

Despite the fact that its central function is synaptic signaling, PLGICs are also expressed in non-neural cells where they play a diversity of roles, including stem cell and cancer proliferation (Young and Bordey, 2009; Zhang et al., 2013; Bhattacharya et al., 2021). GlyR is no exception and is known to be expressed in cells as diverse as hepatocytes, spermatozoa, pancreatic, endothelial, or renal cells (Lynch, 2004; Van den Eynden et al., 2009). As tumor genomic screenings advance, an increasing number of GlyR mutations are being reported in a surprising variety of tumors. For the three GlyR genes, GLRA1–3, cancer-reported mutations display an intriguing clustering partially overlapping with HPX positions (**Figures 1C,D, Supplementary Table S1**). Here, we perform a preliminary exploration of selected GlyR mutations using as model the GLRA3 homomer, which apart of being structurally well characterized in humans also carries the highest frequency of mutations, specially focused on the lower TM2 section (**Figure 1C**). Based on mutational clustering, conservation, and ENM analysis, we select for MD study three TM1 and 2 mutations found in tumors, which are close or overlap with hyperekplexia-mutated positions (S241L, R252S, and V260M) of uncertain functional effect. Our results suggest that

these residue substitutions are far from neutral but profoundly impair channel permeability, selectivity, and desensitization.

METHODS

Structural Data, Sequence Alignment, and Conserved Network Analysis

The reference wildtype structures for closed (PDB ID: 5CFB, **Figure 1A**) and desensitized state (PDB ID: 5VDH; **Figure 1B**) human GlyR GLRA3 homopentamer were obtained from the Protein Data Bank and the series of mutants, S241L, R252S, and V260M were constructed from both states, resulting in eight systems. To select candidate mutations for further study, we focused on the resting 5CFB structure to perform a simple weighting analysis based on the 3D space distribution and degree of conservation as in Orellana et al. (2019b). First, we fetched the information for GLRA1-3 missense mutations reported in the COSMIC database (Tate et al., 2019) (**Supplementary Figures S1, S2**). Conservation scores were retrieved from the ConSurf database (Ashkenazy et al., 2016); to get a simpler overview of residue conservation, sequences for GLRA1-3, GBRA1, and the intensely studied PLGICS *G.violaceus* GLIC and *C. elegans* GluCL were retrieved from the UniProt database (The UniProt Consortium, 2021) and aligned with ClustalW (**Supplementary Figure S1**). Then, in order to evaluate spatial 3D clustering, we applied a simple counting algorithm: each amino acid is represented by its C-alpha carbon, and the number of mutations reported for each position and its neighbors within a 3D-sphere of cutoff radius 9 Å (typical to evaluate residue pairwise interactions) is added to obtain a raw number of hits (i.e., reported mutations within the 3D-sphere) (**Supplementary Figure S2A**), which are then weighted according to their ConSurf scores (**Figure 1D**, bottom). Hence, random isolated mutations or changes in non-conserved areas are filtered out to obtain a final estimate of the conserved spatial mutation concentration around each amino acid. Finally, the contact network between highly conserved residues (i.e., those with ConSurf scores 8–9) was plotted with a chord diagram to visualize interactions across different regions and mutated areas (**Figure 1D**, top).

Principal Component Analysis

Principal component analysis (PCA) (Jolliffe, 2002) is a statistical technique to reveal dominant patterns in noisy data. The diagonalization of the covariance matrix of the system allows obtaining the major axis for statistical variance or principal components (PCs). In this way, complex multidimensional data are mapped to a reduced set of coordinates, which contain the dominant trends explaining data variation. PCA has been widely applied in structural biology to analyze ensembles, usually coming from MD simulations (Amadei et al., 1993, 1996). Protein structures are aligned to a reference in order to compute a covariance matrix, which describes the mean-square deviations in atomic coordinates from their mean position (diagonal elements) and the correlations between their pairwise fluctuations (off-diagonal elements). Diagonalization

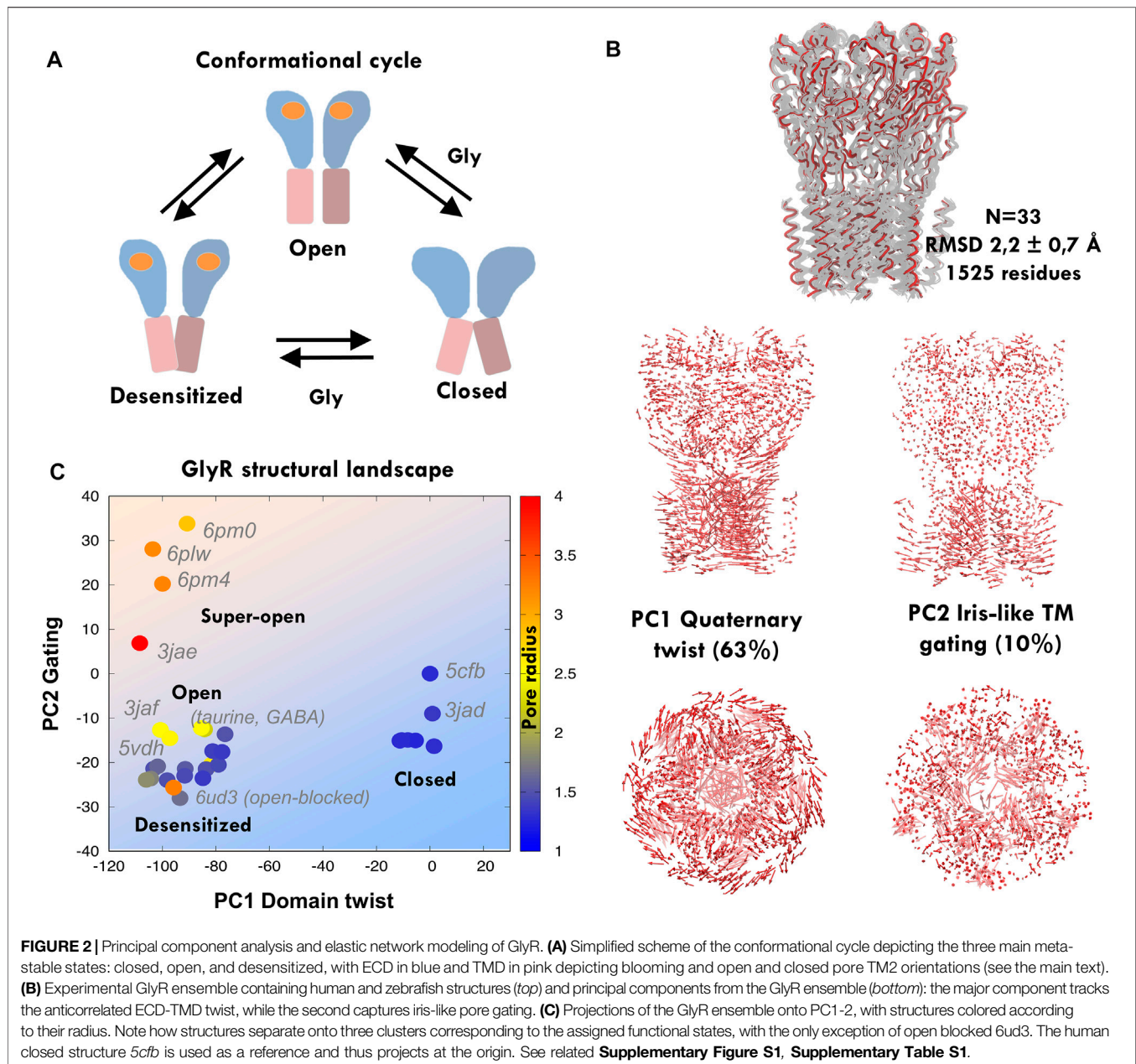
then yields a set of eigenvectors (principal components, PCs) and eigenvalues representing the motions that explain the variation in the atomic coordinates. In the structurally rich ensembles here analyzed, the first two PCs contain, on average, around 60–80% of the ensemble structural variation (Orellana et al., 2016), and provide excellent coordinates to assess mutation effects on MD sampling (Chen et al., 2021a; 2021b). On this framework, a structure i containing N residues is thus accurately characterized by its projections onto the conformational space defined by the major components, PC_k ($k = 1, 2 \dots 3N-6$) (see **Figure 2**)

$$PC_k = [T_{i-0}] \cos \alpha. \quad (1)$$

where T_{i-0} is the difference between the coordinates of i -structure and the *apo* reference, PC is one of the major axes, and α is the angle formed by PC_k and T_{i-0} . Here, we retrieve all available GlyR structures in the Protein Data Bank, corresponding to *H. sapiens*, *D. rerio*, and *S. domesticus*, and after elimination of structures with missing gaps and alignment to the common conserved core, we obtain an ensemble of 33 structures (3jad, 3jae, 3jaf, 5cfb, 5tin, 5vdh, 5vdi, 6plo, 6plp, 6plq, 6plr, 6pls, 6plt, 6plu, 6plv, 6plw, 6plx, 6ply, 6plz, 6pm0, 6pm2-6, 6ubs, 6ubt, 6ud3, 6vm0, 6vm2-3, 7mlu) that aligned to 5cfb with low RMSD. As previously shown by us (Orellana et al., 2016), major PCs are captured, i.e., correlate with the heuristic variables that typically characterize PLGIC conformations (**Supplementary Figure S2B**). Projections were used to also track the time evolution of trajectories (**Figure 4**).

Molecular Dynamics Simulations and Essential Dynamics

We used the CHARMM-GUI web interface to build systems for MD simulation (Jo et al., 2008, 2017), which allowed us to repair missing residues in the crystal structures and build a membrane bilayer containing ~300 phospholipid POPC (1-palmitoyl-2-oleoyl-sn-glycero-3-phosphocholine) molecules. A hexagonal water box was used to reduce the cell volume and overall system size. Membrane-embedded proteins were then solvated using the TIP3P water model. The CHARMM36m force field was used to describe the system (Huang et al., 2016). Potassium (K^+) and chloride (Cl^-) ions were added to maintain the physiological salt (150 mM KCl) concentration to mimic intracellular conditions. Energy minimization, equilibration, and production runs were carried out with GROMACS (Pronk et al., 2013; Abraham et al., 2015), following the CHARMM-GUI Membrane Builder standard protocols (Wu et al., 2014). The temperature was maintained at 303.0 K using the Nose–Hoover thermostat (Nosé, 1984; Hoover, 1985) and pressure was set to 1.0 bar using the Parrinello–Rahman barostat (Parrinello and Rahman, 1981) with semi-isotropic pressure coupling. Hydrogen bonds were constrained using the LINCS algorithm (Hess et al., 1997), short-range van der Waals (vdW), and electrostatic interactions cutoffs were set to 12 Å, and long-range electrostatic interactions were described using the particle mesh Ewald approach (Ewald, 1921; Essmann et al., 1995) with periodic boundary conditions. Production runs were



carried out using a 2 fs time step and writing at every 1 ps interval. Each system was simulated for 300 ns, with four replicas starting from different random seeds. Therefore, in total, we simulated 1.2 μ s for each one of the eight GlyR systems, i.e., from 5CFB/5VDH, with WT/S241L/R252S/V260M sequences. To filter out noise and extract the main collective motions, we performed *essential dynamics* (ED) (Amadei et al., 1993; Daidone and Amadei, 2012) for each system's 1.2 μ s meta-trajectory (**Figure 3A**) using in-house scripts. The relative free energy landscape (FEL) at 300 K was obtained from the probability distribution of the reaction coordinate, R (PC1, PC2) (**Figure 3B**). GROMACS tools with defaults were used to perform the RMSD cluster analysis of the TMD and calculate

the average TM1-2 helicity. For cluster analysis (**Figure 8**), all simulated systems were combined at a 1 ns interval to yield a single and long C_{α} atom 9.6 μ s trajectory of 9600 frames, and an RMSD cut-off of 0.20 nm was selected to obtain lesser and larger clusters. See the summary of all simulations in **Supplementary Table S2**.

Elastic Network Normal Mode Analysis

Elastic network models (ENM) (Atilgan, 2018) are minimal coarse-grained representations of protein structures as beads-and-springs. In the anisotropic network model (ANM), the potential energy of a protein structure—assumed to be at an energy minimum—is defined by a network of interactions with

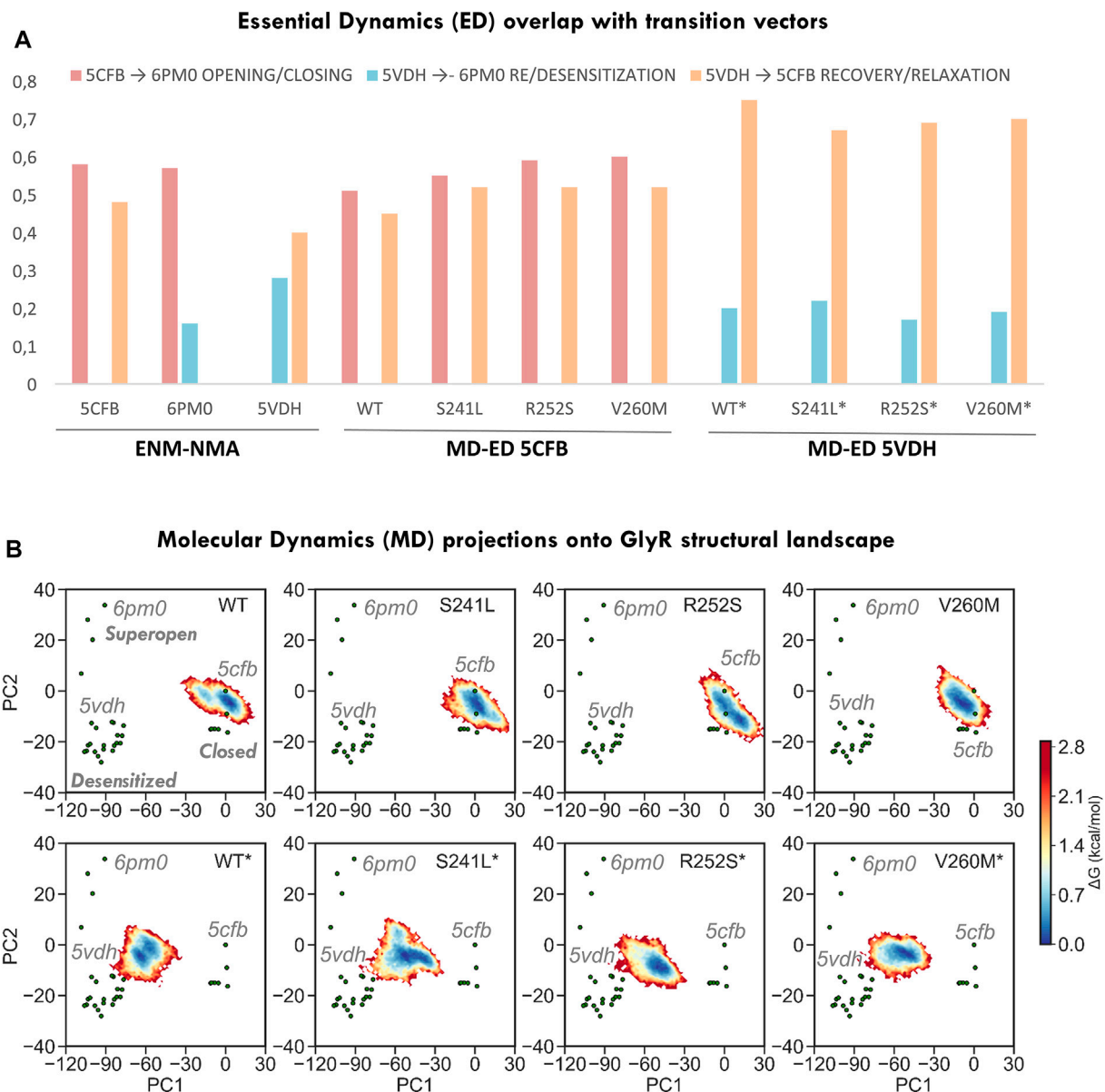


FIGURE 3 | Conformational space sampling by elastic network models and essential dynamics across the three major axis for transition defined by closed (5CFB), desensitized (5VDH), and super-open (6PMO) structures from each PC cluster. **(A)** Overlap between the first 10 ENM modes computed from the three state representatives versus the three transitions (left) and between the first 10 ED modes from 5CFB and 5VDH simulations versus the three transitions (right). **(B)** Relative free energy landscapes for 1.2 us meta-trajectories upon projection onto PC1-2. Note how simulations from 5CFB (top row) extend in the direction of super-open structures, and while for WT GlyR populate two minima, for mutations sample an elongated one. On the contrary, simulations from 5VDH evolve toward the closed cluster, while for WT GlyR they point to 5cfb, mutants tend to evolve to collapsed closed states that project at negative PC2 values. All simulations from 5VDH are indicated with *.

nodes at the C^α atoms coupled by uniform springs (Tirion, 1996; Atilgan et al., 2001). Once the pair force constants K_{ij} are defined, the network potential energy is approached by the parabola:

$$E = \sum_{i,j} K_{ij} (R_{ij} - R_{ij}^0)^2 \quad (2)$$

where R_{ij} and R_{ij}^0 are the instantaneous and equilibrium distances between all nodes. Within normal mode analysis (Case, 1999), the

Hessian matrix of the energy second derivatives is diagonalized, yielding a set of orthonormal $3N-6$ eigenvectors representing the normal modes, which have been shown to accurately predict intrinsic collective motions. Here, we use the nearest-neighbors MD-derived ED-ENM algorithm, which predicts experimental conformational changes (Orellana et al., 2010) and, implemented onto ED-ENM Brownian dynamics (eBDIMS), entire sequences of intermediate states along transition pathways (Orellana et al.,

2016; 2019a). Average thermal fluctuations for each residue pair i , j and each residue i are evaluated as in Atilgan et al. (2001) (Supplementary Figure S2C).

Essential Dynamics and Normal Mode Analysis Similarity Against Experimental Transition Vectors

An experimental conformational change between two conformations R_1 and R_2 can be described by the normalized difference 3N-dimensional vector $\Delta r = (R_2 - R_1) / \|R_2 - R_1\|$ between the two sets of alpha-carbon coordinates, after optimal superimposition of the structures. Therefore, given a motion space from ED or NMA, the degree of similarity or overlap between the directions of the experimental Δr vector and a given k th mode v_k is measured by their angle cosine (Yang et al., 2009):

$$\alpha_k = \frac{\Delta r \cdot v_k}{\|\Delta r\| \|v_k\|} \quad (3)$$

where \cdot designates the dot product and the bars denote the vectors' modulus or magnitude; a cosine close to 1 means that the directions are parallel (Figure 3A). Therefore, the similarity between ANM or ED modes and the transition is evaluated by the cumulative contribution of the first M modes

$$\delta_k = \left(\sum_1^M \alpha_k^2 \right)^{1/2} \quad (4)$$

Here, we consider $M = 10$, which typically cover >90% of the variance (Orellana et al., 2010) (Figure 2A).

Heuristic Channel-Defined Structural Variables

To evaluate channel descriptors as in Orellana et al. (2016) (Figures 5–7, Supplementary Table S3, S4), we used VMD along with in-house tools and scripts written in *python*, *C++*, and *FORTRAN*. The *quaternary twist* motion is the anti-correlated rotational movement of the ECD versus TMD around the channel axis, which decreases as the channel transitions to the open state. Channel closing is also coupled to ECD collapse (un-bloom) to a narrower diameter. The iris-like gating motion can be broken down into two components in the form of tilt and twist motions of the M2 helices that alter the pore radius. Hence, *blooming* was evaluated as the maximal radius of the extracellular domain defined by maximally separated residues at the tip of the five subunits. *Quaternary twist* was calculated as the average rotation angle of each subunit with the vector from extracellular domain and transmembrane domain CM to overall CM on the XY plane. The *tilt and the twist angle of M2 helices* were calculated as an average over five subunits. In order to get comparable angles between subunits, the reference structure (5CFB) was aligned to the center of mass of each M2 helix. X-axis was characterized between two centers of mass: M2 helix and the protein center of mass. The Z-axis was chosen as the

principal of inertia parallel to the symmetry axis. Finally, the Y-axis was defined as the vector normal to the XZ plane. With these axes, the tilt angle is calculated between the projected helical axis onto the XZ plane and the Z-axis and twist angle between the projected helical axis onto the YZ plane and Z-axis. Pore calculations were performed with HOLE (Smart et al., 1996) using 0.5 Å step from C-alpha atoms only. The pore radius at 9' was averaged over a 2.5 Å window in both directions from the center of mass of 9' residues. The average hole profiles were obtained for the structures during the production run using only M2 helices and are reported with their standard deviation. Hydration in the GlyR channel was quantified by calculating the number of water molecules inside the channel pore along the axis normal to the bilayer. To study the conductivity of the GlyR channel in wild type and mutant proteins, we identified the water/ions in the pore and their z axis coordinates (bilayer normal) at every snapshot and plotted them versus simulation time.

RESULTS AND DISCUSSION

GlyR Cancer Mutations and Dominant Hyperekplexia Changes Partially Overlap on TM1-2

As of March 2022, there are around 1000 cases of tumors reported to carry GlyR mutations: 952 for GLRA1, 1196 for GLRA2, and up to 1546 for GLRA3. After removing nonsense and deletion changes, we retrieved 245, 255, and 299 mutations, for GLRA1-3, respectively. Mutations for GLRA1 concentrate in 175 positions (70%), for GLRA2 in 174 (68%), and for GLRA3 in 208 (69%), which represent approximately 50–60% of the GlyR chain (347 positions); a majority of these changes are considered to be passenger mutations due to defective repair mechanisms in neoplastic cells. Nevertheless, as the mutations are not evenly distributed along GLRA sequences but preferentially focused on key conserved regions (Figures 1C,D, Supplementary Figure S1, Supplementary Table S1), we hypothesized they could impact on the receptor function. Particularly, for GLRA3, mutation S241L has high frequency, with over 20 cases reported, in contrast with top GLRA1 and GLRA2 mutations. Moreover, nearly half of the cases (12) of S241L mutation are linked to melanoma, followed by skin carcinoma (8), while in GLRA1-2, they tend to spread across multiple tumor types. A closer look also reveals specific changes recurrently appearing across GLRA1-3 genes and/or often overlapping with HPX mutations sometimes identical (see Figures 1C,D, Supplementary Table S1). Overall, these mutational patterns strongly suggest that at least a fraction of these changes could affect the channel function, which we decided to investigate in more detail for GLRA3, due to the availability of solved human X-ray structures and its significant mutational frequency. We focused our analysis on the resting state, represented by structure 5CFB. To filter out as many random changes as possible, we quantified mutation clustering (Figure 1D bottom, Supplementary Figure S2A) based on the 3D space distribution and degree of conservation as in Orellana et al. (2019b); we also mapped GLRA1-2 and hyperekplexia mutations to

better detect overlapping patterns. We considered not only the raw number of mutations reported but also the recurrence of multiple allele changes onto the same positions (**Supplementary Figure S2A**). Upon weighting the spatial concentration of mutations by their *ConSurf* scores, we were able to identify four broad mutational clusters, which display overlap between hyperekplexia and cancer-reported GLRA1-3 changes: three minor ones at the ECD, located around loop D (residues 65–75), loop A (residues 95–110), and the Cys-loop ECD–TMD interface (residues 140–150), and a major one across TM1-2 (residues 222–244) to TM2 (residues 250–272); note that almost all reported HPX mutations overlap with one of these peaks with a few exceptions (**Figure 1D** bottom), with the notable exception of the most frequent mutation, R271L/Q/P, located at TM2-3 loop. Highest clustering scores were achieved at the area surrounding the TM1-2 loop region, where the selectivity filter and desensitization gate locate, and which contains HPX mutations such as P250T known to prolong desensitization (Saul et al., 1999). This area contains the highest frequency mutation, S241L/P (*ConSurf* score 8), located at the end of TM1, and its contacting neighbor R252S (*ConSurf* score 9), at the end of TM1-2 loop/beginning of TM2. While S241 is close to dominant hyperekplexia change W239C, of unknown functional effect, R252 is mutated in HPX as R252H/C, which results in low expression and activity. Another high-scoring neighbor area upstream TM2, close to 9' gate, contains mutation V260M (*ConSurf* score 8), which corresponds exactly with a dominant HPX change (del Giudice et al., 2001; Castaldo et al., 2004) known to disrupt gating. Importantly, both R252 and V260 are located in the pore-opposing TM2 face, at the level of lower 2' and upper 9' gates (see **Figures 1A,B**, right). To further evaluate the significance of mutations, we also compared mutational patterns with the conserved contact networks of 5CFB (**Figure 1D**, top) and 5VDH (not shown). In contrast with S241 and R252, mostly involved in the local TM1-2 loop connectivity, V260 participates in longer-range intrachain contacts connecting TM2 with TM3; moreover, it also contacts TM2 (T262) across adjacent subunits in the closed but not the desensitized state (*not shown*). Overall, the concentration of these dramatic size, charge, and polarity changes overlapping HPX mutants near the conserved activation and desensitization gates suggests that they are not neutral but can impact receptor stability and conformation.

GlyR Ensemble Encodes Opening and Desensitization Transitions

In spite of the diversified roles of PLGICs, structural studies have revealed an astonishing degree of fold and conformational conservation across species. Our previous studies of the channel GLIC and other model proteins show that the PCA of structural ensembles containing multiple conformations can reveal the pathways for inter-connecting transitions providing an accurate framework to monitor MD sampling (Orellana et al., 2016; Orellana, 2019). Currently, there are dozens of zebrafish and human GlyR structures solved in closed, desensitized, and open and super-open states (**Figure 2A**). We aligned $n = 33$ nearly-intact homo- and heteromeric structures (**Figure 2B**; RMSD = 2.2 ± 0.7 Å) and performed PCA to extract the dominant ensemble motions and then investigate how they correlate with channel

descriptors and annotated functional status. Similar to what is observed for prokaryotic GLIC (Orellana et al., 2016), the first mode (PC1, 63% of the variance) tracks the global quaternary twist and blooming motion ($R = 0.9$ and 0.6), as well as TM2 tilt ($R = -0.8$), while the second mode (PC2, 10% of variance) captures most of TM2 twist and pore gating ($R = 0.7$ and 0.6) (**Figure 2B**, **Supplementary Figure S2B**), separating super-open from desensitized structures (see Methods for definitions). Together, PC1-2 (73% variance) split the structural ensemble onto three to four major clusters (**Figure 2C**): to the right, closed/antagonist-bound structures (pore radius ≈ 1.5 Å, 1.2 Å for 5CFB), and to the left, those with an un-bloomed ECD and a wide-open (top left corner, pore radius > 3 Å e.g., 6PMO) or desensitized central channel (lower left corner, ≈ 1.5 Å, 1.4 Å for 5VDH); the only exception is the open-blocked structure 6UD3. Significantly, structures annotated as open states (6PLO, 6PM2, 6PLY, etc.) appear correctly located as a sub-cluster along the path from fully desensitized to super-open structures (pore radius ≈ 2.5 Å), which supports that PC1-2 space is a suitable framework to annotate channel status based on global correlated features of multiple descriptors. Finally, we also investigated to which extent these large-scale gating movements coupled to opening/desensitization are intrinsic to the different GlyR states, as previously suggested (Bertaccini et al., 2010; Zhu and Hummer, 2010; Zheng and Auerbach, 2011). We took as representatives of the three main PC1-2 clusters our reference human closed (5CFB) and desensitized (5VDH), together with one of the super-open zebrafish structures (6PMO); these three structures altogether broadly define three main transition directions along which the conformational cycle could potentially proceed. ENM from these three distinct states (**Figure 3A**) indicates that while the opening transition could be fairly spontaneous in the absence of a ligand (overlap $\approx 60\%$), the same was less likely for re/desensitization. In contrast, normal modes computed from 5VDH displayed poor overlap with the associated transitions, suggesting a rigid structure with more uncorrelated local motions. Residue fluctuations from 5CFB–ENM (**Supplementary Figure S2C**) also indicated that these mutations are located in a transition region from high [TM1-2 loop (S241L)] to low flexibility (TM2, from R252S to V260M) and thus could have diverse effects despite their proximity, which we then explored with fully atomistic MD.

Molecular Dynamics Reveals Mutations Perturb GlyR Conformational Dynamics

We performed MD simulations from the closed inhibited (PDB: 5CFB) and desensitized (PDB: 5VDH) human GLRA3 homopentamers after removing all ligands (the antagonist strychnine, in the first, and agonists glycine, AM-3607 and ivermectin in the latter), for WT and mutant sequences. Root-mean-square fluctuations (RMSDs) of the C_α atoms versus the initial experimental structures were calculated for all systems to confirm simulation convergence (**Supplementary Figure S3A**) and estimate the overall stability and flexibility of unbound closed and desensitized states upon ligand removal (**Supplementary Figure S3B**). Despite the fact that differences across replicates and GlyR variants were small, a closer look reveals a slightly more rigid

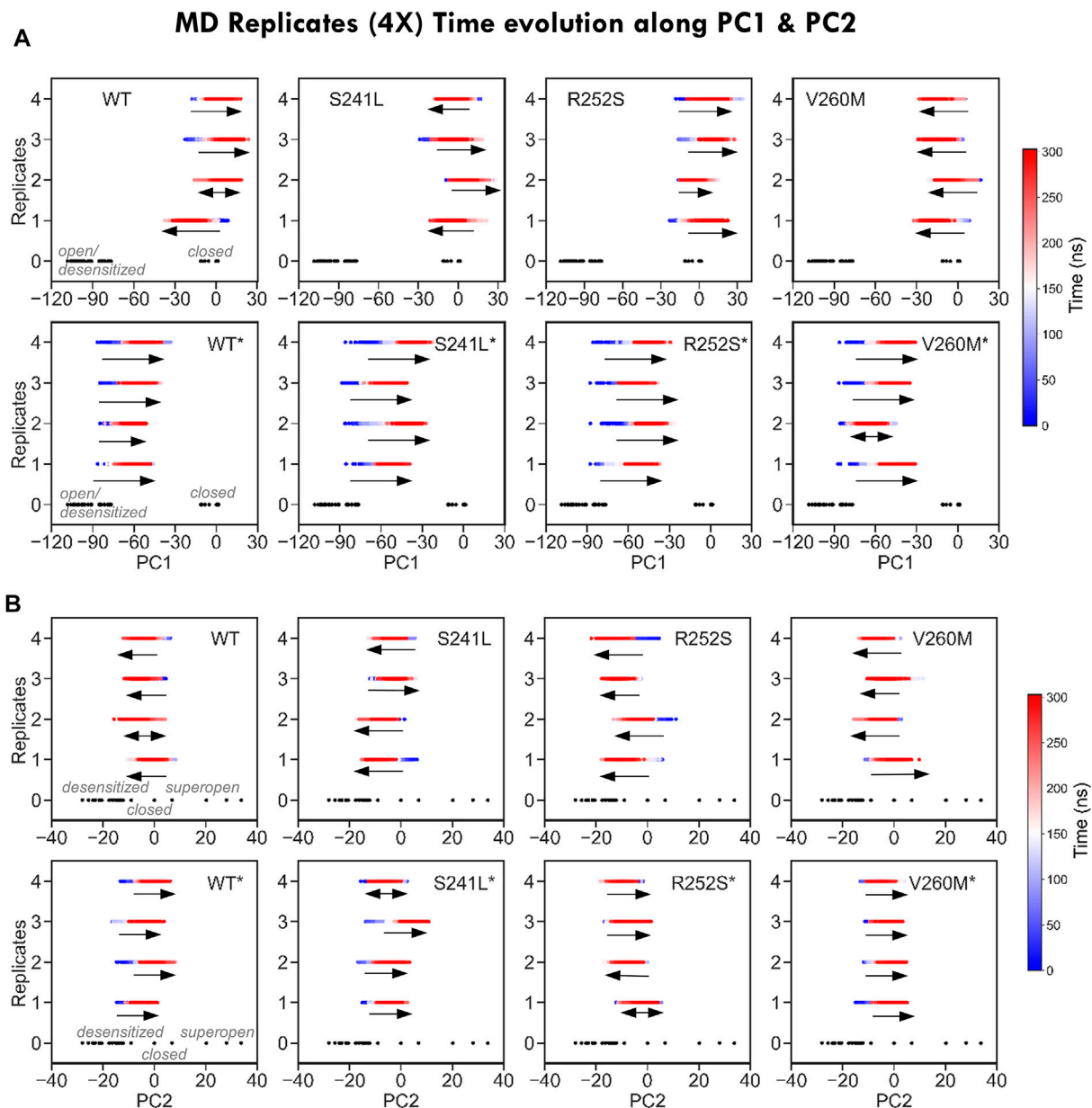
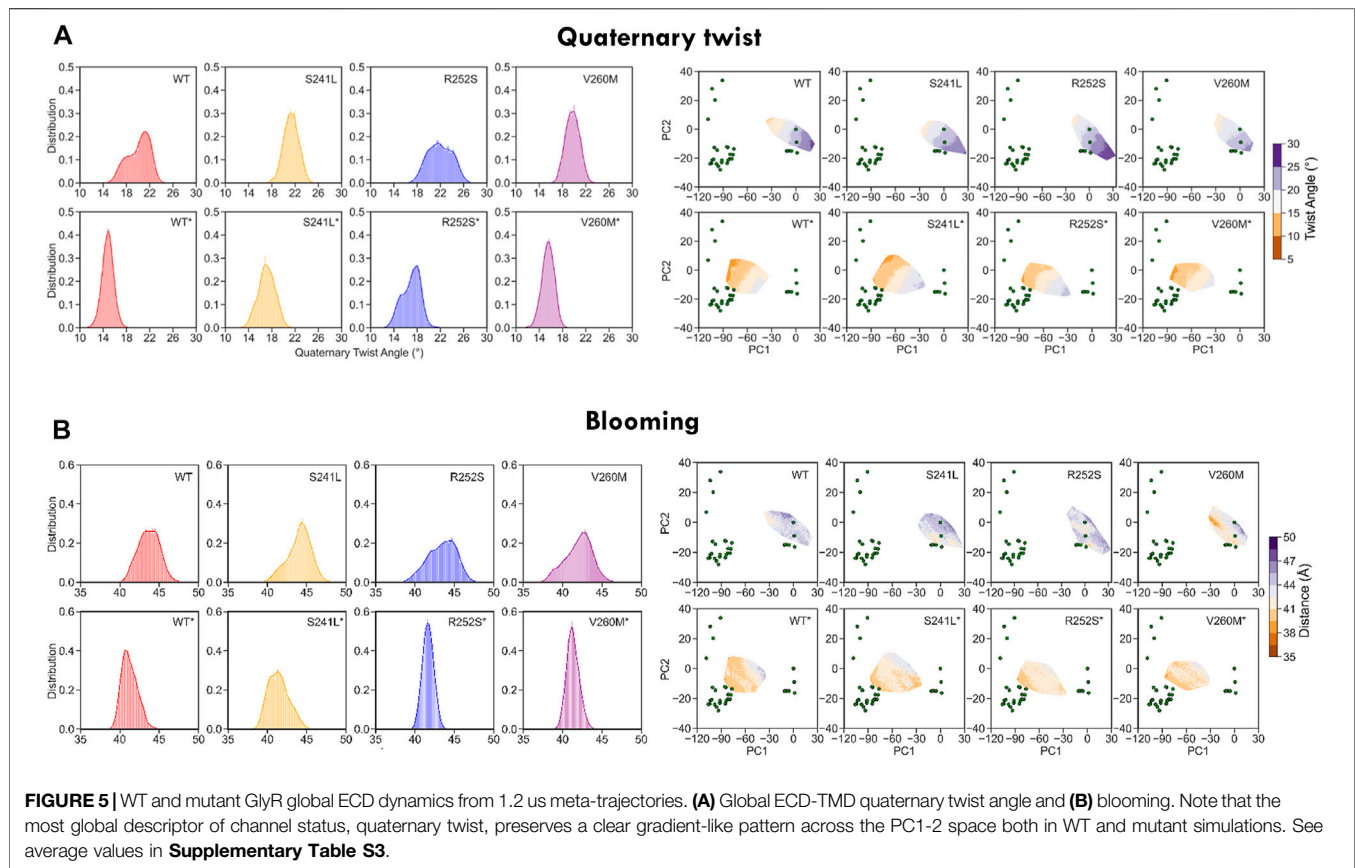


FIGURE 4 | Time evolution of MD replicates along PC1 and PC2. **(A)** Time evolution of MD trajectories along PC1, which separates closed from open/desensitized structures, for each of the four replicates from each system. Note how for simulations from the closed state (top), trajectories evolve in both closed and open/desensitized directions or stay around the starting structure, with the exception of V260M, in which all runs proceed toward the open region to the left. On the contrary, all desensitized state simulations (bottom) progress in the closing direction. **(B)** Time evolution of MD trajectories along PC2, which separates closed from open/desensitized structures, for each of the four replicates from each system. Trajectories stay or evolve toward pore closing, with the exception of S241L and V260M, which have replicates progressing toward opening. On contrast, most simulations from the desensitized state (bottom) evolve toward pore opening, except for R252S*.

desensitized state, with distributions shifted to lower values (**Supplementary Figure S3B**). This is often observed for bound/unbound systems and in agreement with our ENM preliminary analysis. Nevertheless, for both closed and desensitized state simulations, TM1-2 mutations in general shifted RMSD distributions to the right, suggesting increased conformational flexibility. While for R252S, the peak height is clearly shifted toward higher RMSDs suggesting greater thermal fluctuations, in

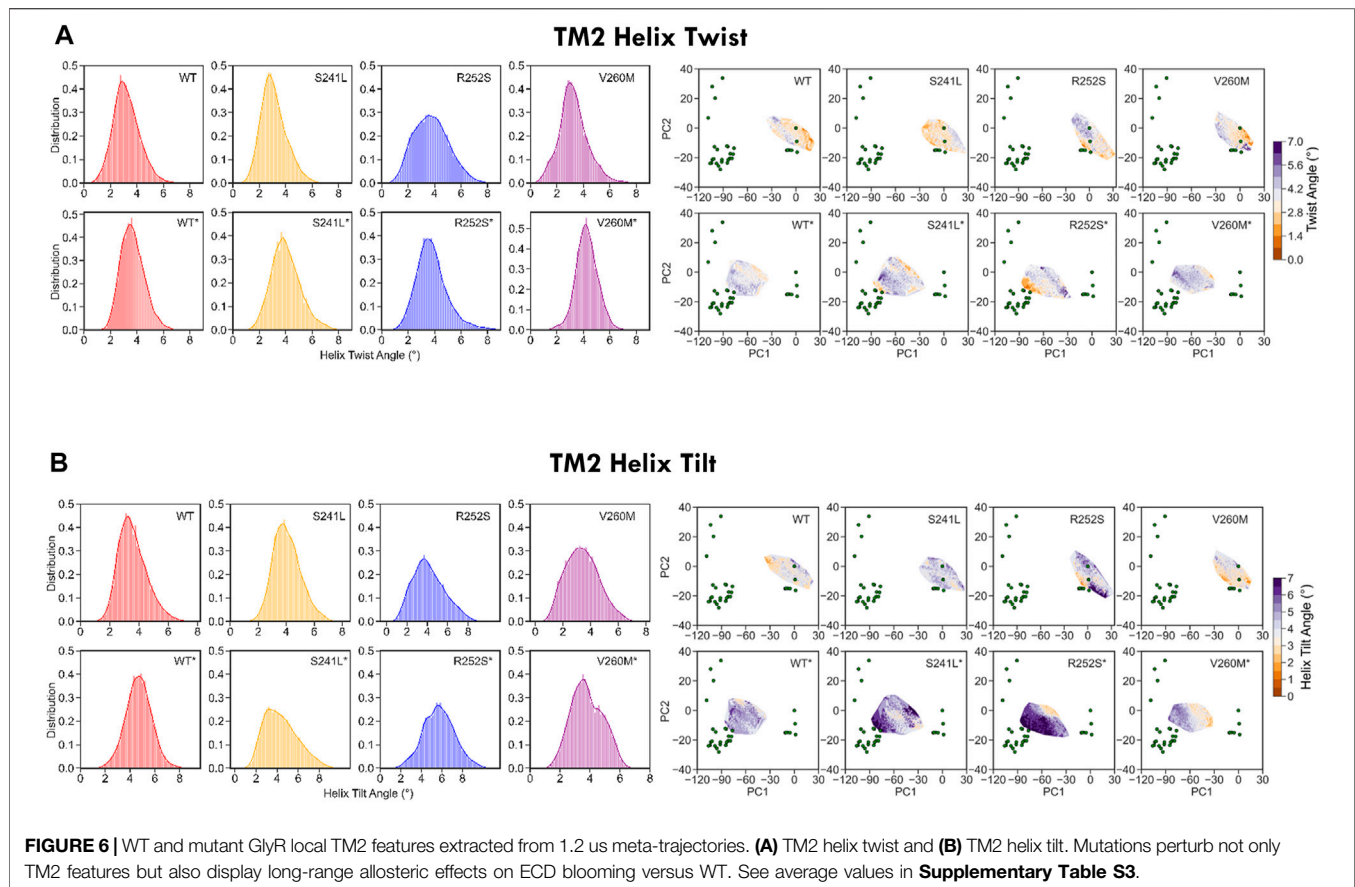
V260M, the distribution spreads over multiple peaks suggestive of different conformational clusters. Interestingly, S241L displays virtually no difference versus WT GlyR for 5CFB simulations, in contrast with 5VDH simulations. Locally, the introduced mutations disrupt highly stable hydrogen bond and salt bridge WT interactions in both the closed and the desensitized receptors, both at the local TM1-2 level and globally (**Supplementary Figures S4A,B**). Significantly, a WT salt bridge between Asp247 and Arg252



present in 5CFB but absent in 5VDH is broken by all three mutations in the closed state. Among mutants, R252S has a major impact on the closed state introducing multiple non-native salt bridges not seen in any WT simulations far away from the mutation site, around TM3-4. Native contacts in this area, which are maintained in both 5CFB and 5VDH simulations, are the most perturbed by mutations; interestingly, V260M closed state simulations display interactions seen in the open-like/desensitized state like Glu300-Lys320. Similar changes are seen in hydrogen bond patterns, with mutations mostly affecting longer-range interactions with TM3 and TM4. Despite these profound reshaping of interactions, TM1-2 local helicity is mostly unaffected (**Supplementary Figure S4C**), only displaying transient and very limited unfolding in desensitized state simulations, focused at helix termini surrounding the TM1-2 loop junction.

Given the long-range impact of mutations in H-bonding and salt bridge connectivity, we then explored their effect on global dynamics by extracting the MD *essential modes* (ED; see Methods) explored by each system (**Figure 3A**) and computing their alignment with the three major transition directions defined from PC1-2 clusters. Consistent with ENM predictions, we observed that simulations from the closed state tend to spontaneously sample toward the direction of the super-open cluster (51% overlap with 5cfb ↔ 6pm0) more than toward the open-like desensitized area (overlap with 5cfb > 5vdh, 0.45%), while simulations from 5VDH tend to relax toward the closed state and barely sample along the open-desensitized axis (76% overlap with 5cfb ↔ 5vdh *versus* 20%). By contrast, all mutants and

specially V260M enhance the opening transition displaying even better alignment with 5cfb ↔ 6pm0 (55–60% versus 50%) while they are slightly less efficient sampling in the recovery direction toward the closed state (overlaps 5cfb ↔ 5vdh 70%), especially in the case of TM1-2 loop mutations. These trends are also visible upon MD projection onto PC1-2 to build the corresponding free energy landscapes (**Figure 3B**) and to examine trajectory time evolution (**Figures 4A,B**). While WT closed simulations sample one major minima around the starting structure and a minor one skewed toward the direction of super-open structures (**Figure 3B** top), mutants show one larger elongated minimum shifted again toward the same super-open direction. Inspection of the simulation PC1-2 time evolution reveals that indeed a fraction of 5CFB trajectories proceed along PC1(blooming) and PC2 (gating) toward un-blooming/pore opening directions characteristic of the open/desensitized state, especially in the case of V260M (**Figure 4A**). By contrast, WT desensitized simulations show two small minima in the direction of 5CFB closed state (at 0.0), while mutant ones, also sampling across the same PC1 direction, point toward lower PC2 values, which are only explored in closed mutant simulations (see below). Accordingly, all 5VDH trajectories uniformly proceed along PC1 toward 5cfb minima (**Figure 4B**), although in terms of PC2 pore gating, the majority evolve toward the super-open cluster. Overall, this suggests a general trend for mutants to favor channel opening while slowing down recovery from desensitization, as is often reported for HPX mutations. Interestingly, although the biological relevance of super-open



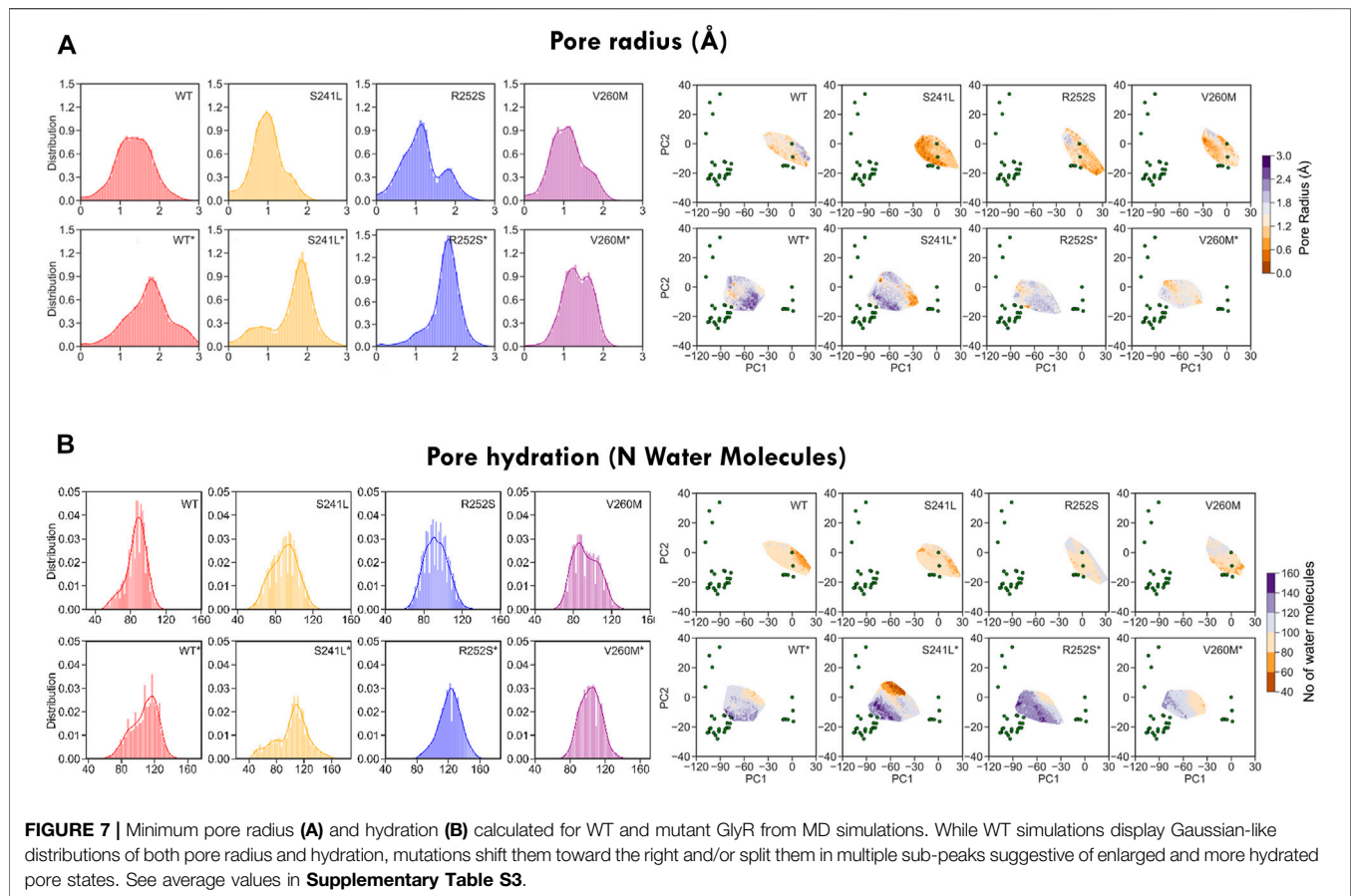
structures has been questioned, projections onto PC1-2 space clearly show that all simulations from the closed state are sampling PC2 toward solved super-open structures, while simulations from the desensitized 6PMO sample mostly PC1 toward the closed state cluster.

Finally, to better characterize the conformational effect of mutations, we also examined the classical heuristic variables describing PLGIC geometry: quaternary twist, blooming, and TM2 tilt and twist angles (**Supplementary Table S3, Figures 5, 6**). As could be expected, the ECD quaternary twist (**Figure 5A**) was higher not only for closed versus open state simulations but also for mutants versus WT trajectories, displaying in all cases a neat gradient across PC1. However, less marked gradients were observed for the rest of channel parameters, as could be expected from their poorer correlations with PCs (**Supplementary Figure S2B**). Apart from the quaternary twist, the ECD configuration is also defined by its maximum radius or blooming, which was shifted to the right by all mutations in both closed and desensitized simulations (**Figure 5B**). Interestingly, ECD blooming appeared more constrained, i.e., un-bloomed (higher peaks) in TM2 R252S* and V260M*, in comparison with S241L*. The impact of mutations was also apparent in local TM2 variables like helix twist and tilt (**Figures 6A,B**), especially upon projection, which revealed heterogeneous distributions across the PC1-2 space. Globally speaking, TM2 twist and tilt increased along PC1 toward the open/desensitized state directions. Nevertheless, while R252S

increased tilt values dramatically in desensitized state simulations but also in the closed state, reaching in both cases the highest values (10.5 and 9.9 Å, respectively), V260M displayed relatively low tilt angles, especially in 5VDH simulations. Notably, S241L displayed only a mild increase, only noticeable in 5VDH simulations. Overall, although TM1-2 mutations have a similar mild allosteric effect on ECD features, they profoundly and differently disrupt the local configuration of the pore, sampling extreme values for TM2 twist and tilt angles, which can appear uncorrelated to PC1 and associated blooming and quaternary twist.

Pore Analysis Shows That TM2 Mutations Perturb Pore Gates and Water-Ion Permeation

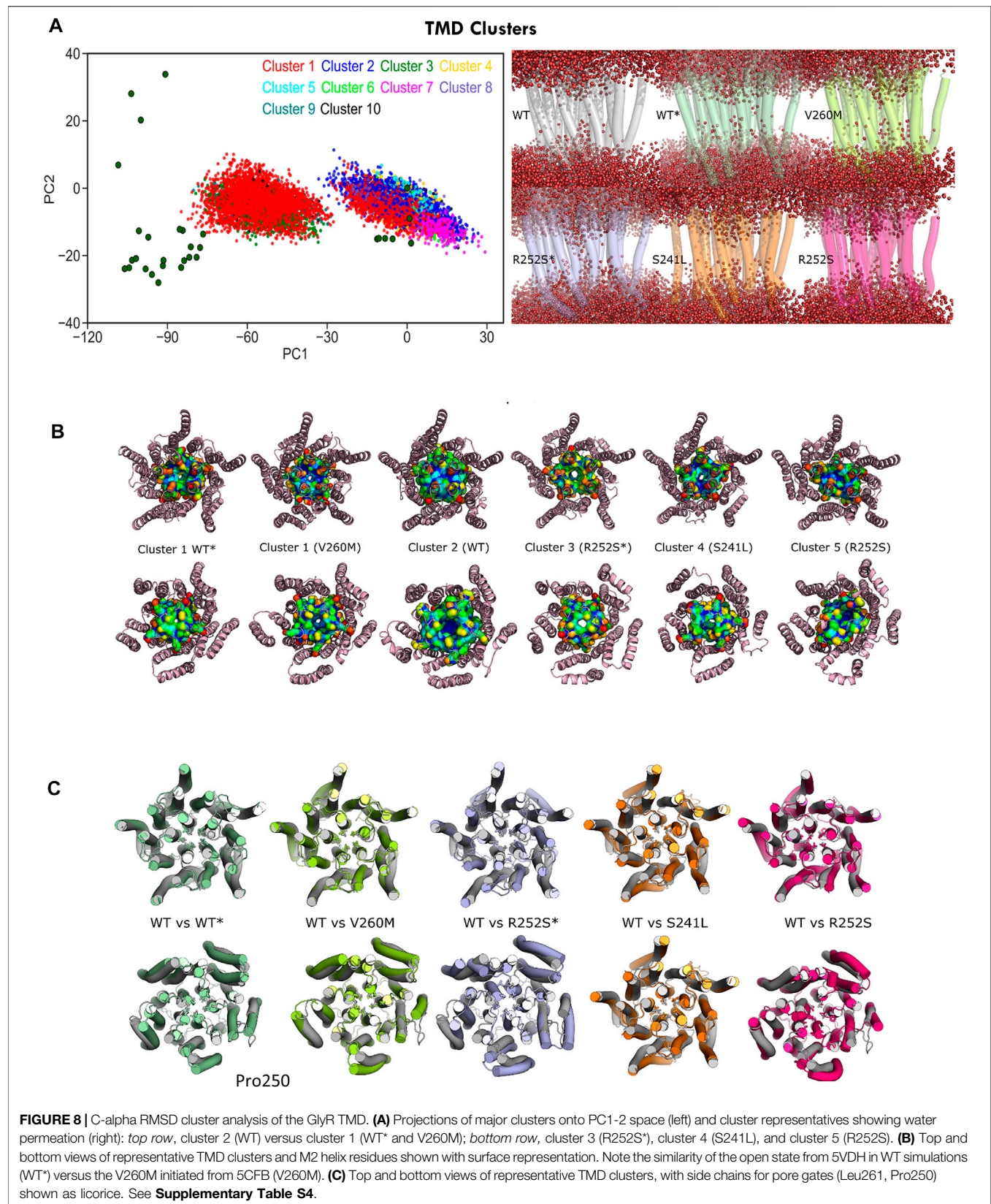
As these heterogeneous TM2 mutant features suggested a major impact on the pore, we investigated in more detail their effect on pore radius and its permeability for water (**Figure 7, Supplementary Table S3**). As could be expected from trajectory time evolution (**Figure 4B, bottom**), WT desensitized simulations from 5VDH, which start with a closed radius of 1.48 Å, quickly evolve opening the pore as seen by broader radius distributions up to a maximum of 3.26 Å (1.7 ± 0.6 Å), in comparison with 5CFB simulations, which start at 1.28 Å and reach up to a maximum of 2.85 Å (1.3 ± 0.5 Å) (see **Figure 7A, Supplementary Table S3**).



Significantly, mutations tend to display broader distributions, generally shifted to the right and with multiple peaks that suggests a diversity of open and closed pore configurations. Differences versus WT simulations are particularly significant for 5CFB simulations, with mutants displaying a clear tail (S241L, V260M) or secondary peak (R252S) at higher nearly open radius close to 2 Å (**Figure 7A**). This shift to the right is also seen for 5VDH mutant simulations with the exception of V260M; notably, secondary peaks at collapsed pore states barely sampled by the WT are also seen for mutants. These pore radius changes translate to variations in water permeation versus the WT protein. The number of water molecules in the channel ranges from 40 to 120 for the closed state GlyR protein, with an average of ≈ 80 water molecules in the channel. This seems to shift toward higher values and with a broader distribution for mutant proteins, which have an average of ≈ 90 water molecules in the channel and maximal values for all mutations around 130–140 (**Supplementary Table S3**). By contrast, simulations from 5VDH have on average less water molecules in the channel, although in the case of TM2 mutants can reach higher hydration than the WT (up to 170 water molecules for TM1-2 loop mutants versus 160 for WT-GlyR) (**Figure 7B**).

To gain more insight into these differently hydrated pore states explored by MD, we performed TMD cluster analysis on the complete trajectory set with GROMACS (**Figure 8**, **Supplementary Table S4**). Simulations initiated from the

desensitized state sampled four clusters: cluster 1, which accounts for nearly half of the total conformations sampled by GlyR from closed and desensitized states, and clusters 3, 9, and 10, which in total, account for 7% of the total population and sample expanded pores up to 2 Å. Interestingly, we observed that this major semi-open cluster 1 conformation (1.5 ± 0.4 Å) was also sampled by both V260M (13% of cluster 1) and R252S (4% of cluster 1) simulations initiated from the closed state, which allowed the observed increased water permeation (**Figure 8A** right). Cluster 2 was mostly sampled by WT closed state simulations (51%) as well as the three mutants studied. In contrast, cluster 3, which features an expanded pore around 1.7 Å, is distinctively assigned for R252S* (95% of the cluster). Clusters 5 and 7 are also unique of R252S closed state simulations and feature a slightly collapsed pore (0.8 Å), also found in cluster 6, which has a mixed population of conformers from neighbor S241L and R252S mutants (see **Supplementary Table S4**). Notably, similar collapsed states, previously observed in simulations (Dämgén and Biggin, 2020), are characterized by loss of the fivefold symmetry of the TMD pentamer (cluster 5 in **Figures 8B,C**). In our simulations, these states accounted, however, for a minor fraction of total sampling and were mostly populated by R252S, which, on the other hand, sampled also expanded pore states like the other mutants as well as WT* trajectories.



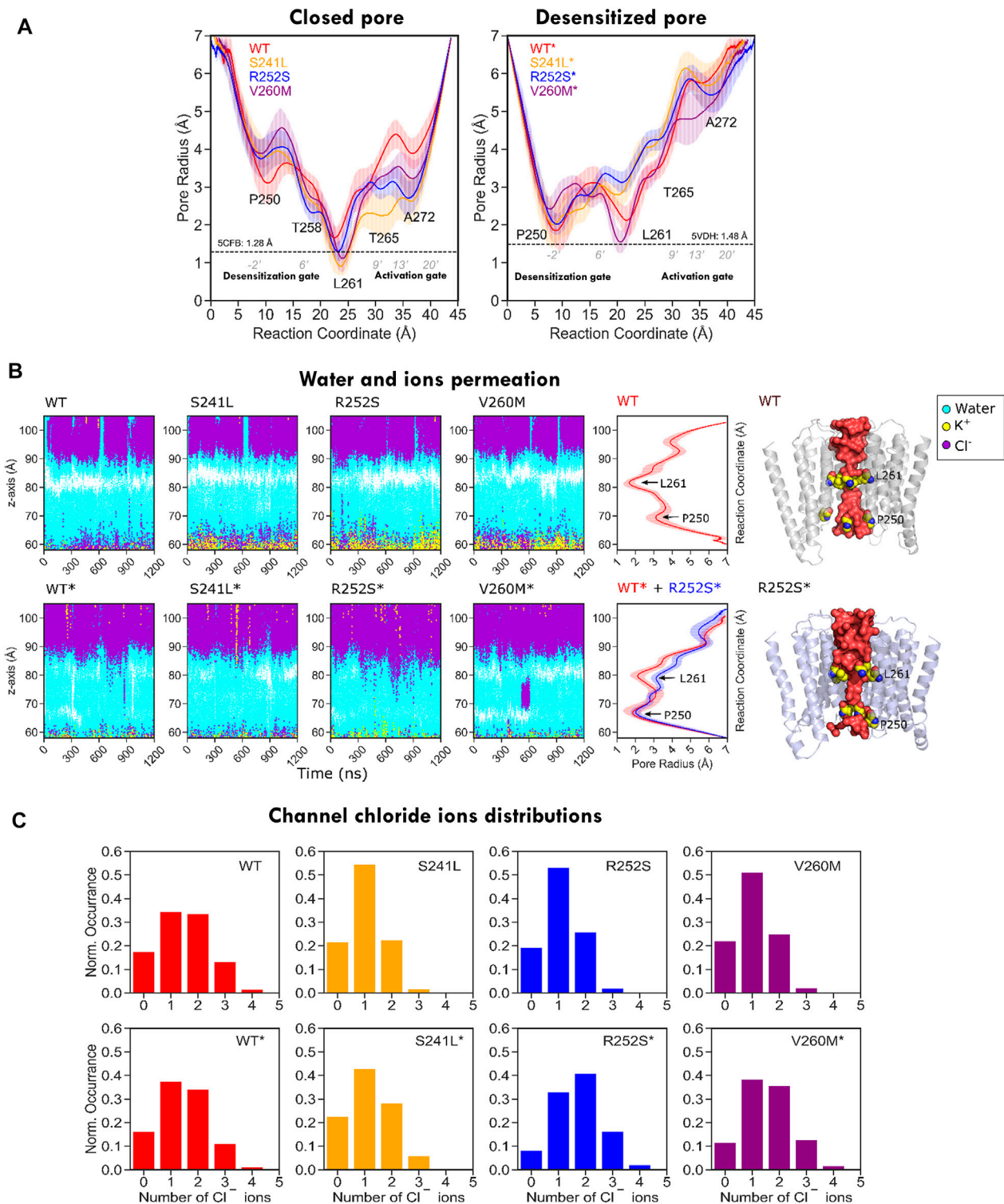


FIGURE 9 | Pore radius profile for WT and mutant GlyR from MD simulations. **(A)** Pore profiles for closed/resting state WT (5CFB) and mutants constructed from it are shown to the left; WT* (5VDH) and mutants constructed from it are shown to the right side. Note how in both closed and desensitized/open state simulations all mutants tend to widen the P250 gate. **(B)** Water and ion permeation across the channel. The closed activation gate in 5CFB simulations (top) appears as a white area around Leu261, missing in desensitized state simulations (bottom). Chloride ions cross the area in WT* and V260M* in relation with permeation events (see **Supplementary Movies S1, S2**); there is also an entry of potassium ions through the selectivity filter (P250) in closed state simulations (yellow), but they stay in the vestibule. **(C)** Chloride ion distribution inside the channels; note the shift to the right for mutants due to the wider channels accommodating a larger number of ions.

From PLGIC structures and mutagenesis work, it is known that there are two major constriction points in the GlyR pore: an upper ring of hydrophobic residues at the 9' position of TM2 (the L9' activation gate, formed by Leu261) and a lower ring of Pro residues at -2' (the P-2' desensitization gate, corresponding to Pro250). While the central L9' gate is closed in antagonist-bound structures (5CFB, 3JAD), in desensitized structures (5VDH, 3JAF) it is P-2' that closes the intracellular "mouth" of the channel. The P-2' is wide-open in the so-called super-open structures (3JAE). In general, despite the observed minority collapsed TMD clusters, all our simulations resulted in pore relaxation versus the initial crystallographic structures, but with substantial differences upon mutation. A closer inspection of pore profiles (**Figure 9A**) revealed that TM1-2 mutants dramatically reshape the central channel in a similar way. In the closed state, mutations expand the lower (P250, 9') but decrease the upper (A272, 20') pore sections, while in the desensitized simulations, they tend to destabilize and enlarge both. Mutations also displayed wider pore fluctuations, remarkable for S241L and V260M. Although the short time scale of our simulations did not allow us to observe complete opening of the channel, some of the sampled clusters, especially for the mutants, reached pore radius around 1.7–1.8 Å, which can allow the passage of a partially hydrated chloride ion (1.8 Å); in such wider pore conformations, water was observed forming continuous molecule chains across the channels. A closer examination of water and ion penetration into the channel revealed that chloride ions penetrate indeed deep into the channel from the enlarged intracellular "mouth", although only for WT* and V260M* simulations, this resulted in complete permeation events (**Figures 9B,C, Supplementary Movies S1, S2**). Notably, the enlarged open mouth at the level of the selectivity filter also allowed the entry of potassium ions to the vestibule in 5CFB simulations.

SUMMARY AND CONCLUSION

Here, we aim to perform a preliminary study of uncharacterized GlyR mutations reported in human tumors. Based on 3D-clustering, conservation, and vicinity or overlap with hyperekplexia changes, we focused on three mutations potentially disrupting gating for further study: one located in the TM1-2 loop, at the "mouth" of the channel (S241L), and two at the back of pore TM2 (R252S and V260M). Our goal was to explore whether they were neutral or perturbed channel dynamics and potentially function. To evaluate functional/conformational status and monitor our simulations, we performed PCA of the current ensemble of GlyR structures, in order to obtain suitable reaction coordinates to build an "experimental" conformational landscape (Orellana et al., 2019a; Orellana, 2019). We confirmed the resulting PCs tracked multiple key channel descriptors providing an automatic and reasonable classification of the solved structures. MD projections on PC1-2 space allowed us to

quantify how trajectories sample large-scale motions correlated with multiple channel features. This provided a framework to analyze sampling by MD simulations of human WT and mutant GlyR. Surprisingly, we found evidence that not only the closed-super-open transition is encoded in the experimental structures but also that they are indeed sampled in unbiased WT simulations in the absence of ligand. While WT simulations from the closed state clearly evolve in the direction of super-open solved structures, simulations from the desensitized state tend to sample the recovery transition back to the closed state and not toward the super-open, as suggested by ENM. Our integrated structural analysis also revealed that mutations perturb sampling in a similar way, enhancing the exploration of the opening direction and disrupting relaxation to the native closed state. These global features relate to the local disruption of TM1-2 contacts, which results in an altered TM2 orientation that favors a wider pore and increased water permeation. Nevertheless, the impact of mutations was clearly distinct, with the mutation R252S, which targets the most conserved residue, resulting in non-native interactions and sampling of collapsed pore states. On the contrary, mutation V260M was the closest in behavior to the closed state and displayed enhanced sampling of the opening transition. Importantly, chloride permeation was only observed for WT* and V260M* simulations from the desensitized state. Functional evidence suggests that the mutation of Arg252 results in non-conducting channels, which would agree with our observations of a profoundly impaired channel. On contrast, the V260M HPX mutant has been shown to result in spontaneous activity and prolonged desensitization, also in agreement with our simulations. Functional data for mutations surrounding S241L are still lacking, but our results suggest a behavior in between the other two, probably closer to WT and V260M in terms of channel permeability and conduction despite its proximity to R252S.

In summary, our analysis indicates, on one side, that the concentration of GLRA1-3 mutations across TM1 and TM2 is very likely not random, and, on the other, that these changes certainly disrupt the GlyR function in the tumor cells carrying them, as seen for HPX. Whether and how disrupting GlyR function can represent an advantage for cancer cells is beyond the scope of this work but certainly deserves further computational as well as functional investigation.

DATA AVAILABILITY STATEMENT

The data and code used for this study are available from the corresponding author LO upon request.

AUTHOR CONTRIBUTIONS

AM performed MD simulations and analysis, and prepared figures under LO supervision. OY provided scripts for channel analysis and contributed to discussions. LO conceived the original idea, performed mutation clustering, ENM, PCA, and ED analysis, designed MD simulations, interpreted results,

prepared figures and wrote the manuscript. All authors participated in data interpretation and manuscript revision.

FUNDING

This work was supported by Cancerfonden Junior Investigator Award (21 0305 JIA 01 H) and Project Grant (CF 21 1471 Pj 2022-24), Jeansson's Foundation 2021, Vetenskapsrådet Starting Grant VR2021-02248 2022-25, and Karolinska Institute KIS, KIF Grants to LO. Simulations were run using the Swedish National Infrastructure for Computing (allocations Q13 SNIC 2021/5-87 and 2021/5-409 to LO).

REFERENCES

- Abraham, M. J., Murtola, T., Schulz, R., Páll, S., Smith, J. C., Hess, B., et al. (2015). GROMACS: High Performance Molecular Simulations through Multi-Level Parallelism from Laptops to Supercomputers. *SoftwareX* 1–2, 19–25. doi:10.1016/j.softx.2015.06.001
- Amadei, A., Linssen, A. B. M., and Berendsen, H. J. C. (1993). Essential Dynamics of Proteins. *Proteins* 17, 412–425. doi:10.1002/prot.340170408
- Amadei, A., Linssen, A. B. M., de Groot, B. L., Berendsen, H. J. C., and Berendsen, H. J. (1996). An Efficient Method for Sampling the Essential Subspace of Proteins. *J. Biomol. Struct. Dyn.* 13, 615–625. doi:10.1080/07391102.1996.10508874
- Ashkenazy, H., Abadi, S., Martz, E., Chay, O., Mayrose, I., Pupko, T., et al. (2016). ConSurf 2016: An Improved Methodology to Estimate and Visualize Evolutionary Conservation in Macromolecules. *Nucleic Acids Res.* 44 (W1), W344–W350. doi:10.1093/nar/gkw408
- Atilgan, A. R., Durell, S. R., Jernigan, R. L., Demirel, M. C., Keskin, O., and Bahar, I. (2001). Anisotropy of Fluctuation Dynamics of Proteins with an Elastic Network Model. *Biophysical J.* 80, 505–515. doi:10.1016/S0006-3495(01)76033-X
- Atilgan, C. (2018). *Computational Methods for Efficient Sampling of Protein Landscapes and Disclosing Allosteric Regions*. 1st ed. Elsevier. doi:10.1016/bs.apcsb.2018.06.001
- Bahar, I., Lezon, T. R., Bakan, A., and Shrivastava, I. H. (2010). Normal Mode Analysis of Biomolecular Structures: Functional Mechanisms of Membrane Proteins. *Chem. Rev.* 110, 1463–1497. doi:10.1021/cr9000095e
- Bertaccini, E. J., Trudell, J. R., and Lindahl, E. (2010). Normal Mode Gating Motions of a Ligand-Gated Ion Channel Persist in a Fully Hydrated Lipid Bilayer Model. *ACS Chem. Neurosci.* 1, 552. doi:10.1021/cn100026t
- Bhattacharya, D., Gawali, V. S., Kallay, L., Toukam, D. K., Koehler, A., Stambrook, P., et al. (2021). Therapeutically Leveraging GABAA Receptors in Cancer. *Exp. Biol. Med.* 246, 2128. doi:10.1177/15353702211032549
- Bode, A., Wood, S.-E., Mullins, J. G. L., Keramidias, A. T. D., Cushion, R. H., Pickrell, W. O., et al. (2013). New Hyperekplexia Mutations Provide Insight into Glycine Receptor Assembly, Trafficking, and Activation Mechanisms. *J. Biol. Chem.* 288, 33745–33759. doi:10.1074/jbc.M113.509240
- Bode, A., and Lynch, J. W. (2013). Analysis of Hyperekplexia Mutations Identifies Transmembrane Domain Rearrangements that Mediate glycine Receptor Activation. *J. Biol. Chem.* 288, 33760–33771. doi:10.1074/jbc.M113.513804
- Bode, A., and Lynch, J. W. (2014). The Impact of Human Hyperekplexia Mutations on glycine Receptor Structure and Function. *Mol. Brain* 7, 2. doi:10.1186/1756-6606-7-2
- Calimet, N., Simoes, M., Changeux, J.-P., Karplus, M., Taly, A., and Cecchini, M. (2013). A Gating Mechanism of Pentameric Ligand-Gated Ion Channels. *Proc. Natl. Acad. Sci.* 110, E3987–E3996. doi:10.1073/pnas.1313785110
- Case, D. A. (1999). Molecular Dynamics and Normal Mode Analysis of Biomolecular Rigidity. *Mol. Biol.* 18, 329–344. doi:10.1007/0-306-47089-6
- Castaldo, P., Stefanoni, P., Miceli, F., Coppola, G., del Giudice, E. M., Bellini, G., et al. (2004). A Novel Hyperekplexia-Causing Mutation in the Pre-transmembrane Segment 1 of the Human glycine Receptor $\alpha 1$ Subunit Reduces Membrane Expression and Impairs Gating by Agonists. *J. Biol. Chem.* 279, 1200. doi:10.1074/jbc.M311021200

ACKNOWLEDGMENTS

LO thanks the Swedish Cancer Foundation (Cancerfonden), the Swedish Research Council (Vetenskapsrådet), the Jeansson's Foundation (Harald och Greta Jeansson's Stiftelse) and Karolinska Institute for generous support.

SUPPLEMENTARY MATERIAL

The Supplementary Material for this article can be found online at: <https://www.frontiersin.org/articles/10.3389/fmolb.2022.890851/full#supplementary-material>

- Cerdan, A. H., and Cecchini, M. (2020). On the Functional Annotation of Open-Channel Structures in the Glycine Receptor. *Structure* 28, 690. doi:10.1016/j.str.2020.05.003
- Cerdan, A. H., Martin, N. É., and Cecchini, M. (2018). An Ion-Permeable State of the Glycine Receptor Captured by Molecular Dynamics. *Structure* 26, 1555. doi:10.1016/j.str.2018.07.019
- Changeux, J.-P. (2014). Protein Dynamics and the Allosteric Transitions of Pentameric Receptor Channels. *Biophys. Rev.* 6, 311–321. doi:10.1007/s12551-014-0149-z
- Chen, J., Wang, L., Wang, W., Sun, H., Pang, L., and Bao, H. (2021a). Conformational Transformation of Switch Domains in GDP/K-Ras Induced by G13 Mutants: An Investigation through Gaussian Accelerated Molecular Dynamics Simulations and Principal Component Analysis. *Comput. Biol. Med.* 135, 4639. doi:10.1016/j.compbiomed.2021.104639
- Chen, J., Zhang, S., Wang, W., Pang, L., Zhang, Q., and Liu, X. (2021b). Mutation-Induced Impacts on the Switch Transformations of the GDP-And GTP-Bound K-Ras: Insights from Multiple Replica Gaussian Accelerated Molecular Dynamics and Free Energy Analysis. *J. Chem. Inf. Model.* 61, 1470. doi:10.1021/acs.jcim.0c01470
- Chung, S.-K., Vanbellinthen, J.-F., Mullins, J. G. L., Robinson, A., Hantke, J., Hammond, C. L., et al. (2010). Pathophysiological Mechanisms of Dominant and Recessive GLRA1 Mutations in Hyperekplexia. *J. Neurosci.* 30, 9612–9620. doi:10.1523/jneurosci.1763-10.2010
- Dämgen, M. A., and Biggin, P. C. (2020). A Refined Open State of the Glycine Receptor Obtained via Molecular Dynamics Simulations. *Structure* 28(1), 130. doi:10.1016/j.str.2019.10.019
- Dacosta, C. J. B., and Baenziger, J. E. (2013). Gating of Pentameric Ligand-Gated Ion Channels: Structural Insights and Ambiguities. *Structure* 21, 1271–1283. doi:10.1016/j.str.2013.06.019
- Daidone, I., and Amadei, A. (2012). Essential Dynamics: Foundation and Applications. *WIREs Comput. Mol. Sci.* 2, 762–770. doi:10.1002/wcms.1099
- Dämgen, M. A., Zaki, A. M., and Biggin, P. C. (2020). Comment on “On the Functional Annotation of Open-Channel Structures in the Glycine Receptor. *Structure* 28 (6), 601–603. doi:10.1016/j.str.2020.04.021
- Del Giudice, E. M., Coppola, G., Bellini, G., Cirillo, G., Succimarra, G., and Pascotto, A. (2001). A Mutation (V260M) in the Middle of the M2 Pore-Lining Domain of the glycine Receptor Causes Hereditary Hyperekplexia. *Eur. J. Hum. Genet.* 9 (11), 873–876. doi:10.1038/sj.ejhg.5200729
- Du, J., Lü, W., Wu, S., Cheng, Y., and Gouaux, E. (2015). Glycine Receptor Mechanism Elucidated by Electron Cryo-Microscopy. *Nature* 526 (7572), 224–229. doi:10.1038/nature14853
- Essmann, U., Perera, L., Berkowitz, M. L., Darden, T., Lee, H., and Pedersen, L. G. (1995). A Smooth Particle Mesh Ewald Method. *J. Chem. Phys.* 103, 8577–8593. doi:10.1063/1.470117
- Ewald, P. P. (1921). Die Berechnung optischer und elektrostatischer Gitterpotentiale. *Ann. Phys.* 369 (3), 253–287. doi:10.1002/andp.19213690304
- Gielen, M., and Corringer, P.-J. (2018). The Dual-Gate Model for Pentameric Ligand-Gated Ion Channels Activation and Desensitization. *J. Physiol.* 596, 1873–1902. doi:10.1113/JP275100

- Hess, B., Bekker, H., Berendsen, H. J. C., and Fraaije, J. G. E. M. (1997). A Linear Constraint Solver for Molecular Simulations. *J. Comput. Chem.* 18 (12), 1463–1472. doi:10.1002/(SICI)1096-987X(199709)18
- Hibbs, R. E., and Gouaux, E. (2011). Principles of Activation and Permeation in an Anion-Selective Cys-Loop Receptor. *Nature* 474, 54–60. doi:10.1038/nature10139
- Hoover, W. G. (1985). Canonical Dynamics: Equilibrium Phase-Space Distributions. *Phys. Rev. A* 31 (3), 1695–1697. doi:10.1103/PhysRevA.31.1695
- Howard, R. J. (2021). Elephants in the Dark: Insights and Incongruities in Pentameric Ligand-Gated Ion Channel Models. *J. Mol. Biol.* 433 (17), 167128. doi:10.1016/j.jmb.2021.167128
- Huang, J., Rauscher, S., Nawrocki, G., Ran, T., Feig, M., De Groot, B. L., et al. (2016). CHARMM36m: An Improved Force Field for Folded and Intrinsically Disordered Proteins. *Nat. Methods* 14, 4067. doi:10.1038/nmeth.4067
- Huang, X., Chen, H., Michelsen, K., Schneider, S., and Shaffer, P. L. (2015). Crystal Structure of Human glycine Receptor $\alpha 3$ Bound to Antagonist Strychnine. *Nature* 526 (7572), 277–280. doi:10.1038/nature14972
- Huang, X., Chen, H., and Shaffer, P. L. (2017a). Crystal Structures of Human GlyR $\alpha 3$ Bound to Ivermectin. *Structure* 25, 945–950.e2. doi:10.1016/j.str.2017.04.007
- Huang, X., Shaffer, P. L., Ayube, S., Bregman, H., Chen, H., Lehto, S. G., et al. (2017b). Crystal Structures of Human glycine Receptor $\alpha 3$ Bound to a Novel Class of Analgesic Potentiators. *Nat. Struct. Mol. Biol.* 24, 108–113. doi:10.1038/nsmb.3329
- Jo, S., Cheng, X., Lee, J., Kim, S., Park, S. J., Patel, D. S., et al. (2017). CHARMM-GUI 10 Years for Biomolecular Modeling and Simulation. *J. Comput. Chem.* 38, 1114–1124. doi:10.1002/jcc.24660
- Jo, S., Kim, T., Iyer, V. G., and Im, W. (2008). CHARMM-GUI: A Web-Based Graphical User Interface for CHARMM. *J. Comput. Chem.* 29, 1859–1865. doi:10.1002/jcc.20945
- Jolliffe, I. T. (2002). *Principal Component Analysis*. doi:10.1007/b98835
- Kumar, A., Basak, S., Rao, S., Gicheru, Y., Mayer, M. L., Sansom, M. S. P., et al. (2020). Mechanisms of Activation and Desensitization of Full-Length glycine Receptor in Lipid Nanodiscs. *Nat. Commun.* 11, 17364. doi:10.1038/s41467-020-17364-5
- Lewis, T. M., Sivilotti, L. G., Colquhoun, D., Gardiner, R. M., Schoepfer, R., and Rees, M. (1998). Properties of Human glycine Receptors Containing the Hyperekplexia Mutation $\alpha 1$ (K276E), Expressed in *Xenopus* oocytes. *J. Physiol.* 507, 25–40. doi:10.1111/j.1469-7793.1998.025bu.x
- Lynch, J. W. (2004). Molecular Structure and Function of the glycine Receptor Chloride Channel. *Physiol. Rev.* 84, 1051. doi:10.1152/physrev.00042.2003
- Lynch, J. W., Zhang, Y., Talwar, S., and Estrada-Mondragon, A. (2017). *Glycine Receptor Drug Discovery*. 1st ed. Elsevier. doi:10.1016/bs.apha.2017.01.003
- Martin, N. E., Malik, S., Calimet, N., Changeux, J.-P., and Cecchini, M. (2017). Un-Gating and Allosteric Modulation of a Pentameric Ligand-Gated Ion Channel Captured by Molecular Dynamics. *PLoS Comput. Biol.* 13 (10), e1005784. doi:10.1371/journal.pcbi.1005784
- Monod, J., Wyman, J., and Changeux, J.-P. (1965). On the Nature of Allosteric Transitions: a Plausible Model. *J. Mol. Biol.* 12, 88–118. doi:10.1016/S0022-2836(65)80285-6
- Nemecz, Á., Prevost, M. S., Menny, A., and Corringer, P.-J. (2016). Emerging Molecular Mechanisms of Signal Transduction in Pentameric Ligand-Gated Ion Channels. *Neuron* 90, 452–470. doi:10.1016/j.neuron.2016.03.032
- Nosé, S. (1984). A Molecular Dynamics Method for Simulations in the Canonical Ensemble. *Mol. Phys.* 52, 255. doi:10.1080/00268978400101201
- Orellana, L., Gustavsson, J., Bergh, C., Yoluk, O., and Lindahl, E. (2019a). EBDIMS Server: Protein Transition Pathways with Ensemble Analysis in 2D-Motion Spaces. *Bioinformatics* 35, 3505–3507. doi:10.1093/bioinformatics/btz104
- Orellana, L. (2019). Large-Scale Conformational Changes and Protein Function: Breaking the In Silico Barrier. *Front. Mol. Biosci.* 6, 117. doi:10.3389/fmolb.2019.00117
- Orellana, L., Rueda, M., Ferrer-Costa, C., Lopez-Blanco, J. R., Chacón, P., and Orozco, M. (2010). Approaching Elastic Network Models to Molecular Dynamics Flexibility. *J. Chem. Theory Comput.* 6, 2910–2923. doi:10.1021/ct100208e
- Orellana, L., Thorne, A. H., Lema, R., Gustavsson, J., Parisian, A., Hospital, A., et al. (2019b). Oncogenic Mutations at the EGFR Ectodomain Structurally Converge to Remove a Steric Hindrance on a Kinase-Coupled Cryptic Epitope. *Proc. Natl. Acad. Sci. U. S. A.* 116, 110009. doi:10.1073/pnas.1821442116
- Orellana, L., Yoluk, O., Carrillo, O., Orozco, M., and Lindahl, E. (2016). Prediction and Validation of Protein Intermediate States from Structurally Rich Ensembles and Coarse-Grained Simulations. *Nat. Commun.* 7, 12575. doi:10.1038/ncomms12575
- Parrinello, M., and Rahman, A. (1981). Polymorphic Transitions in Single Crystals: A New Molecular Dynamics Method. *J. Appl. Phys.* 52. doi:10.1063/1.328693
- Prevost, M. S., Sauguet, L., Nury, H., van Renterghem, C., Huon, C., Poitevin, F., et al. (2012). A Locally Closed Conformation of a Bacterial Pentameric Proton-Gated Ion Channel. *Nat. Struct. Mol. Biol.* 19, 642–649. doi:10.1038/nsmb.2307
- Pronk, S., Páll, S., Schulz, R., Larsson, P., Bjelkmar, P., Apostolov, R., et al. (2013). GROMACS 4.5: A High-Throughput and Highly Parallel Open Source Molecular Simulation Toolkit. *Bioinformatics* 29, 845–854. doi:10.1093/bioinformatics/btt055
- Saul, B., Kuner, T., Sobetzko, D., Brune, W., Hanefeld, F., Meinck, H. M., et al. (1999). Novel GLRA1 Missense Mutation (P250T) in Dominant Hyperekplexia Defines an Intracellular Determinant of glycine Receptor Channel Gating. *J. Neurosci.* 19, 869. doi:10.1523/jneurosci.19-03-00869.1999
- Smart, O. S., Neduvilil, J. G., Wang, X., Wallace, B. A., and Sansom, M. S. P. (1996). HOLE: A Program for the Analysis of the Pore Dimensions of Ion Channel Structural Models. *J. Mol. Graph.* 14. doi:10.1016/S0263-7855(97)00009-X
- Taly, A., Hénin, J., Changeux, J.-P., and Cecchini, M. (2014). Allosteric Regulation of Pentameric Ligand-Gated Ion Channels: An Emerging Mechanistic Perspective. *Channels* 8, 350–360. doi:10.4161/chan.29444
- Tate, J. G., Bamford, S., Jubb, H. C., Sondka, Z., Beare, D. M., Bindal, N., et al. (2019). COSMIC: The Catalogue of Somatic Mutations in Cancer. *Nucleic Acids Res.* 47, D941. doi:10.1093/nar/gky1015
- The UniProt Consortium (2021). UniProt: the Universal Protein Knowledgebase in 2021. *Nucleic Acids Res.* 49, D480–D489. doi:10.1093/nar/gkaa1100
- Tirion, M. M. (1996). Large Amplitude Elastic Motions in Proteins from a Single-Parameter, Atomic Analysis. *Phys. Rev. Lett.* 77, 1905–1908. doi:10.1103/physrevlett.77.1905
- Van den Eynden, J., Ali, S. S., Horwood, N., Carmans, S., Brône, B., Hellings, N., et al. (2009). Glycine and glycine Receptor Signalling in Non-neuronal Cells. *Front. Mol. Neurosci.* 2, 9–12. doi:10.3389/neuro.02.009.2009
- Wu, E. L., Cheng, X., Jo, S., Rui, H., Song, K. C., Dávila-Contreras, E. M., et al. (2014). CHARMM-GUI Membrane Builder toward Realistic Biological Membrane Simulations. *J. Comput. Chem.* 35, 23702. doi:10.1002/jcc.23702
- Yang, L.-W., Eyal, E., Bahar, I., and Kitao, A. (2009). Principal Component Analysis of Native Ensembles of Biomolecular Structures (PCA_NEST): Insights into Functional Dynamics. *Bioinformatics* 25, 606–614. doi:10.1093/bioinformatics/btp023
- Young, S. Z., and Bordey, A. (2009). GABA's Control of Stem and Cancer Cell Proliferation in Adult Neural and Peripheral Niches. *Physiology* 24, 171. doi:10.1152/physiol.00002.2009
- Yu, H., Bai, X. C., and Wang, W. (2021a). Characterization of the Subunit Composition and Structure of Adult Human glycine Receptors. *Neuron* 109, 2707. doi:10.1016/j.neuron.2021.08.019
- Yu, J., Zhu, H., Lape, R., Greiner, T., Du, J., Lü, W., et al. (2021b). Mechanism of Gating and Partial Agonist Action in the glycine Receptor. *Cell* 184, 26. doi:10.1016/j.cell.2021.01.026
- Zhang, X., Zhang, R., Zheng, Y., Shen, J., Xiao, D., Li, J., et al. (2013). Expression of Gamma-Aminobutyric Acid Receptors on Neoplastic Growth and Prediction of Prognosis in Non-small Cell Lung Cancer. *J. Transl. Med.* 11, 102. doi:10.1186/1479-5876-11-102
- Zheng, W., and Auerbach, A. (2011). Decrypting the Sequence of Structural Events during the Gating Transition of Pentameric Ligand-Gated Ion Channels Based on an Interpolated Elastic Network Model. *PLoS Comput. Biol.* 7, e001046. doi:10.1371/journal.pcbi.1001046
- Zhu, F., and Hummer, G. (2010). Pore Opening and Closing of a Pentameric Ligand-Gated Ion Channel. *Proc. Natl. Acad. Sci. U.S.A.* 107, 19814–19819. doi:10.1073/pnas.1009313107

Conflict of Interest: The authors declare that the research was conducted in the absence of any commercial or financial relationships that could be construed as a potential conflict of interest.

Publisher's Note: All claims expressed in this article are solely those of the authors and do not necessarily represent those of their affiliated organizations, or those of the publisher, the editors, and the reviewers. Any product that may be evaluated in this article, or claim that may be made by its manufacturer, is not guaranteed or endorsed by the publisher.

Copyright © 2022 Mhashal, Yoluk and Orellana. This is an open-access article distributed under the terms of the Creative Commons Attribution License (CC BY). The use, distribution or reproduction in other forums is permitted, provided the original author(s) and the copyright owner(s) are credited and that the original publication in this journal is cited, in accordance with accepted academic practice. No use, distribution or reproduction is permitted which does not comply with these terms.



A Multi-Scale Approach to Model K⁺ Permeation Through the KcsA Channel

T. L. Horng^{1*}, R. S. Chen², M. V. Leonardi³, F. Franciolini³ and L. Catacuzzeno^{3*}

¹Department of Applied Mathematics, Feng Chia University, Taichung, Taiwan, ²Department of Life Science, Tunghai University, Taichung, Taiwan, ³Department of Chemistry, Biology and Biotechnology, University of Perugia, Perugia, Italy

OPEN ACCESS

Edited by:

Simone Furini,
University of Siena, Italy

Reviewed by:

Vishwanath Jogini,
D. E. Shaw Research, United States
Igor Vorobyov,
University of California, United States

*Correspondence:

T. L. Horng
tlhorng@fcu.edu.tw
L. Catacuzzeno
luigi.catacuzzeno@unipg.it

Specialty section:

This article was submitted to
Biological Modeling and Simulation,
a section of the journal
Frontiers in Molecular Biosciences

Received: 21 February 2022

Accepted: 16 May 2022

Published: 08 July 2022

Citation:

Horng TL, Chen RS, Leonardi MV,
Franciolini F and Catacuzzeno L (2022)
A Multi-Scale Approach to Model K⁺
Permeation Through the
KcsA Channel.
Front. Mol. Biosci. 9:880660.
doi: 10.3389/fmolb.2022.880660

K⁺ channels allow a very efficient passage of K⁺ ions through the membrane while excluding Na⁺ ions, and these properties are essential for life. The 3D structure of the KcsA K⁺ channel, solved more than 20 years ago, allows to address many relevant aspects of K⁺ permeation and selectivity mechanisms at the molecular level. Recent crystallographic data and molecular dynamics (MD) studies suggest that no water is normally present inside the selectivity filter (SF), which can instead accommodate four adjacent K⁺ ions. Using a multi-scale approach, whereby information taken from a low-level simulation approach is used to feed a high-level model, we studied the mechanism of K⁺ permeation through KcsA channels. More specifically, we used MD to find stable ion configurations under physiological conditions. They were characterized by two adjacent K⁺ ions occupying the more central positions of the SF (sites S2 and S3), while the other two K⁺ ions could be found at the external and internal entrances to the SF. Sites S1 and S4 were instead not occupied by K⁺. A continuum Bikerman–Poisson–Boltzmann model that takes into account the volume of the ions and their dehydration when entering the SF fully confirmed the MD results, showing peaks of K⁺ occupancy at S2, S3, and the external and internal entrances, with S1 and S4 sites being virtually never occupied by K⁺. Inspired by the newly found ion configuration in the SF at equilibrium, we developed a simple kinetic permeation model which, fed with kinetic rate constants assessed from molecular meta-dynamics, reproduced the main permeation properties of the KcsA channel found experimentally, including sublinear current-voltage and saturating conductance-concentration relationships. This good agreement with the experimental data also implies that the ion configuration in the SF we identified at equilibrium would also be a key configuration during permeation.

Keywords: K channels, permeation, KcsA, molecular dynamics, Bikerman–Poisson–Boltzmann, kinetic model, IV curve

STATEMENT OF SIGNIFICANCE

K⁺ channels allow a very efficient passage of K⁺ ions through the membrane while excluding Na⁺ ions, and these properties are essential for life. We studied these mechanisms of K⁺ permeation through KcsA channels using a multi-scale approach, whereby information taken from low-level simulations is used to feed a high-level model. More specifically, we developed a simple kinetic

permeation model which, fed with kinetic rate constants assessed from molecular meta-dynamics, reproduced the main permeation properties of the KcsA channel found experimentally.

INTRODUCTION

K⁺ channels are membrane proteins that allow a very efficient passage of K⁺ ions while excluding Na⁺ ions. They are essential for the establishment of the negative resting potential across the membrane and the repolarization phase of the action potential. The bacterial KcsA channel has been amongst the most studied K⁺ channels, and the first to have its structure solved by X-ray crystallography (Doyle et al., 1998). Soon after the resolution of the crystal structure, the group of Christopher Miller performed electrophysiology experiments on KcsA channels (Lemasurier et al., 2001) and found properties quite similar to those previously found for many mammalian K⁺ channels, such as sublinear current-voltage (IV) relationship under symmetrical K⁺ conditions, outward rectification (i.e., the channel conducts better in the outward direction), and saturating conductance-concentration relationship. Thus, any plausible mechanism of K⁺ permeation through the KcsA channel should explain and reproduce these features observed experimentally.

Structurally, the KcsA channel is formed by the juxtaposition of four identical protein subunits, each composed of two transmembrane segments, TM1 and TM2 (Doyle et al., 1998). Starting from the cytoplasmic side (the bundle crossing), the four TM2s of the KcsA channel form the lining of the water-filled internal cavity, which is ~10 Å wide and extends into the lipid membrane for about two-thirds of its thickness. At the extracellular pore entrance, the four P loops from each subunit form a narrow selectivity filter (SF) that is about 12 Å long and 3 Å wide and allows the passage of only naked ions (without their hydration shell). The SF is formed by a highly conserved sequence of amino acids (TVGYG) that have their carbonyl (hydroxyl in the case of threonine) oxygens pointing toward the center of the pore. Since these oxygens have a partial negative charge, their electrostatic interactions with the permeating K⁺ ions likely contribute to the permeation process.

Our comprehension of the permeation properties of KcsA moved greatly forward when the high-resolution electron density maps allowed us to clearly identify four high electron density positions inside the selectivity filter (called sites S1 to S4, from extracellular to intracellular). Two other electron-dense positions were found: one immediately outside the extracellular entrance (site S0) and the other below S4, at the center of the intracellular cavity (site Scav) (Morais-Cabral et al., 2001). Unfortunately, at that time, it was not possible to determine whether the observed electron densities inside the selectivity filter originated from K⁺ ions or from water, as they give a very similar X-ray diffraction pattern. A number of observations and physicochemical considerations initially suggested that the four binding sites (S1–S4) within the SF were alternately occupied by two K⁺ ions—sitting either in S1 and S3 or in S2 and S4—and two water molecules in the remaining sites (Bernèche and Roux, 2001; Zhou and MacKinnon, 2003).

Later experiments, based on anomalous diffraction X-ray crystallography and solid-state nuclear magnetic resonance, pointed instead to a selectivity filter exclusively occupied by K⁺ ions (Langan et al., 2018; Öster et al., 2019). In accordance, in long MD simulations that allowed to observe thousands of K⁺ permeation events, K⁺ ions were frequently found simultaneously occupying the sites S2 and S3, and the passage of water molecules through the SF was virtually never seen (Furini et al., 2009; Köpfer et al., 2014; Wu, 2017).

In either case, permeation would occur with a K⁺ ion approaching the SF from one side and pushing the single file of K⁺ ions (and possibly water molecules) forward to the other side (Morais-Cabral et al., 2001). This mechanism is usually referred to as knock-on (“soft” or “hard”, depending on the presence or absence of water), meaning that the incoming K⁺ ion pushes forward the single file of whatever is in the SF. Interestingly, Kratochvil and colleagues (Kratochvil et al., 2016) made MD simulations with the SF displaying either KWKW (K-water-K-water; the soft knock-on mechanism) or OKK0 (void-K-K-void; the hard knock-on mechanism) configuration. Their results showed that only an SF in the soft knock-on configuration could predict two-dimensional infrared (2D IR) spectra that matched experimental data from isotope-labeled semi-synthetic KcsA channels and were thus interpreted as evidence against the hard knock-on mechanism. However, a follow-up study using MD simulations found that both mechanisms can generate 2D IR spectra compatible with the experimental data (Kopeck et al., 2018). This study in fact indicated that 2D IR spectroscopy cannot effectively distinguish between these two conduction mechanisms in K⁺ channels.

Unfortunately, none of the mechanisms proposed until now, based on structural considerations and MD results, has been tested for its ability to correctly predict the channel behavior in terms of current-voltage and conductance-concentration relationships. This is because if on one side MD simulations have revealed atomic details of the binding sites and the energetics in the SF, on the other side, they can hardly predict the shape of the IV relationships under different experimental conditions. Even very long simulations can greatly underestimate the channel conductance (i.e., by nearly 40 folds at a voltage of 300 mV as in Jensen et al., 2013). Also, the outcome of other approaches, such as Brownian dynamics (BD) simulation (Bernèche and Roux, 2003) and Poisson–Nernst–Planck (PNP) type models (Furini et al., 2006; Dyrka et al., 2013; Liu and Lu, 2017), employed to compute the IV curves, was rather unsuccessful in predicting the experimental data (Lemasurier et al., 2001). Taking all this together, it appears that more information and new approaches are required to determine the exact mechanism of K⁺ permeation through the SF, and more key physical properties need to be included in the modeling.

To find more quantitative and predictive mechanisms of permeation, kinetic models could be used in conjunction with MD simulations in a multi-scale approach. Kinetic models picture the channel pore in a few stable configurations, and the permeation process as ions hopping from one stable configuration to the next, with an associated probability given

by the rate constant characterizing that transition (Hille, 2001). Although kinetic models can only give an approximate picture of the permeation process, they are able to connect the model output to experimental results through the flux equations that can easily be obtained from the model. This will allow to evaluate the soundness of a postulated permeation process derived from structural data and MD results. One such model has been recently found using long MD simulations, where K^+ permeation through the KcsA channel can be described by a quite simple sequence of Markov states (Domene et al., 2021). In this type of model, which we may define as an association/dissociation model (A/D model, (Nelson, 2011)), the current is produced by the binding of a K^+ ion to the SF on one side of the membrane and the unbinding of another K^+ ion on the other side. In this case, the exit (unbinding) of the K^+ ion is not to be seen as directly linked to (in fact, it is temporally separated from) the entry of a K^+ ion on the other side. Notably, in contrast to the classical knock-on mechanism (Hodgkin and Keynes, 1955), these types of models do predict sublinear IV relationships and saturating current-concentration curves (Nelson, 2011), in line with experimental data.

Based on these considerations, in this study, we tested whether an A/D type permeation model could reproduce the experimentally observed permeation properties from KcsA channels. The approach used in this study was: 1) to exploit MD simulations and structure-based Poisson-Boltzmann (PB) modeling (modified to include steric and dehydration effects) for sketching the A/D reaction scheme of K^+ permeation in the KcsA channel and defining its rate constants; 2) to test the consonance of the kinetic model output with experimental results.

METHODS

Molecular Dynamics

We used the structure of the open conformation of a KcsA channel carrying the E71A mutation that prevents inactivation (PDB code 5VK6, (Cuello et al., 2017)). Previous MD results have shown that both the SF and the intracellular gate of this channel remain in an open-conductive configuration following time extensive simulations (Li et al., 2018). The channel protein was embedded in a membrane with 200 POPC lipid molecules, having a dimension of $100 \times 100 \text{ \AA}$. The system was solvated in two steps, and the distance between the maximum and minimum z coordinates and the water box edges in the z -axis was set to 12 \AA . First, the system was solvated below the membrane plane with a water box of dimensions 102.69, 101.01, and 12.86 (x , y , and z in \AA), using 11,508 TIP3 water (Jorgensen et al., 1983) molecules. Then, it was solvated above the membrane plane with a water box of dimensions 102.69, 101.01, and 12.76 (x , y , and z in \AA), using 11,508 TIP3 water molecules. After the addition of the water molecules, the system presented a total net charge of $14.0 e_0$. The system was then neutralized by adding in a total of 100 Cl^- ions plus 86 K^+ ions, ending up with a salt concentration of 0.4 mol/L .

The MD simulations in the present study were performed employing the NAMD molecular dynamics package (Phillips

et al., 2005). The CHARMM36 force field (MacKerell et al., 1998; Best et al., 2012), with no NBFIX modification, was used in all MD simulations. An initial minimization (2,000 steps) was performed with explicit solvent using the TIP3 water model in the NpT ensemble. A distance cut-off of 12.0 \AA was applied to short-range, non-bonded interactions, and 10.0 \AA for the smothering functions. Long-range electrostatic interactions were treated using the particle-mesh Ewald (PME) method (Darden et al., 1993). Annealing was then performed by raising the temperature from 60 to 300 K, using a simulated temperature ramp of 0.24 ns . The pressure was maintained at 1 atm using the Nosé-Hoover Langevin piston (Martyna et al., 1994; Feller et al., 1995). A distance cut-off of 12.0 \AA was applied to short-range, non-bonded interactions, and 10.0 \AA for the energy switching function. Long-range electrostatic interactions were treated using the PME method. The equations of motion were integrated using the r-RESPA multiple time step scheme (Phillips et al., 2005) to update the short-range interactions every 1 step and long-range electrostatic interactions every 2 steps. The time step of integration was chosen to be 2 fs for all simulations. In this step consisting of 0.29 ns of simulation, all the backbone protein atoms and the K^+ ions in the selectivity filter (in S0 to S4) and immediately outside were restrained. After the annealing, a 1 ns equilibration was performed in which the temperature was maintained at 300 K using Langevin dynamics. Also, during this simulation time, all the backbone protein atoms and the K^+ ions in the selectivity filter (in S0 to S4) and immediately outside were restrained (with a force constant of $1 \text{ kcal}/(\text{mol} \cdot \text{\AA}^2)$). Finally, a fully unrestrained MD simulation was performed.

Adaptive biasing force. The energy profiles associated with the movement of K^+ ions along the selectivity filter were assessed using the adaptive biasing force (ABF) method which allows the calculation of the free energy variation along a coordinate of reaction (Darve et al., 2008; Hénin et al., 2010). ABF is based on the computation of the potential of mean force (PMF) along the reaction coordinate ξ , which is neutralized by the equal and opposite *biasing force* which enables the system to escape from the free energy minima, which otherwise would not allow to study the whole energy landscape. In fact, the biasing force yields a uniform transition coordinate, with only minimal residual barriers that can be easily crossed only owing to thermal fluctuations. The application of the ABF method preserves the main dynamic characteristics, including the random fluctuating force, while flattening the potential of mean force to erase free-energy barriers and, in this way, promoting the transitions between states. All this is done in an adaptive manner, without the need for prior information on the PMF (Comer et al., 2015). This kind of simulation is performed with no constraint in the coordinate reaction ξ , which implies that during the simulation the complete reaction path is discretized into small increments $\delta\xi$ that are explored in a continuous fashion. We started these simulations from the already equilibrated structure of KcsA mentioned earlier and proceeded with the ABFs. To allow the system to stabilize, a total of 30 ns simulation was performed, at the end of which we verified that the assessed energy profile was stable and did not

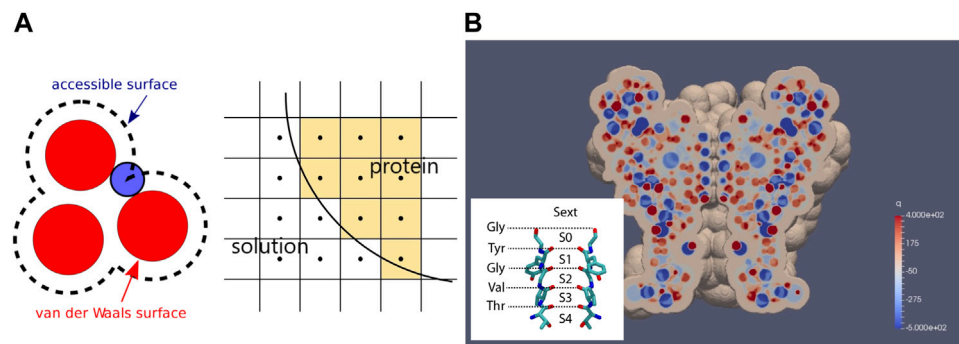


FIGURE 1 | Geometry of the continuum model. **(A)** generation of protein domain by rolling ball mechanism. A mesh with its center inside an accessible surface is classified as a protein mesh. Otherwise, the mesh is classified as a solution mesh. **(B)** cross-section of KcsA with permanent charge distribution. The structure of the narrowest part of the channel, the SF, surrounded by carbonyl oxygens from the TVGYG motifs, with its binding sites, is shown in the inset. Note that unlike conventional notation, here, blue spots denote negative charges and red spots denote positive charges according to the color bar.

change with simulation time. Furthermore, to achieve a high-resolution profile, we performed all the ABF using a $\delta\xi$ of 0.05 Å. During this simulation time, the backbone protein atoms of the channel transmembrane helices, sufficiently far from the selectivity filter, were restrained to a specific range of motion.

Free energy perturbation. To assess the binding free energy for the K^+ ions in the sites of the SF, which is described as $\Delta G_{\text{binding}} = \Delta G_{\text{site}} - \Delta G_{\text{bulk}}$, we performed the free energy perturbation (FEP) (Pearlman, 2002), a technique that allows to calculate the free energy variation of a system in which progressive perturbation changes occur starting from an initial state $\lambda = 0$, to get to the final state $\lambda = 1$. We can refer to this technique as a dual topology approach since both the initial and the final states are defined. As the MD progresses, the potential energy function characteristic of $\lambda = 1$ is scaled into that representative of $\lambda = 0$ by increments of $\delta\lambda = 0.05$. We run the simulation with a total of 35 ps for each $\delta\lambda$, both for the K^+ ions in the bulk water and in the sites to get the binding free energy. The first 15 ps were excluded from the energy ensemble average calculation to allow the system to equilibrate. Soft-core potentials were used with a shifting coefficient for the van der Waals radii of 2.0 Å. Free energy differences were evaluated using the simple overlap sampling (SOS) algorithm of the ParseFEP plugin of VMD (Liu et al., 2012). Six different FEP values were averaged for each system.

Continuum Model

Continuum models like Poisson–Boltzmann (PB) and Poisson–Nernst–Planck (PNP) equations can generally describe ion channels at equilibrium and non-equilibrium conditions, and therefore they can predict long-range behavior and stable configurations of the SF (Eisenberg, 1998; Nonner et al., 1999). However, considering ions as points without volume can deter their applicability under particular conditions, including the narrow SF of the KcsA channel where the negative charges carried by carbonyl oxygens are so strong to bring K^+ ions to saturation levels inside it. This calls for modifications of the classical PB/PNP model to account for the steric effect of ions. To study the equilibrium situation,

we consider, here, the Bikerman–PB model as one such alternative to the classical PB model. Moreover, as ion solvation energy is significant for K^+ ions entering the narrow SF, this energy, calculated with the Born model, was included in our modeling.

Geometry. Using the mutant E71A KcsA structure and the water molecule with a radius of 1.4 Å as the rolling ball, we generated the protein domain in our Cartesian computational mesh as illustrated in **Figure 1A**. A cross-section of the channel together with the distribution of its permanent charges are shown in **Figure 1B**. Note the narrow SF surrounded by carbonyl oxygens, with its structure shown in the inset. The membrane was further compensated to surround the channel protein in our rectangular computation domain, $\Omega = [x_{\min}, x_{\max}] \times [y_{\min}, y_{\max}] \times [z_{\min}, z_{\max}]$. Therefore, the whole computational domain Ω consists of the protein/membrane domain Ω_p and the electrolyte solution domain Ω_s .

Bikerman–PB model. The Helmholtz free energy for the classical PB model is

$$F = U - TS, \quad (1)$$

with the internal energy U and entropy S described as follows:

$$U = \int \left[-\frac{\epsilon}{2} |\nabla\phi|^2 + z_p e p \phi + z_n e n \phi + q \phi + p W_{\text{sol},p} + n W_{\text{sol},n} \right] dV, \quad (2)$$

$$-TS = \int k_B T [p \log(p) - p + n \log(n) - n] dV, \quad (3)$$

where ϕ is the electric potential; p and n are concentrations of cation and anion (K^+ and Cl^- here); z_p and z_n are valencies of cation and anion; q is the permanent charge of protein; e is the elementary charge; $\epsilon = \epsilon_0 \epsilon_r$ is permittivity with ϵ_0 being the permittivity in a vacuum and ϵ_r the dielectric constant (relative permittivity); $W_{\text{sol},p}$, $W_{\text{sol},n}$ are the solvation energy for cation and anion, respectively; T is the temperature. The variation of F with respect to ϕ gives the Poisson equation,

$$-\nabla \cdot (\epsilon(\mathbf{x}) \nabla \phi) = z_p e p + z_n e n + q. \quad (4)$$

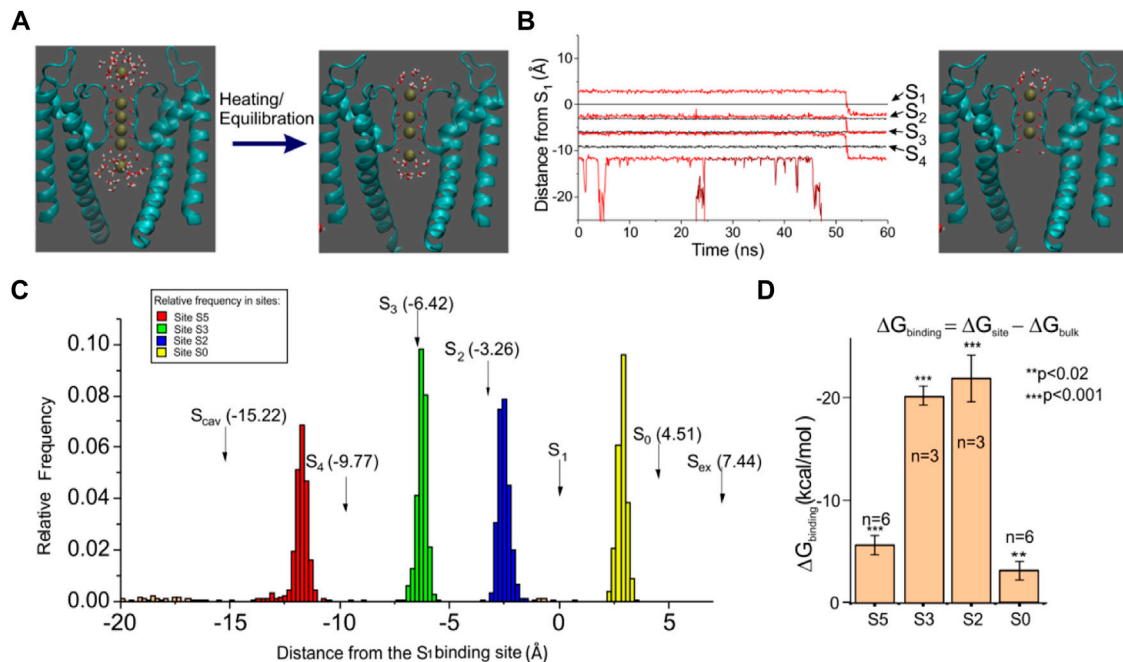


FIGURE 2 | Molecular dynamics of the KcsA channel. **(A)** *left*: KcsA structure and initial K⁺ ion configuration used in our MD simulations. K⁺ ions were placed in sites S1–S4 inside the selectivity filter, at the cavity, and in the site S_{ex} found in X-ray crystallography. *Right*: typical ion configuration found after heating and equilibration. **(B)** *left*: plot of the K⁺ ion position as a function of time for one typical MD simulation. The black lines represent the position of the four SF crystallographic sites (assessed as the center of mass of the eight carbonyl oxygens) while the red lines represent the position of the K⁺ ions. *Right*: SF configuration found at 50 ns, with only three K⁺ ions bound to the SF. **(C)** amplitude histogram of the K⁺ ion position assessed from a 400 ns long MD simulation, showing four preferential positions. The arrows indicate the K⁺ binding sites found in the high-resolution structure. **(D)** binding free energy assessed using the free energy perturbation technique for the four K⁺ binding sites found to be typically occupied in our simulations. The plot reports the difference between the free energy variation obtained following the annihilation of a K⁺ ion in water (ΔG_{bulk}) and a K⁺ ion sitting in a binding site (ΔG_{site}). In the initial configuration, shown on the left of panel A, ions were constrained within ±1 Å from the binding site using a collective variable approach of NAMD. Since the application of a constraint adds an entropy term to the free energy variation (Wang et al., 2006), the same constriction was also applied to the bath K⁺ ion, in order to have the same effect on all free energy values presented.

By doing the variation of F with respect to p and n , we obtain the chemical potentials for cation and anion, respectively.

$$\frac{\partial F}{\partial p} = \mu_p = z_p e \phi + k_B T \log(p) + W_{sol,p}, \quad (5)$$

$$\frac{\partial F}{\partial n} = \mu_n = z_n e \phi + k_B T \log(n) + W_{sol,n}, \quad (6)$$

where solvation energy, based on the Born model, for cation and anion is

$$W_{sol,i} = \frac{z_i^2 e^2}{8\pi\epsilon_0 r_i} \left(\frac{1}{\epsilon_r(x)} - 1 \right), \quad i = p, n, \quad (7)$$

with r_i being the radius of ion i .

Herein, we include the steric effect to improve the classical PB model mentioned earlier. The steric effect has long been approached in modeling by modifying either internal energy or entropy in free energy (Bikerman, 1942; Borukhov et al., 1997; Hornig et al., 2012). Through the entropy approach, Bikerman (Bikerman, 1942) modified classical Boltzmann distribution by adjusting bulk and local ion concentrations via excluded volume. Borukhov, Andelman, and Orland rigorously derived the same formula by adding solvent

entropy through excluded volume into free energy (Borukhov et al., 1997). The Bikerman model has been a popular steric model due to its easiness of application and qualitatively good agreement with experiments. The original Bikerman model has no size distinction among ions, and all ion sizes are designated as a^3 . Many subsequent studies have extended the Bikerman model to include specific ion size via modification of the chemical potential described in (5) and (6) to the following,

$$\mu_p = z_p e \phi + k_B T [\log(p a_p^3) - \log(1 - p a_p^3 - n a_n^3)] + W_{sol,p}, \quad (8)$$

$$\mu_n = z_n e \phi + k_B T [\log(n a_n^3) - \log(1 - p a_p^3 - n a_n^3)] + W_{sol,n}, \quad (9)$$

where a_p^3 and a_n^3 are volumes for cation and anion, respectively. This adjustment was rigorously derived and discussed in the review article by Hornig (Hornig, 2020).

At equilibrium, the chemical potential is uniform everywhere and

$$\mu_p = \mu_{p,b}, \quad \mu_n = \mu_{n,b}, \quad (10)$$

with

$$\mu_{p,b} = k_B T [\log(p_b a_p^3) - \log(1 - p_b a_p^3 - n_b a_n^3)] + W_{sol,p,b}, \quad (11)$$

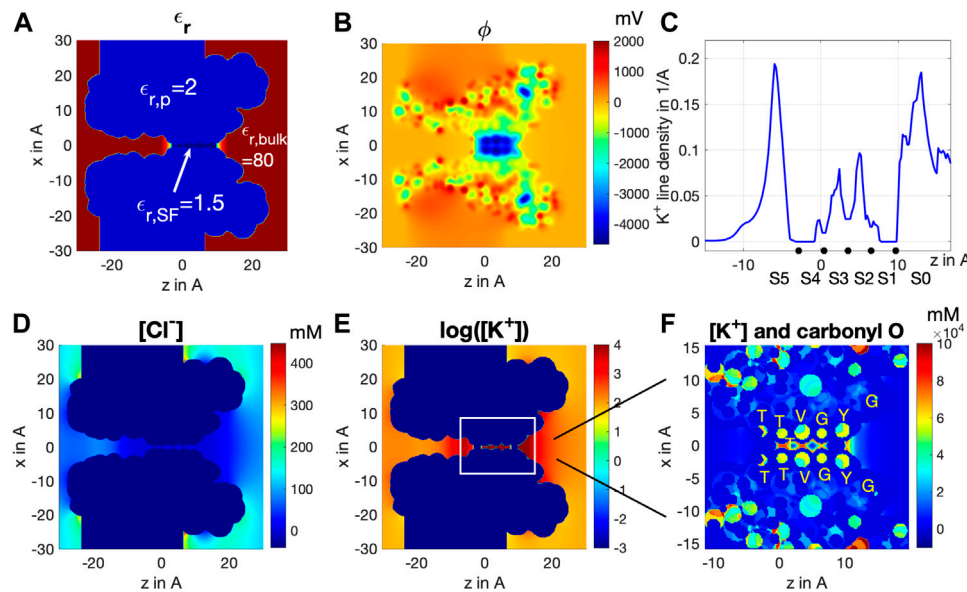


FIGURE 3 | Cross-section distribution of (A) dielectric constant ϵ_r , (B) electric potential ϕ , (C) line density distribution of K^+ ions along the central axis, (D) $[Cl^-]$ and (E) $\log_{10}[K^+]$, at equilibrium ($V = 0$). (F) close-up of cross-section distribution of $[K^+]$ and $-q$ around SF.

$$\mu_{n,b} = k_B T [\log(n_b a_n^3) - \log(1 - p_b a_p^3 - n_b a_n^3)] + W_{sol,n,b}, \quad (12)$$

where the subscript b denotes the bulk situation. Note that ϕ is set to 0 in Eqs. (11) and (12) conventionally for the bulk situation. Eqs. (8)–(12) can solve for p and n :

$$p = \frac{p_b e^{-\beta z_p e \phi} e^{-\beta \Delta W_{sol,p}}}{1 + p_b a_p^3 (\exp(-\beta z_p e \phi) - 1) + n_b a_n^3 (\exp(-\beta z_n e \phi) - 1)}, \quad (13)$$

$$n = \frac{n_b e^{-\beta z_n e \phi} e^{-\beta \Delta W_{sol,n}}}{1 + p_b a_p^3 (\exp(-\beta z_p e \phi) - 1) + n_b a_n^3 (\exp(-\beta z_n e \phi) - 1)}, \quad (14)$$

where $\beta = \frac{1}{k_B T}$, and

$$\Delta W_{sol,i} = \frac{z_i^2 e^2}{8\pi\epsilon_0 r_i} \left(\frac{1}{\epsilon_r(\mathbf{x})} - \frac{1}{\epsilon_{r,b}} \right), \quad i = p, n. \quad (15)$$

Readers are referred to Hornig (2020) for detailed derivation. Note that with $a_p^3 \rightarrow 0$, $a_n^3 \rightarrow 0$, Eqs. (13) and (14) reduce to classical PB distribution,

$$p = p_b e^{-\beta z_p e \phi} e^{-\beta \Delta W_{sol,p}}, \quad (16)$$

$$n = n_b e^{-\beta z_n e \phi} e^{-\beta \Delta W_{sol,n}}, \quad (17)$$

Eq. (4) together with Eqs. (13) and (14) form the governing equation to solve for ϕ in Ω and p, n in Ω_s . Boundary conditions for ϕ at equilibrium are

$$\phi = 0 \text{ at } z = z_{min}, z_{max}, \quad (18)$$

meaning no voltage bias applied across the channel. No-flux boundary conditions are applied to four sides of the computational domain,

$$\frac{\partial \phi}{\partial \mathbf{n}} = 0 \text{ at } x = x_{min}, x_{max}, \text{ and } y = y_{min}, y_{max}, \quad (19)$$

where \mathbf{n} denotes the outward normal direction. The interface conditions between electrolyte and protein/membrane are

$$[\phi] = 0, \quad \left[\epsilon_r \frac{\partial \phi}{\partial \mathbf{n}} \right] = -\sigma, \text{ at } \Gamma = \Omega_p \cap \Omega_s, \quad (20)$$

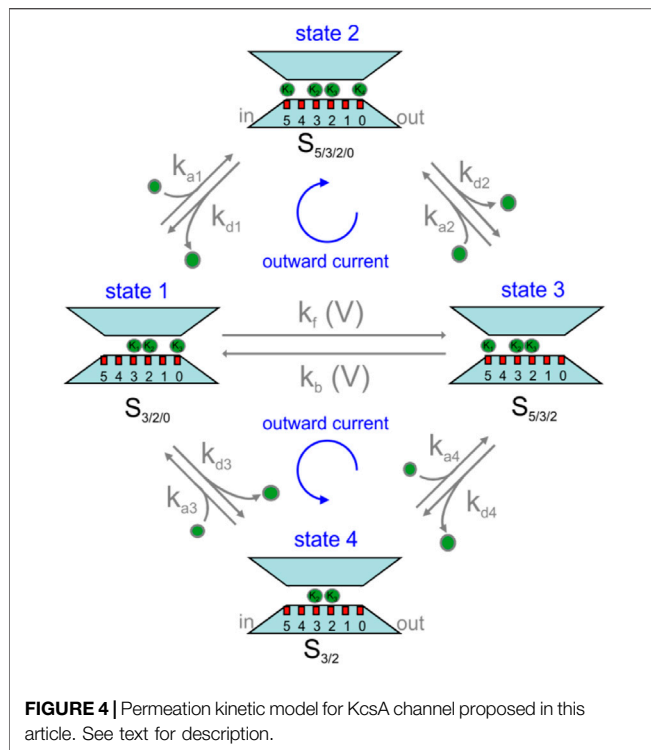
where $[\cdot]$ denotes the jump across the interface Γ and σ is the surface density of permanent charge at the interface. Here, $\sigma = 0$ due to the rolling ball scheme. For computational efficiency, Eq. (4) is augmented to be pseudo-time-dependent,

$$\frac{\partial \phi}{\partial t} = \nabla \cdot (\epsilon(\mathbf{x}) \nabla \phi) + z_p e p + z_n e n + q. \quad (21)$$

We then solve for Eq. (21), instead of Eq. (4), until the steady state is reached. By the framework of the method of lines (MOL), finite volume method (FVM) is first used for the spatial discretization of Eq. (21). Then, the resultant system of ordinary differential equations (ODEs) after semi-discretization in space is integrated in time by RK4 until the steady state is reached.

As mentioned earlier, the steric effect and solvation energy difference are significant inside SF. Herein, we isolate the SF domain from the electrolyte solution domain by defining $\Omega_{SF} = \Omega_s \cap \{z | z \in [-4.15, 11.12]\}$. The physical and numerical parameters used in the current investigation are

1) Bulk solution concentration: $c_0 = 100\text{mM}$.



- 2) Dielectric constant distribution: $\epsilon_{r,bulk} = 80$ at $\Omega_s \setminus \Omega_{SF}$; $\epsilon_{r,p} = 2$ at Ω_p ; and $\epsilon_{r,SF} = 1.5$ at Ω_{SF} . A sharp linear transition from bulk $\epsilon_{r,bulk}$ to $\epsilon_{r,SF}$ is designated at both edges of Ω_{SF} as shown in **Figure 3A**. Debye length based on $\epsilon_{r,SF}$ is $\lambda_{D,SF} = \sqrt{\frac{\epsilon_0 \epsilon_{r,SF} k_B T}{c_0 e^2}} = 1.89 \text{ \AA}$.
- 3) Ion diameter: $a_{K^+} = 2.76 \text{ \AA}$, $a_{Cl^-} = 3.62 \text{ \AA}$, $a_{water} = 2.8 \text{ \AA}$.
- 4) Bulk diffusion coefficients: $D_K = 1.957 \times 10^{-9} \text{ m}^2/\text{s}$, $D_{Cl} = 2.032 \times 10^{-9} \text{ m}^2/\text{s}$.
- 5) Grid size: $\Delta x = \Delta y = \Delta z = 0.2 \text{ \AA}$.
- 6) Computational domain: $\Omega = [x_{min}, x_{max}] \times [y_{min}, y_{max}] \times [z_{min}, z_{max}]$ with $x_{min} = -30$, $x_{max} = 30$, $y_{min} = -30$, $y_{max} = 30$, $z_{min} = -38$, $z_{max} = 35.6$ in \AA .

Note that $\lambda_{D,SF}$ is generally larger than the width of SF, which means that the electric double layers (EDLs) in the SF will overlap. Dielectric constant inside SF, $\epsilon_{r,SF}$, is practically hard to estimate by MD or be measured experimentally. So, here, we treated it as a model parameter. In the beginning, we only knew water inside SF should be far less than in the bulk, and therefore the value should be far less than 80. We have conducted simulations with $\epsilon_{r,SF}$ being set to 10, 8, 6, 4, 2, and 1.5 and discovered the less occupation of S1 and S4 by K^+ ions as $\epsilon_{r,SF}$ decreases mainly due to the increasing solvation energy barrier based on the Born model, **Eq. 15**. The value 1.5 gives a complete absence of K^+ ions at S1 and S4 which agrees best with our MD equilibrium result shown in a later section.

Solution of the Kinetic Model

The solution of the kinetic model was obtained by assuming that the system is at steady state, meaning that the rate of formation of each state is equal to the rate of disappearance, giving a zero rate of change. More specifically, considering a kinetic model having N different states, under steady-state conditions, we can write a system of N equations of the type

$$\sum_j k_{ji} n_j - \sum_j k_{ij} n_i = 0 \text{ for } i = 1, \dots, N, \quad (22)$$

where k_{ji} is the rate constant going from state j to state i , and n_j is the fractional occupancy of state j , with j that varies over all the states connected with state i . Using this system of equations and considering the additional constraint that the sum of fractional occupancies is unity, $\sum_{i=1}^N n_i = 1$, we can find the unknown fractional occupancies of the various states that can then be used to assess the ion current as follows:

$$\text{current} = z_K e \sum_{i,j} (k_{ij} n_i - k_{ji} n_j), \quad (23)$$

where z_K is the valence of a K^+ ion (+1), and i and j vary for all possible transitions $i \rightarrow j$ representing either the entry of a K^+ ion from the intracellular bath or its exit to the extracellular bath.

In our specific case, the kinetic scheme shown in **Figure 4** gives rise to the following system of equations:

$$k_{a3} [K^+]_{ex} n_4 + k_b(V) n_3 + k_{d1} n_2 - n_1 (k_{a1} [K^+]_{in} + k_f(V) + k_{d3}) = 0, \quad (24)$$

$$k_{a1} [K^+]_{in} n_1 + k_{a2} [K^+]_{ex} n_3 - n_2 (k_{d1} + k_{d2}) = 0$$

$$k_{a4} [K^+]_{in} n_4 + k_f(V) n_1 + k_{d2} n_2 - n_3 (k_{a2} [K^+]_{ex} + k_b(V) + k_{d4}) = 0$$

$$k_{d3} n_1 + k_{d4} n_3 - n_4 (k_{a3} [K^+]_{ex} + k_{a4} [K^+]_{in}) = 0$$

where $[K^+]_{ex}$ and $[K^+]_{in}$ represent the extracellular and intracellular K^+ concentrations and n_i represents the fractional occupancy of state i and $n_1 + n_2 + n_3 + n_4 = 1$. The motivation of using the four-states scheme shown in **Figure 4** to describe the permeation pathway and construct the kinetic model accordingly will be explained later. The above linear system of equations was solved at varying voltages and K^+ intracellular and extracellular concentrations, and the n_i were used to assess the current as follows:

$$\text{current} = z_K e (k_{a1} [K^+]_{in} n_1 + k_{a4} [K^+]_{in} n_4 - k_{d1} n_2 - k_{d4} n_3), \quad (25)$$

or equivalently

$$\text{current} = z_K e (k_{d2} n_2 + k_{d3} n_1 - k_{a2} [K^+]_{ex} n_3 - k_{a3} [K^+]_{ex} n_4), \quad (26)$$

As with any cyclic kinetic model, the so-called microscopic reversibility needs to be respected at the equilibrium (zero voltage), that is, the product of the kinetic rate constants in the clockwise direction should equal the product of the rate constants in the counterclockwise direction. In our case, we have three cycles, thus the microscopic reversibility should read:

$$\begin{aligned}
 K_{a1} [K^+]_{in} k_{d2} k_b(0) &= K_{d1} k_f(0) k_{a2} [K^+]_{ex}, \\
 K_{d3} k_{a4} [K^+]_{in} k_b(0) &= K_{a3} [K^+]_{ex} k_f(0) k_{d4} \\
 K_{a1} [K^+]_{in} k_{d2} k_{d4} K_{a3} [K^+]_{ex} &= K_{d1} K_{d3} k_{a4} [K^+]_{in} k_{a2} [K^+]_{ex}
 \end{aligned}
 \quad (27)$$

Multi-scale approach for predicting IV relationships. To predict the IV relationships for the KcsA channel, we considered the association/dissociation model shown in **Figure 4**, with the rate constants assessed from MD data. More specifically, we used the MD ABF method to assess the energy profiles associated with the various transitions present in the kinetic scheme and to estimate the diffusion rate constants outside and inside the selectivity filter of the channel. In order to take into account the effect of the transmembrane voltage on the voltage dependent rate constants of the model, k_b and k_f , an electrostatic energy corresponding to a linear voltage drop through the SF was added to the energy profile. Once these parameters are known, the kinetic rate constants can be estimated using Eqs. (28) and (29), to be described, and the currents under various voltages and K^+ concentrations using Eqs. (25) and (26).

RESULTS

Molecular Dynamics of K^+ Permeation in KcsA Channel

We performed MD simulations starting from the newly determined crystallographic configuration of the selectivity filter of KcsA, with four K^+ ions sitting in the four SF binding sites, very close to each other, plus a K^+ ion in the cavity and another one in the external vestibule (**Figure 2A**, left). Since this configuration was obtained from crystallized channels held at a very low temperature, we first verified if it was also present as a relatively stable configuration at more physiological temperatures, which are easily reached by heating the crystal from 60 to 300 K and letting it equilibrate for about 400 ns. We performed this simulation ten times, each time randomly re-initializing the atoms' velocities, and every time, at the end of the equilibration, we observed a K^+ ion configuration invariably characterized by two K^+ ions at the two most internal binding sites of the selectivity filter (S2 and S3) (**Figure 2A**, right). The S1 and S4 positions were instead empty or rarely occupied by water (water occupancy was $25.2 \pm 7.3\%$ for S1 and $11.5 \pm 1.4\%$ for S4).

Two other K^+ ions were, respectively, found at the intracellular and extracellular entry of the selectivity filter. These K^+ ions were instead only partially hydrated, as they also interacted with the protein residues. More specifically, the K^+ at the external site interacted with the carbonyl oxygens of tyrosine 78, located at the extracellular entry of the selectivity filter, while the K^+ at the intracellular entrance interacted with the hydroxyl oxygens of threonine 75. As can be seen from the frequency plot of **Figure 2C**, neither of the two sites exactly matches the corresponding binding sites found in the crystal (Scav and S0, indicated with arrows in the plot), especially the internal site which was clearly distinct from Scav. The position where we found the internal K^+ site corresponds very closely to the S5 site

found by Jensen et al. (2010) on Kv1.2, so we will refer to it as site S5. As for the external site that was found less distant from the crystal site S0, we kept this name. In any case, these simulations consistently showed the presence of the stable 0/2/3/5 configuration in the SF at the end of equilibration (cf. **Figure 2B**).

We also assessed the binding free energy of the four identified K^+ binding sites, using free energy perturbation (a technique that essentially consists in slowly annihilating the K^+ ion interactions with the environment and assessing the free energy change observed during the process). If the free energy change is significantly higher than for the annihilation of a K^+ ion in water, then we can arguably talk about a K^+ binding site. The bar plot in **Figure 2D** shows that the free energy increase for K^+ annihilation in all the four binding sites is systematically higher than in the bath, meaning that these are all true binding sites for K^+ . Notice, however, the considerably smaller binding free energy for both external sites S0 and S5, compared to the internal sites S2 and S3, which is arguably the basis of the high conduction rates in this channel. In several simulations, we were in fact able to observe the unbinding of K^+ from either the S0 or S5 position (**Figure 2B**, K^+ unbinding from S5, occurring at 45 ns; lowest red trace), followed by a concerted motion of the three remaining ions as a single file along the selectivity filter (**Figure 2B**, concerted transition from 0/2/3 configuration to 2/3/5 configuration).

The Bikerman–PB Continuum Model of KcsA Channel

To verify if the stable 0/2/3/5 configuration, indicated by MD simulations, is a consistent occurrence at steady state, we applied the Bikerman–PB continuum model to the same channel structure used in MD simulations. PB/PNP-type continuum models can generally describe ion channels in equilibrium and non-equilibrium conditions, and therefore could be a useful integrative approach to MD, especially in predicting long-range behavior and stable configurations of the SF (Eisenberg, 1998; Nonner et al., 1999). The computation results based on the Bikerman–PB model for equilibrium situation, $V = 0$ and symmetric K^+ , are shown in **Figure 3**. **Figure 3A** illustrates the channel's cross-sectional view with the dielectric constant values assigned to the significant locations of the channel, namely $\epsilon_{r,p} = 2.0$ in the protein matrix (Ω_p), $\epsilon_{r,SF} = 1.5$ in the SF (Ω_{SF}), and $\epsilon_{r,bulk} = 80$ for the channel vestibules and bulk (Ω_v/Ω_{bulk}). **Figure 3B** shows the distribution of the electric potential ϕ , where we can observe a very negative electric potential distribution along the SF. As a consequence, K^+ is strongly accumulated and Cl^- heavily depleted inside the SF and the entrances (**Figures 3D**, **E**). There are, however, two ion depletion spots at the SF, where no ions are virtually ever found (**Figure 3E**). These two spots are located at sites S1 and S4 of SF, as better illustrated in **Figure 3F**, where $[K^+]$ and $-q$ (minus of permanent charges) are plotted together to show how carbonyl oxygens attract K^+ ions, especially at their ridge where saturation peaks with $[K^+] \approx 80M$ are formed. Note that this extremely high saturation concentration happening at ridges (better presented in panel A of **Supplementary Figure S1**) actually comes from the Bikerman model, Eqs. (8) and (9),

where $\log(1 - pa_p^3 - na_n^3) \approx \log(0^+)$ (to be more specific $\log(1 - pa_p^3 - na_n^3) \approx \log(10^{-5}) \approx -11.5$ according to our simulation data) with $n \approx 0^+$, $p \approx 1/a_p^3$ when K^+ ion saturating and Cl^- ion totally excluded from SF. With $a_{K^+} = 2.76\text{\AA}$, the saturation concentration is $[K^+] \approx 1/a_{K^+}^3 \approx 80M$.

Yet the K^+ distribution along the central axis shown in **Figure 3F** cannot fully reveal the effective residence of K^+ ions in the SF. For this reason, we integrated $[K^+]$ over the xy-plane cross-sectional area of the SF to obtain the line density of K^+ ions as a real measure of the K^+ spatial distribution along the SF, as shown in **Figure 3C**. Notably, we find peaks of K^+ residence at sites S0, S2, S3, and S5, but basically none at sites S1 and S4. The fact that S0 and S5 display much larger peaks than S2 and S3 is mainly due to K^+ ions having much more room at vestibule sites S0 and S5 than S2 and S3 do inside the SF, rather than a real difference in the concentration of the K^+ ion at these sites, as indicated in **Figure 3F**. The slightly higher line density distribution at S2 than at S3 agrees with the observation from MD that S2 is a more stable binding site than S3 (**Figure 2D**) (Noskov et al., 2004). These results fully agree with MD simulations reported in **Figure 2**, showing the presence of a stable 0/2/3/5 configuration. Significant physics stays behind the stability of the 0/2/3/5 configuration, which is illustrated by comparing the results of the Bikerman–PB model with the classical PB model. Readers are referred to supplementary information in this article for further details.

The Association/Dissociation (A/D) Permeation Kinetic Model in KcsA Channel

MD and continuum modeling results shown above inspired us the A/D permeation mechanism shown in **Figure 4**. As we have seen, the channel shows an energetically stable configuration with sites S5, S3, S2, and S0 occupied by K^+ ions and sites S4 and S1 empty (state 2 in **Figure 4**, also cf. first 45 ns simulation of **Figure 2B**). From this 4- K^+ ion configuration, the channel can easily exchange with the bath either the K^+ ion in S5 or in S0, as indicated by the binding energetics of **Figure 2D**. To verify if the stable 0/2/3/5 configuration, indicated by MD simulations, is a consistent occurrence at steady state, we applied the Bikerman–PB continuum. We also considered the occurrence that both K^+ ions in S0 and S5 unbind in rapid succession, and in any case, before either ion in S2 or S3 moved, leaving the selectivity filter in the 2- K^+ configuration (state 4) that we have observed in our MD simulations (data not shown, see also the supplementary movie in (Köpfer et al., 2014)).

From the above considerations, K^+ permeation can be viewed as a K^+ ion binding to either one of the two external sites, S5 or S0, in states 1 or 3, and another K^+ ion being released (unbinding) from the opposite site (upper part of the scheme). In fact, the two events may also occur in the reverse order, with first the unbinding of a K^+ ion and then the binding of another K^+ at the opposite site (lower part of the scheme). In order for the system to give a continuous K^+ flux, we finally need to picture how the two 3- K^+ ion configurations, state 1 and state 3, can interconvert into one another through a single file movement, considering that in our model this inter-conversion must be

voltage dependent. In fact, it is the only voltage-dependent process, given that the voltage applied across the membrane drops mostly inside the selectivity filter (Catacuzzeno et al., 2020), thus leaving the binding and unbinding of K^+ to and from sites S0 and S5 essentially outside the electric field. We are aware that the states of our permeation model shown in **Figure 4** are mainly derived from MD simulations under equilibrium conditions. It is, however, reassuring that a recent study performed on the same E71A mutant KcsA channel, under non-equilibrium conditions, has come up with essentially the same model (Domene et al., 2021).

To verify whether the permeation mechanism considered can predict the experimental current-voltage relationships, we estimated the model rate constants through MD simulations. For rate constants not involving the binding of K^+ ions, namely the inter-conversion rates between states 1 and 3 and all the dissociation constants, k_{ds} , we used the mean first-passage time (MFPT) theory, originating from the Langevin's diffusion model (Szabo, 1979; Cooper, Gates, and Eisenberg, 1988a; Cooper, Gates, and Eisenberg, 1988b; Schulten et al., 1981). According to this theory, a rate constant k can be estimated as the inverse of the mean first-passage time, that is, the time needed to go from the initial state i to the final state f of the transition.

$$k = \left[\tau_f + \tau_b \frac{Z_f}{Z_b} \right]^{-1}, \quad (28)$$

$$Z_{f/b} = \int_{i/f}^b e^{-\frac{U(y)}{kT}} dy$$

$$\tau_{f/b} = \frac{1}{D} \int_{i/f}^b dx \int_x^b e^{-\frac{U(y)-U(x)}{kT}} dy$$

where $U(x)$ is the energy profile associated with the process, D is the diffusion constant, and k and T have their usual meanings. i , b , and f represent respectively the initial position, the point of maximal energy, and the final position along the reaction coordinate.

As for the K^+ association rate constants, k_{as} , we assumed that they are diffusion-limited and assessed their values from the following equation derived from the Smoluchowski (Debye, 1942):

$$k_a = 2 \pi D \left[\int_{r_c}^{\infty} \frac{\exp(U(r)/kT)}{r^2} dr \right]^{-1}, \quad (29)$$

where r_c is the radius of the hemisphere through which K^+ can enter the pore, here considered to be 1.5\AA and D is the bulk K^+ diffusion coefficient. Notice that Eq. (29) is valid only under the assumption that K^+ ions can freely diffuse to the binding site. While this is probably correct for the binding site S0, the binding to site S5 likely involves K^+ diffusion through the more restricted region of the intracellular hydrophobic pore; thus, our estimate of k_{a1} and k_{a4} and the resulting estimated current would likely represent an upper limit.

As can be seen from Eqs. (28) and (29), the association rate constant depends obviously on the energy profile encountered during the process but also on the diffusion constant of K^+ ions approaching the site involved in the transition. We estimated the K^+ diffusion coefficient, both in the bath and the selectivity filter, from MD simulations, as the mean squared fluctuation of the K^+

TABLE 1 | Rate constants evaluated from MD and adjusted by microscopic reversibility.

Rate constant	Value derived from MD (x 10 ⁸)	Value adjusted for microscopic reversibility (x 10 ⁸)
k _{a1}	7.0 s ⁻¹ M ⁻¹	5.0 s ⁻¹ M ⁻¹
k _{d1}	2.1 s ⁻¹	2.5 s ⁻¹
k _{a2}	3.0 s ⁻¹ M ⁻¹	4.0 s ⁻¹ M ⁻¹
k _{d2}	11.0 s ⁻¹	10.0 s ⁻¹
k _{a3}	3.9 s ⁻¹ M ⁻¹	4.0 s ⁻¹ M ⁻¹
k _{d3}	7.0 s ⁻¹	10.0 s ⁻¹
k _{a4}	3.1 s ⁻¹ M ⁻¹	4.0 s ⁻¹ M ⁻¹
k _{d4}	2.4 s ⁻¹	2.0 s ⁻¹
k _i (0)	130.0 s ⁻¹	150.0 s ⁻¹
k _b (0)	38.0 s ⁻¹	30.0 s ⁻¹

ion position along the *z*-direction (Bernèche and Roux, 2001; Bullerjahn et al., 2020). It may be noticed that the value assessed for K⁺ ions in the bath (0.235 ± 0.021 Å²/ps) is slightly higher (yet within 20%) than the experimental value of 0.196 Å²/ps. Inside the selectivity filter, we obtained, as expected, a much lower value for the diffusion coefficient, namely 0.040 ± 0.005 Å²/ps, in substantial accordance with previous measurements (Allen et al., 2000).

We then estimated the energy profile associated with each of the transitions present in the reaction scheme. To this end, we used the adaptive biasing force (ABF) method, where the energy profile is adaptively assessed as the force needed to obtain a uniform distribution of the system along the reaction coordinate. Starting from the uneven distribution of K⁺ ions due to their accumulation at the energy wells of the actual energy profile, additional energy is applied and changed adaptively until the K⁺ distribution of the system is homogeneous along the reaction coordinate, meaning that the biasing energy exactly compensates for the original energy profile. The inverse of the biasing energy is then taken as the energy profile characterizing the process. **Figure 5** shows the application of this method to assess the energy profiles associated with the various reaction steps present in the model considered. In the case of the interconversion between the 3-K⁺ ion configurations (**Figure 5C**), we performed a mono-dimensional ABF in which the reaction coordinate is the center of mass of the three K⁺ ions.

Since we assumed the 3-K⁺ interconversion process to be voltage dependent, the assessment of the rate constants was performed both with the original energy profile and after adding various electric potential differences linearly dropping along the entire profile (**Figure 5F** inset). The plot in **Figure 5F** reports the estimated rate constants as a function of the applied potential.

As with any cyclic reaction, the model considered must respect the principle of microscopic reversibility, imposing that any molecular process and its reverse occur at equal rates, at equilibrium. Notably, the estimated rate constants were quite close to this condition, so we had to modify them only slightly (less than 25%, manually adjusted) to get perfect microscopic reversibility (**Table 1**).

To assess the effects of the diffusional restriction imposed by the intracellular vestibule, we also used the following Smoluchowski version of the association rate constant, where the accessibility to the S5 site is considered through a cylindrical hole of radius r_v instead of a hemispherical surface:

$$k_a = \pi D r_v^2 \left[\int_{r_c}^{l_v} \exp(U(r)/kT) dr \right]^{-1}, \quad (30)$$

Here, l_v represents the length of the intracellular vestibule, approximately 20 Å, and r_c , as before, represents the distance of the adsorbing surface from the binding site, taken as the position of the maximum value along the energy profile. Using this equation, we found that the K⁺ association binding constant k_{a1} , that has a value of 7×10^8 s⁻¹ M⁻¹ assuming a hemispherical absorbing surface, changes to 4.9×10^8 s⁻¹ M⁻¹ with an r_v of 13.5 Å (chosen to get a Ca-Ca distance of Thr112 of 32 Å, as in the 3f5w structure) and to 1.9×10^8 s⁻¹ M⁻¹ using an r_v of 8.5 Å (chosen to get a Ca-Ca distance of Thr112 of 22 Å, as in the 5vk6 structure). Since currents at very high voltages and relatively high concentrations linearly depend on k_{a1} based on **Eq. 25**, these results suggest that the current predicted would depend on the KcsA structure used.

Figure 6 top shows the predicted IV relationships at different K⁺ concentrations and compares them with those observed experimentally. Notably, all the major features of the experimental IVs, namely the amount of current carried, the rectification (less current at negative than positive voltages), the sub-linearity (saturation at highly positive and negative voltages), and the saturation of the chord conductance at high concentrations, appear quite well reproduced. Slightly lower predicted currents than those observed experimentally are instead found at relatively low K⁺ concentrations, especially at negative voltages. We think that this may originate from surface charge effects that would tend to increase the K⁺ concentration close to the channel, especially when the ionic strength is low. The bottom panels compare the conductance-concentration relationship derived at two potentials from our model with those found experimentally. Matching between experimental and modeling data is objectively good.

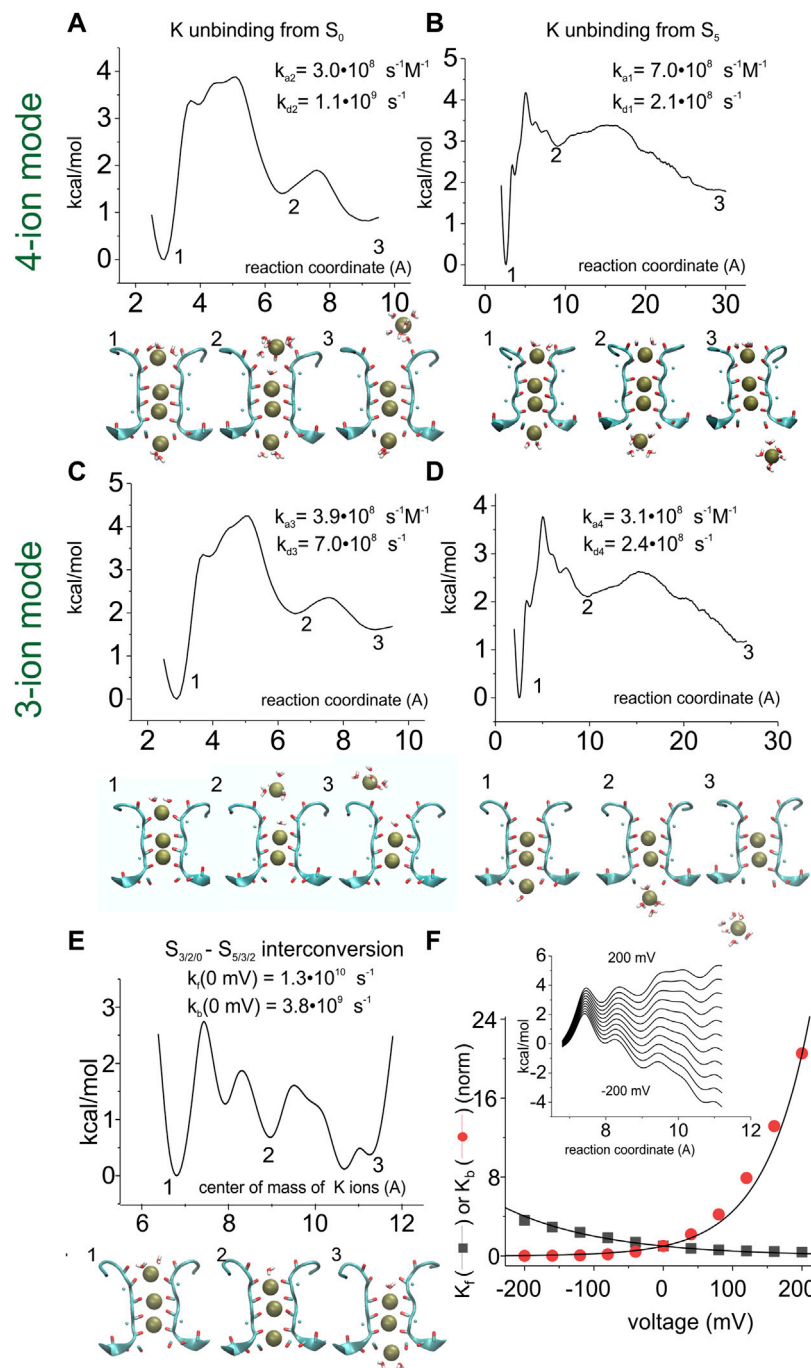


FIGURE 5 | Assessment of the energy profiles and kinetic rate constants for the K⁺ permeation kinetic model. Energy profiles were assessed by using the adaptive biasing force (ABF) 1D method for the K⁺ unbinding from S_0 into the extracellular solution (A when starting from a four-ion configuration, and C when starting from a three-ion configuration of the SF), from S_5 into the intracellular solution (BD), and for the interconversion of the three K⁺ ions inside the SF (E). In (A) and (C), the reaction coordinate is the distance between the most extracellular K⁺ ion and the center of mass of the carbonyl oxygens forming site S1. In (B) and (D), the reaction coordinate is the distance between the most intracellular K⁺ ion and the center of mass of the carbonyl oxygens forming site S4. In (E), the reaction coordinate is the distance between the center of mass of the three K⁺ ions and the center of mass of the carbonyl oxygens of residue 79. (F) inset: energy profile for the 3-K⁺ ion configuration of the selectivity filter, plotted as in panel E but with the addition of linear electrostatic energy of variable amount (corresponding to potential differences from -200 to +200 mV). Compared to panel E, only the part of the energy profile going from configuration $S_3/S_2/S_0$ (energy well #1) to configuration $S_5/S_3/S_2$ (energy well #3) is reported. Main plot: forward and backward rate constants (K_f and K_b in the scheme of Figure 4, respectively) as a function of voltage, assessed from the energy profiles shown in the inset, using Eq. (28). The numbers associated with certain wells in the energy profiles define the configuration shown below the graphs.

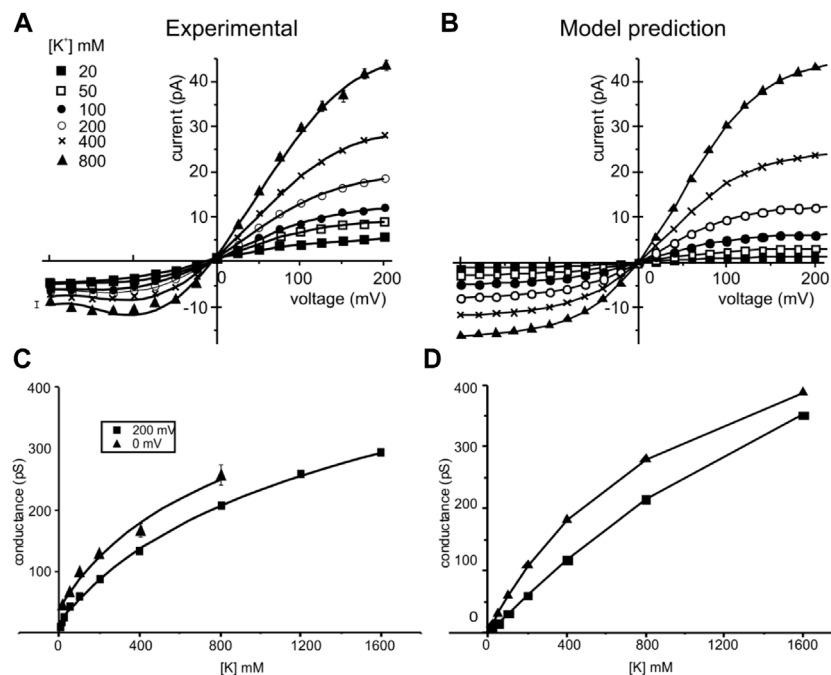


FIGURE 6 | Experimental and simulated current-voltage (IV) and conductance-concentration plots. *Left:* experimental IV relationships (top) of the KcsA channels taken at different symmetrical K^+ concentrations (indicated) and conductance-concentration relationships (bottom) at two membrane potentials. Data are from LeMasurier et al. (2001). *Right:* IV and conductance-concentration relationships predicted by our model using the kinetic scheme of **Figure 4** and rate constants adjusted for microscopic reversibility in **Table 1**. The conditions used in our modeling were the same as those used to obtain the experimental results.

DISCUSSION

Upon heating and equilibrating a K^+ -filled SF, as observed in X-ray crystallography, we found a stable SF configuration consisting of two K^+ ions bound to the crystallographic binding sites S2 and S3, and two additional K^+ ions weakly bound right at the entrances of the selectivity filter, at sites not apparent in the crystal, sites S0 and S5. K^+ ions sitting in these two sites appear only partially hydrated, as they are in part stabilized by the carbonyl oxygens of tyrosine 78 and the hydroxyl oxygens of threonine 75, respectively. The Bikerman–PB continuum model, shown to correctly predict this stable 0/2/3/5 K^+ ion distribution, confirmed the MD-derived configuration and provided clues on the physicochemical determinants behind it.

The configurations found suggested an association-dissociation kinetic model of permeation that could reproduce the experimentally observed conductance saturation and current-voltage sub-linearity, thus showing that an A/D model of permeation could well apply to the KcsA channel. Interestingly, our proposed mechanism is very similar to that found by Domene et al. (2021) where they analyze relatively long (microseconds) MD simulations from the E71A mutant KcsA channel in terms of transition probability matrix. However, in that study, the authors attempted neither to assess the kinetic rate constants related to various SF configurations nor to verify the prediction of the experimental electrophysiological data.

Notice that the experimental data used for comparison in **Figure 6** is actually for WT KcsA (Lemasurier et al., 2001), whereas our multi-scale predictions are carried out using the E71A mutant. This is because there are only a few current-voltage measurements available in the literature for E71A (Hirano et al., 2010; Rotem et al., 2010; McCoy et al., 2014), and none of them has documented current-voltage curves under a wide range of bulk concentrations as carried out by LeMasurier et al. (Lemasurier et al., 2001). WT and E71A might differ in some aspects of the permeation. Generally speaking, the difference in outward current is small between WT and E71A but larger in the inward current (Rotem et al., 2010). It has been explained that E71A mutation reduces the outward rectification by increasing inward current at strong negative voltages, suggesting that the “flipped Asp80” creates a ring of extracellular charges and increases inward current with no effects on the outward current (Rotem et al., 2010). Our results presented in **Figure 6** are in accordance with this observation, though Asp80 remained in the non-flipped position, as in WT, in our MD simulation (**Supplementary Figure S2**). Thus, the subtle current deviation of E71A from WT at strong negative voltages may indeed reflect their minor structural differences around the selective filter. However, it is not clear if the difference can be fully explained by the Asp80 side-chain orientation.

To identify a realistic mechanism of K^+ permeation through KcsA channels, in this study we used a multi-scale approach,

whereby the information obtained from MD and from continuum models at equilibrium is used to postulate a plausible kinetic model of permeation, in terms of both the number, types, and connections between the stable configurations considered and the quantitative values of the rate constants connecting them. Once this step is completed, the kinetic model can be easily verified for its predictive capability of the permeation properties experimentally available. The approach that we used here was necessary because the assessment of the single-channel current by MD typically requires a few weeks on a common workstation, a time that needs to be scaled up correspondingly because these assessments have to be repeated at several membrane potentials to construct more informative current-voltage relationships. This high computational cost strongly limits the range of possible analyses and imposes the use of non-physiological simulation conditions in terms of membrane potentials and ion concentrations. The second shortcoming of an approach fully based on MD simulations is the overwhelming number of details that the resulting trajectories provide (i.e., the positions and the velocities of all the atoms over time) most of which are not relevant for the conduction and selectivity mechanisms. On the contrary, they might be harmful as they could hinder the identification of the effectively relevant features for the process under investigation. The multi-scale approach proposed in this study tries to overcome these two current shortcomings of MD simulations on computational costs and data interpretability by using kinetic models of ion conduction. Possible shortcomings of our approach are instead represented by the limited molecular details taken into account and the use of the diffusion theory when assessing the rate constants.

A multi-scale approach has previously been used by Bernèche and Roux (2003) to predict the current passing through the KcsA channel. Similar to what we did, they derived the energy profile encountered by the ions during permeation as well as the ion diffusion coefficient, from MD, and used this information to predict the ion movements. However, instead of using the kinetic model approach, as we did, the ion permeation was predicted by the Langevin equation that assesses the random movement of a particle along the energy profile. Interestingly, the ion energy profile was assessed by assuming a 1/3 and 2/4 K^+ ion configuration and water between K^+ ions, in accordance with the soft knock-on model more in vogue then. Notably, the resulting energy profile correctly predicted the concentration-current relationship at varying voltages but not the IVs that were heavily hyperlinear and distant from experimental observations.

In the same study, they found that ionic currents in the tens of picoamperes, that is, in the order of those found experimentally in KcsA channels, were obtained with energy barriers of 2-3 kcal/mol (Bernèche and Roux, 2003). These results are in apparent contrast with ours, as we obtain similar currents with an energy barrier about twice as high. Because of this incongruence, we made a few tests on our calculation procedure. First, we checked that the rate constants we assessed using the mean first-passage time theory were compatible with the height of our energy barriers. To this end, we considered a quadratic energy barrier 5 kcal/mol high and a 2 Å

well-to-peak distance, that is, an energy barrier similar to what we obtained for the binding/unbinding of K^+ ions to the external sites (using a diffusion coefficient of 0.235 Å²/ps). Using Kramer's equation, we analytically obtained a kinetic rate constant of about 10⁸ s⁻¹, that is, the same order of magnitude of our kinetic rate constants (cf. Table 1). Second, a rate of 10⁸ ions per second going through the channel pore, each carrying a charge of 1.6 10⁻¹⁹ C is expected to result in a current in the order of 10–20 pA.

Another issue that needs to be addressed in this context is why long MD simulations carried out on the KcsA channel have often resulted in predicted currents significantly smaller than those observed experimentally (Köpfer et al., 2014; Furini and Domene, 2020; Mironenko et al., 2021). Imperfect force fields, lack of an intracellular domain in the structure used in the computation, differences in the phospholipid composition, the use of periodic boundary conditions, or the method for the application of the transmembrane potential have been suggested as possible causes¹. We would like to draw attention here to another possible cause: the size of the intracellular vestibule. K^+ channels conductance has been suggested to heavily depend on the physical dimension of the hydrophobic intracellular vestibule (Naranjo et al., 2016). This makes it possible that the width of the intracellular vestibule of the KcsA structure chosen for MD simulations can be a major cause of the variable current predicted, due to the quite variable dimensions experimentally found in different instances (Cuello et al., 2010a; Cuello et al., 2010b). Notably, simulations using a fairly large intracellular vestibule (Ca-Ca distance at Thr112 of 32 Å, as derived from PDB crystal structure 3f5w (Köpfer et al., 2014)) give KcsA currents in substantial accordance with that found experimentally (up to a factor of 2). By contrast, simulations using a much smaller size for the intracellular vestibule (22 Å, as derived from PDB structure 5vk6 (Furini and Domene, 2020; Domene et al., 2021)) give KcsA currents about one order of magnitude smaller. Our method to calculate the current through KcsA does not include the physical dimension of the intracellular vestibule but uses a rate constant for K^+ binding to S5 assessed by assuming K^+ diffusion through a (large) hemispherical surface surrounding the binding site (thus minimal K^+ diffusion restrains to reach the site). We believe that this is the reason why our modeling predicts K^+ current amplitudes substantially higher than those found by MD and in agreement with those found experimentally. In accordance, a version of the Smoluchowski equation taking into account the diffusional restriction present in the intracellular vestibule results in a reduction in the estimated current.

We have seen that site S5, which we found right at the internal entrance of the SF, can be a major determinant of the K^+ flux through the KcsA channel. Although site S5 is not present in the crystal structure, it has already been seen in previous MD studies

¹Incidentally, the fact that our method, essentially based on equilibrium MD computations, predicts currents close to those experimentally observed would exclude the possibility that the inconsistency derives from an erroneous force field.

of the KcsA channel. Köpfer et al. (Köpfer et al., 2014) reported K^+ ions partially hydrated and bound to site S5, in a position very close to that found in the present study, and suggested to be an important intermediate, in conjunction with site S0, of the permeation process. MD simulations of KcsA channel permeation performed by Domene et al. (Domene et al., 2021) also show K^+ ions sitting at a center of mass position, slightly below the tyrosine hydroxyl oxygens. Although these authors described these K^+ ions as sitting in the cavity (at site S_{cav}), their position was completely different from that shown by the crystal electron density (Morais-Cabral et al., 2001), and in fact more similar to site S5 we found in this study and also found by Köpfer et al. (Köpfer et al., 2014). A K^+ binding site positioned just below the hydroxyl oxygen, and termed S5, was also identified with MD simulations by Jensen et al. (Jensen et al., 2010), using the Kv1.2 channel structure. Our data and the cited literature suggest that partially hydrated K^+ ions interact with the selectivity filter at site S5 in the internal entrance that arguably represents a stable position and an important intermediate for the permeation process of the KcsA channel.

Our data could also make a small contribution to the ongoing debate between hard and soft knock-on permeation models (see (Mironenko et al., 2021) for a recent review) for a recent review. Our equilibrium results showing the stable 0/2/3/5 configuration, with sites 1 and 4 empty (OKK0 configuration), explicitly indicate that water is not present inside the SF. In fact, we never observed water molecules stably sitting in the SF at equilibrium. Although we did not conduct real-time MD simulations that could have disclosed other K^+ configurations in the SF, our results, for what little they can say, are consistent only with the hard knock-on permeation model. We wish to add that absence of water inside the SF during K^+ permeation was also reported by Öster et al.

(Öster et al., 2019), and our OKK0 configuration was found to be the most probable state by Domene et al. (Domene et al., 2021) and a key configuration by Köpfer et al. (Köpfer et al., 2014). Notice that the latter two studies were carried out under permeation conditions.

DATA AVAILABILITY STATEMENT

The raw data supporting the conclusion of this article will be made available by the authors, without undue reservation.

AUTHOR CONTRIBUTIONS

MVL and LC performed molecular dynamics; T-LH performed continuum modeling; FF, T-LH, R-SC, and LC wrote the paper. All authors approved the final version of the manuscript.

FUNDING

This research was funded by the Ministry of Science and Technology of Taiwan with grant numbers: MOST 110-2115-M-035-003-MY2 (T-LH).

SUPPLEMENTARY MATERIAL

The Supplementary Material for this article can be found online at: <https://www.frontiersin.org/articles/10.3389/fmolb.2022.880660/full#supplementary-material>

REFERENCES

- Allen, T. W., Kuyucak, S., and Chung, S.-H. (2000). Molecular Dynamics Estimates of Ion Diffusion in Model Hydrophobic and KcsA Potassium Channels. *Biophys. Chem.* 86, 1–14. doi:10.1016/s0301-4622(00)00153-8
- Bernèche, S., and Roux, B. (2003). A Microscopic View of Ion Conduction through the K^+ Channel. *Proc. Natl. Acad. Sci. U. S. A.* 100, 8644–8648. doi:10.1073/pnas.1431750100
- Bernèche, S., and Roux, B. (2001). Energetics of Ion Conduction through the K^+ Channel. *Nature* 414, 73–77. doi:10.1038/35102067
- Best, R. B., Zhu, X., Shim, J., Lopes, P. E. M., Mittal, J., Feig, M., et al. (2012). Optimization of the Additive CHARMM All-Atom Protein Force Field Targeting Improved Sampling of the Backbone ϕ , ψ and Side-Chain χ_1 and χ_2 Dihedral Angles. *J. Chem. Theory Comput.* 8, 3257–3273. doi:10.1021/ct300400x
- Bikerman, J. J. (1942). XXXIX. Structure and Capacity of Electrical Double Layer. *Lond. Edinb. Dublin Philosophical Mag. J. Sci.* 33, 384–397. doi:10.1080/14786444208520813
- Borukhov, I., Andelman, D., and Orland, H. (1997). Steric Effects in Electrolytes: A Modified Poisson-Boltzmann Equation. *Phys. Rev. Lett.* 79, 435–438. doi:10.1103/physrevlett.79.435
- Bullerjahn, J. T., von Bülow, S., and Hummer, G. (2020). Optimal Estimates of Self-Diffusion Coefficients from Molecular Dynamics Simulations. *J. Chem. Phys.* 153, 024116. doi:10.1063/5.0008312
- Catacuzzeno, L., Sforza, L., and Franciolini, F. (2020). Voltage-dependent Gating in K Channels: Experimental Results and Quantitative Models. *Pflugers Arch. - Eur. J. Physiol.* 472, 27–47. doi:10.1007/s00424-019-02336-6
- Comer, J., Gumbart, J. C., Hénin, J., Lelièvre, T., Pohorille, A., and Chipot, C. (2015). The Adaptive Biasing Force Method: Everything You Always Wanted to Know but Were Afraid to Ask. *J. Phys. Chem. B* 119, 1129–1151. doi:10.1021/jp506633n
- Cooper, K. E., Gates, P. Y., and Eisenberg, R. S. (1988a). Diffusion Theory and Discrete Rate Constants in Ion Permeation. *J. cooper Biol.* 106, 95–105. doi:10.1007/bf01871391
- Cooper, K. E., Gates, P. Y., and Eisenberg, R. S. (1988b). Surmounting Barriers in Ionic Channels. *Quart. Rev. Biophys.* 21, 331–364. doi:10.1017/s0033583500004480
- Cuello, L. G., Cortes, D. M., and Perozo, E. (2017). The Gating Cycle of a K^+ Channel at Atomic Resolution. *Elife* 6. doi:10.7554/eLife.28032
- Cuello, L. G., Jogini, V., Cortes, D. M., Pan, A. C., Gagnon, D. G., Dalmas, O., et al. (2010). Structural Basis for the Coupling between Activation and Inactivation Gates in K^+ Channels. *Nature* 466, 272–275. doi:10.1038/nature09136
- Cuello, L. G., Jogini, V., Cortes, D. M., and Perozo, E. (2010). Structural Mechanism of C-type Inactivation in K^+ Channels. *Nature* 466, 203–208. doi:10.1038/nature09153
- Darden, T., York, D., and Pedersen, L. (1993). Particle Mesh Ewald: AnN-Log(N) Method for Ewald Sums in Large Systems. *J. Chem. Phys.* 98, 10089–10092. doi:10.1063/1.464397
- Darve, E., Rodríguez-Gómez, D., and Pohorille, A. (2008). Adaptive Biasing Force Method for Scalar and Vector Free Energy Calculations. *J. Chem. Phys.* 128, 144120. doi:10.1063/1.2829861
- Debye, P. (1942). Reaction Rates in Ionic Solutions. *Trans. Electrochem. Soc.* 82, 265. doi:10.1149/1.3071413
- Domene, C., Ocello, R., Masetti, M., and Furini, S. (2021). Ion Conduction Mechanism as a Fingerprint of Potassium Channels. *J. Am. Chem. Soc.* 143, 12181–12193. doi:10.1021/jacs.1c04802

- Doyle, D. A., Cabral, J. M., Pfuetzner, R. A., Kuo, A., Gulbis, J. M., Cohen, S. L., et al. (1998). The Structure of the Potassium Channel: Molecular Basis of K⁺ Conduction and Selectivity. *Science* 280, 69–77. doi:10.1126/science.280.5360.69
- Dyrka, W., Bartuzel, M. M., and Kotulski, M. (2013). Optimization of 3D Poisson-Nernst-Planck Model for Fast Evaluation of Diverse Protein Channels. *Proteins* 81, 1802–1822. doi:10.1002/prot.24326
- Eisenberg, B. (1998). Ionic Channels in Biological Membranes: Natural Nanotubes. *Acc. Chem. Res.* 31, 117–123. doi:10.1021/ar950051e
- Feller, S. E., Zhang, Y., Pastor, R. W., and Brooks, B. R. (1995). Constant Pressure Molecular Dynamics Simulation: The Langevin Piston Method. *J. Chem. Phys.* 103, 4613–4621. doi:10.1063/1.470648
- Furini, S., Beckstein, O., and Domene, C. (2009). Permeation of Water through the KcsA K⁺ channel. *Proteins* 74, 437–448. doi:10.1002/prot.22163
- Furini, S., and Domene, C. (2020). Critical Assessment of Common Force Fields for Molecular Dynamics Simulations of Potassium Channels. *J. Chem. Theory Comput.* 16, 7148–7159. doi:10.1021/acs.jctc.0c00331
- Furini, S., Zerbetto, F., and Cavalcanti, S. (2006). Application of the Poisson-Nernst-Planck Theory with Space-dependent Diffusion Coefficients to KcsA. *Biophysical J.* 91, 3162–3169. doi:10.1529/biophysj.105.078741
- Hénin, J., Fiorin, G., Chipot, C., and Klein, M. L. (2010). Exploring Multidimensional Free Energy Landscapes Using Time-Dependent Biases on Collective Variables. *J. Chem. Theory Comput.* 6, 35–47.
- Hille, B. (2001). *Ion Channels of Excitable Membranes*. 3rd Edn. Sinauer: Sunderland.
- Hirano, M., Takeuchi, Y., Aoki, T., Yanagida, T., and Ide, T. (2010). Rearrangements in the KcsA Cytoplasmic Domain Underlie its Gating. *J. Biol. Chem.* 285, 3777–3783. doi:10.1074/jbc.M109.084368
- Hodgkin, A. L., and Keynes, R. D. (1955). The Potassium Permeability of a Giant Nerve Fibre. *J. Physiol.* 128, 61–88. doi:10.1113/jphysiol.1955.sp005291
- Hornig, T.-L., Lin, T.-C., Liu, C., and Eisenberg, B. (2012). PNP Equations with Steric Effects: A Model of Ion Flow through Channels. *J. Phys. Chem. B* 116, 11422–11441. doi:10.1021/jp305273n
- Hornig, T. L. (2020). Review and Modification of Entropy Modeling for Steric Effects in the Poisson-Boltzmann Equation. *Entropy (Basel)* 22, 632. doi:10.3390/e22060632
- Jensen, M. Ø., Borhani, D. W., Lindorff-Larsen, K., Maragakis, P., Jogini, V., Eastwood, M. P., et al. (2010). Principles of Conduction and Hydrophobic Gating in K⁺ Channels. *Proc. Natl. Acad. Sci. U.S.A.* 107, 5833–5838. doi:10.1073/pnas.0911691107
- Jensen, M. Ø., Jogini, V., Eastwood, M. P., and Shaw, D. E. (2013). Atomic-level Simulation of Current-Voltage Relationships in Single-File Ion Channels. *J. Gen. Physiol.* 141, 619–632. doi:10.1085/jgp.201210820
- Jorgensen, W. L., Chandrasekhar, J., Madura, J. D., Impey, R. W., and Klein, M. L. (1983). Comparison of Simple Potential Functions for Simulating Liquid Water. *J. Chem. Phys.* 79, 926–935. doi:10.1063/1.445869
- Kopec, W., Köpfer, D. A., Vickery, O. N., Bondarenko, A. S., Jansen, T. L. C., de Groot, B. L., et al. (2018). Direct Knock-On of Desolvated Ions Governs Strict Ion Selectivity in K⁺ Channels. *Nat. Chem.* 10, 813–820. doi:10.1038/s41557-018-0105-9
- Köpfer, D. A., Song, C., Gruene, T., Sheldrick, G. M., Zachariae, U., and De Groot, B. L. (2014). Ion Permeation in K⁺ Channels Occurs by Direct Coulomb Knock-On. *Science* 346, 352–355. doi:10.1126/science.1254840
- Kratochvil, H. T., Carr, J. K., Matulef, K., Annen, A. W., Li, H., Maj, M., et al. (2016). Instantaneous Ion Configurations in the K⁺ Ion Channel Selectivity Filter Revealed by 2D IR Spectroscopy. *Science* 353, 1040–1044. doi:10.1126/science.aag1447
- Langan, P. S., Vandavasi, V. G., Weiss, K. L., Afonine, P. V., el Omari, K., Duman, R., et al. (2018). Anomalous X-Ray Diffraction Studies of Ion Transport in K⁺ Channels. *Nat. Commun.* 9, 4540–4545. doi:10.1038/s41467-018-06957-w
- Lemasurier, M., Heginbotham, L., and Miller, C. (2001). KcsA. *J. Gen. Physiol.* 118, 303–314. doi:10.1085/jgp.118.3.303
- Li, J., Ostmeier, J., Cuello, L. G., Perozo, E., and Roux, B. (2018). Rapid Constriction of the Selectivity Filter Underlies C-type Inactivation in the KcsA Potassium Channel. *J. Gen. Physiol.* 150, 1408–1420. doi:10.1085/jgp.201812082
- Liu, P., Dehez, F., Cai, W., and Chipot, C. (2012). A Toolkit for the Analysis of Free-Energy Perturbation Calculations. *J. Chem. Theory Comput.* 8, 2606–2616. doi:10.1021/ct300242f
- Liu, X., and Lu, B. (2017). Incorporating Born Solvation Energy into the Three-Dimensional Poisson-Nernst-Planck Model to Study Ion Selectivity in KcsA K⁺ Channels. *Phys. Rev. E* 96, 62416. doi:10.1103/physreve.96.062416
- MacKerell, A. D., Bashford, D., Bellott, M., Dunbrack, R. L., Evanseck, J. D., Field, M. J., et al. (1998). All-atom Empirical Potential for Molecular Modeling and Dynamics Studies of Proteins. *J. Phys. Chem. B* 102, 3586–3616. doi:10.1021/jp973084f
- Martyna, G. J., Tobias, D. J., and Klein, M. L. (1994). Constant Pressure Molecular Dynamics Algorithms. *J. Chem. Phys.* 101, 4177–4189. doi:10.1063/1.467468
- McCoy, J. G., Rusinova, R., Kim, D. M., Kowal, J., Banerjee, S., Jaramillo Cartagena, A., et al. (2014). A KcsA/MloK1 Chimeric Ion Channel Has Lipid-dependent Ligand-Binding Energetics. *J. Biol. Chem.* 289, 9535–9546. doi:10.1074/jbc.M113.543389
- Mironenko, A., Zachariae, U., de Groot, B. L., and Kopec, W. (2021). The Persistent Question of Potassium Channel Permeation Mechanisms. *J. Mol. Biol.* 433, 167002. doi:10.1016/j.jmb.2021.167002
- Morais-Cabral, J. H., Zhou, Y., and MacKinnon, R. (2001). Energetic Optimization of Ion Conduction Rate by the K⁺ Selectivity Filter. *Nature* 414, 37–42. doi:10.1038/35102000
- Naranjo, D., Moldenhauer, H., Pincuntureo, M., and Diaz-Franulic, I. (2016). Pore Size Matters for Potassium Channel Conductance. *J. Gen. Physiol.* 148, 277–291. doi:10.1085/jgp.201611625
- Nelson, P. H. (2011). A Permeation Theory for Single-File Ion Channels: One- and Two-step Models. *J. Chem. Phys.* 134, 165102. doi:10.1063/1.3580562
- Nonner, W., Chen, D. P., and Eisenberg, B. (1999). Progress and Prospects in Permeation. *J. Gen. Physiol.* 113, 773–782. doi:10.1085/jgp.113.6.773
- Noskov, S. Y., Bernèche, S., and Roux, B. (2004). Control of Ion Selectivity in Potassium Channels by Electrostatic and Dynamic Properties of Carbonyl Ligands. *Nature* 431, 830–834. doi:10.1038/nature02943
- Öster, C., Hendriks, K., Kopec, W., Chevelkov, V., Shi, C., Michl, D., et al. (2019). The Conduction Pathway of Potassium Channels Is Water Free under Physiological Conditions. *Sci. Adv.* 5, 6756. doi:10.1126/sciadv.aaw6756
- Pearlman, D. A. (2002). A Comparison of Alternative Approaches to Free Energy Calculations. *J. Phys. Chem.* 98, 1487–1493. doi:10.1021/j100056a020
- Phillips, J. C., Braun, R., Wang, W., Gumbart, J., Tajkhorshid, E., Villa, E., et al. (2005). Scalable Molecular Dynamics with NAMD. *J. Comput. Chem.* 26, 1781–1802. doi:10.1002/jcc.20289
- Rotem, D., Mason, A., and Bayley, H. (2010). Inactivation of the KcsA Potassium Channel Explored with Heterotetramers. *J. Gen. Physiol.* 135, 29–42. doi:10.1085/jgp.200910305
- Schulten, K., Schulten, Z., and Szabo, A. (1981). Dynamics of Reactions Involving Diffusive Barrier Crossing. *J. Chem. Phys.* 74, 4426–4432. doi:10.1063/1.441684
- Szabo, A. (1979). Theory of Polarized Fluorescent Emission in Uniaxial Liquid Crystals. *J. Chem. Phys.* 72, 4620–4626. doi:10.1063/1.439704
- Wang, J., Deng, Y., and Roux, B. (2006). Absolute Binding Free Energy Calculations Using Molecular Dynamics Simulations with Restraining Potentials. *Biophysical J.* 91, 2798–2814. doi:10.1529/biophysj.106.084301
- Wu, D. (2017). Dynamic Water Patterns Change the Stability of the Collapsed Filter Conformation of the KcsA K⁺ Channel. *PLoS One* 12, e0186789. doi:10.1371/journal.pone.0186789
- Zhou, Y., and MacKinnon, R. (2003). The Occupancy of Ions in the K⁺ Selectivity Filter: Charge Balance and Coupling of Ion Binding to a Protein Conformational Change Underlie High Conduction Rates. *J. Mol. Biol.* 333, 965–975. doi:10.1016/j.jmb.2003.09.022

Conflict of Interest: The authors declare that the research was conducted in the absence of any commercial or financial relationships that could be construed as a potential conflict of interest.

Publisher's Note: All claims expressed in this article are solely those of the authors and do not necessarily represent those of their affiliated organizations, or those of the publisher, the editors, and the reviewers. Any product that may be evaluated in this article, or claim that may be made by its manufacturer, is not guaranteed or endorsed by the publisher.

Copyright © 2022 Hornig, Chen, Leonardi, Franciolini and Catacuzzeno. This is an open-access article distributed under the terms of the Creative Commons Attribution License (CC BY). The use, distribution or reproduction in other forums is permitted, provided the original author(s) and the copyright owner(s) are credited and that the original publication in this journal is cited, in accordance with accepted academic practice. No use, distribution or reproduction is permitted which does not comply with these terms.



Chanalyzer: A Computational Geometry Approach for the Analysis of Protein Channel Shape and Dynamics

Andrea Raffo¹, Luca Gagliardi², Ulderico Fugacci^{1*}, Luca Sagresti^{3,4,5},
Simone Grandinetti^{3,6}, Giuseppe Brancato^{3,4,5}, Silvia Biasotti^{1*} and Walter Rocchia^{1,2*}

¹Istituto di Matematica Applicata e Tecnologie Informatiche "E. Magenes", Consiglio Nazionale delle Ricerche, Genova, Italy, ²CONCEPT Lab, Istituto Italiano di Tecnologia, Genova, Italy, ³Scuola Normale Superiore, Pisa, Italy, ⁴Istituto Nazionale di Fisica Nucleare (INFN), Pisa, Italy, ⁵Consorzio Interuniversitario per lo sviluppo dei Sistemi a Grande Interfase (CSGI), Sesto Fiorentino, Italy, ⁶Dipartimento di Ingegneria Civile ed Industriale, Università di Pisa, Pisa, Italy

OPEN ACCESS

Edited by:

Luca Maragliano,
Marche Polytechnic University, Italy

Reviewed by:

Toni Giorgino,
National Research Council (CNR), Italy
Gianluca Lattanzi,
University of Trento, Italy

*Correspondence:

Ulderico Fugacci
ulderico.fugacci@ge.imati.cnr.it
Silvia Biasotti
silvia.biasotti@ge.imati.cnr.it
Walter Rocchia
walter.rocchia@iit.it

Specialty section:

This article was submitted to
Biological Modeling and Simulation,
a section of the journal
Frontiers in Molecular Biosciences

Received: 01 May 2022

Accepted: 13 June 2022

Published: 25 July 2022

Citation:

Raffo A, Gagliardi L, Fugacci U,
Sagresti L, Grandinetti S, Brancato G,
Biasotti S and Rocchia W (2022)
Chanalyzer: A Computational
Geometry Approach for the Analysis of
Protein Channel Shape and Dynamics.
Front. Mol. Biosci. 9:933924.
doi: 10.3389/fmolb.2022.933924

Morphological analysis of protein channels is a key step for a thorough understanding of their biological function and mechanism. In this respect, molecular dynamics (MD) is a very powerful tool, enabling the description of relevant biological events at the atomic level, which might elude experimental observations, and pointing to the molecular determinants thereof. In this work, we present a computational geometry-based approach for the characterization of the shape and dynamics of biological ion channels or pores to be used in combination with MD trajectories. This technique relies on the earliest works of Edelsbrunner and on the NanoShaper software, which makes use of the alpha shape theory to build the solvent-excluded surface of a molecular system in an aqueous solution. In this framework, a channel can be simply defined as a cavity with two entrances on the opposite sides of a molecule. Morphological characterization, which includes identification of the main axis, the corresponding local radius, and the detailed description of the global shape of the cavity, is integrated with a physico-chemical description of the surface facing the pore lumen. Remarkably, the possible existence or temporary appearance of fenestrations from the channel interior towards the outer lipid matrix is also accounted for. As a test case, we applied the present approach to the analysis of an engineered protein channel, the mechanosensitive channel of large conductance.

Keywords: channel and pore characterization, computational geometry, molecular surface, molecular dynamics, skeletonization, alpha shapes theory, ion channels

1 INTRODUCTION

Ion channels (Kew and Davies, 2009; Lemoine et al., 2012) are a biological class of prominent pharmacological importance and are targets for over 20% of drugs on the market. Moreover, to expand their use beyond the natural one, ion channels have been successfully modified to confer them new artificial gating mechanisms through the combination of molecular biology and protein engineering (Banghart et al., 2006). In addition to membrane proteins, channel-like passages can be also found in other relevant intracellular proteins, as in ferritin where channels regulate ion uptake and release (Chandramouli et al., 2016). Therefore, characterizing the structural and dynamic features of ion channels can significantly improve our understanding of their functioning and unveil the more subtle details of their mechanism, which are often elusive

to experimental observations. In this context, molecular dynamics (MD) simulations have proven very valuable to investigate channel behavior with atomistic detail, thus integrating biological and crystallographic information and helping achieve a more comprehensive understanding of channel function (Treptow and Klein, 2012). As an example, MD simulations have been fruitfully applied to describe pathways and barriers for ion translocation in a pentameric ligand-gated ion channel (Di Maio et al., 2015) or to gain new insights into the peculiar gating mechanism of an engineered protein (Chandramouli et al., 2015), the mechanosensitive channel of large conductance (MscL) equipped with a light-triggered gating, as originally proposed by Feringa and coworkers (Koçer et al., 2005). MD also proved to be instrumental in the characterization and design of biological pore constructs for biotechnological applications (Spitaleri et al., 2021).

Here, we propose a novel computational tool for the automatic recognition and structural characterization of a protein channel from a given MD trajectory, rooted in the alpha shape complex analysis and the notion of discrete flow as described in (Edelsbrunner et al., 1998), see more details in **Section 2.1**. Alpha shape theory is also at the basis of how the NanoShaper software builds the protein Solvent-Excluded Surface (SES) and finds cavities and pockets (Decherchi and Rocchia, 2013). This method enriches the capabilities of NanoShaper to identify and characterize cavities in molecular structures (Decherchi et al., 2018) and is focused more specifically on the identification of permanent or transient channels formed within a protein, from which it was dubbed Chanalyzer. Notably, it does not require predefined user parameters for channel identification, such as the notion of membrane plane, it is numerically robust and well-suited for analyzing a large collection of molecular configurations as issued from extended MD simulations of biological systems. In addition, the method supports a detailed geometric analysis based on the concepts of skeleton and centerline and identifies both channels ends through the use of graph-based techniques. The identification of the channels is computationally efficient and a proximity strategy has been adopted to accelerate the calculation of channel entrance and exit from one MD frame to the following one. Interestingly, its extensive geometric characterization allows for the identification of the channel main axis, but also of possible ancillary tunnels and potential fenestrations facing the lipid membrane. It also provides a geometric approximation of the local section orthogonal to the central axis of the lumen, to more easily identify symmetry-breaking configurations and anomalies. To validate the present approach and to show the complete set of geometrical information that it provides, we analyzed a number of MD trajectories of an engineered protein channel, the mechanosensitive channel of large conductance (MscL). Overall, results show a very good agreement with previous calculations of channel local radius, as well as the provisioning of new information thus supporting the routine use of Chanalyzer for the detailed study of protein channels in a large variety of biological systems.

2 METHODS

2.1 Preliminary Concepts on Alpha Shape Theory

A popular representation of macromolecules is the union of possibly overlapping spherical balls, each of them representing an atom. Using computational geometry concepts, the relative distances among the atoms are captured by the Voronoi diagrams (Voronoi, 1908) and Delaunay simplices (Delaunay et al., 1934). These concepts are fundamental for defining and delimiting both the space occupied by the molecule and its complement (Edelsbrunner and Mücke, 1994). The illustration of the Delaunay triangulation (Dt) of a simplified molecule, represented in 2D as a set of disks of the same radius, is shown in **Supplementary Figure S1** in the supplemental material (disks are in light gray). The Dt triangulates the convex hull of the centers of the disks, representing the atoms. It reports a *complex*, which is basically a set of triangles or tetrahedra in the space. The part of the complex that corresponds to the molecule is the so-called *alpha shape* and corresponds to triangles that cover only regions inside the union of the disks and, in degenerate cases, contains also segments and isolated points. In the figure, the alpha shape is represented by gray triangles and bold black edges. The complement can be organized into connected components. With respect to the figure, there are three components, the largest one is represented in light blue. The small black arrows indicate the edges of the complement external to the alpha shape. These edges can be envisaged as part of a degenerate triangle having the third vertex at the infinity. Starting from these edges, it is possible to define a direction of visit for the component, the so-called discrete flow, and to determine how deep that component is. Components without external edges – such as the one in light red on the right – correspond to internal voids; components with one external edge (mouth) correspond to pockets; components with two mouths correspond to channels.

2.2 Geometric Processing

2.2.1 Trajectory Post-Processing

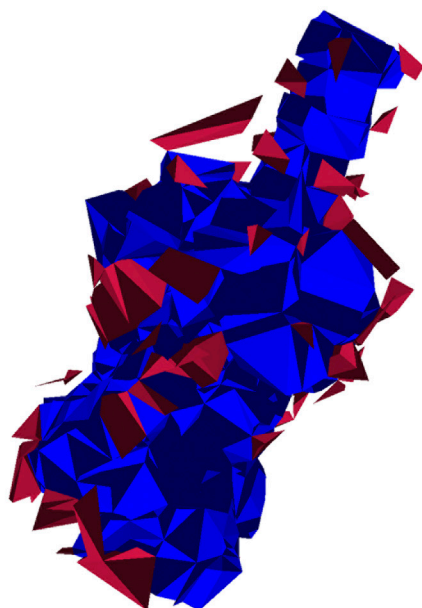
The trajectory is converted from the original *dcd* to the multiple *pdb* format using the VMD tool (Humphrey et al., 1996), after excluding water molecules and ions. Then it is split into individual frames and finally annotated with the atomic radii information. Finally, only the information on atom centers and radii is retained in *a.xyzr* file, which is the standard input of NanoShaper (Decherchi and Rocchia, 2013).

2.2.2 Channel Identification

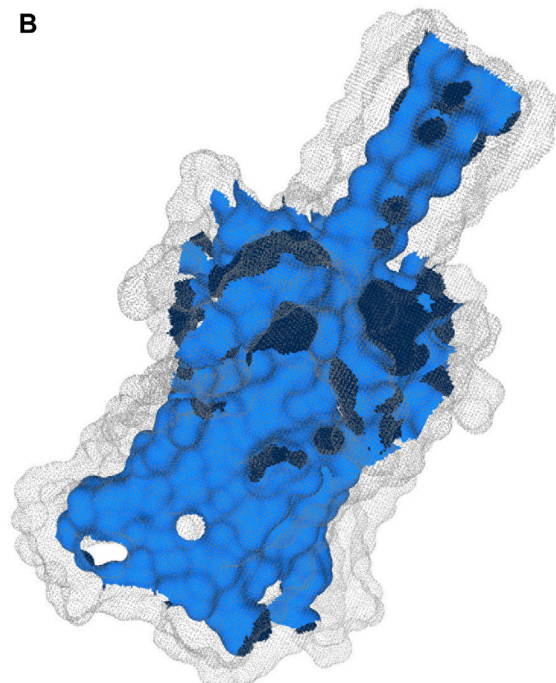
We build our method to identify channels on the alpha shape theory (Edelsbrunner and Mücke, 1994). A molecule is here modeled as a collection of three-dimensional balls, one ball per atom; since the radius varies with the different atoms, we build their weighted Delaunay triangulation (wDT) using the routines in (The CGAL Project, 2013). We then obtain a *simplicial complex* whose nodes correspond to the atoms and volumetric elements are tetrahedra. As a convention, it is

INPUT	PRE-PROCESSING	CHANALYZER-CORE	OUTPUT
Structure (.pdb, .gro ...) Trajectory (.trr, .dcd ...) Radii (.pqr)	Conversion to .mpdb (e.g., catdcd) Conversion to .xyzr for each frame (Chanalyzer.preproc.py)	(A) Extraction of the tetrahedral representation of the channel (B) Channel projection onto the SES generated via NanoShaper (C) Skeletonization and extraction of source and target points (D) Centerline computation and geometry processing	Centerline per frame (point cloud in ASCII) Min/max distance from the channel Mesh of the channel (.off)

A



B



C



D

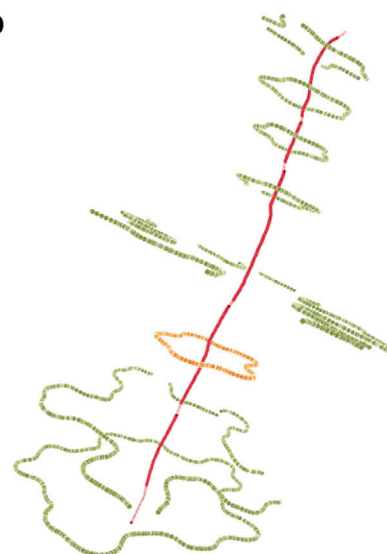


FIGURE 1 | Pipeline of Chanalyzer. At the top, the basic flow is described. **(A)** Identification of the connected components of tetrahedra that are not entirely inside the SES. Each component represents a cavity (in blue the largest one, ascribed to the channel, in red the other ones, which are discarded); **(B)** the intersection of the blue component with the SES identifies the channel surface; **(C)** skeletonization (in green) revealing a footprint of the pentameric structure and the source-target path (in red); **(D)** centerline in red and several sections (in orange the central one).

assumed that the faces of the convex hull of the wDT are virtually connected to a point at infinity. We characterize this structure using the discrete-flow procedure as detailed in (Edelsbrunner et al., 1998). The discrete-flow aims at identifying the tetrahedra of the simplicial complex that are in the complement of the molecule and is defined on the basis of geometric considerations on how much a tetrahedron is “obtuse” and its circumcenter spans over external tetrahedra. In more detail, starting from the tetrahedra that include the infinity point (those tetrahedra are external by definition), the flow induces a partial ordering between couples of adjacent tetrahedra. At this point, using a graph depth-first visiting scheme driven by the discrete-flow ordering, we identify the tetrahedra that descend from the infinity: each arc of the graph identifies a connected component of tetrahedra that is a potential cavity of interest, as discussed in (Liang et al., 1998). **Figure 1A** visualizes the connected components of tetrahedra obtained during the graph visiting.

The connected component having the largest volume, shown in blue in **Figure 1A**, corresponds to the volumetric approximation of the channel. To estimate geometric properties, this tetrahedral approximation is projected onto the molecular surface, here built *via* NanoShaper as a triangular mesh approximation of the SES. The SES triangular mesh is processed to keep only those triangles having the barycenter inside the tetrahedral approximation of the channel. This extraction is based on the query of a k-d tree. It is worth noting that other molecular surface representations and other software to compute the MS could in principle be employed too; we here rely on NanoShaper as it also bases the MS computation on the SES definition *via* alpha shape theory and weighted Delaunay triangulations.

2.2.3 Geometric Characterization

The outcome of **Section 2.2.2** is a portion of the SES that roughly corresponds to the channel, *see* an example in **Figure 1B**. In a generic case, such a surface is expected to be roughly tubular in shape but, in some particular cases, it can present bi- or multi-furcations, whose biological or biophysical implications might need some attention. To characterize such a surface portion, we firstly extract the mean curvature flow skeleton (Tagliasacchi et al., 2012) using its CGAL implementation, which is an approximation of the medial axis of the channel. Even if intuitive and very popular in computer graphics, the skeleton is strongly sensitive to surface perturbations and corners, as visible in **Figure 1C**. Therefore its robust identification requires particular caution.

Skeleton Identification and Pruning

The skeleton of the cavity previously extracted *via* CGAL does not present a linear structure but it may contain several ramifications and ancillary paths preventing a clear identification of the channel and its main entrances (*see* **Figure 1C**). In order to overcome this limitation, we adopted a pruning procedure extracting from the skeleton the path that best represents the main direction along which the channel structure develops. Once this is done, we can also locate the two main entrances,

discriminating them from possible lateral alternatives. This pruned representation of the skeleton is extracted by retrieving in the skeleton graph a path with the property of maximizing both length and straightness. In order to achieve this, a score $s(\gamma)$ is defined for each path γ of the graph as follows:

$$s(\gamma) := \frac{\text{length}(\gamma)^2}{\text{tortuousness}(\gamma)}, \quad (1)$$

where $\text{length}(\gamma)$ is the number of edges that compose γ and $\text{tortuousness}(\gamma)$ is a positive real number close to zero when γ is rectilinear and steadily increases as the path loses its rectilinear behavior. It is calculated as the average distance of the nodes of p from the straight line connecting its start and end nodes. Thus, paths assuming high score values are both straight and long while curved/short paths present low score values. The pruning algorithm considers the shortest paths connecting all the pairs of vertices of the skeleton graph and computes the score value for each of them. Then, the shortest path γ having the maximum score value is elected as the core skeleton of the channel and adopted as input to the next steps of the channel identification pipeline. In **Figure 1C** we superimpose the output of the pruning algorithm, red dots, to the curve skeleton obtained with CGAL.

Centerline Computation

To study tubular geometries with complex morphologies we here employ the Vascular Modeling ToolKit (VMTK) (Piccinelli et al., 2009), a standard software package for the geometric analysis of vessels segments. Given source and target points, VMTK can provide a number of useful quantities about the global morphological properties, such as the unit vectors of local Frenet-frames of the centerline which, in turn, allow to compute curvature and torsion. The skeleton pruning step allows Chanalyzer to focus on the channel axis and, potentially, to consider secondary entrances.

Extraction of Visible Contour of a Channel

The previous steps of the procedure allow projecting the identified channel on the molecular surface. In order to better analyze the channel and compute information about its shape, it can be useful to consider, rather than all the portion of the surface identified as composing the channel, just the part of it which is visible from the centerline. The extraction of this visible contour of the channel is achieved by clipping the channel surface with planes that are orthogonal to the centerline itself. More specifically, given a point p of the centerline, π_p is defined as the plane passing through p and orthogonal to t_p where t_p is the tangent vector of the centerline at the point p . Intersecting π_p with the channel surface, the section S_p of the channel at level p is retrieved. One can expect that such a section is a simple and closed curve but, in practice, S_p can also consist of multiple connected components not all visible from the point p . In order to extract from S_p the portion visible from p , we consider a suitable sampling of the rays starting from p and belonging to π_p and for each of them, we return the points of S_p intersecting the selected ray and visible from p . More properly, we represent the points of S_p as a graph G whose vertices are the points of S_p and whose

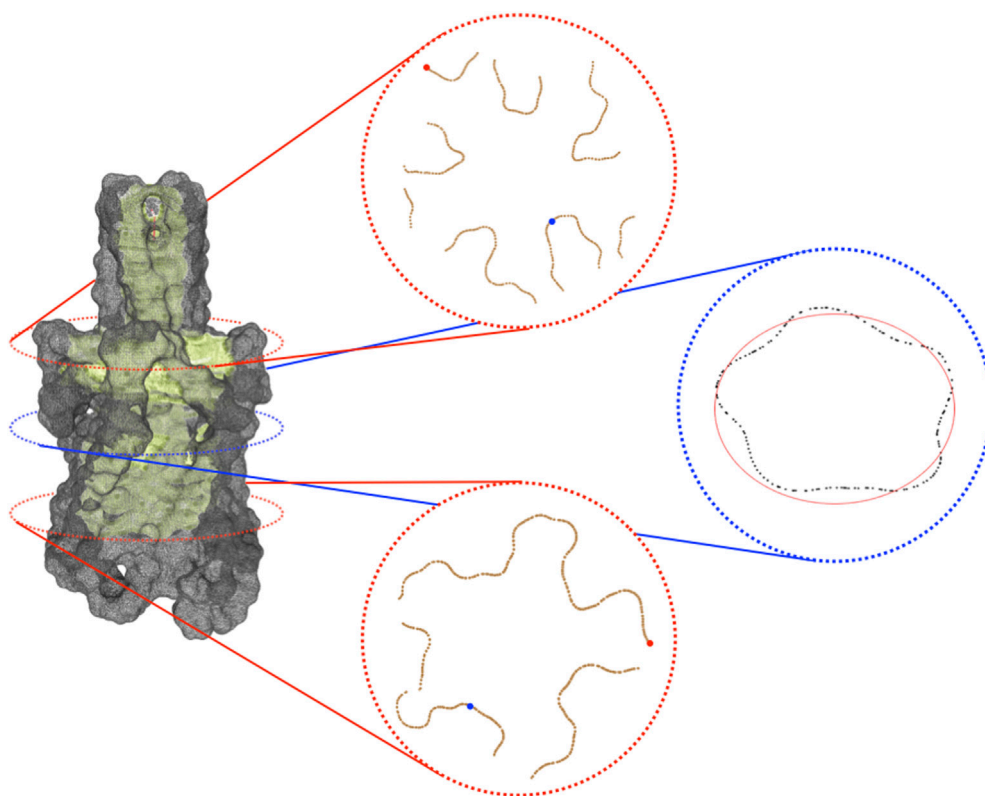


FIGURE 2 | Visible contour of a channel. On the left, is the visible contour of the channel (in light green) and the molecular surface (in grey). On the right, three sections of the visible contour: on the top, the section coinciding with the bifurcation of the skeleton; in the middle, the central section of the channel; at the bottom, a section clearly revealing the pentalobated nature of the channel. In each section, we spotlight some of the geometric features provided by the proposed approach. Specifically, in the top and in the bottom sections, the closest and the farthest points to the centerline are represented in blue and red, respectively. In the middle section, the ellipse (depicted in red) that best fits it is shown. Its knowledge allows retrieving further information about the local channel shape, such as its eccentricity.

edges consist of the pairs of points of S_p closer than a given threshold. Given a ray r , we select, among the points of S_p close to r , the one which is the closest to p and then we return the connected components of G containing such a vertex. The collection of connected components retrieved by varying the ray will represent a suitable pruning of section S_p and a good candidate for representing the contour of the channel at the level of p . The knowledge of the sections of the channel contour opens various possibilities for visualizing and analyzing the shape of the channel itself. Finally, in **Figure 1E** we depict the centerline obtained with VMTK along with some channel sections. For instance, for each point p of the centerline, it is possible to evaluate the closest and the farthest points of the contour section (and the corresponding distances) to p as well as evaluate the symmetry, the radius, and the shape of the various contour sections (see **Figure 2**), for instance fitting a contour section with an elliptical template using the Hough transform (Romanengo et al., 2019).

2.2.4 From Individual Structures to Trajectory Analysis

In **Sections 2.2.2** and **2.2.3** we described how to analyze an individual structure. This procedure can be fruitfully extended to

many frames extracted from an MD trajectory, taking advantage of the fact that the displacement of the molecule between two consecutive frames is limited. Therefore, we perform the full procedure of skeleton identification only on the first frame. Then, for the $(i + 1)$ -th frame, we use an initial guess regions for the entrances the borders of the surface closest to the channel's entrances frame i . If we notice a significant discrepancy between the centerlines of two consecutive frames, we reinitialize the procedure.

2.2.5 Computational Complexity

The theoretical computational costs for extracting the simplicial complex and identifying the connected components between which to identify the channel are both $O(n \log n)$ on the number of atoms considered. For the geometric characterization of the channel, the cost is: $O(t \log t + m \cdot s)$ for the identification of the channel surface where t is the number of vertices of the SES, m is the number of atoms of the channel, s is the number of vertices of the channel mesh; the skeleton costs $O(s^2)$, while the centerline and its characterization occur in $O(s \log s) + O(s \cdot r)$ operations where r is the number of points where we estimate the centerline.

The worst-case complexity of the skeleton pruning is $O(v \cdot e + v^2)$ where v and e are the number of vertices and edges of the skeleton, respectively.

The extraction of the visible contour of a channel for a point p of the centerline has worst-case complexity $O(s + d \cdot |S_p|)$ where d is the number of directions or rays on which the visibility is evaluated and $|S_p|$ is the number of points which the section of the channel surface orthogonal to the centerline at p consists of. For all the points of the centerline, the complexity of such a procedure is $O(s \cdot r + d \cdot |S| \cdot r)$ where r is the number of points of the centerline and $|S|$ is the maximum number of points composing a section. Assuming that the number of SES vertices of the protein goes as $O(n^2)$ and that the size of the channel is somehow limited, a rough estimate of the overall complexity is $O(n^2 \log(n))$.

2.3 Molecular Dynamics Simulations

The studied molecular systems are four variants of the engineered MscL channel, a pentameric protein channel, originally investigated in (Chandramouli et al., 2015) (PDB code 2OAR). Each variant differs from the others in the way residue 21 is functionalized among the five subunits. In this functionalization, a photo-activating ligand, namely the 6-nitroveratryl alcohol, which splits into 6-nitrosoveratryl aldehyde and a free acid upon light irradiation, was attached through a Cysteine-selective alkylating reagent to the residue 21 of each protein monomer (more details can be found in (Chandramouli et al., 2015)). Concerning the MD simulations, the adopted force field is CHARMM (v.27 (MacKerell et al., 1998)) for the protein and (v.36 (Klauda et al., 2010)) for the lipid. The parameters for the photo-activating ligand have been computed through QM calculations at the DFT level of theory. The water model is TIP3P, while the ionic concentration of K^+ and Cl^- is set to 1 M. Equilibration is carried out for about 10 ns in the NpT ensemble, followed by the production run according to the NVT ensemble under normal conditions ($T = 300$ K). For nonbonded interactions, a cutoff of 12 Å is used. All simulations are performed with periodic boundary conditions, treating the long-range electrostatic interactions with the Particle Mesh Ewald (PME) algorithm (Darden et al., 1993).

3 RESULTS

The Chanalyzer approach is applied to the analysis of the MscL system in order to compare the present analysis to the one originally carried out (Chandramouli et al., 2015). In that work, a variable number of modifications of the MscL channel was applied to generate corresponding molecular models by attaching a photo-activating ligand at residue 21 to the five monomers of the protein, as experimentally tested by Feringa and collaborators (Koçer et al., 2005). We focused on four of these functionalized systems, namely the NL, 1, 3, and 5L, having 0, 1, 3, and 5 photo-activating ligands, respectively. In the analysis reported in (Chandramouli et al., 2015), snapshots of the MD trajectory were superimposed and fed to the HOLE software (Smart et al., 1996) after removing the side chains, to measure the radius of the channel of the different generated models. This was

aimed at highlighting the symmetry breakage and at confirming the progressive engineered expansion of the channel radius with the sequential addition of negative charges upon photo-ligand removal. This effect is apparent in **Figure 3** where the computed average radii evaluated along the longitudinal channel axis (i.e., at different z values) by the present approach and by the HOLE software (Smart et al., 1996) are shown. Averages are performed over about 150 MD configurations for each considered system and a re-binning procedure is used along the z -axis. The agreement between Chanalyzer (solid lines) and HOLE (dashed lines) data is extremely good, with results basically indistinguishable in most regions and abundantly within the standard deviation in correspondence of local minima and saddle points. The observed systematic shift in pore radius (from 5L to NL) supports an increasing role of the residual charges, thus confirming the previously observed charge-mediated MscL gating (Birkner et al., 2012).

In two of the simulated systems, namely NL and 1L, potassium ion percolation was also observed. It is therefore interesting to compare how close are ion permeation paths to the centerlines of the corresponding MscL channels. Note, however, that ion translocation pathways can be affected by local and specific steric or electrostatic effects induced by residue side chains, not accounted for in our evaluation of the centerline which is based only on backbone atoms. In **Figure 4**, the centerlines, as returned by Chanalyzer, and the average trajectories followed by the K^+ ions in the NL and 1L systems are depicted. In the latter case, the average is carried over the multiple MD configurations and a re-binning is performed along the z -axis. The general trend is that in those locations where the radius is smaller, as expected, ions are more constrained towards the centerline. However, around $z = 10$ Å the ions tend to be more displaced towards the channel walls as compared to other locations with similar radii. This is likely a consequence of the net electrostatic attraction of the charged residues, upon photo-ligand removal. Interestingly, this suggests that a systematic comparison between centerlines and ion trajectories could be used as an indirect way to probe the local interactions between ions and residues along the channel and can be helpful in suggesting preferential mechanisms affecting translocation.

4 DISCUSSION

We presented here the application of the Chanalyzer geometric approach to the analysis of the channel morphology and dynamics of four differently functionalized forms of the MscL system, as a test case. Computational geometry has been already exploited to study the details of molecular structures. For instance, cavities and tunnels arising at the molecular surface of a protein have been studied with the NanoShaper software (Decherchi et al., 2013; Decherchi and Rocchia, 2013). In the field of protein channels, a popular analysis tool is provided by the HOLE software (Smart et al., 1996), which finds the maximum radius of a sphere centered within the channel starting from a given point (provided by the user to be inside the channel), so as that it does not overlap with the van der Waals interior surface of the pore and makes that sphere proceed and adapt its size throughout

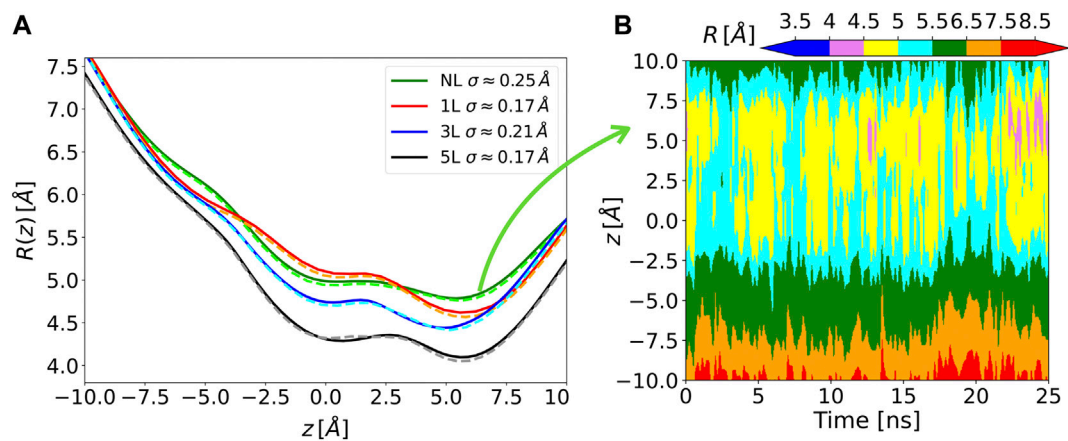


FIGURE 3 | (A) Solid lines, time-averaged channel radius along with the axial z position for each of the considered systems as obtained by Chanalyzer with associated SD (in the legend). Dashed lines, the same radius derived via the HOLE software. **(B)** Example of the dynamical behavior for the no-ligand system. The colormap is associated with the instantaneous value of the radius, as returned by Chanalyzer.

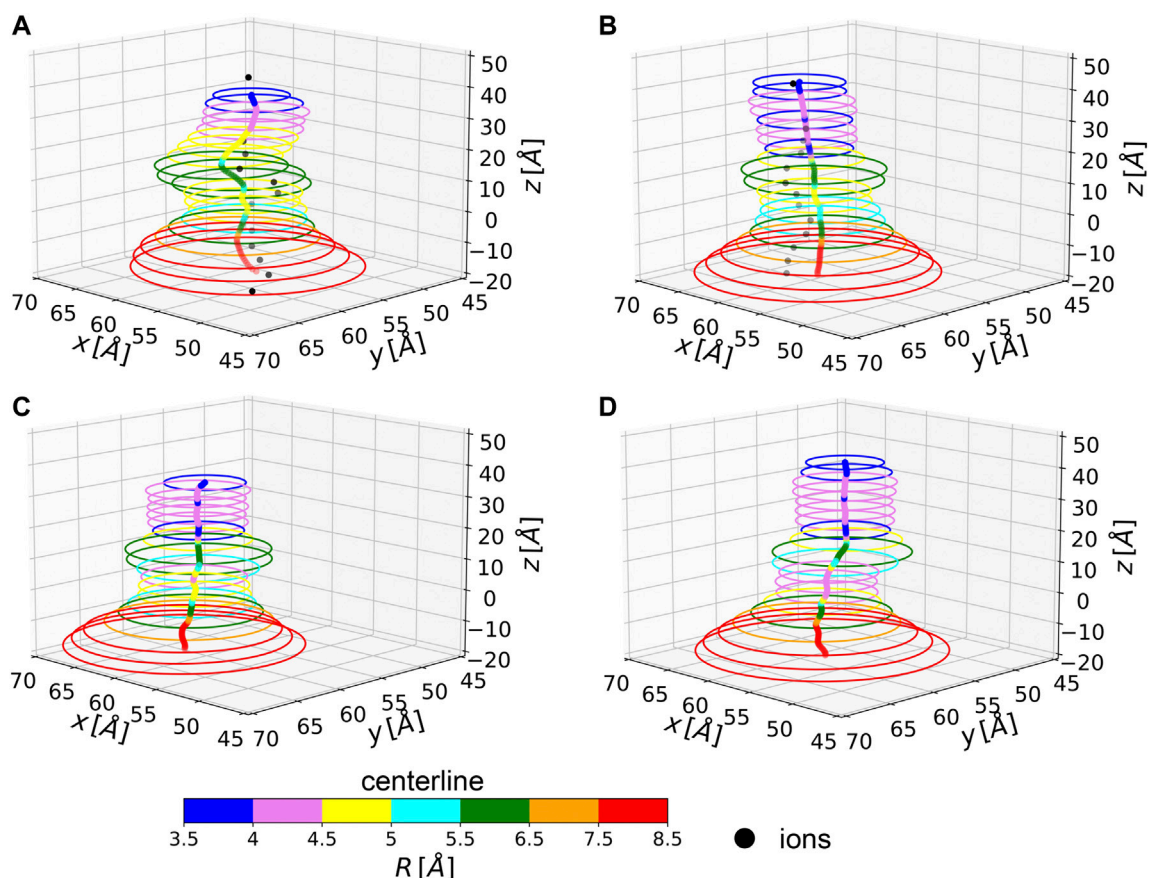


FIGURE 4 | Average centerlines. Colors code for the size of the associated radius. Black dots are average ion positions for the permeating configurations. From top to bottom and left to right: **(A)** NL, **(B)** 1L, **(C)** 3L, and **(D)** 5L.

the channel, assumed to be nearly rectilinear. Successively, two tools have been developed by the same group, namely CAVER (Petřek et al., 2006) and its improved version, MOLE (Petřek et al., 2007), to explore routes between protein clefts and cavities. CAVER's underlying algorithm is based on a skeleton search using a three-dimensional grid. Finally, MolAxis (Yaffe et al., 2008), a more recent tool also based on alpha shape theory, was successfully applied to the 5HT3 receptor (Di Maio et al., 2015) to identify lateral ion channels besides the central longitudinal one. However, MolAxis still strongly relies on user parametrization and can suffer from method-specific artifacts and approximations. While further improvements to the Chanalyzer project are still needed and its development is currently ongoing, it already sets up a framework that enables the accurate evaluation of several channel features that start from the purely geometric analysis but can easily integrate other relevant physico-chemical information, e.g. the chemical nature (i.e., atom identification) of the pore lumen as it inherits the properties of the SES calculated by NanoShaper. Remarkably, the fact that Chanalyzer does not need user-specific parameterization, such as a predetermined direction of the channel axis, does represent a clear advantage in the treatment of those cases where the geometrical shape is not predominantly tubular and may present bi- or multi-furcations, as well as ancillary pathways towards the surrounding lipid matrix. These so-called fenestrations may have relevant biological or biophysical implications still not well known (Jorgensen et al., 2016). For such reasons, we believe that biophysical modeling can significantly benefit from user-friendly and versatile geometric approaches, such as Chanalyzer.

DATA AVAILABILITY STATEMENT

The datasets presented in this study can be found in online repositories. The names of the repositories and accession numbers can be found on github at: <https://github.com/rea1991/Chanalyzer> and: <https://github.com/concept-lab/mpdb2xyzr.git> or on Zenodo with DOIs: 10.5281/zenodo.6610045 and 10.5281/zenodo.6509652.

REFERENCES

- Banghart, M. R., Volgraf, M., and Trauner, D. (2006). Engineering Light-Gated Ion Channels†. *Biochemistry* 45, 15129–15141. doi:10.1021/bi0618058
- Birkner, J. P., Poolman, B., and Koçer, A. (2012). Hydrophobic Gating of Mechanosensitive Channel of Large Conductance Evidenced by Single-Subunit Resolution. *Proc. Natl. Acad. Sci. U.S.A.* 109, 12944–12949. doi:10.1073/pnas.1205270109
- Chandramouli, B., Di Maio, D., Mancini, G., Barone, V., and Brancato, G. (2015). Breaking the Hydrophobicity of the MscL Pore: Insights into a Charge-Induced Gating Mechanism. *PLOS ONE* 10, e0120196–19. doi:10.1371/journal.pone.0120196
- Chandramouli, B., Bernacchioni, C., Di Maio, D., Turano, P., and Brancato, G. (2016). Electrostatic and Structural Bases of Fe²⁺ Translocation through Ferritin Channels. *J. Biol. Chem.* 291, 25617–25628. doi:10.1074/jbc.M116.748046
- Darden, T., York, D., and Pedersen, L. (1993). Particle Mesh Ewald: AnN-Log(N) Method for Ewald Sums in Large Systems. *J. Chem. Phys.* 98, 10089–10092. doi:10.1063/1.464397

AUTHOR CONTRIBUTIONS

WR and SB designed the overall approach; AR, UF, and SB designed and implemented the geometric procedure, processing the xyzr files to obtain the centerlines and the geometric properties of the channels. WR pre-processed the MD trajectories to obtain the xyzr for each trajectory frame. LG analyzed the results of the method along the trajectory, calculating the local radii with the results of HOLE and the ionic percolation paths. LS, SG, and GB chose the biological system, provided the MD trajectories, and performed the analysis with the HOLE program. All authors contributed to manuscript writing and revision and approved the submitted version.

FUNDING

This work was supported by internal funding of the various institutions.

ACKNOWLEDGMENTS

Many thanks are due to Michela Spagnuolo who encouraged the authors to embark on and persevere with this topic, believing in the work for a decade now. AR, SB, and UF thank Chiara Romanengo for the precious discussions and hints on channel geometric characterization. AR further thanks Daniela Bejan for the precious discussions on molecular surfaces and their representations.

SUPPLEMENTARY MATERIAL

The Supplementary Material for this article can be found online at: <https://www.frontiersin.org/articles/10.3389/fmolb.2022.933924/full#supplementary-material>

- Decherchi, S., Colmenares, J., Catalano, C. E., Spagnuolo, M., Alexov, E., and Rocchia, W. (2013). Between Algorithm and Model: Different Molecular Surface Definitions for the Poisson-Boltzmann Based Electrostatic Characterization of Biomolecules in Solution. *Commun. Comput. Phys.* 13, 61–89. doi:10.4208/cicp.050711.111111s
- Decherchi, S., and Rocchia, W. (2013). A General and Robust Ray-Casting-Based Algorithm for Triangulating Surfaces at the Nanoscale. *PLoS ONE* 8, e59744. doi:10.1371/journal.pone.0059744
- Decherchi, S., Spitaleri, A., Stone, J., and Rocchia, W. (2018). NanoShaper-VMD Interface: Computing and Visualizing Surfaces, Pockets and Channels in Molecular Systems. *Bioinformatics* 35, 1241–1243. doi:10.1093/bioinformatics/bty761
- Delaunay, B. (1934). Sur la sphere vide. A la me'moire de Georges Voronoi. *Izv. Akad. Nauk. SSSR, Otd. Mat. i Estestv. Nauk.* 7, 1–2.
- Di Maio, D., Chandramouli, B., and Brancato, G. (2015). Pathways and Barriers for Ion Translocation through the 5-HT_{3A} Receptor Channel. *PLoS ONE* 10, e0140258. doi:10.1371/journal.pone.0140258
- Edelsbrunner, H., Facello, M., and Liang, J. (1998). On the Definition and the Construction of Pockets in Macromolecules. *Discrete Appl. Math.* 88, 83–102. doi:10.1016/S0166-218X(98)00067-5

- Edelsbrunner, H., and Mücke, E. P. (1994). Three-dimensional Alpha Shapes. *ACM Trans. Graph.* 13, 43–72. doi:10.1145/174462.156635
- Humphrey, W., Dalke, A., and Schulten, K. (1996). VMD: Visual Molecular Dynamics. *J. Mol. Graph.* 14, 33–38. doi:10.1016/0263-7855(96)00018-5
- Jorgensen, C., Darré, L., Oakes, V., Torella, R., Pryde, D., and Domene, C. (2016). Lateral Fenestrations in K⁺-Channels Explored Using Molecular Dynamics Simulations. *Mol. Pharm.* 13, 2263–2273. doi:10.1021/acs.molpharmaceut.5b00942
- Kew, J., and Davies, C. (2009). *English Ion Channels: From Structure to Function*. 1 edition. Oxford; New York: Oxford University Press, 00000.
- Klauda, J. B., Venable, R. M., Freites, J. A., O'Connor, J. W., Tobias, D. J., Mondragon-Ramirez, C., et al. (2010). Update of the Charmm All-Atom Additive Force Field for Lipids: Validation on Six Lipid Types. *J. Phys. Chem. B* 114, 7830–7843. doi:10.1021/jp101759q
- Koçer, A., Walko, M., Meijberg, W., and Feringa, B. L. (2005). A Light-Actuated Nanovalve Derived from a Channel Protein. *Science* 309, 755–758. doi:10.1126/science.1114760
- Lemoine, D., Jiang, R., Taly, A., Chataigneau, T., Specht, A., and Grutter, T. (2012). Ligand-Gated Ion Channels: New Insights into Neurological Disorders and Ligand Recognition. *Chem. Rev.* 112, 6285–6318. doi:10.1021/cr3000829
- Liang, J., Woodward, C., and Edelsbrunner, H. (1998). Anatomy of Protein Pockets and Cavities: Measurement of Binding Site Geometry and Implications for Ligand Design. *Protein Sci.* 7, 1884–1897. doi:10.1002/pro.5560070905
- MacKerell, A. D., Bashford, D., Bellott, M., Dunbrack, R. L., Evanseck, J. D., Field, M. J., et al. (1998). All-atom Empirical Potential for Molecular Modeling and Dynamics Studies of Proteins. *J. Phys. Chem. B* 102, 3586–3616. doi:10.1021/jp973084f
- Petrík, M., Košinová, P., Koča, J., and Otyepka, M. (2007). Mole: A Voronoi Diagram-Based Explorer of Molecular Channels, Pores, and Tunnels. *Structure* 15, 1357–1363. doi:10.1016/j.str.2007.10.007
- Petrík, M., Otyepka, M., Banáš, P., Košinová, P., Koča, J., and Damborský, J. (2006). Caver: A New Tool to Explore Routes from Protein Clefts, Pockets and Cavities. *BMC Bioinforma.* 7. doi:10.1186/1471-2105-7-316
- Piccinelli, M., Veneziani, A., Steinman, D. A., Remuzzi, A., and Antiga, L. (2009). A Framework for Geometric Analysis of Vascular Structures: Application to Cerebral Aneurysms. *IEEE Trans. Med. Imaging* 28, 1141–1155. doi:10.1109/TMI.2009.2021652
- Raffo, A., Fugacci, U., and Biasotti, S. (2022). Chanalyzer: a Computational Geometry Approach for the Analysis of Protein Channel Shape and Dynamics. *Zenodo*. doi:10.5281/zenodo.6610045
- Romanengo, C., Biasotti, S., and Falcidieno, B. (2019). “HT-based Recognition of Patterns on 3D Shapes Using a Dictionary of Mathematical Curves,” in *Smart Tools and Apps for Graphics - Eurographics Italian Chapter Conference*. Editors M. Agus, M. Corsini, and R. Pintus (Reims, France: The Eurographics Association). doi:10.2312/stag.20191361
- Smart, O. S., Neduvilil, J. G., Wang, X., Wallace, B. A., and Sansom, M. S. P. (1996). Hole: A Program for the Analysis of the Pore Dimensions of Ion Channel Structural Models. *J. Mol. Graph.* 14, 354–360. doi:10.1016/S0263-7855(97)00009-X
- Spitaleri, A., Garoli, D., Schütte, M., Lehrach, H., Rocchia, W., and De Angelis, F. (2021). Adaptive Nanopores: A Bioinspired Label-free Approach for Protein Sequencing and Identification. *Nano Res.* 14, 328–333. doi:10.1007/s12274-020-3095-z
- Tagliasacchi, A., Alhashim, I., Olson, M., and Zhang, H. (2012). Mean Curvature Skeletons. *Comput. Graph. Forum* 31, 1735–1744. doi:10.1111/j.1467-8659.2012.03178.x
- The CGAL Project (2013). *CGAL User and Reference Manual*. 4.3 edn. CGAL Editorial Board. Available at: https://doc.cgal.org/4.3/Manual/how_to_cite_cgal.html
- Treptow, W., and Klein, M. L. (2012). Computer Simulations of Voltage-Gated Cation Channels. *J. Phys. Chem. Lett.* 3, 1017–1023. doi:10.1021/jz300089g
- Voronoi, G. (1908). Nouvelles applications des paramètres continus à la théorie des formes quadratiques. Premier mémoire. Sur quelques propriétés des formes quadratiques positives parfaites. *J. für die reine und angewandte Math. (Crelles J.* 1908, 97–102. doi:10.1515/crll.1908.133.97
- Yaffe, E., Fishelovitch, D., Wolfson, H. J., Halperin, D., and Nussinov, R. (2008). Molaxis: Efficient and Accurate Identification of Channels in Macromolecules. *Proteins* 73, 72–86. doi:10.1002/prot.22052

Conflict of Interest: The authors declare that the research was conducted in the absence of any commercial or financial relationships that could be construed as a potential conflict of interest.

Publisher's Note: All claims expressed in this article are solely those of the authors and do not necessarily represent those of their affiliated organizations, or those of the publisher, the editors, and the reviewers. Any product that may be evaluated in this article, or claim that may be made by its manufacturer, is not guaranteed or endorsed by the publisher.

Copyright © 2022 Raffo, Gagliardi, Fugacci, Sagresti, Grandinetti, Brancato, Biasotti and Rocchia. This is an open-access article distributed under the terms of the Creative Commons Attribution License (CC BY). The use, distribution or reproduction in other forums is permitted, provided the original author(s) and the copyright owner(s) are credited and that the original publication in this journal is cited, in accordance with accepted academic practice. No use, distribution or reproduction is permitted which does not comply with these terms.



OPEN ACCESS

EDITED BY

Matteo Masetti,
University of Bologna, Italy

REVIEWED BY

Giulio Alberini,
Fondazione Istituto Italiano di
Tecnologia, Italy
Melissa Alegría-Arcos,
Universidad de las Américas, Chile

*CORRESPONDENCE

Fatemeh Khalili-Araghi,
akhilili@uic.edu

SPECIALTY SECTION

This article was submitted to Biological
Modeling and Simulation,
a section of the journal
Frontiers in Molecular Biosciences

RECEIVED 09 June 2022

ACCEPTED 22 August 2022

PUBLISHED 28 September 2022

CITATION

Fuladi S, McGuinness S and
Khalili-Araghi F (2022), Role of TM3 in
claudin-15 strand flexibility: A molecular
dynamics study.
Front. Mol. Biosci. 9:964877.
doi: 10.3389/fmolb.2022.964877

COPYRIGHT

© 2022 Fuladi, McGuinness and Khalili-Araghi. This is an open-access article distributed under the terms of the [Creative Commons Attribution License \(CC BY\)](#). The use, distribution or reproduction in other forums is permitted, provided the original author(s) and the copyright owner(s) are credited and that the original publication in this journal is cited, in accordance with accepted academic practice. No use, distribution or reproduction is permitted which does not comply with these terms.

Role of TM3 in claudin-15 strand flexibility: A molecular dynamics study

Shadi Fuladi¹, Sarah McGuinness² and Fatemeh Khalili-Araghi^{1*}

¹Department of Physics, University of Illinois at Chicago, Chicago, IL, United States, ²Department of Bioengineering, University of Illinois at Chicago, Chicago, IL, United States

Claudins are cell-cell adhesion proteins within tight junctions that connect epithelial cells together. Claudins polymerize into a network of strand-like structures within the membrane of adjoining cells and create ion channels that control paracellular permeability to water and small molecules. Tight junction morphology and barrier function is tissue specific and regulated by claudin subtypes. Here, we present a molecular dynamics study of claudin-15 strands within lipid membranes and the role of a single-point mutation (A134P) on the third transmembrane helix (TM3) of claudin-15 in determining the morphology of the strand. Our results indicate that the A134P mutation significantly affects the lateral flexibility of the strands, increasing the persistence length of claudin-15 strands by a factor of three. Analyses of claudin-claudin contact in our μ second-long trajectories show that the mutation does not alter the intermolecular contacts (interfaces) between claudins. However, the dynamics and frequency of interfacial contacts are significantly affected. The A134P mutation introduces a kink in TM3 of claudin-15 similar to the one observed in claudin-3 crystal structure. The kink on TM3 skews the rotational flexibility of the claudins in the strands and limits their fluctuation in one direction. This asymmetric movement in the context of the double rows reduces the lateral flexibility of the strand and leads to higher persistence lengths of the mutant.

KEYWORDS

tight junctions (TJ), claudin-15, ion channels, molecular dynamics, molecular mechanics

Introduction

Tight junctions (TJs) are macromolecular structures that connect the apical surface of epithelial cells. In freeze-fracture electron microscopy, they appear as a network of linear strands in the cell membrane (Farquhar and Palade 1963; Goodenough and Revel 1970; Claude and Goodenough 1973; Staehelin 1973), and form a barrier to control transport of small molecules across epithelia (Fromter and Diamond 1972; Staehelin 1974; Claude 1978; Van Itallie and Anderson 2006). Disruption of TJ and their barrier function can lead to numerous diseases pertaining to liquid retention in tissues (Clayburgh et al., 2004; Shen et al., 2011). As key components of tight junctions, claudins polymerize into strands which regulate paracellular permeability across epithelial tissue layers (Van Itallie and Anderson

2006; Mineta et al., 2011; Yamazaki et al., 2011; Günzel and Yu 2013; Tamura and Tsukita 2014; Milatz et al., 2017). So far, 27 members (subtypes) of the claudin family are identified in mammals (Mineta et al., 2011). Claudin subtypes express subtype-specific functional differences as well as subtype-specific strand morphology, and can even assemble into heterogeneous strands with other subtypes (Inai et al., 2010; Milatz et al., 2010; Tamura and Tsukita 2014). Although the mechanism of assembly is still a mystery, our understanding of claudin strand assembly has improved by the structural insights revealed by recent crystallographic structures (Suzuki et al., 2014; Saitoh et al., 2015; Shinoda et al., 2016; Nakamura et al., 2019), and the functional models derived for claudin channels (Furuse and Tsukita 1999; Rossa et al., 2014a; Suzuki et al., 2015; Milatz et al., 2017; Alberini et al., 2018; Samanta et al., 2018).

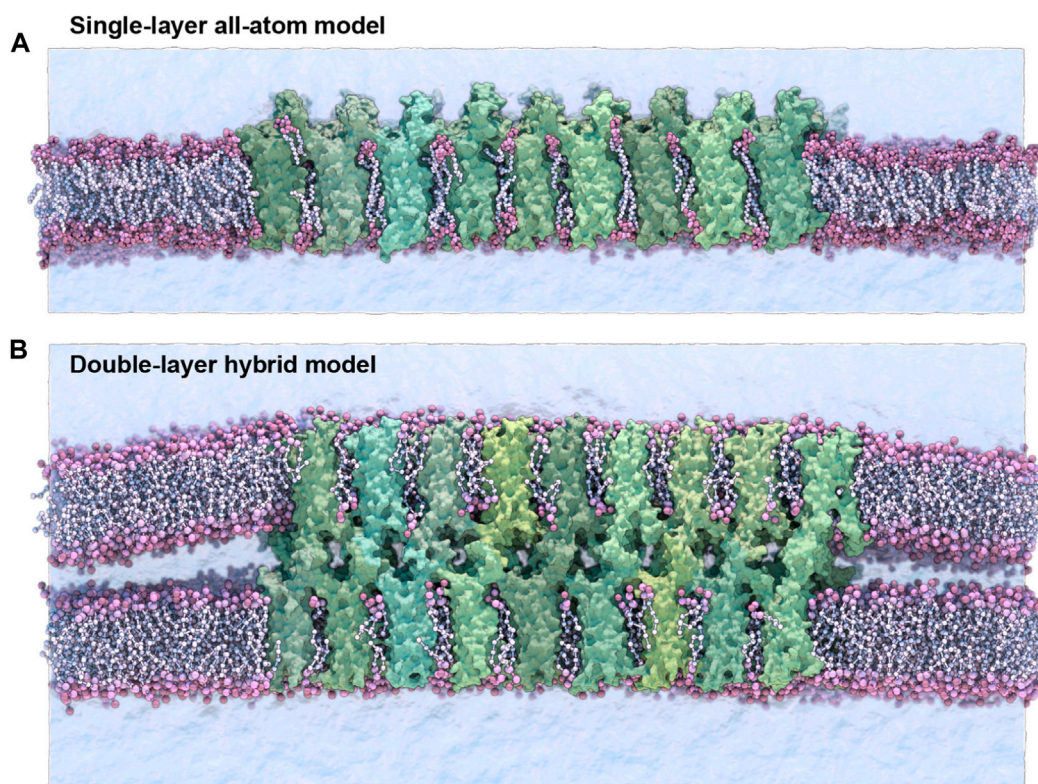
Claudins are tetra-span membrane proteins with two extracellular segments, ECS1 and ECS2, which form a five-strand β -sheet close to the surface of the membrane (Suzuki et al., 2015, 2014; Shinoda et al., 2016; Nakamura et al., 2019; Vecchio and Stroud 2019). Claudin strands in TJs are formed by *cis*-interactions between monomers in the same membrane and *trans*-interactions between extracellular segments of monomers between two cells (Piontek et al., 2008; Krause et al., 2015; Piontek et al., 2017; Tsukita et al., 2019; Piontek et al., 2020). One of the models for claudin strand polymerization, inspired by the crystallographic structure of mouse claudin-15 and cysteine cross-linking experiments, proposed that claudins assemble into an anti-parallel double row within the membrane which is then attached to a similar structure on an adjacent cell (Suzuki et al., 2015). This architecture of claudin strands originally proposed by Suzuki et al. (Suzuki et al., 2015) was later verified by molecular dynamics (MD) simulations and docking studies of claudin-15 to generate plausible architectures of claudin strands, including evidence for cation-selective claudin pore transport (Alberini et al., 2018, 2017; Irudayanathan et al., 2018; Samanta et al., 2018; Zhao et al., 2018).

In this model, the *cis*-interactions involve side-by-side interactions of claudins at the extracellular side involving the third transmembrane helix TM3, ECS2 and a short extracellular helix ECH that is parallel to the membrane (Piontek et al., 2008; Krause et al., 2015; Suzuki et al., 2015; Piontek et al., 2017; Alberini et al., 2018; Samanta et al., 2018). Critical to the proposed architecture is another set of *cis*-interactions between two anti-parallel rows of claudins in the membrane leading to “face-to-face” dimerization of β -sheets to generate the pipe-like structure of claudin pores (Suzuki et al., 2015). Studies of claudin strands in fibroblasts show that claudin strands are dynamic with the ability to arch, bend, and form new branches through remodeling (Sasaki et al., 2003; Van Itallie et al., 2017; Zhao et al., 2018). However, the molecular basis for claudin strand branching, bending, and remodeling remains unaccounted for in this model (Suzuki et al., 2015).

We recently developed a mechanistic model that describes the molecular nature of strand flexibility within this context (Fuladi et al., 2021). In our model, claudins form interlocking tetrameric ion channels that slide with respect to each other to accommodate local curvature of the strand without loss of function. Simulations of claudin-15 strands at large scale showed that this movement is facilitated by flexible side-by-side *cis*-interactions that allow rotation and displacement of claudin monomers with respect to each within the membrane (Fuladi et al., 2021).

Recent crystallographic structures of claudin-3 and two of its mutants P134A and P134G suggests that *cis*-interactions between claudins is indirectly affected by a single mutation at position 134 on the third transmembrane helix (TM3) of claudin-3 (Nakamura et al., 2019). In members of the mammalian claudin family, this position is mainly occupied by glycine, proline (as in claudin-3), or alanine (as in claudin-15). With a protein structure very similar to claudin-15, TJ strands formed by claudin-3 showed a distinct morphology with sparsely distributed almost linear strands. On the other hand, the TJ strands formed by two claudin-3 mutants, P134A and P134G, appeared to be highly flexible with many hairpin curves similar to those formed by claudin-15. Structural comparison of wild-type (WT) claudin-3 with its mutants indicates that the proline residue at position 134 bends the third transmembrane helix (TM3) toward the membrane pulling the entire extracellular domain toward the membrane by approximately 8°. Intriguingly, mutations of P134 to a glycine or alanine recovered the highly flexible TJ morphology with many hairpin curves, similar to the TJs formed by claudin-15. It was therefore suggested that the kink in the secondary structure of TM3 might limit the mobility of claudins in the strand by indirectly stabilizing the *cis*-interactions between them (Nakamura et al., 2019). However, this remains to be seen in claudin-15.

Here, we present a molecular dynamics (MD) study of claudin-15 strands in lipid membranes and compare mechanical properties of wild-type (WT) and A134P mutant strands. We show that the A134P mutation significantly affects the lateral flexibility and the persistence length of the strands. Moreover, our analyses of the simulation trajectories and side-by-side *cis*-interactions between claudins reveal the molecular mechanism for the increased stiffness of the mutant strands. We used a combination of all-atom and hybrid resolution models for our simulations. The all-atom simulations were used as benchmarks and control simulations to establish the stability of the models and to identify inter-atomic interactions with more accuracy. On the other hand, the hybrid resolution models (Fuladi et al., 2021), while preserving the atomic nature of the protein, allowed us to study the dynamics of the strands at large scales (sub- μ m) and at long time scales required for persistence length calculations.

**FIGURE 1**

Single-layer and double-layer claudin-15 strands. **(A)** All-atom model of the single-layer claudin-15 strand in a single POPC lipid bilayer including 18 monomers (30 nm). **(B)** Double-layer claudin-15 strands embedded in two parallel POPC lipid bilayers represented at hybrid resolution with 36 monomers and 18 paracellular channels (30 nm). Additional systems of claudin-15 strands with 63 and 135 nm lengths were also simulated.

Materials and methods

System setup

Four sets of claudin-15 strand models were prepared for molecular dynamics (MD) simulations. Two systems of “single layer” claudin-15 strands corresponding to wild-type and the A134P mutant in a POPC lipid bilayer were constructed and simulated with atomic resolution. In addition, two sets of claudin-15 strands in a double membrane system were constructed for the wild-type (WT) and A134P mutant at various lengths (30–135 nm) and were simulated at hybrid resolution as described below (Figure 1).

The initial structure of wild-type (WT) claudin-15 strands were based on our refined model of claudin-15 channels with twelve monomers embedded in two parallel lipid membranes (Samanta et al., 2018). The “single-layer” models of claudin-15 in the POPC bilayer were constructed by selecting a single layer of claudin strands with their surrounding lipid bilayer in the refined model and replicating it three times along its length to build a 30 nm claudin-15 strand with 18 monomers (Figure 1A). Two patches of POPC lipid bilayers (20 nm × 10 nm) were added on

the two ends of the system to separate the system from its periodic images. The system was then solvated and neutralized with 150 mM of NaCl salt via the molecular visualization program VMD (Humphrey et al., 1996). The resulting system consists of 18 claudin-15 monomers, 2,043 lipid molecules, 183,888 water molecules, and 1,038 Na⁺ and Cl[−] ions in a 20 nm × 50 nm × 26 nm simulation box with a total of 877 K atoms. The A134P mutant system was prepared by mutating the alanine (A) at position 134 on the claudin-15 sequence to proline (P) in this model using the Mutator Plugin (version 1.5) of VMD (Humphrey et al., 1996).

The WT and the A134P mutant single-layer systems were simulated at all-atom resolution for 547 ns as described below. In the first step, the protein backbone and lipid head groups were restrained harmonically with a force constant of 2 kcal/mol.Å² and the lipid tails were equilibrated for 200 ps at constant volume and temperature. In the next step, the lipid head groups were released and the system was equilibrated at constant pressure for 2 ns, after which, the two extracellular loops of claudins (residues 33–44 of ECS1 and residues 148–155 of ECS2) were released to move freely while the rest of the protein backbone was gradually released by decreasing the force constant to 1.0, 0.75, 0.5, and

0.25 kcal/mol.Å² over 45 ns. After releasing all restraints, the system was equilibrated freely for 500 ns at constant pressure.

Two sets of claudin-15 strands corresponding to the WT and A13P mutant were prepared in a double-membrane system (here referred to as the “double-layer” systems). The initial structure of the double-layer systems was the refined model of claudin-15 channels with twelve monomers (3 claudin-15 channels) (Samanta et al., 2018), which was replicated along the strand to create 30 nm, 63 nm, and 135 nm-long strands. These systems consist of 36, 84, and 180 claudin monomers in two parallel POPC lipid membranes (Figure 1B). The ions in the equilibrated refined model of the three-channels system (150 mM NaCl) were replicated along with the protein and lipid bilayers to construct the three large systems. Four patches of 20 nm × 10 nm POPC lipid bilayers were added at the two ends of the system to separate the claudin strands from their periodic images. The three systems with 36, 84, and 180 claudins before adding water molecules consist of 640 K, 1.2 M and 2.2 M atoms. The corresponding A134P mutant systems for each strand were then generated in VMD Humphrey et al., 1996 by mutating the alanine (A) at position 134 to proline (P).

The six double-layer systems were then converted into hybrid-resolution models using the PACE forcefield Han et al., 2010; Wan et al., 2011; Han and Schulten 2012. PACE forcefield models lipids and solvents consistent with the MARTINI forcefield (Marrink et al., 2007), while proteins are represented by a united-atom (UA) model, where heavy atoms and polar hydrogens are explicitly represented. The conversion was performed using the python scripts provided by Han's laboratory at (<http://web.pkusz.edu.cn/han/>) to convert protein, lipids, and ions into the hybrid model. The resulting system was then solvated by adding MARTINI water molecules (Marrink et al., 2007). This was done using the VMD solvate plugin and by specifying the MARTINI forcefield. The hybrid model systems ranging from 20 nm × 50 nm × 26 nm to 20 nm × 150 nm × 26 nm consist of 192 K, 365 K, and 735 K particles.

The six double-layer systems were equilibrated for 1.125 μs following a process similar to the equilibration of the all-atom system. Briefly, by harmonically restraining the protein backbone and lipid head groups with a force constant of 2 kcal/mol.Å², the lipid tails were equilibrated for 200 ps at constant volume and temperature. The lipid head groups were then released and the systems were equilibrated for 2 ns at constant pressure and temperature. Finally, the two extracellular loops of claudins (residues 33–44 of ECS1 and residues 148–155 of ECS2) were released to move freely while the rest of the protein backbone was gradually released by decreasing the force constant to 1.0, 0.75, 0.5, and 0.25 kcal/mol.Å² over 70 ns. The equilibration process was performed with a time step of 2 fs. The simulations were then followed by 1.055 μs of simulation time at constant pressure, using a time step of 2 fs for the first 140 ns and a time step of 3 fs for the last 915 ns.

Molecular dynamics simulations

MD simulations were performed using the program NAMD (Phillips et al., 2005). All-atom simulations were carried out using CHARMM36 forcefield for proteins (MacKerell et al., 1998; MacKerell Jr et al., 2004; Best et al., 2012, ions Jorgensen et al., 1983), and phospholipids (Klauda et al., 2010) with the TIP3P water model (Jorgensen et al., 1983). These simulations were carried out with a time-step of 1 fs and assuming periodic boundary conditions. Langevin dynamics with a friction coefficient of $\gamma = 5 \text{ ps}^{-1}$ was used to keep the temperature constant at 333 K. The Langevin Nosé-Hoover method (Feller et al., 1995) was used to maintain the pressure at 1 atm in constant pressure simulations. Long-range electrostatic forces were calculated using the particle mesh Ewald method (Darden et al., 1993) with a grid spacing of at least 1 Å in each direction. The simulations used a time-step of 1, 2, and 4 fs for bonded, short-range nonbonded, and long-range electrostatic interactions calculations, respectively. A 1-4 rule is applied to the calculation of nonbonded interactions. Additional restraints were applied by enforcing a harmonic potential with a force constant of 2.0 kcal/mol.Å², unless otherwise stated.

The hybrid resolution PACE models were simulated assuming periodic boundary conditions and using a time-step of 2 fs or 3 fs. The dielectric constant is set to 15 as recommended for MARTINI simulations with non-polarizable water (Marrink et al., 2007). The electrostatic interactions are switched to zero between 9 Å and 12 Å, and the van der Waals interactions cutoff is set to 12 Å. Langevin dynamics with a friction coefficient of $\gamma = 5 \text{ ps}^{-1}$ was used to keep the temperature constant at 333 K. The Langevin Nosé-Hoover method (Feller et al., 1995) was used to maintain the pressure at 1 atm in constant pressure simulations. The hybrid-resolution PACE simulations were carried out with a special version of NAMD 2.9 in which this capability is implemented.

TM3 tilt and bending angle calculations

The tilt angle of the third transmembrane helix (TM3) in claudins is defined as the angle between the helical axis and the bilayer normal. The helical axis of TM3 in all-atom simulations of WT and A134P mutant was calculated using the HELANAL algorithm using the MDAnalysis library (Sugeta and Miyazawa 1967; Kumar and Bansal 1996, 1998; Bansal et al., 2000) and was averaged over the last 100 ns of the trajectories with a frequency of 60 ps. The bending angle of TM3 at position 134 is defined as the angle between the two vectors connecting A134/P134 to the two ends of the TM3 helix. The two points defining the endpoints of TM3 are residue 123 on the cytoplasmic side and residue 141 on the extracellular side of TM3. The position of Cα of these residues is used to calculate the bending angle, which is averaged over the last 100 ns of the trajectories with a frequency of 60 ps.

Curvature calculations

The local curvature of the strands in the plane of the membrane is calculated for the longest double-layer system (135 nm with 180 claudins) for the WT and the A134P mutant. The local curvature is estimated as the reciprocal of the radius of tangential circles fitted to the strands. For these calculations, claudin strands are projected into a two-dimensional polymer in the plane of the membrane. The center of mass of the each four pore-forming claudins constitutes a data point i marked as (x_i, y_i) . For the two 135 nm-strands, 44 data points are recorded. To determine the radius at each position i , a circle is fitted to the data points between $i-5, i+5$ (for $i = 6, \dots, 39$). The best fit is determined via least-square linear regression and the local radius r_i is used to calculate the curvature (r_i^{-1}). For each system, the last 600 ns of the simulation trajectories with a frequency of 60 ps are used for these calculations. Twelve data points from the ends of the strands were excluded from these calculations to exclude the effect of interaction of the strands with their images across the periodic boundaries.

Persistence length calculations

We calculated the persistence length (l_p) of claudin-15 strands from equilibrium MD simulation trajectories. We used the worm-like chain approximation (Gittes et al., 1993; Marko and Siggia 1995; Wiggins and Nelson 2006) to estimate the persistence length of the strands in the plane of membrane from thermal fluctuation in the strands. In these calculations, claudin strands are considered two-dimensional linear polymers in the plane of the membrane that are made of discrete segments. Each four pore-forming claudins are considered to be a segment located at position \vec{r}_i , where \vec{r}_i is the center of mass of the four claudins.

At each point on the strand \vec{r}_i , the tangent angle ϕ_i is determined as the angle corresponding to the tangent vector $\vec{\tau}_i = \frac{(\vec{r}_{i+1} - \vec{r}_{i-1})}{|\vec{r}_{i+1} - \vec{r}_{i-1}|}$. The persistence length is defined as the distance along the strand over which the tangent angles become uncorrelated. Assuming a discrete strand made of segments with length δs , the contour length between any two points i and j on the strand is estimated to be $s = |i - j|\delta s$. We defined the contour fragment δs to be the distance between two segments $\delta s_i = \frac{1}{2} (|\vec{r}_{i+1} - \vec{r}_i| + |\vec{r}_i - \vec{r}_{i-1}|)$ averaged over all segments during the simulation time; $\delta s = \langle \delta s_i \rangle$.

The persistence length l_p is then calculated as the length over which the correlation between the tangent angles defined as $\langle \cos(\phi(s) - \phi(0)) \rangle$ is dropped by a factor of e :

$$\langle \cos(\phi(s) - \phi(0)) \rangle = \exp\left(-\frac{s}{2l_p}\right) \quad (1)$$

The factor of two in the denominator is due to the two-dimensional nature of the strands. We calculated the persistence length for three WT strands and the three A134P strands in the double-layer systems

with lengths ranging from 30 to 135 nm. The last 600 ns of the simulations trajectories were used for this calculation with a frequency of 60 ps. The slope of the initial decay of the logarithm of the cosine correlation functions is used to calculate the persistence length. The number of points included in curve fitting is determined by an R-squared cut-off of 0.95.

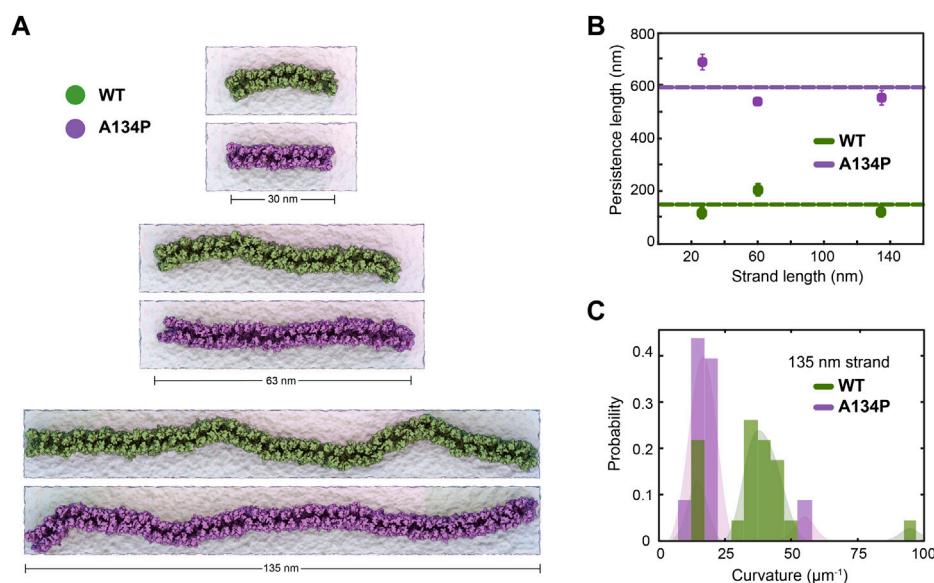
The calculations for the persistence length, curvature and the helical kink of TM3 were performed in VMD using in-house tcl scripts to extract the data and the analyses were performed in MATLAB. The scripts are available from: <https://biophys.lab.uic.edu/script-library/>

Results and discussion

In order to investigate the impact of TM3 structure on the flexibility of claudin-15 strands, we carried out MD simulations of the wild-type (WT) and A134P mutant claudin-15 strands in double- and single-layer membrane systems (Figure 1). These models of claudin strands were generated based on our previously refined structure of claudin-15 strands (Samanta et al., 2018; Fuladi et al., 2021) in accordance with the proposed architecture of Suzuki et al. (Suzuki et al., 2015). Eight systems of various lengths, ranging from 30 to 135 nm with 26–180 claudin monomers were studied. Due to the large size of the systems and the time scales required to capture the strand fluctuations ($\sim \mu$ seconds), we carried out the double-membrane strand simulations at a hybrid resolution using the PACE forcefield Han et al., 2010; Wan et al., 2011; Han and Schulten 2012. The PACE forcefield combines a united atom (UA) representation of proteins with a coarse-grained (CG) model of lipids and solvents to efficiently capture the dynamics of the strands at large scales (Han and Schulten 2014; Deeng et al., 2016; Jewel et al., 2017; Ward et al., 2017; Fuladi et al., 2021), allowing us to calculate the persistence length of the WT and mutant strands and compare their lateral flexibility. To assess the effect of A134P mutation on conformational changes of the protein and side-by-side *cis*-interactions between claudin monomers, the WT and A134P mutant strands were simulated at atomic resolution in a single lipid membrane. These simulations enabled us to compare the secondary structure of TM3 in WT and A134P mutant strands within a more realistic environment and to perform a more detailed analysis of the side-by-side (*cis*-) interactions between neighboring monomers.

Claudin-15 strand stability

We assessed the structural stability of claudin-15 strands in “single-layer” and “double-layer” membrane systems simulated at various lengths. The two single-layer systems of WT and A134P mutant were stable during the 500 ns simulations. The average root mean square deviation (RMSD) of claudin-15 backbones with respect to their initial structures was 3.0 ± 1.0 Å for the WT strand

**FIGURE 2**

TM3 bending restrict claudin-15 strand flexibility. (A) Equilibrated configuration of WT and A134P strands of various lengths simulated for 1 μ s in double parallel lipid bilayers and hybrid resolution, show the “curvy” morphology of claudin-15 strands as opposed to the more “straight” shapes of A134P mutant strands. (B) The strand persistence length is calculated for each length of WT and A134P claudin-15 strands. The horizontal lines show the average persistence length for WT and A134P mutant strands. (C) The distribution of local curvature along the length of the longest simulated strand (135 nm) is calculated for WT and A134P strands.

and 2.8 ± 0.5 Å for the mutant strand. Interestingly, claudin monomers were slightly more stable in the mutant strand. The RMSD of claudin pairs with respect to their initial conformation, an indication of the stability of the side-by-side interactions, was also comparable for the WT and mutant strands (3.2 ± 0.6 Å for the WT and 3.0 ± 0.3 Å for the mutant backbones).

The double-layer systems simulated at hybrid resolution were stable during the 1 μ s simulation trajectories with an average RMSD of 4.3 ± 0.1 Å for the WT and 4.4 ± 0.1 Å for the mutant strands with respect to the initial structure. The protein stability is comparable in all-atom and the hybrid-resolution models. We have previously reported a detailed comparison of structural properties of claudin strands in hybrid-resolution and atomic simulations showing similar stabilities of two models (Fuladi et al., 2021). In the double membrane systems, the tetrameric claudin channels formed between the two membranes were also stable with an average RMSD of 6.7 ± 0.3 Å for the WT and 6.6 ± 0.2 Å for the mutant strand backbone with respect to the initial structures.

A134P mutation reduces lateral flexibility of claudin-15 strands

The A134P mutant is expected to affect the two-dimensional rigidity of claudin strands in the membrane (Nakamura et al., 2019). We calculated the persistence length of claudin strands in

the double-layer systems and compared it between the WT and mutant strands. The persistence length (l_p) is an indication of lateral flexibility of the strands in the plane of membrane and is directly related to their bending rigidity as well as the temperature (Fuladi et al., 2021). The persistence length was calculated for the six double-layer systems of WT and A134P mutant with lengths ranging from 30 to 135 nm. The calculations are similar to our previous work (Fuladi et al., 2021), and are briefly described in the Methods section. In summary, l_p is calculated as the distance over which the direction of the strand becomes uncorrelated and is estimated from exponential decays of the correlation function of tangent vectors over the length of the strand. We calculated the persistence length from thermal fluctuations of the strand in equilibrium simulations over μ -long trajectories (Figures 2A,B). The persistence length of the WT strands was 150.0 nm with a standard deviation of 48.9 nm across the three systems, while the A134P mutant strands had an average persistence length of 590.2 nm with a standard deviation of 79.3 nm. The WT persistence length is consistent with our previously reported values for claudin-15 (~ 174 nm) (Fuladi et al., 2021), and falls within experimentally estimated values of claudin-15 (Zhao et al., 2018). The only experimental measurement of the persistence length in claudin-15 is from analyses of local curvature of the strands in freeze-fracture electron microscopy of the WT claudin-15 by Zhao et al. (Zhao et al., 2018) with a relatively large error bar (191 ± 184 nm).

The larger persistence length of the A134P mutant strands in comparison to the WT claudin-15 strands (~ 3.5 fold) indicates that the A134P mutants are less flexible with a relatively high bending modulus. The bending rigidity of the strands, and thus, their persistence length is directly related to the average curvature of the strands over time (Fuladi et al., 2021). We calculated the average curvature of the strands over time for the longest (135 nm-long) strand simulated here for the WT and the A134P mutant (Figure 2C). The average local curvature of the WT strand is approximately $36.5 \mu\text{m}^{-1}$, while the local curvature of the A134P strand is significantly lower with a sharper distribution averaged at $19.8 \mu\text{m}^{-1}$. The ~ 3.5 fold increase of the persistence length in the A134P mutant in our simulations is consistent with the lower curvature of the mutant strands in comparison to the WT strands (Figures 2B,C) and indicates that the mutation significantly reduces the lateral flexibility of claudin-15 strands.

The A134P mutant is similar structurally to claudin-3, which is shown to have a distinct architecture with straight strands (Nakamura et al., 2019). Interestingly, mutation of P134 in claudin-3 to an alanine (A), as in claudin-15, reproduces the signature curvature of claudin-15 strand morphology (Nakamura et al., 2019). However, this site of interest had not yet been investigated in claudin-15. These simulations indicate that claudin-15 significantly decreases bending flexibility of the strands similar to those observed in freeze-fracture electron microscopy of claudin-3 (Nakamura et al., 2019), suggesting that residue 134 plays a key role in lateral flexibility of the strands. However, we can not yet rule out the role of other transmembrane residues in claudin assembly (Rossa et al., 2014a) and their contribution to strand flexibility.

As we showed in our previous work, claudin-15 strand flexibility is mostly attributed to flexible *cis*-interfaces between neighboring claudins (Fuladi et al., 2021). In particular, we showed that there are three sets of side-by-side *cis*-interaction between claudins pivoted at the extracellular helix (ECH), which confer flexibility to the strands. Residues 143–147 located on the extracellular end of TM3 play a key role in defining one set of these interfacial interactions. Mutation of P134 of TM3 in claudin-3 is shown to affect the secondary structure of TM3, and thus, it is not surprising that it affects the strand flexibility. To understand the molecular mechanism of strand flexibility and the effect of A134 mutation on the interfacial interactions, we investigated the secondary structure of TM3 in the all-atom simulations of WT and A13P mutant claudin-15 strands and analyzed the frequency of side-by-side *cis*-interactions and its implications on strand flexibility.

A134P mutation results in TM3 bending

TM3 is the longest transmembrane helix in claudin-15 with 36 residues and extends beyond the membrane into extracellular solution (Figure 3A). In claudin-15, A134 is located in the middle

of TM3 near the extracellular lipid-water interface. A proline at the position of this residue is expected to create a bend in the TM3 helix as observed in the crystal structure of claudin-3 (Nakamura et al., 2019) and claudin-4 (Shinoda et al., 2016) and transmembrane helices of other membrane proteins (von Heijne 1991; Cordes et al., 2002). This is while the structures of claudin-15 Suzuki et al., 2014 and claudin-19 (Saitoh et al., 2015) with alanine at this position, and P134A/G claudin-3 mutants (Nakamura et al., 2019) show a relatively straight conformation of the TM3 helix.

Simulation trajectories of claudin-15 strands in a single membrane indicate that, in the WT strand, TM3 is helical with a helical axis that is tilted by $8.3^\circ \pm 2.2^\circ$ with respect to the membrane normal. Upon mutation of A134P, while the tilt angle of the helix does not change in the membrane, the mutation results in bending of the helix at position 134, where the extracellular end of the helix bends toward the membrane. The average bending angle of TM3 changes from $168.4^\circ \pm 3.5^\circ$ in WT claudin-15– $162.5^\circ \pm 3.5^\circ$ in A134P mutant (Figures 3A,B). The shift in the bending angle of claudin-15 after A134P mutation ($\sim 6^\circ$ difference) is comparable to the difference observed between WT and P134A/G mutants claudin-3 ($\sim 8^\circ$ difference) (Nakamura et al., 2019).

Superposition of the WT and A134P monomers shows that in the A134P mutant, the extracellular domains including, ECS1 with five β -strands, the loop between β_1 and β_2 , and the extracellular helix (ECH), and ECS2 are inclined toward the membrane in the direction of the TM3 bending (Figure 3A). Simulation and analyses of the extracellular domain of claudins indicate that these domains are relatively rigid and form the backbone of paracellular pores (Alberini et al., 2018; Samanta et al., 2018). In claudin-15, the extracellular domains are directly connected to TM3 by residues 150–154 of the ECS2 loop. The conformation of ECS2 is stabilized by salt bridge between K155 and N148 (Figure 3D), as identified in the crystal structure and MD simulations of claudin-15 (Suzuki et al., 2014; Samanta et al., 2018) and homology models of claudin-5 (Piontek et al., 2008). This interaction was conserved in $\sim 83\%$ of the simulation time in A134P mutant strand monomers and in $\sim 86\%$ of the time in WT strand monomers.

Another key interaction for stabilizing the structure of extracellular domain in claudin-15 is between the sidechain of an extended arginine R79 on TM2 and the backbone of F65 on ECH and L58 on the β -sheets (Figure 3E). This interaction which was observed in the crystal structure of claudin-15 (Suzuki et al., 2014) is important in stabilizing the extracellular β -sheets and keeping the short extracellular helix ECH in place, i.e. parallel to the membrane and perpendicular to TM2. This set of interactions was maintained for 97% of the simulation time in A134P mutant monomers and 85.5% in WT monomers. It is through these robust interactions that the extracellular domains maintain a rigid conformation that is critical for the tetrameric assembly of claudins into paracellular pores.

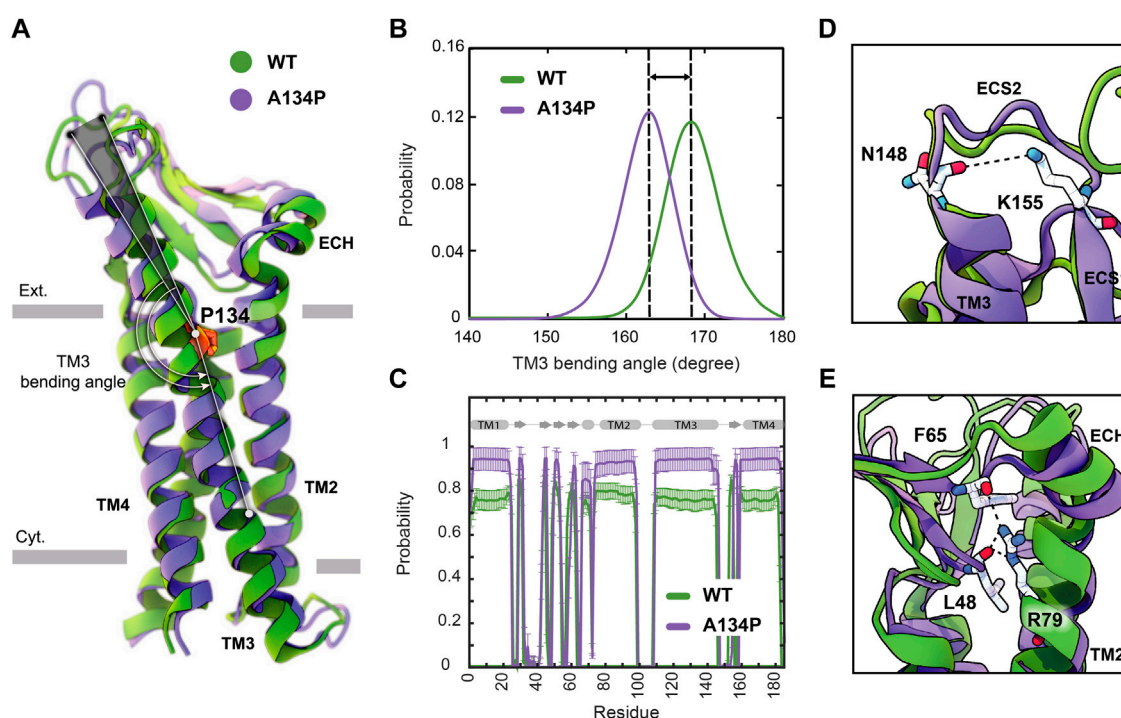


FIGURE 3

A134P mutation results in the bending of TM3. (A) Superposition of WT and A134P mutant claudin-15 monomers exhibits the bent structure of TM3 after A134P mutation. Gray bars suggest boundaries of the outer (Ext.) and inner (Cyt.) leaflets of the lipid bilayer. (B) TM3 bending angle for the WT and A134P mutant monomers is calculated over the last 100 ns of the simulation trajectories of single-layer strands. (C) The secondary structure of helices and β -strands in WT and A134P monomers show structural stability of the monomers over the last 250 ns of simulation time. Key interactions within each monomer, in the form of (D) a salt bridge between N148 and K155 stabilizes the structure of ECS2, and (E) interactions between the backbone of F65 and L48 β -strands and side chain of R79 on TM2 stabilize the β -sheets and orientation of ECH. These interactions are maintained in mutant monomers (shown in purple) similar to WT monomers (shown in green).

Despite the bent structure of TM3 and the shift in extracellular domains positioning, the overall secondary structure of mutant monomers was maintained 91.6% of the simulation time for helices and 75.9% for β -strands in A134P mutant monomers, compared with 83.8% and 78.3% for the WT monomers (Figure 3C). As indicated by these results, mutant monomers are more stable and rigid in their structures compared with WT monomers. The rigidity of the structure of mutant monomers is projected into mutant strands dynamics, with lower fluctuations in their shapes and minimal deviations of monomers from the straight arrangement. To explain the effect of bent TM3 and the rigidity in mutant monomers on strands flexibility further, we explored the flexibility of *cis*-interactions in WT and mutant monomers.

Effect of TM3 bending on *cis*-interactions

The linear arrangement of claudins in a row in the membrane is maintained through two sets of *cis*-interactions; a set of side-by-side *cis*-interactions as observed in the crystal structure of claudin-15 (Suzuki et al., 2014), as well as a set of “face-to-face” *cis*-interactions between two anti-parallel claudin rows originally

proposed by Suzuki et al. (Suzuki et al., 2015). TM3 is one of the main contact points between neighboring claudins. Residues 146 and 147 on the extracellular end of TM3 are critical for side-by-side *cis*-interactions and strand formation (Piontek et al., 2008, 2011; Suzuki et al., 2014; Samanta et al., 2018).

We have recently proposed a model for claudin strand flexibility, in which the lateral flexibility of the strands is attributed to flexible side-by-side interactions between claudin monomers (Fuladi et al., 2021). In this model, claudin-15 monomers move as tetrameric units within the strands. In this movement tetrameric units forming ion channels slide with respect to each other to adjust to the local curvature of strands imposed by external restraints. Those simulations revealed three dominant side-by-side interfaces pivoted at the extracellular helix ECH (residues 66–71) as claudins monomers rotate/slide with respect to each other within the strand. Interactions between ECH (S68) and the extracellular end of TM3 (F146) (Figure 4A) are one of the three interfacial interactions and are dominant at zero or positive (outward) curvatures of the strands. The second set of interactions is between ECH (S67) and ECS2 (E157) (Figure 4A) that are again mostly present at zero or positive curvatures of the

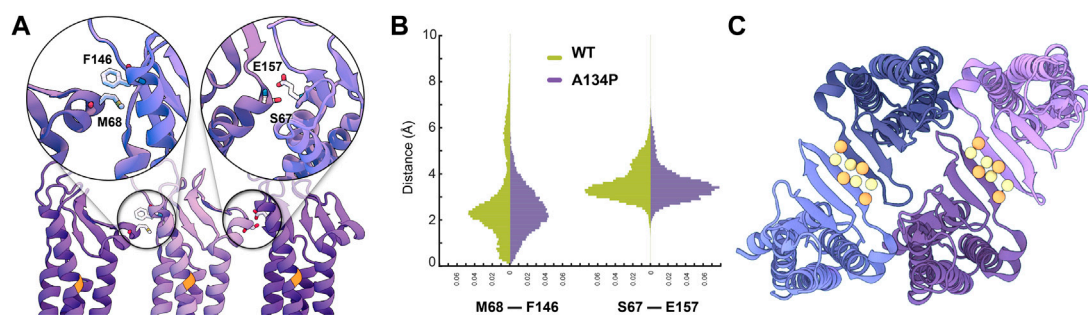


FIGURE 4

Side-by-side *cis*-interactions between WT and A134P claudin-15 strands. **(A)** A snapshot of three claudin-15 monomers in the single-layer strands after 500 ns of simulation in all-atom resolution highlighting two sets of side-by-side *cis*-interactions. **(B)** Pair-wise distance distribution of M68 (ECH)–F146 (TM3) and S67 (ECH)–E157 (ECS2) in the all-atom simulation of the single-layer WT and A134P mutant claudin-15 strands. The extended tail of the distribution in the case of WT suggests more flexible side-by-side interactions in the WT compared to the A134P mutant. **(C)** “Face-to-face” interactions between claudins are maintained through hydrogen bonds between the backbone of the β -sheets of claudins. These interactions are maintained throughout the simulation of both WT and mutant strands. The position of C_{α} of residues involved in hydrogen-bonding is highlighted as spheres.

strands (Fuladi et al., 2021). At negative (inward) curvatures, both of these interaction sets are weakened and are replaced by interactions between ECH and ECS1.

Analyses of our all-atom simulation trajectories indicate that both ECH-TM3 and ECH-ECS2 interacting interfaces are present in the WT and A134P claudin-15 strands (Figure 4B). However, the distribution of the pair-wise distances between the residues involved in these two sets differs between the WT and A134P mutant. The extended distribution of pair-wise distances (up to 10 Å) in the WT claudin-15 strand indicates loose interactions between neighboring monomers and a more flexible *cis*-interface. The extended tail of the distribution corresponds to instances in which these interactions are replaced with those involving ECH and ECS1 dominant at negative (inward) curvatures. In contrast, the sharp distance distribution of pairwise distances (up to 6 Å) in the A134P mutant indicates tight interactions and therefore a more rigid configuration for the strands. In the WT trajectories, the TM3-ECH interface represented here by M68-F146 interaction is only present in ~82% of the simulation time, while the same interaction is maintained for ~95% of the simulation time in the A134P mutant. The TM3-ECH interactions are mostly present at zero (straight) or positive (outward) curvatures and are expected to vanish at negative (inward) curvatures (Fuladi et al., 2021). Similarly, the interactions between ECH and ECS2 (S67 and E157) is less maintained in the WT compared to the mutant. Both of these interactions are dominant in the straight configuration of A134P mutant consistent with our previous results (Fuladi et al., 2021), however, the configurations dominant at negatively curved strands corresponding to the extended tail of ECH-TM3 distance distribution are only present in the WT strand. This indicates that mutation of A134P in TM3 strengthens the interactions between TM3 and ECH, and limits its replacement with alternative interactions including ECS1. Thus, these simulations provide the molecular basis of the increased

persistence length and decreased flexibility of claudin-15 strand upon A134P mutation.

While side-by-side *cis*-interactions demonstrated variations between the WT and A134P mutant strands, other inter-molecular interactions were well-maintained. The face-to-face interactions formed between the claudins in opposing rows of the same membrane were not affected by the A134P mutation. The antiparallel double-row arrangement of claudins in a single lipid membrane is stabilized through hydrogen bonds between two β 4 strands of neighboring claudins (Figure 4C). The average distance between the β -strands of claudins over the last 15 ns of the simulation was comparable for the WT (3.34 ± 1.52 Å) and mutant (2.83 ± 0.03 Å) systems, indicating that face-to-face interactions were not affected by the TM3 bending in A134P mutant strands.

These simulations corroborate the results of the double-layer systems by indicating that the A134P mutation reduces the lateral flexibility of claudin-15 strands. The broader range of *cis*-interfaces observed in WT strands allowed interacting monomers in the same membrane to rotate relative to their neighboring monomer, resulting in higher curvature of the WT strands. Conversely, the *cis*-interfaces became rigid due to a bent TM3 in A134P mutant claudins, which explains the lower flexibility of the A134P mutant and the more straight shape of tight junction strands in claudin-3 (Nakamura et al., 2019). A tight *cis*-interface limits relative movement of claudins and inhibits bending of the strands (to negative curvatures).

Conclusion

We investigated mechanical flexibility of claudin-15 strands and the effect of a single point mutation A134P on lateral

flexibility of the strands. The A134 residue is located on the third transmembrane helix (TM3) of claudin-15 and is not directly involved in claudin-claudin interactions. However, it was recently suggested that the distinct morphology of tight junctions formed with claudin-3 is due to a proline at this position, and mutation of P134 to an alanine (A) in claudin-3 resulted in strands similar to claudin-15 (Nakamura et al., 2019). Here, we investigated the reverse effect in claudin-15, i.e. mutation of A134 to proline (P) in claudin-15 via MD simulations. Our results reveal that the A134P mutation increases the persistence length of claudin-15 by more than 3x, consistent with the comparatively straight shape of claudin-3 strands (Nakamura et al., 2019).

Our results indicate that the A134P mutation does not establish any new contacts between neighboring claudins nor does it eliminate any of the previously reported contacts (Suzuki et al., 2014; Fuladi et al., 2021). However, it does change the dynamics of the strand fluctuations. In a recent model describing the dynamics of claudin-15 strands, we showed that lateral flexibility of claudin strands is due to flexible side-by-side *cis*-interactions pivoted at the short extracellular helix ECH (Fuladi et al., 2021). Mutation of A134 to proline locks this pivoted movement to switch between two out of three interfaces with limited occurrence of the third interface. Considering that the strands are made of an anti-parallel double row of claudins, this subtle change results in a relatively straight shape of the mutant strands. The mutation might also indirectly affect other potential *cis*-interfaces to influence strand morphology (Rossa et al., 2014a; Rossa et al., 2014b; Gong et al., 2015; Irudayanathan et al., 2018).

These findings corroborate the role of *cis*-interactions in conferring flexibility to the strand and their effect on strand morphology. They elucidate the indirect role of transmembrane helices, not necessarily on claudin assembly, but on modulating their dynamic properties by providing a microscopic description for large-scale properties of the strand at micro-meter length scales.

References

- Alberini, G., Benfenati, F., and Maragliano, L. (2017). A refined model of claudin-15 tight junction paracellular architecture by molecular dynamics simulations. *PLoS One* 12, e0184190. doi:10.1371/journal.pone.0184190
- Alberini, G., Benfenati, F., and Maragliano, L. (2018). Molecular dynamics simulations of ion selectivity in a claudin-15 paracellular channel. *J. Phys. Chem. B* 122, 10783–10792. doi:10.1021/acs.jpcc.8b06484
- Bansal, M., Kumar, S., and Velavan, R. (2000). Helanal: A program to characterise helix geometry in proteins. *J. Biomol. Struct. Dyn.* 17, 769–932.
- Best, R. B., Zhu, X., Shim, J., Lopes, P. E., Mittal, J., Feig, M., et al. (2012). Optimization of the additive charmm all-atom protein force field targeting improved sampling of the backbone ϕ , ψ and side-chain χ_1 and χ_2 dihedral angles. *J. Chem. Theory Comput.* 8, 3257–3273. doi:10.1021/ct300400x
- Claude, P., and Goodenough, D. A. (1973). Fracture faces of zonulae occludentes from tight and leaky epithelia. *J. Cell. Biol.* 58, 390–400. doi:10.1083/jcb.58.2.390
- Claude, P. (1978). Morphological factors influencing transepithelial permeability: A model for the resistance of the zonula occludens. *J. Membr. Biol.* 39, 219–232. doi:10.1007/BF01870332
- Clayburgh, D., Shen, L., and Turner, J. (2004). A porous defense: The leaky epithelial barrier in intestinal disease. *Lab. Invest.* 84, 282–291. doi:10.1038/labinvest.3700050
- Cordes, F. S., Bright, J. N., and Sansom, M. S. (2002). Proline-induced distortions of transmembrane helices. *J. Mol. Biol.* 323, 951–960. doi:10.1016/s0022-2836(02)01006-9
- Darden, T., York, D., and Pedersen, L. (1993). Particle mesh ewald: An $N \log(N)$ method for Ewald sums in large systems. *J. Chem. Phys.* 98, 10089–10092. doi:10.1063/1.464397
- Deeng, J., Chan, K.-Y., van der Sluis, E. O., Berninghausen, O., Han, W., Gumbart, J., et al. (2016). Dynamic behavior of trigger factor on the ribosome. *J. Mol. Biol.* 428, 3588–3602. doi:10.1016/j.jmb.2016.06.007

Data availability statement

The original contributions presented in the study are included in the article/Supplementary Material, further inquiries can be directed to the corresponding author.

Author contributions

All authors contributed to the writing of the manuscript. FK-A and SF designed the research. SF carried out the simulations. SF and SM analyzed the data and prepared the manuscript.

Funding

The work of FK-A, SF, and SM was supported by the National Science Foundation CAREER award to FK-A (MCB-1846021). This research is part of the Frontera computing project at the Texas Advanced Computing Center. Frontera is made possible by National Science Foundation award OAC-1818253.

Conflict of interest

The authors declare that the research was conducted in the absence of any commercial or financial relationships that could be construed as a potential conflict of interest.

Publisher's note

All claims expressed in this article are solely those of the authors and do not necessarily represent those of their affiliated organizations, or those of the publisher, the editors and the reviewers. Any product that may be evaluated in this article, or claim that may be made by its manufacturer, is not guaranteed or endorsed by the publisher.

- Farquhar, M. G., and Palade, G. E. (1963). Junctional complexes in various epithelia. *J. Cell. Biol.* 17, 375–412. doi:10.1083/jcb.17.2.375
- Feller, S. E., Zhang, Y., Pastor, R. W., and Brooks, B. R. (1995). Constant pressure molecular dynamics simulation: The Langevin piston method. *J. Chem. Phys.* 103, 4613–4621. doi:10.1063/1.470648
- Fromter, E., and Diamond, J. (1972). Route of passive ion permeation in epithelia. *Nat. New Biol.* 235, 9–13. doi:10.1038/newbio235009a0
- Fuladi, S., McGuinness, S., Shen, L., Weber, C. R., and Khalili-Araghi, F. (2021). Molecular mechanism of claudin-15 strand flexibility. *bioRxiv*. doi:10.1101/2021.12.07.471660
- Furuse, M., and Tsukita, S. (1999). Manner of interaction of heterogeneous claudin species within and between tight junction strands. *J. Cell. Biol.* 147, 891–903. doi:10.1083/jcb.147.4.891
- Gittes, F., Mickey, B., Nettleton, J., and Howard, J. (1993). Flexural rigidity of microtubules and actin filaments measured from thermal fluctuations in shape. *J. Cell. Biol.* 120, 923–934. doi:10.1083/jcb.120.4.923
- Gong, Y., Renigunta, V., Zhou, Y., Sunq, A., Wang, J., Yang, J., et al. (2015). Biochemical and biophysical analyses of tight junction permeability made of claudin-16 and claudin-19 dimerization. *Mol. Biol. Cell.* 26, 4333–4346. doi:10.1091/mbc.E15-06-0422
- Goodenough, D. A., and Revel, J. P. (1970). A fine structural analysis of intercellular junctions in the mouse liver. *J. Cell. Biol.* 45, 272–290. doi:10.1083/jcb.45.2.272
- Günzel, D., and Yu, A. S. L. (2013). Claudins and the modulation of tight junction permeability. *Physiol. Rev.* 93, 525–569. doi:10.1152/physrev.00019.2012
- Han, W., and Schulten, K. (2014). Fibril elongation by A β 17–42: Kinetic network analysis of hybrid-resolution molecular dynamics simulations. *J. Am. Chem. Soc.* 136, 12450–12460. doi:10.1021/ja507002p
- Han, W., and Schulten, K. (2012). Further optimization of a hybrid united-atom and coarse-grained force field for folding simulations: Improved backbone hydration and interactions between charged side chains. *J. Chem. Theory Comput.* 8, 4413–4424. doi:10.1021/ct300696c
- Han, W., Wan, C.-K., Jiang, F., and Wu, Y.-D. (2010). PACE force field for protein simulations. 1. full parameterization of version 1 and verification. *J. Chem. Theory Comput.* 6, 3373–3389. doi:10.1021/ct1003127
- Humphrey, W., Dalke, A., and Schulten, K. (1996). Vmd: Visual molecular dynamics. *J. Mol. Graph.* 14, 33–38. doi:10.1016/0263-7855(96)00018-5
- Inai, T., Kamimura, T., Hirose, E., Iida, H., and Shibata, Y. (2010). The protoplasmic or exoplasmic face association of tight junction particles cannot predict paracellular permeability or heterotypic claudin compatibility. *Eur. J. Cell. Biol.* 89, 547–556. doi:10.1016/j.ejcb.2010.01.003
- Irudayanathan, F. J., Wang, X., Wang, N., Willsey, S. R., Seddon, I. A., and Nangia, S. (2018). Self-assembly simulations of classic claudins—Insights into the pore structure, selectivity, and higher order complexes. *J. Phys. Chem. B* 122, 7463–7474. doi:10.1021/acs.jpcc.8b03842
- Jewel, Y., Liu, J., and Dutta, P. (2017). Coarse-grained simulations of conformational changes in the multidrug efflux transporter acrb. *Mol. Biosyst.* 13, 2006–2014. doi:10.1039/c7mb00276a
- Jorgensen, W. L., Chandrasekhar, J., Madura, J. D., Impey, R. W., and Klein, M. L. (1983). Comparison of simple potential functions for simulating liquid water. *J. Chem. Phys.* 79, 926–935. doi:10.1063/1.445869
- Klauda, J. B., Venable, R. M., Freites, J. A., O'Connor, J. W., Tobias, D. J., Mondragon-Ramirez, C., et al. (2010). Update of the charmm all-atom additive force field for lipids: Validation on six lipid types. *J. Phys. Chem. B* 114, 7830–7843. doi:10.1021/jp101759q
- Krause, G., Protze, J., and Piontek, J. (2015). Assembly and function of claudins: Structure-function relationships based on homology models and crystal structures. *Semin. Cell. Dev. Biol.* 42, 3–12. doi:10.1016/j.semcdb.2015.04.010
- Kumar, S., and Bansal, M. (1998). Geometrical and sequence characteristics of α -helices in globular proteins. *Biophys. J.* 75, 1935–1944. doi:10.1016/S0006-3495(98)77634-9
- Kumar, S., and Bansal, M. (1996). Structural and sequence characteristics of long alpha helices in globular proteins. *Biophys. J.* 71, 1574–1586. doi:10.1016/S0006-3495(96)79360-8
- MacKerell, A. D., Jr, Feig, M., and Brooks, C. L., III (2004). Extending the treatment of backbone energetics in protein force fields: Limitations of gas-phase quantum mechanics in reproducing protein conformational distributions in molecular dynamics simulations. *J. Comput. Chem.* 25, 1400–1415. doi:10.1002/jcc.20065
- MacKerell, A. J., Bashford, D., Bellot, M., Dunbrack, R. L., Evanseck, J., Field, M., et al. (1998). All-atom empirical potential for molecular modeling and dynamics studies of proteins. *J. Phys. Chem. B* 102, 3586–3616. doi:10.1021/jp973084f
- Marko, J. F., and Siggia, E. D. (1995). Stretching dna. *Macromolecules* 28, 8759–8770. doi:10.1021/ma00130a008
- Marrink, S. J., Risselada, H. J., Yefimov, S., Tieleman, D. P., and De Vries, A. H. (2007). The martini force field: Coarse grained model for biomolecular simulations. *J. Phys. Chem. B* 111, 7812–7824. doi:10.1021/jp071097f
- Milatz, S., Krug, S. M., Rosenthal, R., Günzel, D., Müller, D., Schulzke, J.-D., et al. (2010). Claudin-3 acts as a sealing component of the tight junction for ions of either charge and uncharged solutes. *Biochim. Biophys. Acta* 1798, 2048–2057. doi:10.1016/j.bbame.2010.07.014
- Milatz, S., Piontek, J., Hempel, C., Meoli, L., Grohe, C., Fromm, A., et al. (2017). Tight junction strand formation by claudin-10 isoforms and claudin-10a/-10b chimeras. *Ann. N. Y. Acad. Sci.* 1405, 102–115. doi:10.1111/nyas.13393
- Mineta, K., Yamamoto, Y., Yamazaki, Y., Tanaka, H., Tada, Y., Saito, K., et al. (2011). Predicted expansion of the claudin multigene family. *FEBS Lett.* 585, 606–612. doi:10.1016/j.febslet.2011.01.028
- Nakamura, S., Irie, K., Tanaka, H., Nishikawa, K., Suzuki, H., Saitoh, Y., et al. (2019). Morphologic determinant of tight junctions revealed by claudin-3 structures. *Nat. Commun.* 10, 816. doi:10.1038/s41467-019-08760-7
- Phillips, J., Braun, R., Wang, W., Gumbart, J., Tajkhorshid, E., Villa, E., et al. (2005). Scalable molecular dynamics with NAMD. *J. Comput. Chem.* 26, 1781–1802. doi:10.1002/jcc.20289
- Piontek, A., Rossa, J., Protze, J., Wolburg, H., Hempel, C., Günzel, D., et al. (2017). Polar and charged extracellular residues conserved among barrier-forming claudins contribute to tight junction strand formation. *Ann. N. Y. Acad. Sci.* 1397, 143–156. doi:10.1111/nyas.13341
- Piontek, J., Fritzsche, S., Cording, J., Richter, S., Hartwig, J., Walter, M., et al. (2011). Elucidating the principles of the molecular organization of heteropolymeric tight junction strands. *Cell. Mol. Life Sci.* 68, 3903–3918. doi:10.1007/s00018-011-0680-z
- Piontek, J., Krug, S. M., Protze, J., Krause, G., and Fromm, M. (2020). Molecular architecture and assembly of the tight junction backbone. *Biochim. Biophys. Acta. Biomembr.* 1862, 183279. doi:10.1016/j.bbame.2020.183279
- Piontek, J., Winkler, L., Wolburg, H., Müller, S., Zuleger, N., Piel, C., et al. (2008). formation of tight junction: Determinants of homophilic interaction between classic claudins. *FASEB J.* 22, 146–158. doi:10.1096/fj.07-8319com
- Rossa, J., Ploeger, C., Vorreiter, F., Saleh, T., Protze, J., Günzel, D., et al. (2014a). Claudin-3 and claudin-5 protein folding and assembly into the tight junction are controlled by non-conserved residues in the transmembrane 3 (TM3) and extracellular loop 2 (ECL2) segments. *J. Biol. Chem.* 289, 7641–7653. doi:10.1074/jbc.M113.531012
- Rossa, J., Protze, J., Kern, C., Piontek, A., Günzel, D., Krause, G., et al. (2014b). Molecular and structural transmembrane determinants critical for embedding claudin-5 into tight junctions reveal a distinct four-helix bundle arrangement. *Biochem. J.* 464, 49–60. doi:10.1042/BJ20140431
- Saitoh, Y., Suzuki, H., Tani, K., Nishikawa, K., Irie, K., Ogura, Y., et al. (2015). Tight junctions. Structural insight into tight junction disassembly by *Clostridium perfringens* enterotoxin. *Science* 347, 775–778. doi:10.1126/science.1261833
- Samanta, P., Wang, Y., Fuladi, S., Zou, J., Li, Y., Shen, L., et al. (2018). Molecular determination of claudin-15 organization and channel selectivity. *J. Gen. Physiol.* 150, 949–968. doi:10.1085/jgp.201711868
- Sasaki, H., Matsui, C., Furuse, K., Mimori-Kiyosue, Y., Furuse, M., and Tsukita, S. (2003). Dynamic behavior of paired claudin strands within apposing plasma membranes. *Proc. Natl. Acad. Sci. U. S. A.* 100, 3971–3976. doi:10.1073/pnas.0630649100
- Shen, L., Weber, C. R., Raleigh, D. R., Yu, D., and Turner, J. R. (2011). Tight junction pore and leak pathways: A dynamic duo. *Annu. Rev. Physiol.* 73, 283–309. doi:10.1146/annurev-physiol-012110-142150
- Shinoda, T., Shinya, N., Ito, K., Ohsawa, N., Terada, T., Hirata, K., et al. (2016). Structural basis for disruption of claudin assembly in tight junctions by an enterotoxin. *Sci. Rep.* 6, 33632. doi:10.1038/srep33632
- Staehelein, L. A. (1974). Structure and function of intercellular junctions. *Int. Rev. Cytol.* 39, 191–283. doi:10.1016/s0074-7696(08)60940-7
- Staehelein, L. (1973). Further observations on the fine structure of freeze-cleaved tight junctions. *J. Cell. Sci.* 13, 763–786. doi:10.1242/jcs.13.3.763
- Sugeta, H., and Miyazawa, T. (1967). General method for calculating helical parameters of polymer chains from bond lengths, bond angles, and internal-rotation angles. *Biopolymers* 5, 673–679. doi:10.1002/bip.1967.360050708
- Suzuki, H., Nishizawa, T., Tani, K., Yamazaki, Y., Tamura, A., Ishitani, R., et al. (2014). Crystal structure of a claudin provides insight into the architecture of tight junctions. *Science* 344, 304–307. doi:10.1126/science.1248571
- Suzuki, H., Tani, K., Tamura, A., Tsukita, S., and Fujiyoshi, Y. (2015). Model for the architecture of claudin-based paracellular ion channels through tight junctions. *J. Mol. Biol.* 427, 291–297. doi:10.1016/j.jmb.2014.10.020

- Tamura, A., and Tsukita, S. (2014). Paracellular barrier and channel functions of TJ claudins in organizing biological systems: Advances in the field of barrierology revealed in knockout mice. *Semin. Cell. Dev. Biol.* 36, 177–185. doi:10.1016/j.semcdb.2014.09.019
- Tsukita, S., Tanaka, H., and Tamura, A. (2019). The claudins: From tight junctions to biological systems. *Trends biochem. Sci.* 44, 141–152. doi:10.1016/j.tibs.2018.09.008
- Van Itallie, C. M., and Anderson, J. M. (2006). Claudins and epithelial paracellular transport. *Annu. Rev. Physiol.* 68, 403–429. doi:10.1146/annurev.physiol.68.040104.131404
- Van Itallie, C. M., Tietgens, A. J., and Anderson, J. M. (2017). Visualizing the dynamic coupling of claudin strands to the actin cytoskeleton through ZO-1. *Mol. Biol. Cell.* 28, 524–534. doi:10.1091/mbc.E16-10-0698
- Vecchio, A. J., and Stroud, R. M. (2019). Claudin-9 structures reveal mechanism for toxin-induced gut barrier breakdown. *Proc. Natl. Acad. Sci. U. S. A.* 116, 17817–17824. doi:10.1073/pnas.1908929116
- von Heijne, G. (1991). Proline kinks in transmembrane α -helices. *J. Mol. Biol.* 218, 499–503. doi:10.1016/0022-2836(91)90695-3
- Wan, C.-K., Han, W., and Wu, Y.-D. (2011). Parameterization of PACE force field for membrane environment and simulation of helical peptides and helix-helix association. *J. Chem. Theory Comput.* 8, 300–313. doi:10.1021/ct2004275
- Ward, M. D., Nangia, S., and May, E. R. (2017). Evaluation of the hybrid resolution pace model for the study of folding, insertion, and pore formation of membrane associated peptides. *J. Comput. Chem.* 38, 1462–1471. doi:10.1002/jcc.24694
- Wiggins, P. A., and Nelson, P. C. (2006). Generalized theory of semiflexible polymers. *Phys. Rev. E Stat. Nonlin. Soft Matter Phys.* 73, 031906. doi:10.1103/PhysRevE.73.031906
- Yamazaki, Y., Tokumasu, R., Kimura, H., and Tsukita, S. (2011). Role of claudin species-specific dynamics in reconstitution and remodeling of the zonula occludens. *Mol. Biol. Cell.* 22, 1495–1504. doi:10.1091/mbc.E10-12-1003
- Zhao, J., Krystofiak, E. S., Ballesteros, A., Cui, R., Van Itallie, C. M., Anderson, J. M., et al. (2018). Multiple claudin-claudin cis interfaces are required for tight junction strand formation and inherent flexibility. *Commun. Biol.* 1, 50. doi:10.1038/s42003-018-0051-5

Frontiers in Molecular Biosciences

Explores biological processes in living organisms
on a molecular scale

Focuses on the molecular mechanisms
underpinning and regulating biological processes
in organisms across all branches of life.

Discover the latest Research Topics

[See more](#) →

Frontiers

Avenue du Tribunal-Fédéral 34
1005 Lausanne, Switzerland
frontiersin.org

Contact us

+41 (0)21 510 17 00
frontiersin.org/about/contact



Frontiers in Molecular Biosciences

